

Search For the Rare Decay $K_L \rightarrow \pi^0 \pi^0 \mu^+ \mu^-$

by

David Graham Phillips II
Seattle, WA

B.S., University of Washington, 2003

A Dissertation presented to the Graduate Faculty
of the University of Virginia in Candidacy for the Degree of
Doctor of Philosophy

Department of Physics
University of Virginia

May, 2009

Search For the Rare Decay $K_L \rightarrow \pi^0 \pi^0 \mu^+ \mu^-$

© Copyright by

David Graham Phillips II

All Rights Reserved

May, 2009

Abstract

This thesis describes the search for $K_L \rightarrow \pi^0 \pi^0 \mu^+ \mu^-$, which was conducted using data collected by the KTeV Experiment at Fermi National Accelerator Laboratory in Batavia, Illinois. Although this decay mode is possible within the Standard Model, it is limited to a very narrow band of phase space. The HyperCP Experiment has recently observed three $\Sigma^+ \rightarrow p \mu^+ \mu^-$ events within a narrow dimuon mass range of $213.8 \text{ MeV}/c^2$ to $214.8 \text{ MeV}/c^2$. This suggests that the process could occur via a neutral intermediary particle, $\Sigma^+ \rightarrow p X^0 \rightarrow p \mu^+ \mu^-$, with an X^0 mass of $214.3 \text{ MeV}/c^2 \pm 0.5 \text{ MeV}/c^2$. Since the X^0 has a light mass and a low interaction probability, then it is most likely a new neutral boson that exists beyond the Standard Model. Recent theoretical predictions suggest that the decay mode $K_L \rightarrow \pi^0 \pi^0 \mu^+ \mu^-$ can also occur via the aforementioned neutral boson: $K_L \rightarrow \pi^0 \pi^0 X^0 \rightarrow \pi^0 \pi^0 \mu^+ \mu^-$. Therefore, in addition to a Standard Model measurement, the search for $K_L \rightarrow \pi^0 \pi^0 \mu^+ \mu^-$ is also carried out in an effort to address the viability of X^0 in explaining the HyperCP phenomena.

Measurement of the upper limits presented in this thesis were performed using blind analysis techniques. The upper limit of the decay $K_L \rightarrow \pi^0 \pi^0 \mu^+ \mu^-$ has been measured in this thesis to be $BR(K_L \rightarrow \pi^0 \pi^0 \mu^+ \mu^-) < 8.63 \times 10^{-11}$ at 90% confidence level. In addition, this thesis has measured the upper limit of the decay $K_L \rightarrow \pi^0 \pi^0 X^0 \rightarrow \pi^0 \pi^0 \mu^+ \mu^-$ to be $BR(K_L \rightarrow \pi^0 \pi^0 X^0 \rightarrow \pi^0 \pi^0 \mu^+ \mu^-) < 9.44 \times 10^{-11}$ at the 90% confidence level.

To my family for all of their love and support.

Allen gewidmet, von denen ich lernte.

Contents

List of Figures	v
List of Tables	x
1 Introduction	1
1.1 Neutral Kaons: A General Background	2
1.1.1 Charge, Parity and CP	2
1.1.2 The CKM Matrix	4
1.1.3 The Mass and Weak Eigenstates of the Neutral Kaons	7
1.2 $K_L \rightarrow \pi^0 \pi^0 \mu^+ \mu^-$	11
1.2.1 $K_L \rightarrow \pi^0 \pi^0 \mu^+ \mu^-$ In the Standard Model	11
1.2.2 $K_L \rightarrow \pi^0 \pi^0 \mu^+ \mu^-$ Beyond the Standard Model	14
1.3 Previous Measurements	16
2 The KTeV Experiment	17
2.1 Creation of the Neutral K_L Beams	19
2.1.1 Incident Proton Beam	21
2.1.2 Resulant Neutral K_L Beams	22
2.2 The KTeV Detector	26
2.2.1 Vacuum Decay Region	29
2.2.2 Charged Particle Spectrometer	31
2.2.3 Transition Radiation Detectors	36
2.2.4 Trigger Hodoscopes	39
2.2.5 Cesium Iodide Electromagnetic Calorimeter	39
2.2.6 Muon Identification System	45
2.2.7 90° Accidental Counter	51
3 Trigger and Associated Event Selection	53
3.1 Level 1 Trigger	54
3.1.1 Level 1 Signals	55

3.2	Level 2 Trigger	58
3.2.1	Hardware Cluster Counter	59
3.2.2	DC Hit Counters	62
3.3	Trigger Definitions	63
3.3.1	The Dimuon Trigger	63
3.3.2	The 2E-NCLUS Trigger	65
3.4	Level 3 Trigger	67
4	Event Reconstruction	69
4.1	Tracking	70
4.1.1	TDC and SOD	70
4.1.2	Track Finding Procedure	72
4.2	Clustering	76
4.2.1	Hardware Clustering	76
4.2.2	Software Clustering	77
4.2.3	Cluster Positioning	77
4.2.4	Cluster Energy Corrections	78
4.3	Vertexing	82
4.3.1	Track-Cluster Matching	83
4.3.2	Neutral Vertex Reconstruction	84
5	Monte Carlo Simulation	88
5.1	Production of Kaon Beams in Monte Carlo	89
5.2	Simulation of K_L Decays	92
5.2.1	The Signal Mode $K_L \rightarrow \pi^0 \pi^0 \mu^+ \mu^-$	92
5.2.2	The Normalization Mode $K_L \rightarrow \pi^0 \pi^0 \pi_D^0$	92
5.2.3	Charged Pions and Backgrounds	93
5.3	Particle Tracing and Interactions	95
5.3.1	Pair Production	96
5.3.2	Bremsstrahlung	98
5.3.3	δ -Rays	99
5.3.4	Multiple Scattering	101
5.3.5	Energy Loss in the Muon System	102
5.4	Detector Simulation	103
5.4.1	Photon Vetoes	103
5.4.2	Spectrometer System	104
5.4.3	VV' Hodoscope System	107
5.4.4	CsI Calorimeter Simulation	107
5.4.5	Muon ID System	110
5.5	Accidental Overlays	111
5.6	Trigger Simulation	112
5.7	Monte Carlo Samples	112

6	Branching Ratio Analysis	114
6.1	Data Reduction Procedure	115
6.1.1	E799 Data Runs	115
6.1.2	E799 Split Procedure	116
6.1.3	Crunch Procedure	117
6.1.4	Bad Spill Cut	122
6.2	Protocol of the Analysis	130
6.2.1	Motivation for Blind Analyses	130
6.2.2	Defining the Masked Signal Box Regions	132
6.3	Signal Mode Analysis	136
6.3.1	Initial Requirement on $m_{\mu\mu\gamma\gamma\gamma}$ and p_T^2	139
6.3.2	Requirements on $E_{cl}(\text{track})$ and p_{track}	139
6.3.3	Requirements on $m_{\gamma\gamma}$ and $m_{\mu\mu}$	144
6.3.4	Backgrounds to the Signal Mode	144
6.3.5	Opening the Masked Signal Boxes	153
6.4	Normalization Mode Analysis	160
6.4.1	Normalization Mode Analysis Requirements	160
6.4.2	K_L Flux Calculation	170
6.5	Uncertainties in the Flux	171
6.5.1	Branching Ratio of $K_L \rightarrow \pi^0\pi^0\pi^0$	171
6.5.2	Statistical Errors	172
6.5.3	Variation of Analysis Requirements	172
6.5.4	1999 p_z Distribution	174
6.5.5	Muon ID System Efficiency	174
6.5.6	Summary of Systematic Errors	178
6.6	Upper Limit on the Branching Ratio	179
7	Conclusion	181
	Bibliography	183

List of Figures

1.1	Box diagram depicting oscillations between the strong eigenstates of the neutral kaon.	7
1.2	(i) Tree diagram depicting $K^0 \rightarrow \pi^+\pi^-$ via W^\pm exchange. (ii) Penguin diagram depicting the same decay via the \bar{u} , \bar{c} , \bar{t} quark states.	10
2.1	A diagram of the Fermilab Accelerator Chain circa 1999. During fixed-target experiments such as KTeV, the recycler and the anti-proton source are not used. Schematic courtesy of the Fermilab Photo Archive [31].	20
2.2	Top view of the NM2 enclosure.	23
2.3	Top view of the KTeV detector in E799 configuration.	27
2.4	3D view of the KTeV detector in E799 configuration.	28
2.5	Cross-section of a KTeV Ring Counter. RC's were placed perpendicular to the beam direction with the outer radius bordering the inner edge of the vacuum decay region.	30
2.6	Side view of the KTeV Charged Particle Spectrometer with drift chambers and analysis magnet. In order to increase acceptance, the cross-sectional area of each drift chamber increases with distance from the target.	32
2.7	Schematic of wires within a drift chamber. The charged particle path is denoted by a solid arrow, while an ionization electron is illustrated with a dotted line.	35
2.8	Cross-section of a Spectrometer Anti.	37
2.9	Cross-section of a TRD plane.	38
2.10	V and V' trigger hodoscope banks.	40
2.11	3D view of the KTeV Cesium Iodide Electromagnetic Calorimeter. . .	41
2.12	Diagram of the Collar Anti. The bold black lines represent the position of the Collar Anti, whereas the small squares denote the crystals located in the inner region of the CsI.	46
2.13	Top view of the Muon Identification System.	46

2.14	A diagram of the Hadron Anti. The dimensions of the HA were 2.24 m \times 2.24 m.	48
2.15	MU2 counter bank. Dashed lines denote counter overlap regions. . . .	50
2.16	MU3X and MU3Y counter banks.	51
3.1	Possible HCC bit patterns and their weights for 2 \times 2 crystal arrays. Shaded blocks indicate that a bit has been turned <i>on</i>	61
3.2	Wire hit arrangements in a DC plane pair and the hit counts returned by the Kumquats and Bananas. Shaded circles indicate a DC anode wire with an in-time hit.	63
4.1	SOD Classification System.	73
4.2	SOD X-View distribution for tracks in a number of 1999 $K_L \rightarrow \pi^0 \pi^0 \pi_D^0$ normalization mode events. The distribution is centered on the cell spacing 6.35 mm, but the mean is brought down slightly by isolated hits located at 0.0 mm.	74
4.3	Mean E/p vs. p of K_{e3} calibrations electrons in small blocks. The plot was made after all cluster energy corrections (except the fudge factor) were applied. The fudge factor cancels out any small deviations in E/p with p [43].	82
4.4	Top-view illustration of three possible π^0 pairing combinations from four photons. Each π^0 is assumed to come from a two photon vertex. Numbers one through six are the photon vertex numbers. The best π^0 pairing is taken to be the one with the lowest χ_z^2 . In this case, picture (i) contains the best pairing.	87
6.1	Reconstructed π^0 mass (before π^0 mass cut) for the first of two π^0 s (labeling is arbitrary) in the 1997 MC.	118
6.2	Reconstructed π^0 mass (before π^0 mass cut) for the first of two π^0 s (labeling is arbitrary) in the 1999 MC.	119
6.3	Distribution of the variable E/p for one of two tracks in the signal mode trigger of the 1999 data. The peak at zero stems from MIPs, while the peak at one originates mainly from electrons and positrons.	121
6.4	Distribution of number of hits in MU3x for the 1999 data immediately after the MU3x hit requirement was implemented.	123
6.5	Distribution of number of hits in MU3x for the 1999 $K_L \rightarrow \pi^0 \pi^0 \mu^+ \mu^-$ MC immediately after the MU3x hit requirement was implemented.	124
6.6	Distribution of bad spills for the 1997 data set after the first crunch stage. The meaning of each bit is given in Table 6.1.	128
6.7	Distribution of bad spills for the 1999 data set after the first crunch stage.	129

6.8	p_T^2 vs. $m_{\mu\mu\gamma\gamma\gamma}$ scatter plot for 1999 $K_L \rightarrow \pi^0\pi^0\mu^+\mu^-$ MC events after all crunch requirements have been implemented. The masked signal box is open and is shown for display purposes only.	133
6.9	p_T^2 vs. $m_{\mu\mu\gamma\gamma\gamma}$ scatter plot for 1999 $K_L \rightarrow \pi^0\pi^0 X^0 \rightarrow \pi^0\pi^0\mu^+\mu^-$ MC events after all crunch requirements have been implemented. The masked signal box is open and is shown for display purposes only. . .	134
6.10	p_T^2 vs. $m_{\mu\mu\gamma\gamma\gamma}$ scatter plot for the 1999 data set after all crunch requirements have been implemented. The masked signal box (labeled <i>Masked Signal Box #1</i>) is closed.	135
6.11	$ p_{T,\mu\mu}^2 - p_{T,\pi\pi}^2 $ vs. $m_{\mu\mu}$ scatter plot for 1999 $X^0 \rightarrow \mu^+\mu^-$ MC events after all crunch requirements have been implemented. The masked signal box associated with this decay is open and is shown for display purposes only.	137
6.12	$ p_{T,\mu\mu}^2 - p_{T,\pi\pi}^2 $ vs. $m_{\mu\mu}$ scatter plot for the 1999 data set after all crunch requirements have been implemented. The masked signal box (labeled <i>Masked Signal Box #2</i>) is closed.	138
6.13	Distributions for $m_{\mu\mu\gamma\gamma\gamma}$ in the 1997 $K_L \rightarrow \pi^0\pi^0\mu^+\mu^-$ MC (top) and 1997 $K_L \rightarrow \pi^0\pi^0 X^0 \rightarrow \pi^0\pi^0\mu^+\mu^-$ MC (bottom) after all crunch requirements and just before the first requirement on $m_{\mu\mu\gamma\gamma\gamma}$ was implemented.	140
6.14	Distributions for $m_{\mu\mu\gamma\gamma\gamma}$ in the 1999 $K_L \rightarrow \pi^0\pi^0\mu^+\mu^-$ MC (top) and 1999 $K_L \rightarrow \pi^0\pi^0 X^0 \rightarrow \pi^0\pi^0\mu^+\mu^-$ MC (bottom) after all crunch requirements and just before the first requirement on $m_{\mu\mu\gamma\gamma\gamma}$ was implemented.	141
6.15	Distributions for p_T^2 in the 1997 $K_L \rightarrow \pi^0\pi^0\mu^+\mu^-$ MC (top) and 1997 $K_L \rightarrow \pi^0\pi^0 X^0 \rightarrow \pi^0\pi^0\mu^+\mu^-$ MC (bottom) after the requirement on $m_{\mu\mu\gamma\gamma\gamma}$ and just before the requirement on p_T^2 was implemented. . .	142
6.16	Distributions for p_T^2 in the 1999 $K_L \rightarrow \pi^0\pi^0\mu^+\mu^-$ MC (top) and 1999 $K_L \rightarrow \pi^0\pi^0 X^0 \rightarrow \pi^0\pi^0\mu^+\mu^-$ MC (bottom) after the requirement on $m_{\mu\mu\gamma\gamma\gamma}$ and just before the requirement on p_T^2 was implemented. . .	143
6.17	Distributions for $E_{cl}(\text{track1})$ in the 1997 $K_L \rightarrow \pi^0\pi^0\mu^+\mu^-$ MC (top) and 1997 $K_L \rightarrow \pi^0\pi^0 X^0 \rightarrow \pi^0\pi^0\mu^+\mu^-$ MC (bottom) after the requirement on p_T^2 and just before the requirement on $E_{cl}(\text{track})$ was implemented. The requirement on $E_{cl}(\text{track})$ was applied to both clusters associated with tracks.	145
6.18	Distributions for $E_{cl}(\text{track1})$ in the 1999 $K_L \rightarrow \pi^0\pi^0\mu^+\mu^-$ MC (top) and 1999 $K_L \rightarrow \pi^0\pi^0 X^0 \rightarrow \pi^0\pi^0\mu^+\mu^-$ MC (bottom) after the requirement on p_T^2 and just before the requirement on $E_{cl}(\text{track})$ was implemented. The requirement on $E_{cl}(\text{track})$ was applied to both clusters associated with tracks.	146

6.19	Distributions for p_{track1} in the 1997 $K_L \rightarrow \pi^0\pi^0\mu^+\mu^-$ MC (top) and 1997 $K_L \rightarrow \pi^0\pi^0X^0 \rightarrow \pi^0\pi^0\mu^+\mu^-$ MC (bottom) after the requirement on $E_{cl}(\text{track})$ and just before the requirement on p_{track} was implemented. The requirement on p_{track} was applied to both tracks. . .	147
6.20	Distributions for p_{track1} in the 1999 $K_L \rightarrow \pi^0\pi^0\mu^+\mu^-$ MC (top) and 1999 $K_L \rightarrow \pi^0\pi^0X^0 \rightarrow \pi^0\pi^0\mu^+\mu^-$ MC (bottom) after the requirement on $E_{cl}(\text{track})$ and just before the requirement on p_{track} was implemented. The requirement on p_{track} was applied to both tracks. . .	148
6.21	Distributions for the first of two reconstructed π^0 masses in the 1997 $K_L \rightarrow \pi^0\pi^0\mu^+\mu^-$ MC (top) and 1997 $K_L \rightarrow \pi^0\pi^0X^0 \rightarrow \pi^0\pi^0\mu^+\mu^-$ MC (bottom) after the requirement on p_{track} and just before the requirement on $m_{\gamma\gamma}$ was implemented. The requirement on $m_{\gamma\gamma}$ was applied to both reconstructed π^0 masses.	149
6.22	Distributions for the first of two reconstructed π^0 masses in the 1999 $K_L \rightarrow \pi^0\pi^0\mu^+\mu^-$ MC (top) and 1999 $K_L \rightarrow \pi^0\pi^0X^0 \rightarrow \pi^0\pi^0\mu^+\mu^-$ MC (bottom) after the requirement on p_{track} and just before the requirement on $m_{\gamma\gamma}$ was implemented. The requirement on $m_{\gamma\gamma}$ was applied to both reconstructed π^0 masses.	150
6.23	Distributions for $m_{\mu\mu}$ in the 1997 $K_L \rightarrow \pi^0\pi^0\mu^+\mu^-$ MC (top) and 1997 $K_L \rightarrow \pi^0\pi^0X^0 \rightarrow \pi^0\pi^0\mu^+\mu^-$ MC (bottom) after the requirement on $m_{\gamma\gamma}$ and just before the requirement on $m_{\mu\mu}$ was implemented.	151
6.24	Distributions for $m_{\mu\mu}$ in the 1999 $K_L \rightarrow \pi^0\pi^0\mu^+\mu^-$ MC (top) and 1999 $K_L \rightarrow \pi^0\pi^0X^0 \rightarrow \pi^0\pi^0\mu^+\mu^-$ MC (bottom) after the requirement on $m_{\gamma\gamma}$ and just before the requirement on $m_{\mu\mu}$ was implemented.	152
6.25	p_T^2 vs. $m_{\mu\mu\gamma\gamma\gamma\gamma}$ scatter plots for the 1999 $K_{\mu 4}$ background MC sample after all crunch requirements. The top plot is $K_{\mu 4}$ MC when the charged pion decays ($\pi^+ \rightarrow \mu^+\nu_\mu$, $\pi^- \rightarrow \mu^-\bar{\nu}_\mu$) and the bottom plot is when the charged pion in the $K_{\mu 4}$ MC punches through. The masked signal box is open and is shown for display purposes only.	154
6.26	p_T^2 vs. $m_{\mu\mu\gamma\gamma\gamma\gamma}$ scatter plot for the 1997 data set (top) after masked signal box #1 was opened. $ p_{T,\mu\mu}^2 - p_{T,\pi\pi}^2 $ vs. $m_{\mu\mu}$ scatter plot for the 1997 data set (bottom) after masked signal box #2 was opened. The dotted blue box indicates an opened masked signal box.	155
6.27	p_T^2 vs. $m_{\mu\mu\gamma\gamma\gamma\gamma}$ scatter plot for the 1999 data set (top) after masked signal box #1 was opened. $ p_{T,\mu\mu}^2 - p_{T,\pi\pi}^2 $ vs. $m_{\mu\mu}$ scatter plot for the 1999 data set (bottom) after masked signal box #2 was opened. The dotted blue box indicates an opened masked signal box.	156
6.28	p_T^2 vs. $m_{\mu\mu\gamma\gamma\gamma\gamma}$ scatter plot for the 1997 $K_L \rightarrow \pi^0\pi^0\mu^+\mu^-$ MC after all analysis requirements were implemented. The blue box indicates the location of masked signal box #1, which is open in the MC.	158

6.29	$ p_{T,\mu\mu}^2 - p_{T,\pi\pi}^2 $ vs. $m_{\mu\mu}$ scatter plot for the 1997 $K_L \rightarrow \pi^0\pi^0 X^0 \rightarrow \pi^0\pi^0\mu^+\mu^-$ MC after all analysis requirements were applied. The blue box indicates the location of masked signal box #2, which is open in the MC.	159
6.30	1997 $m_{ee\gamma\gamma\gamma\gamma}$ data/MC overlay just before requirement on this variable (top) and data/MC ratio immediately after the requirement had been implemented (bottom). Dots are data and histogram is MC. Normalization mode requirements are indicated in magenta.	162
6.31	1999 $m_{ee\gamma\gamma\gamma\gamma}$ data/MC overlay just before requirement on this variable (top) and data/MC ratio immediately after the requirement had been implemented (bottom). Dots are data and histogram is MC.	163
6.32	1997 p_T^2 data/MC overlay just before requirement on this variable (top) and data/MC ratio after all analysis requirements were implemented (bottom). Dots are data and histogram is MC.	164
6.33	1999 p_T^2 data/MC overlay just before requirement on this variable (top) and data/MC ratio after all analysis requirements were implemented (bottom). Dots are data and histogram is MC.	165
6.34	1997 $m_{\gamma\gamma}$ data/MC overlay for one of two reconstructed π^0 's just before requirement on this variable (top) and data/MC ratio after all analysis requirements were implemented (bottom). Dots are data and histogram is MC.	166
6.35	1999 $m_{\gamma\gamma}$ data/MC overlay for one of two reconstructed π^0 's just before requirement on this variable (top) and data/MC ratio after all analysis requirements were implemented (bottom). Dots are data and histogram is MC.	167
6.36	1997 Z_{vtx} data/MC overlay just before requirement on this variable (top) and data/MC ratio after all analysis requirements were implemented (bottom). Dots are data and histogram is MC.	168
6.37	1999 Z_{vtx} data/MC overlay just before requirement on this variable (top) and data/MC ratio after all analysis requirements were implemented (bottom). Dots are data and histogram is MC.	169
6.38	Data/MC ratio for the 1997 p_z distribution. Notice that the slope is consistent with zero.	175
6.39	Data/MC ratio for the 1999 p_z distribution before weighting. Note that the slope is noticeably non-zero.	176
6.40	Data/MC ratio for the 1999 p_z distribution after weighting. Notice that the slope is now consistent with zero.	177

List of Tables

1.1	Theoretical upper limits for $Br(\Sigma^+ \rightarrow pX^0 \rightarrow p\mu^+\mu^-)$ in the case of a scalar X^0 (top entry) and a vector X^0 (middle entry) . The bottom entry is the experimental limit measured by HyperCP.	15
1.2	Theoretical predictions for $Br(K_L \rightarrow \pi^0\pi^0X^0 \rightarrow \pi^0\pi^0\mu^+\mu^-)$. The subscripts P and A signify pseudoscalar and axial vector, respectively.	16
2.1	Run periods of E799 and E832.	19
3.1	L1 trigger symbols and their definitions for the dimuon trigger.	64
3.2	L2 trigger symbols and their definitions for the dimuon trigger.	64
3.3	L1 trigger symbols and their definitions for the 2E-NCLUS trigger.	66
3.4	L2 trigger symbols and their definitions for the 2E-NCLUS trigger.	66
3.5	Level 3 Requirements for the Dimuon and 2E-NCLUS Triggers.	68
5.1	Parameters determined by Malensek after fitting data from production of charged kaons on a 0.5 m Be target [44]. Units are produced particles per <i>steradian-GeV/c-incident proton</i>	90
5.2	Branching Ratios for K_L and π^0 decay modes [45].	94
5.3	Radiation length of select detector elements upstream of the CsI. Helium Bag 1a slowly filled with air over the 1997 run, but was replaced with an air tight Helium Bag in the 1999 run. DC1U was composed of Helium Bag 1b, the mylar windows for DC1 and the DC1 chamber gas. Helium Bag 2 was located between DC1 and DC2.	97
5.4	Probability of bremsstrahlung for upstream detector components.	100
5.5	Number of generated MC events for signal modes, normalization mode and all signal mode background samples. (D) refers to charged pion decay and (P) refers to charged pion punch-through. The branching ratio for the normalization mode was calculated in Section 5.2.2, while branching ratios for the background samples were obtained from Ref. [45]. *This branching ratio was estimated in Ref. [29].	113

6.1	1997 signal mode crunch requirement summary. Requirements are listed in the order in which they were implemented.	122
6.2	1999 signal mode crunch requirement summary. Requirements are listed in the order in which they were implemented.	125
6.3	1997 normalization mode crunch requirement summary. Requirements are listed in the order in which they were implemented.	125
6.4	1999 normalization mode crunch requirement summary. Requirements are listed in the order in which they were implemented. Note that the 1999 2E-NCLUS data set was pre-crunched.	126
6.5	E799 bad spill cut summary. The cut applies to the signal and normalization modes.	127
6.6	1997 signal mode analysis requirement summary. A_{MC,γ^*} signifies the acceptance for $K_L \rightarrow \pi^0\pi^0\mu^+\mu^-$ MC, while A_{MC,X^0} represents the acceptance for $K_L \rightarrow \pi^0\pi^0X^0 \rightarrow \pi^0\pi^0\mu^+\mu^-$ MC. Requirements are listed in the order in which they were implemented. Crunch level requirements are included in the calculation of total acceptance.	157
6.7	1999 signal mode analysis requirement summary. A_{MC,γ^*} signifies the acceptance for $K_L \rightarrow \pi^0\pi^0\mu^+\mu^-$ MC, while A_{MC,X^0} represents the acceptance for $K_L \rightarrow \pi^0\pi^0X^0 \rightarrow \pi^0\pi^0\mu^+\mu^-$ MC. Requirements are listed in the order in which they were implemented. Crunch level requirements are included in the calculation of total acceptance.	157
6.8	Normalization mode analysis requirement summary for the 1997 and 1999 data sets. Requirements are listed in the order in which they were implemented.	161
6.9	Normalization mode analysis requirement summary for the 1997 and 1999 $K_L \rightarrow \pi^0\pi^0\pi_D^0$ MC. Requirements are listed in the order in which they were implemented. Total acceptance is calculated by including all crunch and analysis requirements.	170
6.10	Summary of statistical errors on the signal and normalization mode acceptances.	173
6.11	Summary of systematic errors on the K_L flux.	178

Acknowledgments

At long last, it's finished! Endlich, die Arbeit ist fertig! Graduate School has been a tremendous learning experience that I shall never forget. Many people say that this will be the last thesis produced by the KTeV collaboration. I sincerely hope that this is not the case, as there are still a lot of interesting physics analyses that could be performed with the KTeV data sets.

Successful completion of this analysis would not have been possible without the assistance of many people. I would like to begin with expressing tremendous gratitude towards my advisor Bradley Cox, who has provided his guidance and insight from day one of graduate school. I would also like to thank Alexander Ledovskoy and Michael Ronquest for their help throughout this endeavor and for patiently teaching me the basics of the KTeV analysis framework and experiment. In addition, thanks go out to Leo Bellantoni of Fermi National Accelerator Laboratory for helping me get this analysis started. Keeping the hep cluster at the University of Virginia fully functional throughout the duration of this work could not have been possible without the help of Andrew Norman and Chad Materniak. To their efforts in maintaining the cluster and providing invaluable computing advise, I express my sincere gratitude. I am also thankful towards the following members of the high energy physics community for their friendship and invigorating discussions throughout the years: Michael Arenton, Sergio Conetti, Richard Imlay, Bob Hirosky, Bob Tschirhart, Ron Ray, Marj Corcoran, Rick Kessler, Dave Cockerill, Ken Bell, Al Tobias, David Smith, Michael

Balazs, Rachel Yohay, Shannon Zelitch and Emmanuel Munyangabe.

Surviving graduate school would not have been possible without the support of many close friends, all of whom I am extremely thankful to. First, I would like to begin by thanking all of my past and present fellow residents at the 104: Luke Langsjoen, Ryan Blair, Susan Vecchio, Jason Manning and Hussain Zaidi. You all have helped to make Charlottesville a truly great place to live. I would also like to express thanks towards Michael Carl, Erica Johnson, Crystal Capay, Grace Lee, William Hasselberger and Rebecca Jakob for being a constant source of support and encouragement throughout the years.

Finally, I would like to thank my parents, grandparents, my sister and the rest of my family. This work would have been impossible without your constant love, encouragement and support.

David Graham Phillips II

Charlottesville, Virginia

April 16, 2009

Chapter 1

Introduction

This thesis describes a search for the rare decay $K_L \rightarrow \pi^0 \pi^0 \mu^+ \mu^-$. The search was conducted using data taken from the KTeV experiment at Fermi National Accelerator Laboratory (Fermilab) in Batavia, Illinois. The aforementioned decay process is interesting in its own regard and difficult to detect. The general procedure of this analysis is to design a number of cuts that efficiently filter out background events and isolate $K_L \rightarrow \pi^0 \pi^0 \mu^+ \mu^-$. Section 1.1 gives a brief introduction to the physics of the neutral kaon system, which includes an overview of CP violation in the Standard Model. Section 1.2 presents the physics of the $K_L \rightarrow \pi^0 \pi^0 \mu^+ \mu^-$ decay and discusses how the neutral kaon system may be linked to physics beyond the Standard Model. The following chapters 2 through 7 provide an in-depth description of the KTeV experiment and the procedures used in these analyses.

1.1 Neutral Kaons: A General Background

Symmetries and conservation laws are two of the crucial cornerstones of physics. Symmetries of nature have been studied by many civilizations since ancient times. Laws such as the conservation of energy, momentum and angular momentum are well-known. These two cornerstones are linked by Noether's Theorem, which in application reveals that every symmetry in nature is linked to a conservation law. Conservation of momentum results from the invariance of a system that has symmetry under translations in space. By construction, conservation of angular momentum occurs when a system is symmetric with respect to rotation. Furthermore, since the laws of physics are invariant (symmetric) under translations in time, then energy is conserved. This can be extended to the invariance of mass in relativity, which stems from the conservation of energy and momentum in a closed system. Such invariance principles and symmetries are central in the study of physical phenomena.

1.1.1 Charge, Parity and CP

The three important symmetries of particle physics are charge conjugation (C), Parity (P) and Time Reversal (T). Together these three symmetries lay out the foundation of particle physics. In general, the charge conjugation operator C changes the sign of the charge and magnetic moment of a particle. However, in relativistic quantum mechanics C changes a particle state to its anti-particle state. In both cases, the operator C leaves spin and all co-ordinates unchanged. The parity operator P

changes the sign of all spatial co-ordinates, thus reversing the momentum of a particle state without flipping its spin. In self-explanatory fashion, the time reversal operator T reverses the direction of time in a physical process.

Until the mid-twentieth century, physicists strongly believed that all physical processes were invariant under C , P and T individually. In the early fifties, a problem known as the *tau-theta puzzle* caught physicists in a quandary. The problem centered around two strange mesons, known as τ and θ , that were identical in every respect except for one crucial feature: they decayed into states of opposite parity. Both particles decay via the weak interaction. In 1956, Lee and Yang suggested that τ and θ were actually the same particle (now known as the charged kaon), but one of these decays violates parity [1]. They knew that conservation of parity had been extensively proven in regards to the electromagnetic and strong interactions. However, at that time, there had been no tests for conservation of parity in the weak interaction. They therefore suggested an experimental test, which was carried out by C.S. Wu in 1957 [2]. In her test, Wu found that parity was maximally violated. The result was shocking. In fact, maximal parity violation and charge conjugation violation turned out to be typical of the weak interaction.

However, in spite of C and P being maximally violated in the weak interaction individually, the combination of C and P seemed to be perfectly conserved. Theorists and experimentalists alike seemed content with the idea of conservation of CP in the weak interaction. However, nearly a decade later in 1964, the experimentalists struck

again. This time around, Cronin and Fitch discovered CP violation in the decay $K_2 \rightarrow \pi^+ \pi^-$ [3].

1.1.2 The CKM Matrix

In order to fully understand the neutral kaon system, one must first learn about the underlying quark substructure. In total, there are six quarks and they are divided into three generations:

$$\begin{pmatrix} u \\ d \end{pmatrix}, \begin{pmatrix} c \\ s \end{pmatrix}, \begin{pmatrix} t \\ b \end{pmatrix}$$

In addition, there are six leptons and they are also divided into three generations:

$$\begin{pmatrix} \nu_e \\ e \end{pmatrix}, \begin{pmatrix} \nu_\mu \\ \mu \end{pmatrix}, \begin{pmatrix} \nu_\tau \\ \tau \end{pmatrix}$$

The weak interaction allows quark transitions to take place within and between quark generations. Mixing due to the weak force is described by a 3×3 unitary matrix known as the Cabibbo-Kobayashi-Maskawa (CKM) matrix [4]:

$$\begin{pmatrix} d' \\ s' \\ b' \end{pmatrix} = V_{CKM} \begin{pmatrix} d \\ s \\ b \end{pmatrix}, V_{CKM} = \begin{pmatrix} V_{ud} & V_{us} & V_{ub} \\ V_{cd} & V_{cs} & V_{cb} \\ V_{td} & V_{ts} & V_{tb} \end{pmatrix} \quad (1.1)$$

More precisely, the CKM matrix portrays how the weak interaction quark eigenstates (d', s' and b') are related to the quark mass eigenstates (d, s and b) by effectively

describing the probability of weak transitions between specified quark eigenstates. For example, the matrix element V_{us} details the likelihood of an $s \rightarrow u + W^-$ transition. Due to the unitarity condition, the CKM matrix elements are not independent. The standard representation of the CKM matrix employs three mixing angles θ_{12} , θ_{13} , θ_{23} and a CP phase δ_{13} [5]:

$$V_{CKM} = \begin{pmatrix} c_{12}c_{13} & s_{12}c_{13} & s_{13}e^{-i\delta_{13}} \\ -s_{12}c_{23} - c_{12}s_{23}s_{13}e^{-i\delta_{13}} & c_{12}c_{23} - s_{12}s_{23}s_{13}e^{-i\delta_{13}} & s_{23}c_{13} \\ s_{12}s_{23} - c_{12}c_{23}s_{13}e^{-i\delta_{13}} & -c_{12}s_{23} - s_{12}c_{23}s_{13}e^{-i\delta_{13}} & c_{23}c_{13} \end{pmatrix}, \quad (1.2)$$

where $s_{ij} = \sin\theta_{ij}$, $c_{ij} = \cos\theta_{ij}$ and the indices $i,j = 1,2,3$ are the *generation* labels. The two indices on each mixing angle signify the mixing between two specific generations. Mixing between two given generations will vanish, when one of the three mixing angles vanishes. This is best exemplified by the case of Cabibbo mixing, in which mixing only occurs between the first two generations in the limit $\theta_{13} = \theta_{23} = 0$. Here, the Cabibbo angle θ_{12} represents mixing between the first two generations [6]. The CP phase δ_{13} is located in the range $0 \leq \delta_{13} < 2\pi$. A non-zero value of δ_{13} indicates CP violation. One should also note that mixing between lepton generations is also possible and is described by an analogous mixing matrix. However, a discussion of lepton mixing phenomena is outside the scope of this thesis.

Widely employed by experimental particle physicists is an approximation to the aforementioned parametrization by Wolfenstein [7]. By expanding all elements of the

CKM matrix in powers of $\lambda = \sin\theta_{12}$, Wolfenstein repackages the matrix as:

$$V_{CKM} = \begin{pmatrix} 1 - \frac{\lambda^2}{2} & \lambda & A\lambda^3(\rho - i\eta) \\ -\lambda & 1 - \frac{\lambda^2}{2} & A\lambda^2 \\ A\lambda^3(1 - \rho - i\eta) & -A\lambda^2 & 1 \end{pmatrix} + \sum_{n=4}^N O(\lambda^n), \quad (1.3)$$

Orders λ^4 and higher may be found in [8]. The four parameters λ , A , ρ and η are obtained experimentally. They are currently given as [9,10]:

$$\begin{aligned} \lambda &= 0.2252 \pm 0.0008 \pm 0.0021, \\ A &= 0.818^{+0.007}_{-0.017}, \\ \bar{\eta} &= 0.340^{+0.017}_{-0.045}, \\ \bar{\rho} &= 0.221^{+0.064}_{-0.028}, \end{aligned} \quad (1.4)$$

where

$$\begin{aligned} \bar{\eta} &= \eta \left(1 - \frac{\lambda^2}{2}\right), \\ \bar{\rho} &= \rho \left(1 - \frac{\lambda^2}{2}\right). \end{aligned} \quad (1.5)$$

In the Wolfenstein parametrization, the magnitude of the complex phase η describes CP violating phenomena. For lower order terms in λ , these effects are only manifest in the V_{ub} and V_{td} elements of the CKM matrix. However, one can readily observe CP violating effects in the kaon sector through higher order terms of order λ^4 and λ^5 , which would appear in the V_{ts} and V_{cd} matrix elements respectively. The next section will discuss in detail how the Standard Model explains CP violation in the neutral kaon system.

1.1.3 The Mass and Weak Eigenstates of the Neutral Kaons

The neutral kaon belongs to a class of particles known as strange mesons. A strange meson possesses two quarks, one of which is a strange quark. In the case of a neutral kaon, the other quark is a down quark. Produced in the strong interaction, the two strong interaction eigenstates of the neutral kaon are:

$$\begin{aligned} K^0 &= d\bar{s}(S = +1), \\ \bar{K}^0 &= \bar{d}s(S = -1), \end{aligned} \tag{1.6}$$

where S is the quantum number for strangeness. Strangeness is not conserved under the weak interaction. As a result, oscillations between the two eigenstates of the neutral kaon can occur via a second order weak interaction ($\Delta S = 2$), as illustrated in Figure 1.1.

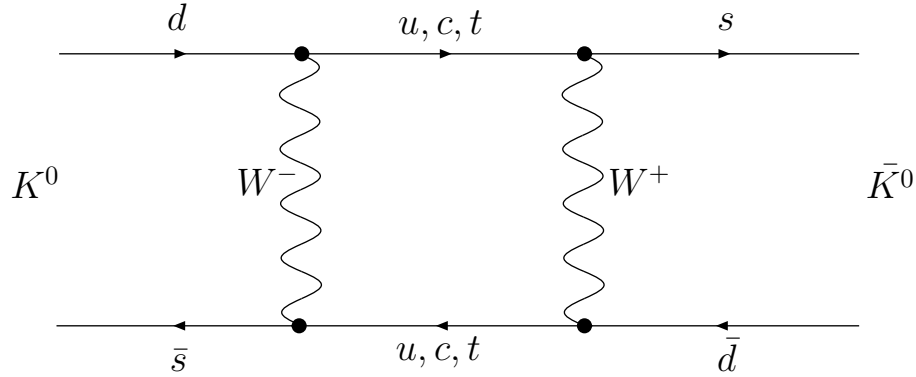


Figure 1.1: Box diagram depicting oscillations between the strong eigenstates of the neutral kaon.

Due to these oscillations, the strong eigenstates do not describe the mass eigen-

states of the neutral kaon system. Gell-Mann and Pais therefore proposed formulating eigenstates of C [11]:

$$\begin{aligned} |K_1\rangle &= \frac{1}{\sqrt{2}}(|K^0\rangle + |\bar{K}^0\rangle), \\ |K_2\rangle &= \frac{1}{\sqrt{2}}(|K^0\rangle - |\bar{K}^0\rangle). \end{aligned} \quad (1.7)$$

Now $C|K^0\rangle = |\bar{K}^0\rangle$ and $C|\bar{K}^0\rangle = |K^0\rangle$, so by construction:

$$\begin{aligned} C|K_1\rangle &= |K_1\rangle, \\ C|K_2\rangle &= -|K_2\rangle. \end{aligned} \quad (1.8)$$

This shows that K_1 and K_2 are eigenstates of C with eigenvalues $+1$ and -1 respectively. In addition, $CP|K^0\rangle = |\bar{K}^0\rangle$ and $CP|\bar{K}^0\rangle = |K^0\rangle$, so K_1 and K_2 are also eigenstates of CP with K_1 being referred to as the CP -even state, while K_2 is known as the CP -odd state:

$$\begin{aligned} CP|K_1\rangle &= |K_1\rangle, \\ CP|K_2\rangle &= -|K_2\rangle. \end{aligned} \quad (1.9)$$

Already mentioned in section 1.1.1, CP violation was initially discovered in a decay of the K_2 particle. This means that the weak eigenstates K_1 and K_2 are also not suitable candidates for mass eigenstates of the neutral kaon system. As an alternative, the weak eigenstates are expressed as:

$$\begin{aligned} |K_L\rangle &= \frac{1}{\sqrt{1+|\epsilon|^2}}(|K_2\rangle + \epsilon|K_1\rangle), \\ |K_S\rangle &= \frac{1}{\sqrt{1+|\epsilon|^2}}(|K_1\rangle + \epsilon|K_2\rangle). \end{aligned} \quad (1.10)$$

In the two above relations, K_L and K_S are the long-lived and short-lived states of the neutral kaon respectively. According to the most recent measurements, the mean lifetime of the K_L is nearly 566 times longer than that of the K_S [12,13]. The coefficient ϵ represents the amount of *indirect* CP violation within the structure of the K_L and K_S wavefunctions, which manifests as a result of neutral kaon mixing described earlier. Basically, the K_L and the K_S contain a small admixture of incorrect CP , which is represented by ϵ . The value of the parameter ϵ was initially measured to be on the order of 2.3×10^{-3} [3].

However, *direct* CP violation within the K_L can also occur, such as when the K_2 ($CP = -1$) decays into $\pi^+\pi^-$ ($CP = +1$) [3]. Essentially, anytime a state of pure CP within K_L or K_S decays into a state of different CP , this is referred to as *direct* CP violation and is denoted by the parameter ϵ' . According to the Standard Model, *direct* CP violation arises due to interference between the tree diagram in figure 1.2(i) and the penguin diagram in figure 1.2(ii) [14].

Direct CP violation is sought out experimentally by measuring $\text{Re}(\frac{\epsilon'}{\epsilon})$, where to first order:

$$\frac{\Gamma(K_L \rightarrow \pi^+\pi^-)/\Gamma(K_S \rightarrow \pi^+\pi^-)}{\Gamma(K_L \rightarrow \pi^0\pi^0)/\Gamma(K_S \rightarrow \pi^0\pi^0)} \simeq 1 + 6\text{Re}\left(\frac{\epsilon'}{\epsilon}\right). \quad (1.11)$$

If $\text{Re}(\frac{\epsilon'}{\epsilon})$ is measured to be non-zero, then this indicates *direct* CP violation in the neutral kaon system.

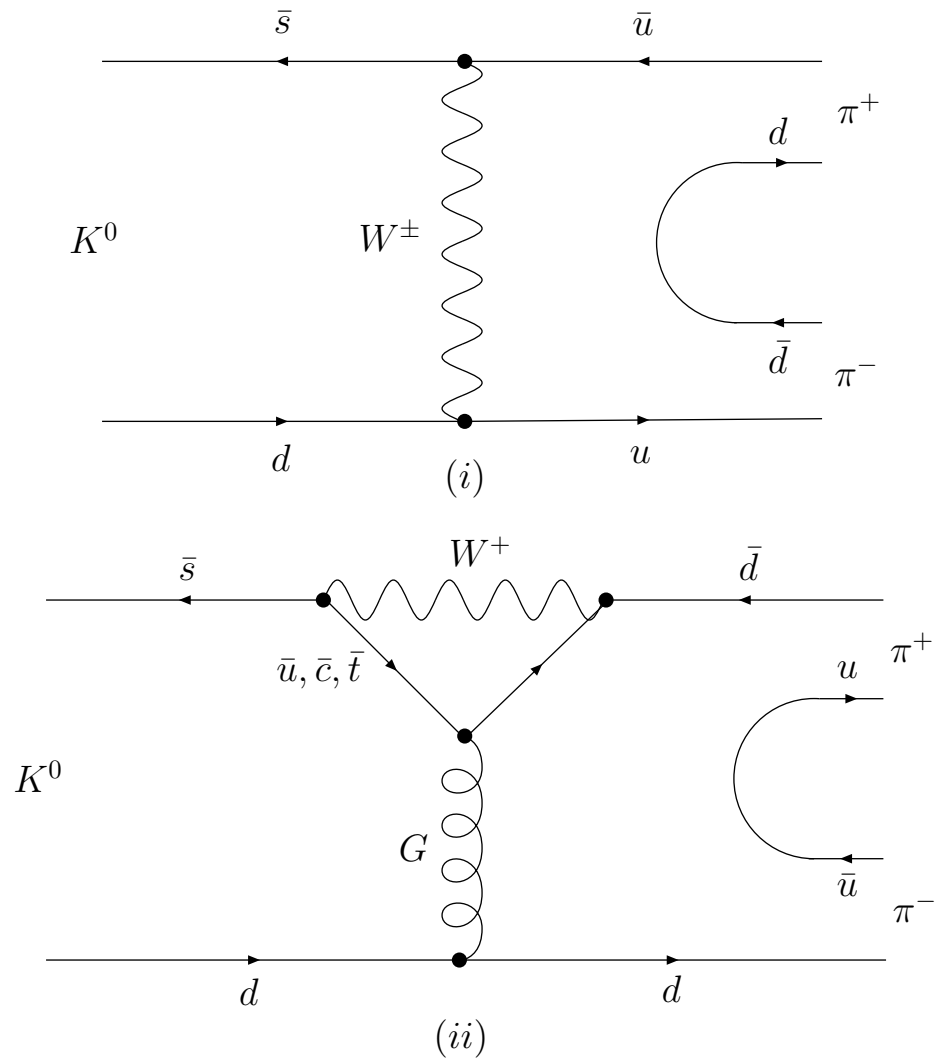


Figure 1.2: (i) Tree diagram depicting $K^0 \rightarrow \pi^+\pi^-$ via W^\pm exchange. (ii) Penguin diagram depicting the same decay via the $\bar{u}, \bar{c}, \bar{t}$ quark states.

1.2 $K_L \rightarrow \pi^0 \pi^0 \mu^+ \mu^-$

In the Standard Model, the dimuon system within the $K_L \rightarrow \pi^0 \pi^0 \mu^+ \mu^-$ mode arises via an off-shell photon. Beyond the Standard Model, there are other possible origins of the dimuon. In 2005, the HyperCP experiment announced the observation of three events for the decay $\Sigma^+ \rightarrow p \mu^+ \mu^-$ located at an invariant dimuon mass of (214.3 ± 0.5) MeV [21]. Due to the narrow dimuon mass range of these three events, a new neutral boson (X^0) with a mass of (214.3 ± 0.5) MeV has been suggested as the intermediary particle for the dimuon system, allowing the HyperCP decay to occur via the following process: $\Sigma^+ \rightarrow p X^0 \rightarrow p \mu^+ \mu^-$. The X^0 introduces a potential new contribution ($K_L \rightarrow \pi^0 \pi^0 X^0 \rightarrow \pi^0 \pi^0 \mu^+ \mu^-$) to the branching ratio of $K_L \rightarrow \pi^0 \pi^0 \mu^+ \mu^-$. The aforementioned contribution would enhance the branching ratio to a level higher than the possible sensitivity of this analysis and, in that regard, provides a direct test to the viability of X^0 as an explanation of the HyperCP result.

1.2.1 $K_L \rightarrow \pi^0 \pi^0 \mu^+ \mu^-$ In the Standard Model

The decay $K_L \rightarrow \pi^0 \pi^0 \mu^+ \mu^-$ is interesting from a theoretical perspective, since it serves as a direct probe of chiral perturbation theory to the fourth ($O(p^4)$) and sixth ($O(p^6)$) orders. In some regards, a measurement of $K_L \rightarrow \pi^0 \pi^0 \gamma$ could seem to be more accessible than $K_L \rightarrow \pi^0 \pi^0 \mu^+ \mu^-$ since the former decay has a far higher branching ratio than the latter. The amplitude of $K_L \rightarrow \pi^0 \pi^0 \gamma$ vanishes at $O(p^4)$ for real photons in chiral perturbation theory. Moreover, the decay $K_L \rightarrow \pi^0 \pi^0 \gamma$

has a serious background from $K_L \rightarrow 3\pi^0$ (with one missing photon). When viewing the problem from that standpoint, a measurement of $K_L \rightarrow \pi^0\pi^0\mu^+\mu^-$ is preferable, since it has a small background. However, detection of the decay $K_L \rightarrow \pi^0\pi^0\mu^+\mu^-$ is difficult due to the narrow band of phase space available to this mode. Due to limitations of phase space, the branching ratio of $K_L \rightarrow \pi^0\pi^0\mu^+\mu^-$ is highly suppressed. Although a Standard Model calculation of the branching ratio of $K_L \rightarrow \pi^0\pi^0\mu^+\mu^-$ has not yet been performed, the matrix element for this decay may still be evaluated by substituting m_μ for m_e in the matrix element for $K_L \rightarrow \pi^0\pi^0e^+e^-$ and taking the appropriate limits [22].

The amplitude of $K_L \rightarrow \pi^0\pi^0\mu^+\mu^-$ is divided into two terms. The first term uses the lowest multipole in the matrix element of $K_L \rightarrow \pi^0\pi^0\gamma$, which is a first order E2 transition [23]:

$$A_{E2}(K_L \rightarrow \pi^0(p_1)\pi^0(p_2)\gamma(k)) = \frac{e|f_s|g_{E2}}{M_K^4} \frac{(p_1 - p_2) \cdot k}{\Lambda^2} [(\epsilon^\mu \cdot p_{1\mu})(k \cdot p_2) - (\epsilon^\mu \cdot p_{2\mu})(k \cdot p_1)], \quad (1.12)$$

where $\epsilon^\mu = (\frac{e}{k^2})\bar{u}(k_-)\gamma^\mu v(k_+)$ is the photon polarization four-vector. Λ is a mass parameter that characterizes the effective size ($\Lambda \propto R^{-1}$) of the interaction region and p_1 , p_2 and k are the four-momenta of the indicated particles. The factor $|f_s|$ is determined by:

$$\Gamma(K_S \rightarrow \pi^+\pi^-) = \frac{|f_s|^2}{16\pi M_K} \sqrt{1 - \frac{4m_\pi^2}{M_K^2}}. \quad (1.13)$$

The reader may have noticed that an extra factor of $e|f_s|$ was included in the above

relation. Ref. [24] uses the factor $e|f_s|g_{E1}$ (in the corresponding E1 term) as a constant of dimension mass, whereas the authors in Ref. [23] use g_{E2} as a constant with the dimensions of mass. The former formulation is more advisable in the context of this thesis, since it is already actively used in the KTeV Monte Carlo generator.

The second term is a virtual photon amplitude associated with the process $K_L \rightarrow \pi^0 \pi^0 \gamma^*$ [23]:

$$A_{\gamma^*}(K_L \rightarrow \pi^0 \pi^0 \gamma^*) = \frac{e|f_s|g_{CR}}{M_K^2} \Phi(k^2, p \cdot k) [(p \cdot k)k_\mu - k^2 p_\mu] \epsilon^\mu, \quad (1.14)$$

where $p = p_1 + p_2$, $k = k_+ + k_-$ and $g_{CR} = \frac{-\langle R^2 \rangle M_K^2}{3}$. $\langle R^2 \rangle$ is the mean square charge radius of K^0 . After some repackaging, the function $\Phi(k^2, p \cdot k)$ has been calculated in chiral perturbation theory to be [25]:

$$\begin{aligned} \Phi(k^2, p \cdot k) = & \frac{eg}{192\pi^2 F^3} \left\{ \ln \frac{M_K^2}{m_\pi^2} \left(\frac{s_\pi - m_\pi^2}{s_\pi - M_K^2} \right) + \left(\frac{M_K^2 - m_\pi^2}{M_K^2 - s_\pi} \right) \left[G\left(\frac{k^2}{4M_K^2}\right) \right. \right. \\ & \left. \left. - G\left(\frac{k^2}{4m_\pi^2}\right) \right] + 3w_s - \frac{1}{3} + G\left(\frac{k^2}{4m_\pi^2}\right) \right\} + O(p^6), \end{aligned} \quad (1.15)$$

where k^2 spans the range $\{0, (M_K - 2m_\pi)^2\}$ and $s_\pi = (p_1 + p_2)^2$. F is the pion decay constant in lowest order ($F \approx F_\pi = 93 \text{ MeV}$) and g is the octet coupling constant determined from $K \rightarrow 2\pi$ decays ($g \simeq 3.14 \times 10^{-7}$). For $x \leq 1$,

$$G(x) = 2 \left(\frac{1}{x} - 1 \right) \left[\sqrt{\frac{1}{x} - 1} \arcsin \sqrt{x} - 1 \right]. \quad (1.16)$$

The final important step in formulating the decay rate is calculating the square of

the total amplitude. Performing this operation yields:

$$\begin{aligned}
|A_{E2}A_{\gamma^*}| &= -\frac{2}{3} \left(\frac{e^2|f_s|}{k^2 M_K^2 \Lambda} \right)^2 \text{Re}(g_{E2} < R^2 > \Phi(k^2, p \cdot k)^*) [(p_1 - p_2) \cdot k] \Upsilon_{\mu\nu} L_{\mu\nu}^{\mu\nu}, \\
|A_{E2}|^2 &= 2 \left(\frac{e^2|f_s|g_{E2}}{k^2 M_K^4 \Lambda^2} \right)^2 [(p_1 - p_2) \cdot k]^2 K_{\mu\nu} L_{\mu\nu}^{\mu\nu}, \\
|A_{\gamma^*}|^2 &= 2 \left(\frac{e^2|f_s| < R^2 >}{3k^2} \right)^2 \Phi(k^2, p \cdot k)^2 \kappa_{\mu\nu} L_{\mu\nu}^{\mu\nu},
\end{aligned} \tag{1.17}$$

where

$$\begin{aligned}
L_{\mu\nu}^{\mu\nu} &= \frac{1}{2} \sum_{\mu spins} [\bar{u}(k_-) \gamma^\mu v(k_+)] [\bar{u}(k_-) \gamma^\nu v(k_+)]^* \\
&= \frac{1}{2} \text{Tr}[(\gamma_\mu k_-^\mu + m_\mu) \gamma^\mu (\gamma_\nu k_+^\mu + m_\mu) \gamma^\nu]
\end{aligned} \tag{1.18}$$

is the rank 2 tensor associated with the muon vertex and

$$\begin{aligned}
K_{\mu\nu} &= [(k \cdot p_2)p_{1\mu} - (k \cdot p_1)p_{2\mu}] [(k \cdot p_2)p_{1\nu} - (k \cdot p_1)p_{2\nu}], \\
\kappa_{\mu\nu} &= [(p \cdot k)k_\mu - k^2 p_\mu] [(p \cdot k)k_\nu - k^2 p_\nu], \\
\Upsilon_{\mu\nu} &= [(k \cdot p_2)p_{1\mu} - (k \cdot p_1)p_{2\mu}] [(p \cdot k)k_\nu - k^2 p_\nu].
\end{aligned} \tag{1.19}$$

1.2.2 $K_L \rightarrow \pi^0 \pi^0 \mu^+ \mu^-$ Beyond the Standard Model

Discussion of $K_L \rightarrow \pi^0 \pi^0 \mu^+ \mu^-$ beyond the Standard Model has focused on a decay channel in which the dimuon originates from a new neutral boson X^0 of mass 214.3 MeV. Early studies rule out the possibility of scalar or vector couplings (see Table 1.1), thereby leaving an axial vector or pseudoscalar X^0 as the only viable candidates for the HyperCP particle [26,27]. One recent model suggests that the X^0 can be identified with the light pseudoscalar Higgs boson in the next-to-minimal

Decay Mode	Branching Ratio	Ref.
$\Sigma^+ \rightarrow pX_S^0 \rightarrow p\mu^+\mu^-$	$< 6.0 \times 10^{-11}$	[26]
$\Sigma^+ \rightarrow pX_V^0 \rightarrow p\mu^+\mu^-$	$< 3.0 \times 10^{-11}$	[26]
$\Sigma^+ \rightarrow pX^0 \rightarrow p\mu^+\mu^-$	$(3.1_{-1.9}^{+2.4}(stat) \pm 1.5(syst)) \times 10^{-8}$	[21]

Table 1.1: Theoretical upper limits for $Br(\Sigma^+ \rightarrow pX^0 \rightarrow p\mu^+\mu^-)$ in the case of a scalar X^0 (top entry) and a vector X^0 (middle entry) . The bottom entry is the experimental limit measured by HyperCP.

supersymmetric Standard Model (NMSSM) [28]. In light of these recent studies, this thesis will attempt to experimentally determine whether a pseudoscalar X^0 provides an accurate explanation for the phenomenon observed by HyperCP. The interaction of a pseudoscalar X^0 is described by [26,27]:

$$L_{int} = [\bar{d}(ig_q\gamma_5)sX_P^0 + h.c.] + i\bar{\mu}g_\mu\gamma_5\mu X_P^0 \quad (1.20)$$

The above relation only assumes a quark coupling that leads to a flavor changing $s \rightarrow \bar{d}X^0$ process. This leads to an amplitude of the form [27]:

$$A(K_L \rightarrow \pi^0\pi^0X_P^0) = \frac{\sqrt{2}\text{Re}(g_q)\{F[(p_1 + p_2) \cdot p_H] + G[(p_1 - p_2) \cdot p_H] + Rp_H^2\}}{M_K(m_s + m_d)}, \quad (1.21)$$

where $F = 5.832$, $G = 4.703$, g_q is the flavor changing coupling and

$$R = \frac{M_K(p_1 + p_2 + p_H) \cdot p_2}{f_\pi(p_1 + p_2 + p_H) \cdot (p_1 + p_2)}. \quad (1.22)$$

Decay Mode	Branching Ratio	Ref.
$K_L \rightarrow \pi^0 \pi^0 X_P^0 \rightarrow \pi^0 \pi^0 \mu^+ \mu^-$	8.02×10^{-9} $(8.3_{-6.6}^{+7.5}) \times 10^{-9}$	[27] [26]
$K_L \rightarrow \pi^0 \pi^0 X_A^0 \rightarrow \pi^0 \pi^0 \mu^+ \mu^-$	$(1.0_{-0.8}^{+0.9}) \times 10^{-10}$	[26]

Table 1.2: Theoretical predictions for $Br(K_L \rightarrow \pi^0 \pi^0 X^0 \rightarrow \pi^0 \pi^0 \mu^+ \mu^-)$. The subscripts P and A signify pseudoscalar and axial vector, respectively.

1.3 Previous Measurements

This thesis shall present the first experimental study of $K_L \rightarrow \pi^0 \pi^0 \mu^+ \mu^-$. There have been no published calculations of the branching ratio of this decay inside the Standard Model. A list of beyond the Standard Model theoretical predictions for $K_L \rightarrow \pi^0 \pi^0 \mu^+ \mu^-$ can be found in Table 1.2.

Chapter 2

The KTeV Experiment

The primary motivation of the KTeV experiment is the investigation of CP violating phenomena in the neutral kaon system. "KTeV" is an acronym which stands for "Kaons at the Tevatron". The Tevatron is a particle accelerator at Fermilab. KTeV is actually composed of two closely intertwined experiments known as E799 and E832. The main focus of E832 was an accurate measurement of the direct CP-violation parameter $\text{Re}(\epsilon'/\epsilon)$ to the 10^{-4} level. A determination of the parameter $\text{Re}(\epsilon'/\epsilon)$ was performed using $K_{L,S} \rightarrow \pi\pi$ decays. The central objective of E799 was the search for the direct-CP violating decay $K_L \rightarrow \pi^0 e^+ e^-$. However, E799 also had a broader agenda, which included the study of a large variety of rare K_L , pion and hyperon decays. The search for $K_L \rightarrow \pi^0 \pi^0 \mu^+ \mu^-$ was performed by analyzing data from E799.

In order to facilitate the specific studies to be carried out by the two experiments,

they both had different experimental setups. E832 employed an active regenerator to produce parallel K_L and K_S beams, which are necessary for the measurement of $\text{Re}(\epsilon'/\epsilon)$. The regenerator was removed from E799, which resulted in two parallel K_L beams. In addition, a series of transition radiation detectors (TRDs) were inserted in E799 for enhanced charged particle discrimination. Absorber and collimator settings were also changed for E799.

Both experiments were divided into three distinct run periods, which are displayed in Table 2.1. KTeV started with E832 in late October 1996. After running for two months, they then took a one month break and switched over to E799 in late January of 1997 and ran until late March of 1997. This aforementioned period is referred to as the *Winter Run*. KTeV then switched back to E832 just a day later, then after four months of data taking returned back to E799 mode for an additional five weeks. This period of E799 data taking from the end of July until the beginning of September is known as the *Summer Run*. The summer run and the winter run are known collectively as the *1997 Run*. Many detector improvements were made during the two year shutdown period after the 1997 run. E832 resumed taking data in June 1999 and changed over to E799 in September 1999. This run period lasted until mid January 2000 and referred to as the *1999 Run*.

Experiment	E832	E799	E832	E799	E832	E799
Start	10/1996	1/1997	3/1997	7/1997	6/1999	9/1999
End	12/1996	3/1997	7/1997	9/1997	9/1999	1/2000

Table 2.1: Run periods of E799 and E832.

2.1 Creation of the Neutral K_L Beams

The KTeV experiment was located in the Neutrino-Muon (NM) fixed-target beamline at Fermilab. KTeV belongs to a genre of particle physics experiments known as *fixed-target experiments*. The other genre of particle physics experiments at Fermilab are located on the Tevatron and are referred to as *collider experiments*. The Fermilab accelerator chain, which includes the Tevatron and fixed-target beamline, is depicted in Figure 2.1. At Fermilab, the protons and antiprotons in the Tevatron travel in opposite directions and their collisions are studied in collider experiments using a detector oriented around an interaction region. In Fermilab fixed-target experiments, the proton beam from the Tevatron is aimed at a volume of target material. The product of the proton beam interacting with the target material is the emission of a plethora of different daughter particles from the target, which are selectively filtered to produce a neutral kaon beam for the KTeV experiment. This process will be described in the remainder of this section.

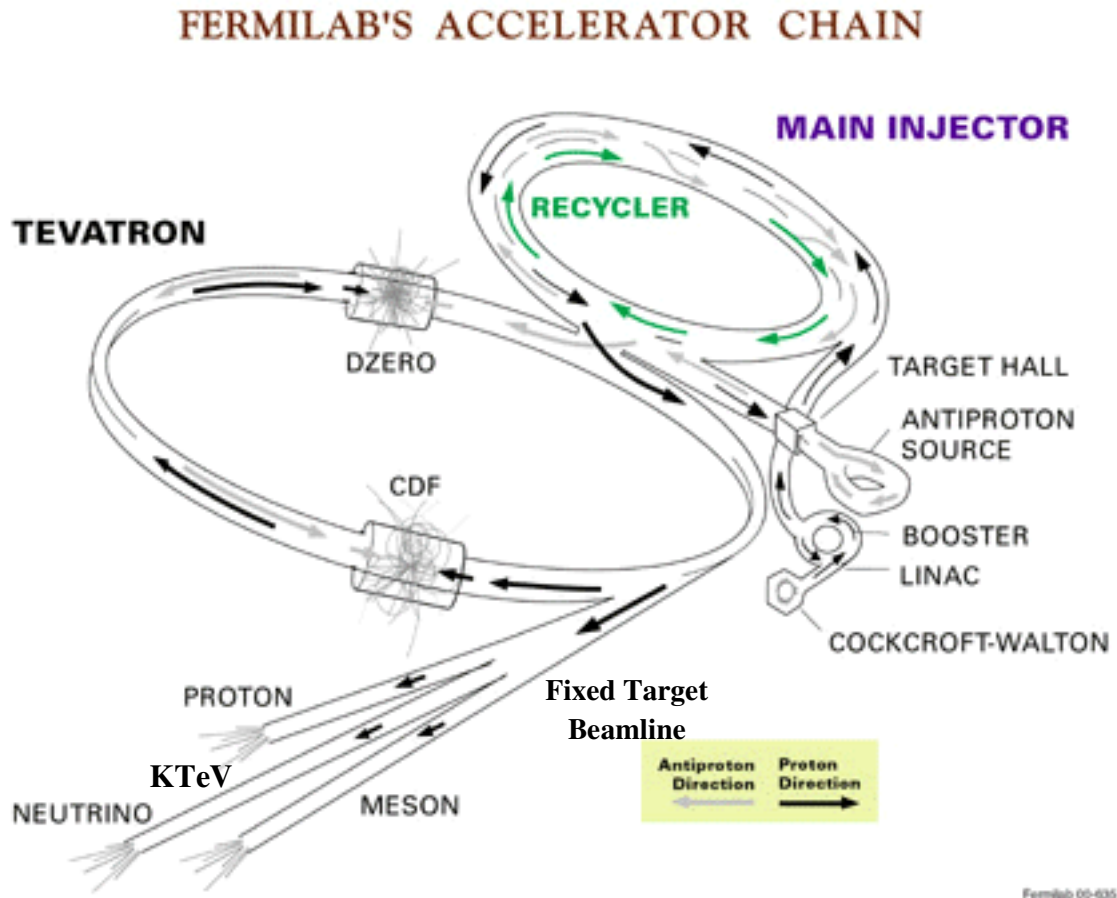


Figure 2.1: A diagram of the Fermilab Accelerator Chain circa 1999. During fixed-target experiments such as KTeV, the recycler and the anti-proton source are not used. Schematic courtesy of the Fermilab Photo Archive [31].

2.1.1 Incident Proton Beam

The KTeV adventure begins at the Tevatron, where protons can be accelerated to energies up to 1 TeV. During KTeV running, protons transported to the NM beamline from the Tevatron were accelerated to an energy of 800 GeV. This acceleration occurred over a span of 40 seconds and is referred to as the *off-spill period*. The period after acceleration, in which the protons were continuously delivered to the NM beamline, is called the *on-spill period*. The on-spill period lasted for approximately 20 seconds during the 1997 run. The on-spill period for the 1999 run improved to 40 seconds, while the off-spill period remained unchanged.

The protons in the Tevatron are accelerated by 53.1 MHz radiofrequency (RF) resonant cavities. This gives the proton beam a micro-structure in addition to the spill macro-structure described in the previous paragraph. Essentially, the protons arrived in 1-2 ns pulses spaced by 19 ns, where each 2 ns pulse was known as an *RF Bucket*. The intensity of protons delivered to the NM beamline for the 1997 run was between 2×10^{12} and 4×10^{12} protons per spill. As a result of an increase in spill length in 1999, between 6×10^{12} and 10×10^{12} protons per spill were delivered during the 1999 run. Before striking the target, the proton beam was focused to a transverse width of less than $250 \mu\text{m}$. The target was located in a beamline area known as the NM2 enclosure. KTeV employed a 30 cm long Beryllium Oxide (BeO) rod with a 3 mm^2 square cross-section as its target. BeO was chosen as the target material due to its resistance to thermal stresses. The length of the target corresponds to 1.1 proton

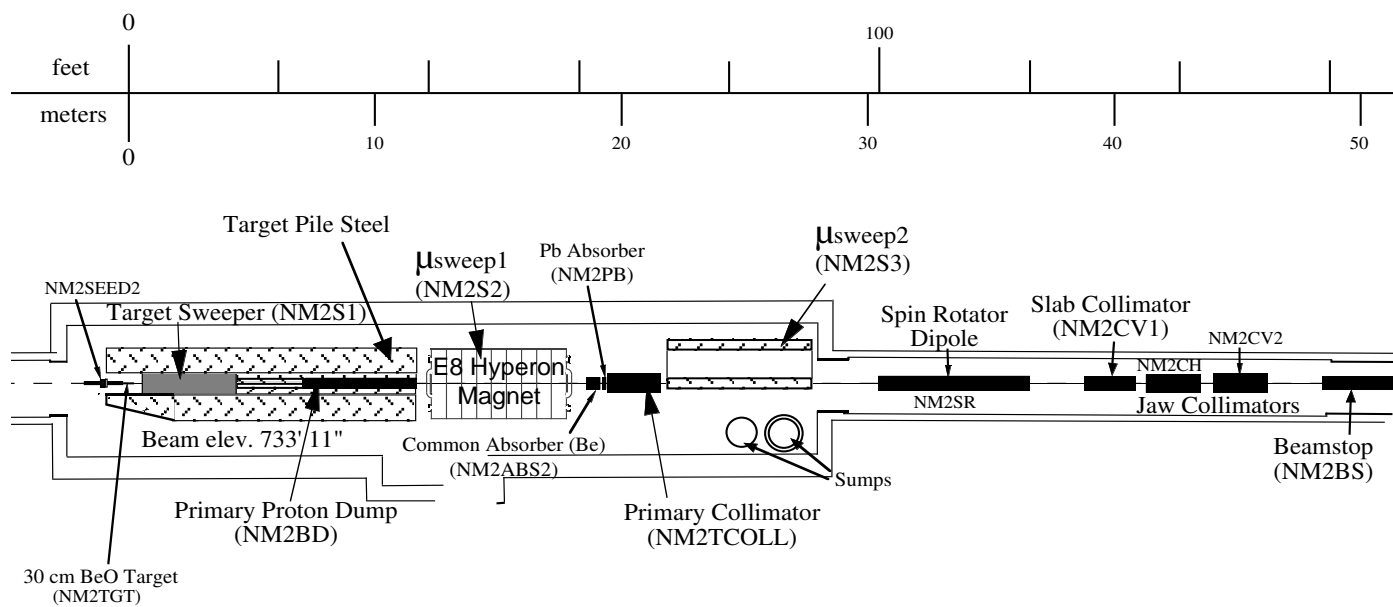
interaction lengths, which optimized kaon production efficiency. The center of the target is defined as the origin of the KTeV co-ordinate system. The length of the target (or that vector which is parallel to the area vector defining the cross-section) is defined as the z direction. The $+z$ direction is parallel to the *downstream* beam direction and points from the target to the detector. By construction, the $-z$ direction is referred to as the *upstream* direction. The $+y$ direction points upward and the $+x$ direction completes the right-handed co-ordinate system. In order to maximize the neutral kaon to neutron ratio in the resultant beam, the angle of the incident proton beam was directed 4.8 mrad downward with respect to the $+z$ axis.

2.1.2 Resultant Neutral K_L Beams

After striking the target, an array of charged and neutral particles were produced. Comparatively speaking, the beam exiting the target material contained mainly undesirable particles and a handful of neutral kaons. A series of sweepers, collimators and absorbers were set up in the NM2 enclosure in order to eliminate any charged particles or photons within the beam. A diagram of the NM2 enclosure is shown in Figure 2.2.

The first obstacle in the NM2 enclosure was the *target sweeper*, which extended from 0.6 m to 4.4 m along the z -axis. The target sweeper diverted the remaining protons into a beam dump by applying a 475 MeV/c transverse momentum (P_t) kick in the $-y$ -direction. This beam dump is referred to as the *primary proton dump* and

Figure 2.2: Top view of the NM2 enclosure.



is a 4.5 m water-cooled block of copper located downstream of the target sweeper. Since the beam dump was offset below the beamline, neutral particles were allowed to pass freely.

The next obstacle was the first of three muon sweepers, which were designed to clear muons out of the beam. Known as *μ sweep1*, this magnet imparted a 3.8 GeV/c P_t kick to the muons in the $+x$ direction in order to shove them out of the beam. *μ sweep1* extended from 12.3 m to 17.8 m along the z -axis. A 7.6 cm (14 radiation length) *Pb absorber* located 18.5 m downstream of the target converted photons to electron-positron pairs, which were later swept away.

A short distance downstream of the Pb absorber was the *Primary Collimator*, which was used to create the initial shape of the parallel K_L beams. The collimator was a 2 m long brass block with two tapered rectangular holes pointing back to the target. The tapering of the holes corresponded to a 0.8 mrad angle with the z -axis. During the winter run, the dimensions of the holes at the downstream face of the collimator measured 1.18×1.29 cm. Their size was increased to 1.62×1.73 cm for the summer and 1999 runs.

Immediately after departing the primary collimator, the beam entered a vacuum region located at $z = 21.8$ m. The vacuum region was contained at the upstream end by a 0.127 mm thick titanium window. Just downstream of the window was *μ sweep2*, a magnet stretching from $z = 21.9$ m to $z = 27.7$ m. This is the magnet which sweeps away any charged particles that were created through interaction with the Pb

absorber, primary collimator and titanium window. In the winter run, the magnet imparted a $3.14 \text{ GeV}/c \ P_t$ kick to accomplish this task, whereas in the summer and 1999 runs only a $1.85 \text{ GeV}/c \ P_t$ kick was applied.

Located at $z = 30.5 \text{ m}$, a 6 m long *Spin Rotator Dipole Magnet* was implemented for hyperon studies. This magnet had no effect on the spinless neutral kaons. At 38.8 m and extending to 40.8 m was a stainless steel wedge called the *Slab Collimator*. Initially, the collimator was used in the winter run to safeguard against crossover between beams. However, the collimator was later found to be unnecessary and was therefore removed for the summer and 1999 runs.

A pair of iron blocks were employed as beam stops downstream of the slab collimator. The iron blocks were situated back-to-back and their total thickness amounted to 6 m . The upstream face of the beam stops was located at 46.6 m . These beam stops were only moved into place as a safety measure during access to the experiment. Additionally, during certain detector calibration runs they were used to create muon beams.

The *Defining Collimator* performed the final, definitive shaping of the beams. Situated at $z = 85 \text{ m}$, the collimator was a 3 m long iron and tungsten block with two tapered holes. The dimensions of the holes at the downstream face measured 4.4 cm^2 during the winter run and 5.2 cm^2 during the summer and 1999 runs. After passing through the defining collimator, the beams then encountered the 3 m long *Final Sweeper* magnet at $z = 90 \text{ m}$. Through interactions with the defining collimator

or via upstream decays, any residual charged particles generated were removed by the final sweeper before the beams entered the detector.

After exiting the final sweeper, the neutral beams then voyaged into the detector. The contents of the beam at this point consisted of neutrons, K_L 's and neutral hyperons. The ratio of neutrons to K_L 's was roughly 3:1 and the number of hyperons present was negligible in comparison. Due to their long lifetime, the interaction of neutrons with the detector was confined to accidental activity. The neutral hadron rate was 25 - 50 MHz. Finally, the two beams had a width of 0.50 mrad during the winter run, a width of 0.59 mrad during the summer and 1999 runs, and were separated by 1.6 mrad along the x -axis.

2.2 The KTeV Detector

The KTeV detector began at $z = 94$ m and ended at $z = 196.4$ m. By providing measurements of various charged particle and photon attributes, the detector was a vital tool in trigger decisions and decay reconstruction. Schematics of the KTeV detector are given in Figures 2.3 and 2.4. The primary components of the detector will be discussed in the remainder of this chapter.

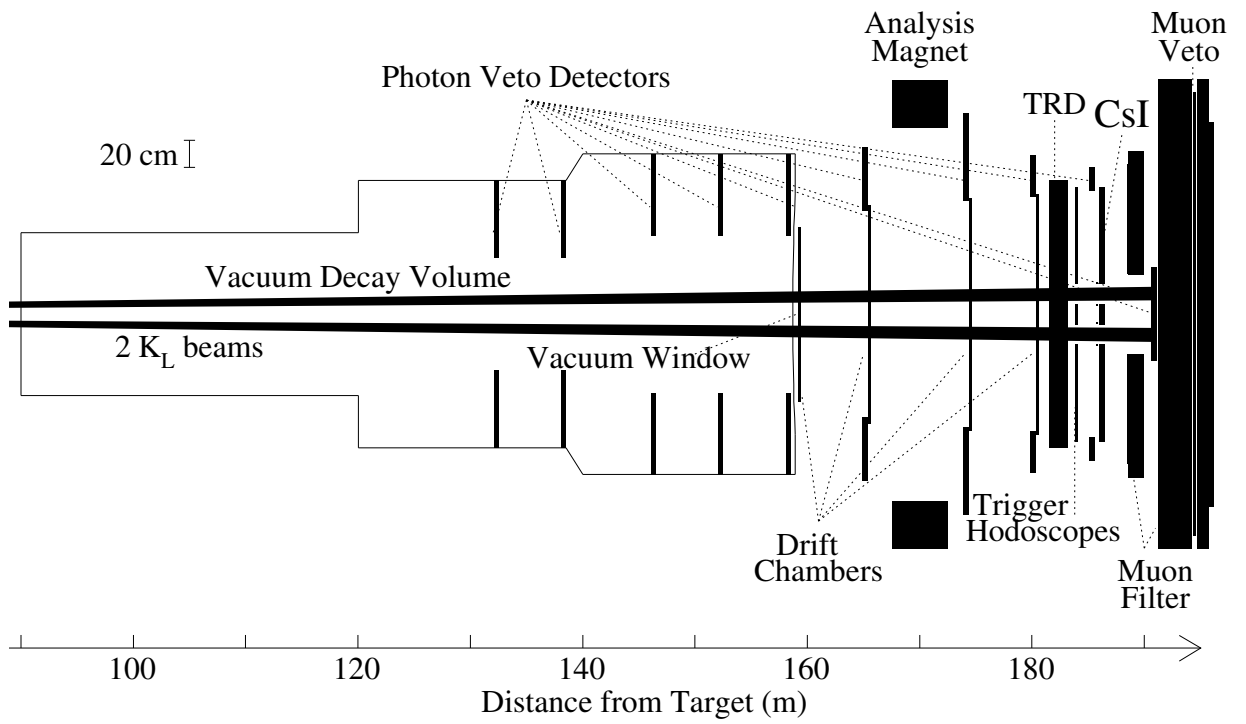


Figure 2.3: Top view of the KTeV detector in E799 configuration.

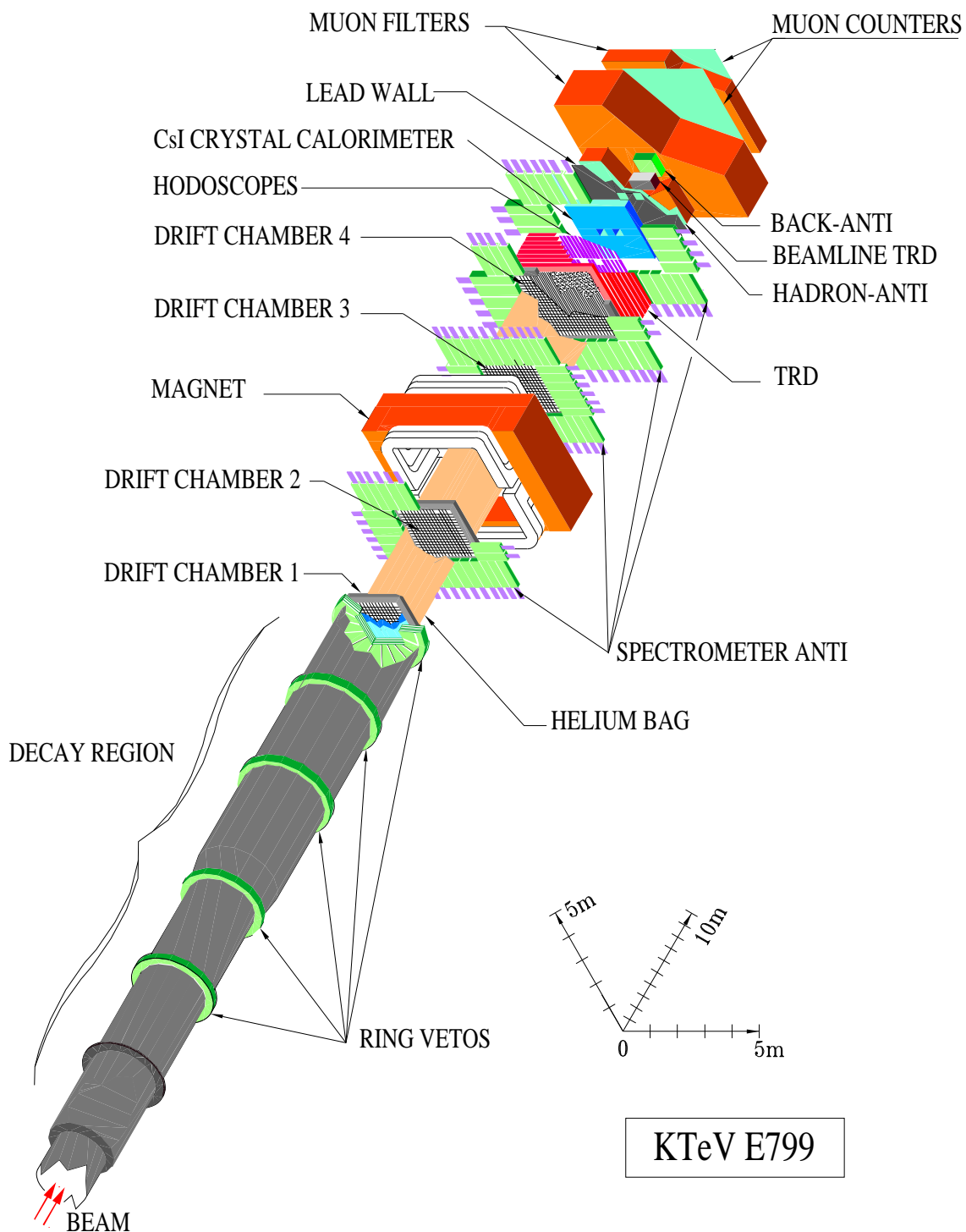


Figure 2.4: 3D view of the KTeV detector in E799 configuration.

2.2.1 Vacuum Decay Region

The 65 m long *Vacuum Decay Region* is the first component of the KTeV detector. In order to minimize the interactions of decaying kaons with other particles, the pressure in the vacuum region was maintained at 1 μ Torr. Only decays which occurred in the vacuum region were accepted for this analysis. The vacuum decay region and the detector as a whole were built with a conical structure in an effort to increase geometric acceptance. At the upstream end of the decay region the diameter was 46 cm, whereas at the downstream end the diameter was 2.44 m. Containing a vacuum in such a large volume required sealing the end of the decay region with a robust vacuum window. In addition, photon conversions and bremsstrahlung needed to be kept low, so a thin window was also necessary. A Mylar laminated Kevlar window did the job well. A 0.25 mm thick piece of Mylar proved to be an excellent gas seal, while the 0.6 mm thick piece of Kevlar was enough to withstand the 30 tons of differential pressure exerted on the window. The Mylar-Kevlar window amounted to a total thickness of 0.0015 radiation lengths.

Ring Counters

Inside the vacuum decay region were five photon veto detectors called *Ring Counters* (RC). Each RC consists of multiple layers of lead-scintillator sandwich totaling 16 radiation lengths. The RC's were designed to detect photons (of energy greater than 100 MeV) leaving the vacuum region before they reached the spectrometer or

the calorimeter. The RC's, displayed in figure 2.5, had square inner apertures and circular perimeters. The two upstream RC's had an inner aperture of 0.84 m^2 and an outer radius of 1.00 m. The three downstream RC's had an inner aperture of 1.18 m^2 and an outer radius of 1.44 m.

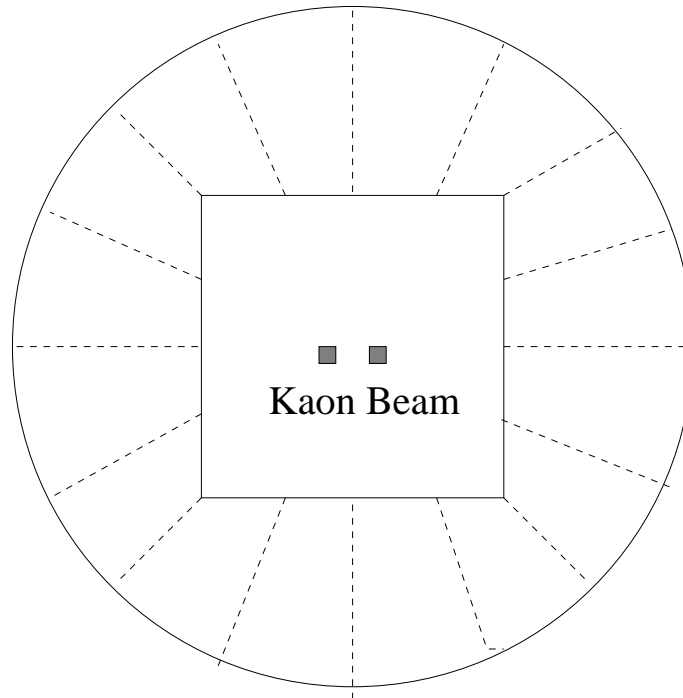


Figure 2.5: Cross-section of a KTeV Ring Counter. RC's were placed perpendicular to the beam direction with the outer radius bordering the inner edge of the vacuum decay region.

RC signals were collected by scintillator fibers and guided to photomultiplier tubes (PMT) mounted on the edge of each counter. The PMT signals were then digitized, discriminated and sent to Level 1 trigger electronics. Signals were only sent to the Level 1 trigger to be used as a veto if a minimum in-time energy of 0.5 GeV was deposited in any one of the RC's.

2.2.2 Charged Particle Spectrometer

The *Charged Particle Spectrometer*, as depicted in figure 2.6, employed four *Drift Chambers* (DC) and an *Analysis Magnet* to measure the momenta and trajectories of charged particles from K_L decays. Plastic bags filled with Helium were placed between each spectrometer element to reduce scattering of charged tracks compared to the scattering they would have encountered in air. The spectrometer measured momenta by recording the bend of a charged particle as it passed through a known magnetic field. One can find the initial trajectory of a given charged particle through the spectrometer by measuring the positions of a track in the two upstream drift chambers. By construction, the final trajectory of a charged particle is given through measuring the position of a track in the downstream pair of drift chambers. One can then extract the momentum of the charged particle by taking the quotient of the P_t kick from the magnetic field with the change in track direction.

Analysis Magnet

The analysis magnet was an electromagnetic dipole that created a field oriented in the y -direction. In the 1997 runs, the momentum kick given to relativistic charged particles in the x - z plane was 205 MeV/c. The P_t kick for the 1999 run was lowered to a value of 150 MeV/c in order to increase acceptance for certain rare K_L decay modes. The polarity of the magnetic field was changed every one or two days during data taking. This operation was performed in order to minimize systematic

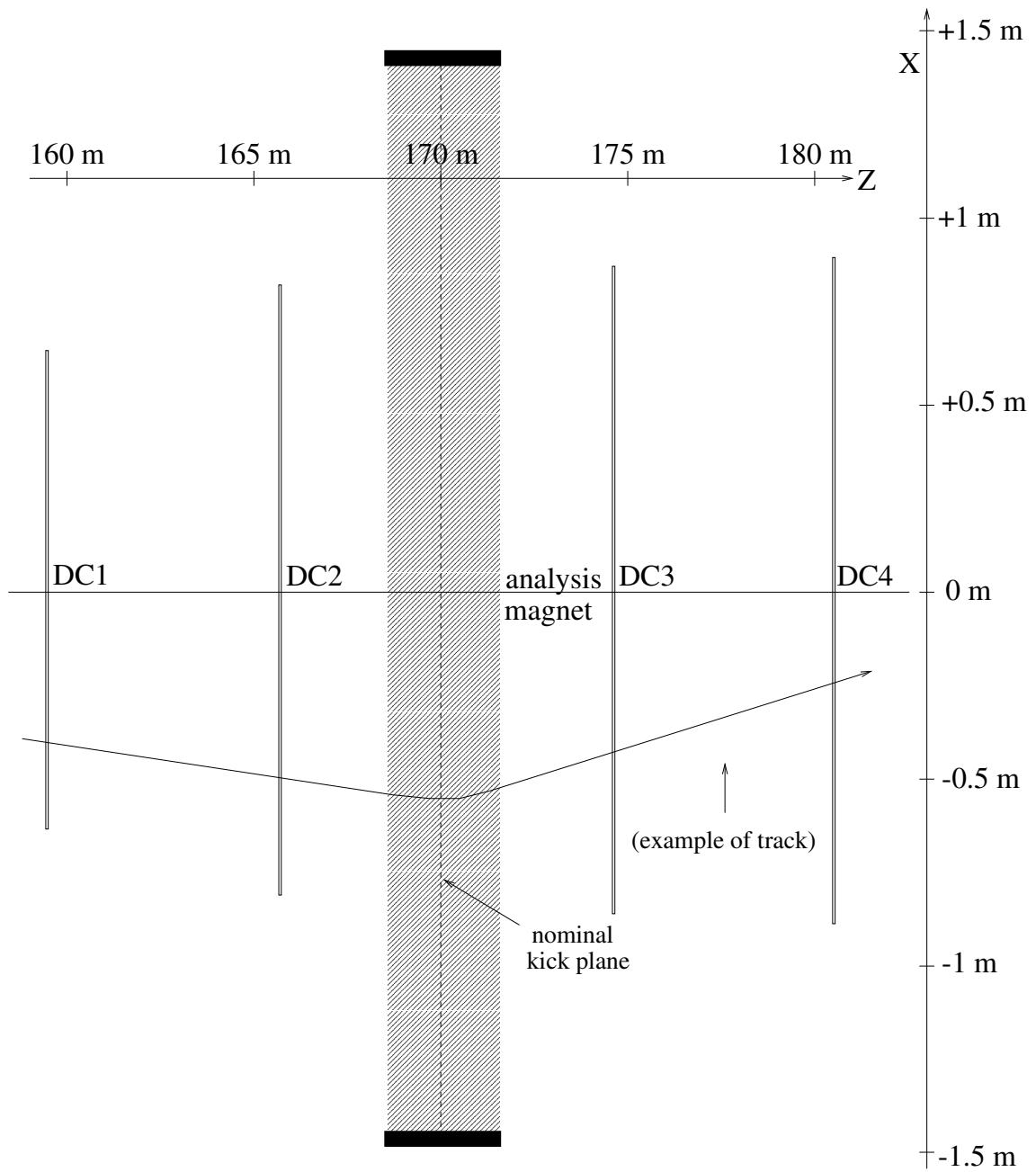


Figure 2.6: Side view of the KTeV Charged Particle Spectrometer with drift chambers and analysis magnet. In order to increase acceptance, the cross-sectional area of each drift chamber increases with distance from the target.

effects stemming from the direction of deflection of negatively and positively charged particles.

Drift Chambers

The DC's used the drift times of electrons in gas to measure the x -position (X View) and y -position (Y View) of charged particles. The DC's were filled with a gas that could be ionized by charged particle tracks. This ionization released electrons, which were accelerated towards the nearest anode sense wire. The electric potential from the voltage difference between the cathode field wires and the anode sense wires allowed this electron acceleration process to occur. These electrons then begin a chain reaction in which more electrons are liberated and the resulting avalanche of electrons creates a current on the anode sense wire that can be measured. The position of the charged particle could be deduced from the position of the signal-carrying anode wires coupled with the time that the current arrived.

The DC exterior was composed of aluminum frames and Mylar windows on the upstream and downstream face, which sealed the gas within the chambers. There were four anode sense wire planes in each DC; the first pair were oriented in the x -direction (for the Y View), while the second pair were oriented in the y -direction (for the X View). The anode sense wires are surrounded by six cathode field wires in a hexagonal orientation, thus forming a honeycomb of Geiger-Müller tubes. All wires are oriented parallel to one another. The width of each hexagonal cell (in x)

was 12.7 mm. Each set of wire planes were offset by half a cell width in order to resolve left-right ambiguity. The cathode field wires were 100 μm in diameter and made of gold-plated aluminum. The anode sense wires were composed of gold-plated tungsten and had a diameter of 25 μm . The width of each hexagonal cell (in x) was 12.7 mm. A schematic of drift chamber wire geometry is shown in figure 2.7.

Each drift chamber is filled with a mixed gas composed of 49.5% argon, 49.5% ethane and 1.0% isopropyl alcohol. The alcohol absorbed harmful ultraviolet light, which caused deposits on chamber wires and reduced chamber lifetime. The voltage difference between the anode sense wires and the cathode field wires was held between 2450 V and 2600 V for the 1997 runs. These high-voltage settings yielded an electron drift speed of 50 $\mu\text{m}/\text{ns}$ and a drift time of 200 ns. During the time period between the 1997 and 1999 runs, the anode sense wires were cleaned and various electronics were upgraded, which allowed the DC's to function at a higher gain while using a lower voltage difference. The voltage difference was confined to the range of 2350 V to 2400 V during the 1999 run. Running at lower voltages is a great benefit, since this significantly reduced noise levels.

The signals collected on the anode sense wires were amplified and discriminated with chamber-mounted electronics, then digitized by time to digital converters (TDC). Drift times were calculated from TDC counts, which coupled with hit positions on anode sense wires gave one the information needed to reconstruct charged particle tracks. The precision of TDC counts was 0.5 ns. The resolution of charged track hit

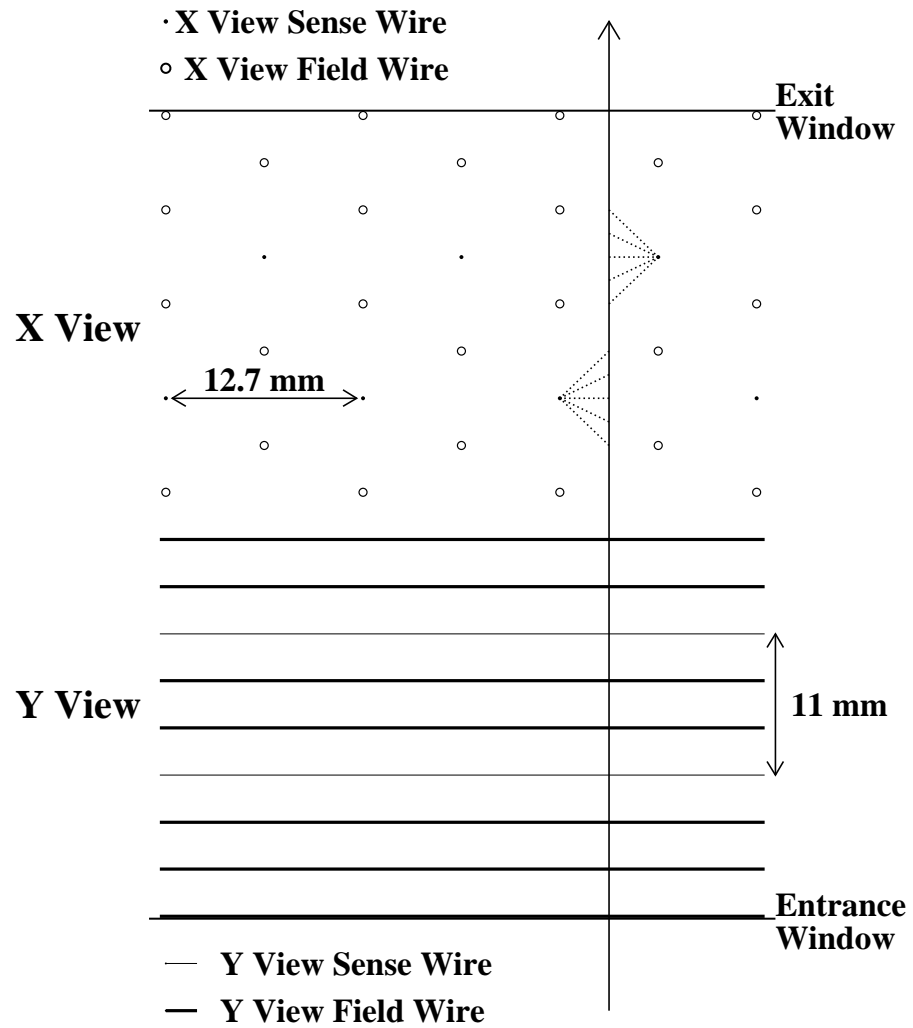


Figure 2.7: Schematic of wires within a drift chamber. The charged particle path is denoted by a solid arrow, while an ionization electron is illustrated with a dotted line.

positions was 100 μm , while the momentum resolution of the spectrometer is given as

$$\frac{\sigma_P}{P} = 0.38\% \oplus 0.016\%P, \quad (2.1)$$

with P in units of GeV/c [32]. The constant term in the above expression stems from multiple scattering effects and the linear term comes from the finite position resolution of the DC's.

Spectrometer Anti Counters

The *Spectrometer Anti Counters* (SA's) serve as photon veto detectors that surround DC2, DC3 and DC4. Much like the RC's, the SA's are composed of multiple layers of lead-scintillator which total 16 radiation lengths. Unlike the RC's, the inner and outer apertures of each SA are square. Essentially, the SA's were designed to detect particles exiting the detector at steep angles. Events with an energy greater than 0.4 GeV in any of the SA's were vetoed. A cross-sectional diagram of an SA is given in Figure 2.8.

2.2.3 Transition Radiation Detectors

A *Transition Radiation Detector* (TRD) is an instrument used for discrimination between electrons and charged pions. There were eight TRD planes in the KTeV detector beginning at $z = 181.1$ m with each successive TRD plane spaced at 31 cm intervals. The surface area of each TRD was 2.1×2.1 m². Each TRD plane had

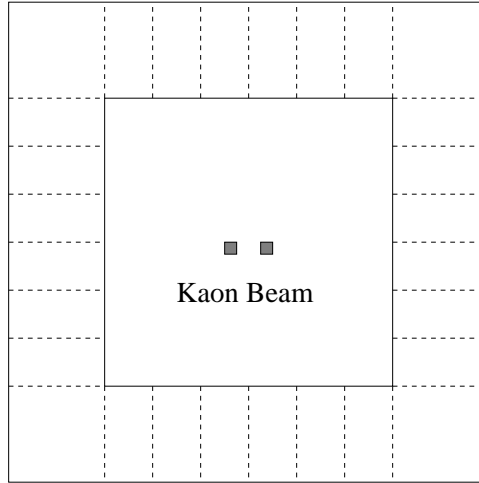


Figure 2.8: Cross-section of a Spectrometer Anti.

a radiator mounted on the front with a multiwire proportional chamber (MWPC) on the back. The radiators are each 15 cm thick and are composed of randomly oriented $17\ \mu\text{m}$ diameter polypropylene fibers with a density of $0.05\ \text{gm/cm}^3$. When highly relativistic electrons pass through the radiators, transition radiation X-rays are produced, whereas other charged particles will only leave an ionization energy. The next step in X-ray detection is the MWPC, which is filled with a recirculating mixture of 80% Xenon and 20% CO_2 . X-rays are detected when they ionize the gas in the MWPC and the resulting avalanche electrons create a signal in the anode sense wires. A diagram of a KTeV TRD plane is given in figure 2.9. Each radiator had two $15\times 15\ \text{cm}^2$ holes to allow for passage of the neutral beams. In order to eliminate any transition radiation X-rays in the beam region, all MWPC anode wires were plated to increase their diameters by a factor of five and effectively dampen out the detector

in these areas. The TRD system had an e^\pm/π^\pm rejection of better than 200:1 at 90% electron efficiency [33]. The TRD system was not employed in this analysis.

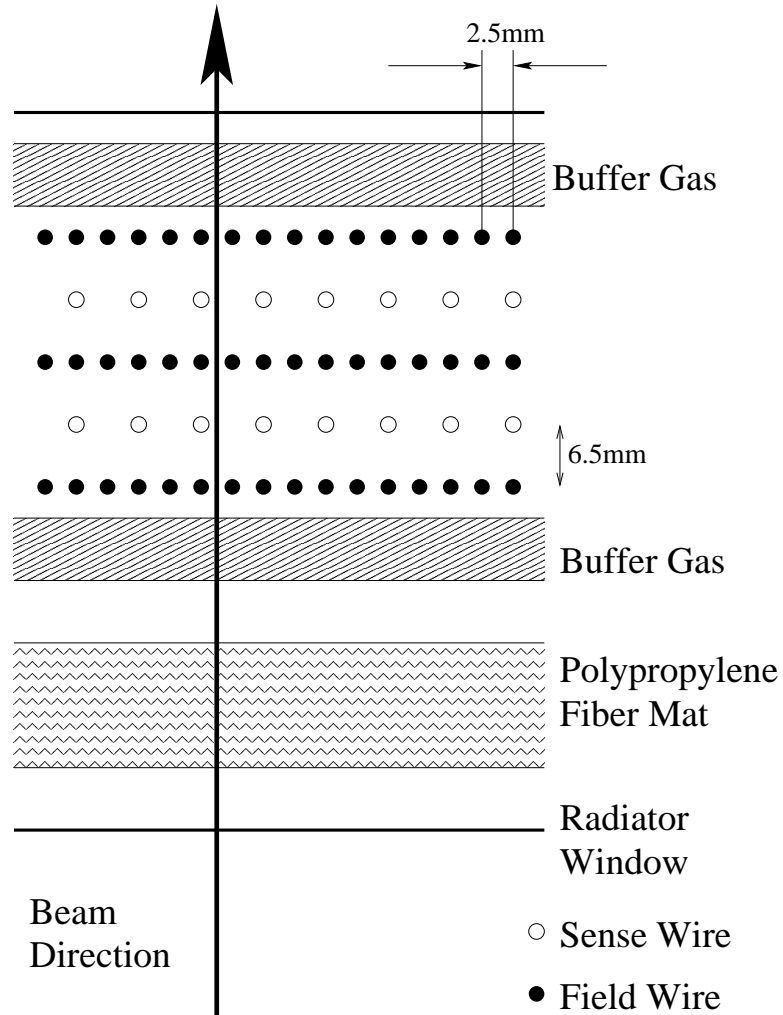


Figure 2.9: Cross-section of a TRD plane.

2.2.4 Trigger Hodoscopes

The Level 1 Trigger required notification of the existence of charged particles on a faster timescale than the DC's could supply. Necessity brought forth the *V and V' trigger hodoscope planes*, which are depicted in figure 2.10. Both planes are located at $z = 183.9$ m; V is the upstream plane and V' is the downstream plane. The V hodoscope plane has 32 paddles, whereas the V' hodoscope plane possesses only 30 paddles. In addition, both planes contained paddles of varying widths to ensure charged particles would not slip through the cracks. The scintillator paddles are 1 cm thick and each plane is 1.9×1.9 m². Two 14×14 cm² holes were cut in each plane to allow for passage of the neutral beams and prevent radiation damage to the calorimeter. PMT's are connected to each scintillator paddle to collect signals from charged particle tracks.

2.2.5 Cesium Iodide Electromagnetic Calorimeter

The KTeV *Cesium Iodide Electromagnetic Calorimeter* (CsI) was constructed to measure electron and photon energies. The energy of incident photons could be determined in the range spanning 2 GeV to 80 GeV. Located at 186 m downstream from the target, the CsI was composed of 3100 0.5 m long Cesium Iodide crystals arranged into a 1.9 m \times 1.9 m square array. In the outer region, there are 868 crystals with a 5 cm \times 5 cm square cross-section. In the inner region are the other 2232 crystals, which have a 2.5 cm \times 2.5 cm square cross-section. The small crystals yield

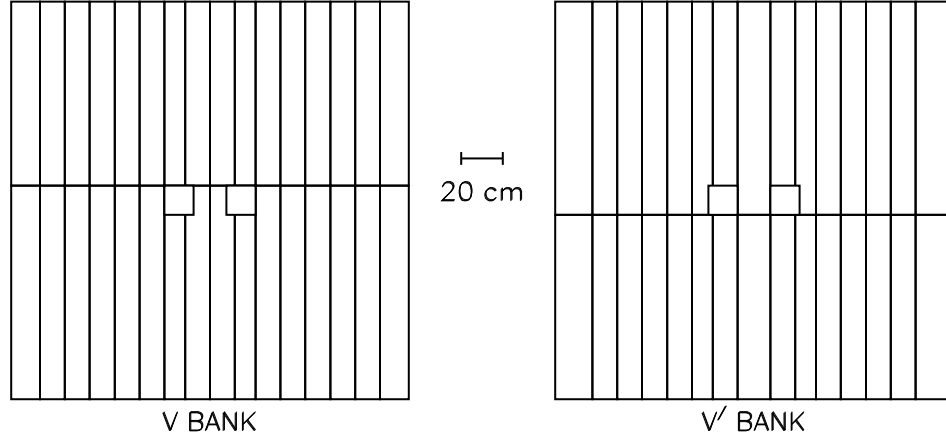


Figure 2.10: V and V' trigger hodoscope banks.

better position resolution, which is ideal for the inner region where the density of energy clusters is higher. There are two 15 cm \times 15 cm square beam holes located at $y = 0$ and $x = \pm 15$ cm to allow the neutral beams to pass through the CsI without damaging the crystals. A diagram of the CsI is given in figure 2.11.

Cesium Iodide Crystals

The length of each crystal corresponds to 27 radiation lengths or 1.4 nuclear interaction lengths. This ensures that nearly all photon and electron energies are deposited within the CsI, while minimum ionizing particles (MIPs) such as muons and high energy pions will only leave a fraction of their energy in the CsI. The average light yield in each crystal was measured to be about 20 photoelectrons per

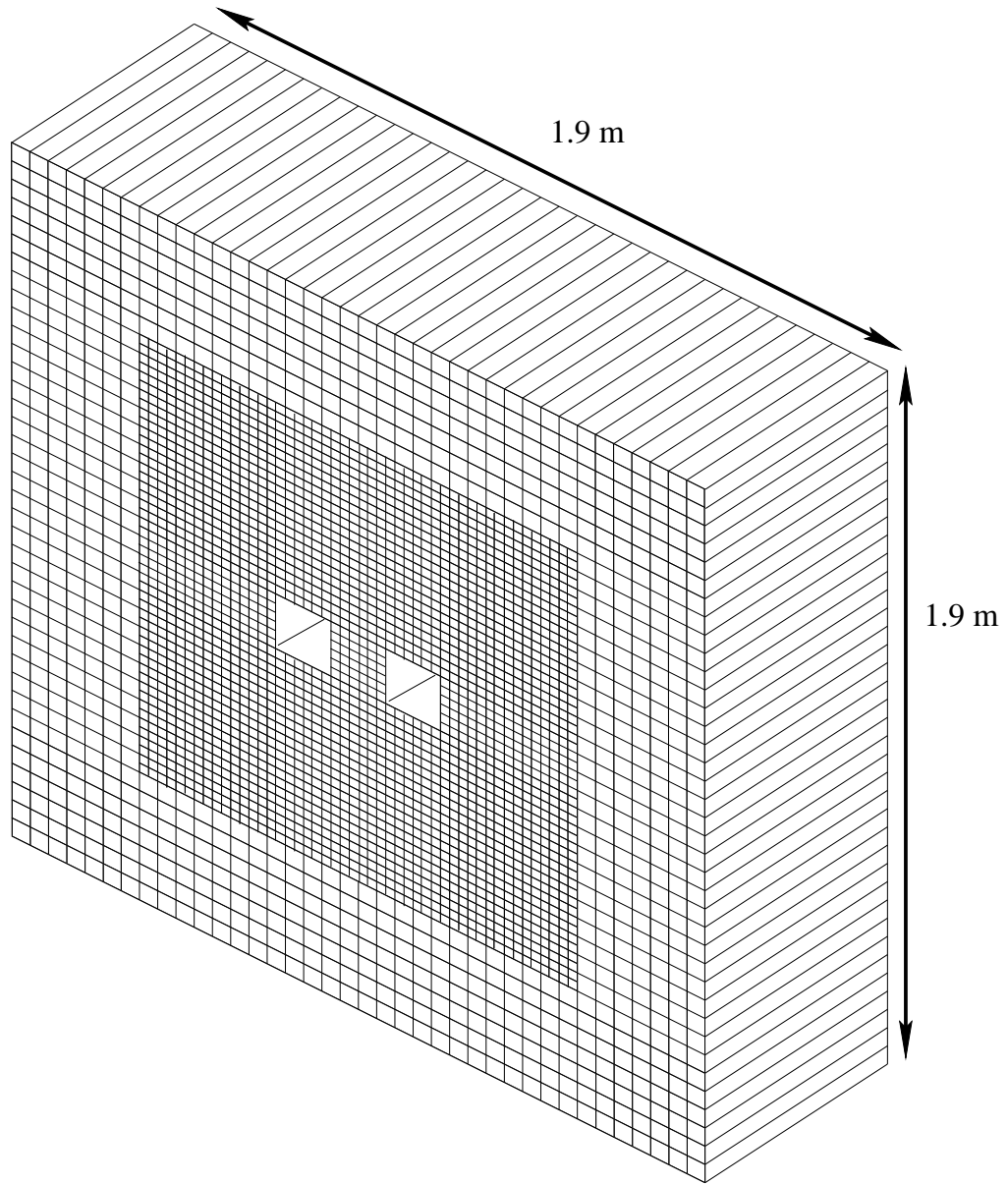


Figure 2.11: 3D view of the KTeV Cesium Iodide Electromagnetic Calorimeter.

MeV of deposited energy. This scintillation light is composed of a *fast* component and a *slow* component. The slow contribution peaks at a wavelength of 480 nm and has a decay time of 1 μ s. The fast component peaks at 305 nm and has a decay time of 25 ns.

A non-uniform scintillation response was found along the length of each crystal. To counteract this effect, each crystal was wrapped in 13 μ m thick black and/or reflective mylar. The type and alignment of the wrapping varied from crystal to crystal based on the scintillation response of each individual crystal. After the wrapping procedure, the scintillation responses were measured to be uniform to within 5% [34].

Energy Resolution

The CsI has a superlative energy resolution of

$$\frac{\sigma_E}{E} = 0.45\% \oplus \frac{2\%}{\sqrt{E}}, \quad (2.2)$$

with E in units of GeV [35]. The constant term results from a number of effects such as noise, light leakage and non-uniformities. The second term stems from the photostatistics of the scintillation light. Position resolution was measured to be 1 mm in the small crystals and 1.8 mm in the large crystals.

Optical Readout

All crystals are optically coupled to PMTs with transparent silicone cookies. In addition, there was a filter in the optical coupling to remove the slow component

of scintillation light, which would have otherwise caused pileup. The face of each large crystal was attached to a 6-stage 1.5 inch PMT, while the smaller crystals were coupled to 5-stage 0.75 inch PMTs. The operating voltages of the PMTs ranged from 900 V to 1500 V with a gain of about 5000. The voltages of each individual PMT tuned the thresholds for the *Hardware Cluster Counter*. The signal from the final dynode stage of each PMT was employed by the E-Total system of the Level 1 trigger. The anode signal was sent to a *Digital Photomultiplier Tube* (DPMT) board for digitization and buffering.

Digitization

Each DPMT board was composed of an 8-bit flash analog-to-digital converter (ADC), a charge integrator and encoder (QIE) and a driver-buffer-clock (DBC). The QIE divided the anode signal current among eight capacitors, each receiving a different fraction of the incoming anode current ($I/2, I/4, I/8, \dots, I/256$). The voltage across each capacitor is then integrated and compared to reference voltages to determine which value is within the correct digitizing range. The selected voltage was then digitized by the ADC and stored as a mantissa. A 3-bit exponent output from the QIE containing the selected current range was also stored.

Every QIE contains four sets of identical capacitor circuits that constantly read out time slices in a round-robin fashion. The mantissa and exponent output bits are written to a FIFO (first-in, first-out) buffer in the DBC. If an event passes the trigger,

then the DPMT buffer is sent off to the *pipeline*. The pipeline is a VME buffer and sparsification system that can be engineered to satisfy each trigger's CsI output needs [36].

Calibration

The CsI was calibrated with light from a dye laser, which had a wavelength of 380 nm. Light pulses from the laser were delivered through an optical fiber to each crystal. These light pulses flagged various time-dependent CsI problems. During special runs known as laser scans, the response of each crystal across the entire DPMT dynamic range was scanned by turning a variable filter wheel in front of the laser source. The laser pulses were also sent to PIN diodes, thus providing a suitable reference. A linear relationship was observed between the charge as seen by the PIN diode and the ADC output from the DPMT. The offset and slope for each DPMT range were used as calibration constants.

The detector energy was calibrated by studying electrons from $K_L \rightarrow \pi^\pm e^\mp \nu_e$ (K_{e3}) decays. Studying the ratio of E/p for the aforementioned decays allows one to find a conversion factor from charge to energy (Q/E) for each channel. In the expression E/p, E represents the electron shower energy from the CsI, while p is the track momentum measured by the spectrometer. Since electrons deposit the vast majority of their energy in the CsI, E/p was expected to be very close to 1. Q/E for each channel was chosen as the value which yielded an E/p spectrum centered around

1 for K_{e3} electrons.

Collar Anti Counters

The *Collar Anti* frames the beam holes of the CsI. Composed of three layers of tungsten-scintillator sandwich and spanning 9.7 radiation lengths along z , the CA was designed to veto on events with particles that hit the face of the CsI near the beam holes. Naturally, one would need to veto on the aforementioned particles due to potential leakage of shower energy into the hole, which would cause a mismeasurement in particle energy. Each segment of the square frames was 1.5 cm wide and was individually equipped with a PMT and read out. A veto signal was relayed to the Level 1 trigger if a minimum of 14 GeV of energy was deposited in any segment in a given event.

2.2.6 Muon Identification System

The *Muon Identification System* is a series of particle filters and scintillator counter planes designed to identify muons by filtering out other charged particles. The location of the muon ID system (depicted in figure 2.13) is downstream of the CsI.

Lead Wall and Hadron Anti Counters

The first two pieces of the muon ID system serve the purpose of identifying pions. Located immediately downstream of the CsI was a 10 cm thick lead wall composed

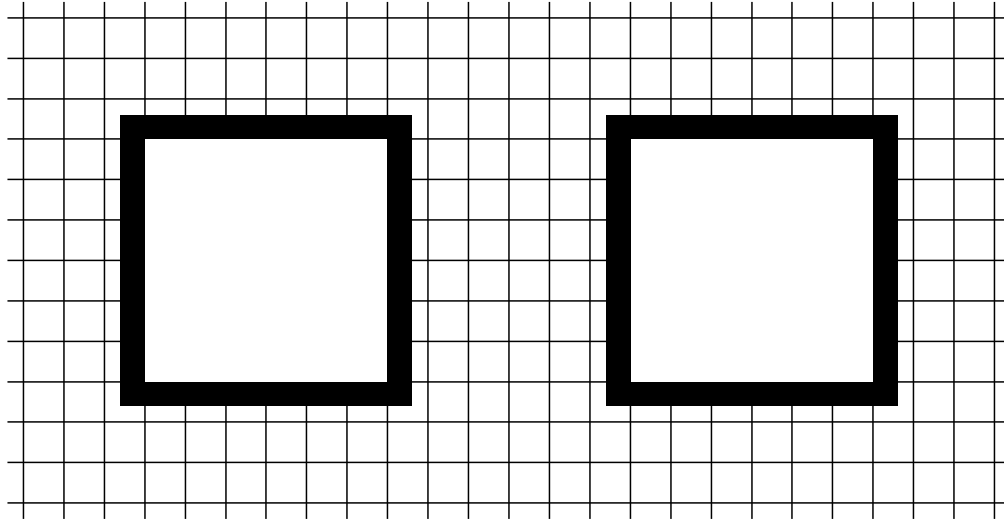


Figure 2.12: Diagram of the Collar Anti. The bold black lines represent the position of the Collar Anti, whereas the small squares denote the crystals located in the inner region of the CsI.

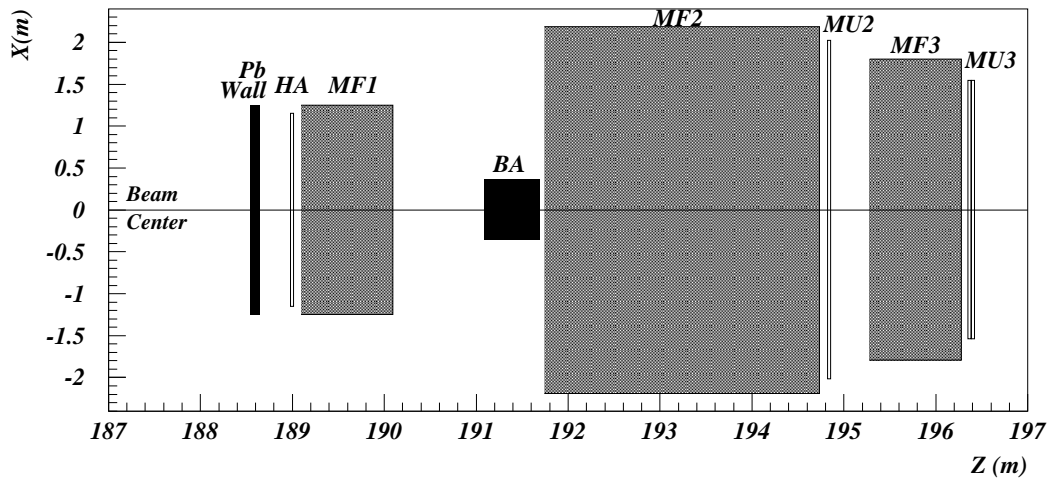


Figure 2.13: Top view of the Muon Identification System.

of lead bricks. The dimensions of each lead brick were 5 cm \times 10 cm \times 20 cm. The lead wall absorbed any residual electromagnetic showers leaking out of the CsI and induced hadronic showers for those hadrons that have not yet showered in the CsI. A plane of 28 non-overlapping scintillator counters known as the *Hadron Anti* (HA) detects the hadronic showers from the lead wall. The PMT signals provided by the HA counters were made into an analog sum, which was used by a number of triggers to veto events with hadronic activity. The lead wall and HA each have a rectangular hole that allows for passage of neutral beams. The dimensions of the hole in the lead wall measure 60 cm wide and 30 cm high, whereas the HA hole dimensions are 64 cm wide and 34 cm high. A diagram of the HA is given in figure 2.14.

Muon Filter 1 and Back Anti Counters

Muon Filter 1 (MF1) is a 1 m thick steel barrier located directly behind the HA. MF1 provided protection for the HA against backslash off the neutral beam dump located further downstream. To allow for passage of neutral beams, there is a 60 cm \times 30 cm hole in the center of MF1.

The *Back Anti* (BA) is a detector composed of thirty radiation lengths of lead-scintillator sandwich. Centered in the path of the neutral beams, it had a width of 60 cm and a height of 30 cm. The aim of the BA was to veto photons lost down one of the CsI beam holes. Unfortunately, neutral beam causes so much activity in the BA that efficient particle detection is hardly attainable. The BA is not employed in

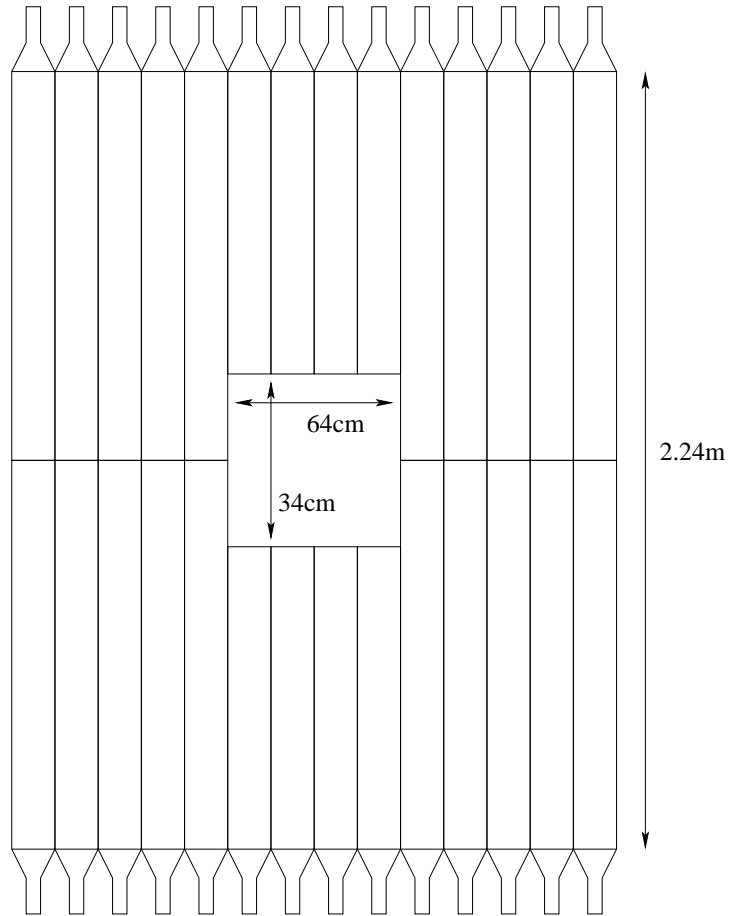


Figure 2.14: A diagram of the Hadron Anti. The dimensions of the HA were 2.24 m \times 2.24 m.

this analysis.

Muon Filter 2 and MU2

Muon Filter 2 (MF2) served as the neutral beam dump. At 3 m thick and composed of 44 m^2 of battleship steel, this barrier stopped a large majority of hadronic activity. MF2 was chosen to have a large volume in order to optimize muon rejection efficiency. This holds true even for muons that will undergo large scattering in the steel.

MU2 is a plane of 56 $150\text{ cm} \times 15\text{ cm} \times 1.5\text{ cm}$ scintillator counters, which overlapped by 1 cm with adjacent counters along the sides and ends. The counters in MU2 overlapped to prevent muons from passing undetected through any open space. In general, MU2 is used as an acceptance detector for muon calibration triggers. A diagram of MU2 is given in figure 2.15.

Muon Filter 3 and MU3

Muon Filter 3 (MF3) is an additional 1 m steel barrier downstream of MU2. A muon would need a minimum momentum of 7 GeV/c to pass through the lead wall and the three muon filters, while there's a 0.5% probability that a hadronic shower from a 20 GeV/c pion could leak through to MU3 [37]. All in all, the lead wall and three muon filters add up to a total of 31 nuclear interaction lengths.

MU3 is composed of two planes of 40 non-overlapping scintillator counters (see

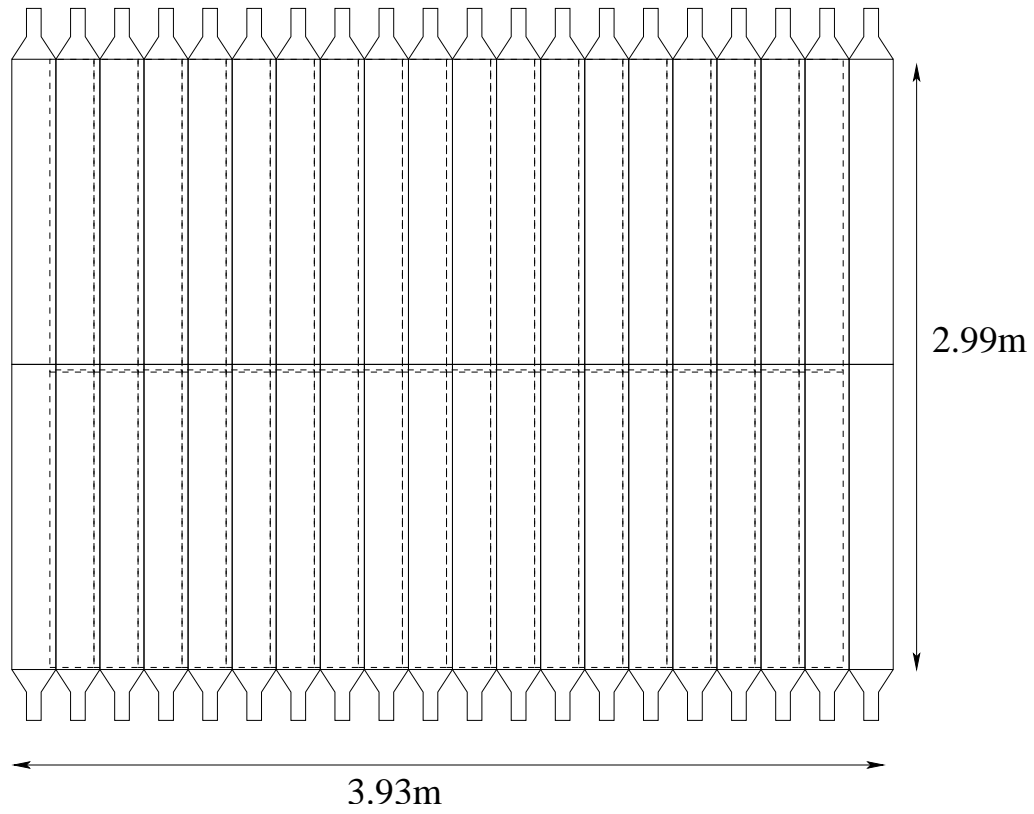


Figure 2.15: MU2 counter bank. Dashed lines denote counter overlap regions.

figure 2.16). These planes are used to trigger on rare decays with muons in the final state. The hit resolution in x and y is 15 cm.

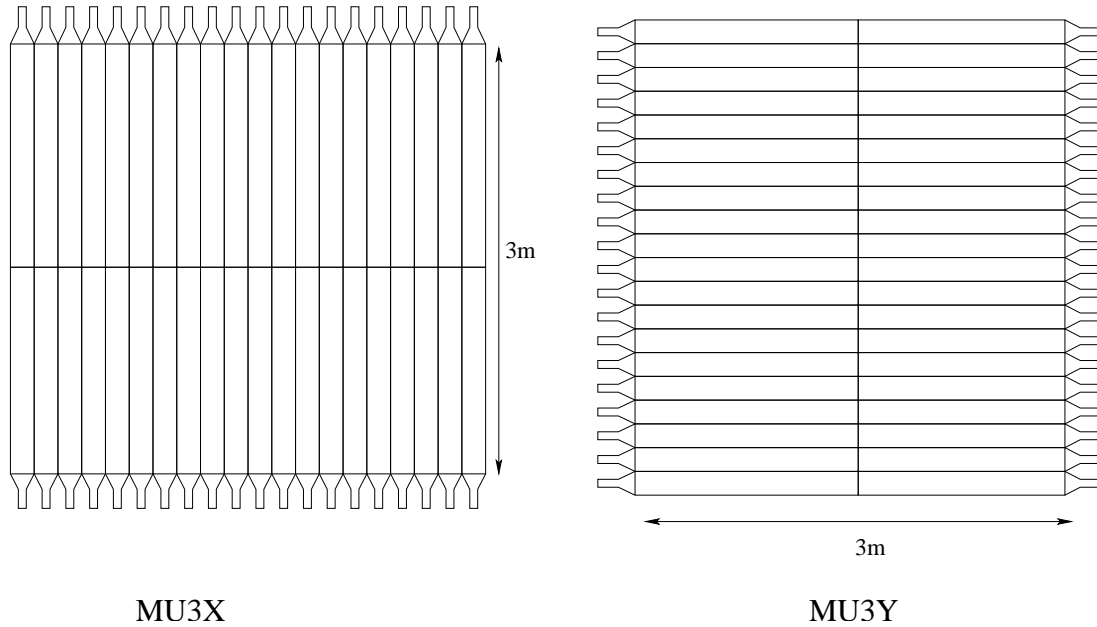


Figure 2.16: MU3X and MU3Y counter banks.

2.2.7 90° Accidental Counter

Another important element that has yet to be discussed is the *90° Accidental Counter*. A hole in the target shielding oriented perpendicular to the beam direction allowed one to monitor accidental detector activity that does not stem from K_L decays. Observing such accidental activity is important, since it can occur at the same time as a K_L decay, thus distorting K_L decay signatures. This device was composed of three scintillator counters located 1.8 m from the target along the $+x$ -axis. A

coincidence of all three scintillator counters fired an accidental trigger, which would be stored for later use in Monte Carlo simulation. Once again, the 90° Accidental Counter views a part of target space that is separate from the beam. Therefore, accidental activity was projected to be proportional to beam intensity, yet uncorrelated with K_L decays in the detector.

Chapter 3

Trigger and Associated Event Selection

As mentioned in Section 2.2.1, the only events accepted for this analysis were those in which the kaons decayed in the vacuum region. The rate of kaon decays in the aforementioned region was roughly 1 MHz. Since the data acquisition system (DAQ) could only record events at a maximum rate of 1 kHz [38], a multi-stage trigger system was incorporated into the DAQ. This served the dual purpose of selectively choosing meaningful events and reducing the incoming data to a sustainable rate.

The full trigger was comprised of two hardware components (Level 1 and Level 2) and a software component (Level 3). Accepted events were recorded and analyzed in 16 separate categories, which were each associated with a different beam trigger. $K_L \rightarrow \pi^0 \pi^0 \mu^+ \mu^-$ signal mode events and $K_L \rightarrow \pi^0 \pi^0 \pi_D^0$ normalization mode events

were identified with different beam triggers (Trigger 5 and Trigger 1 respectively). A detailed description of the trigger constituents shall be given in the following sections.

3.1 Level 1 Trigger

The Level 1 Trigger processed up to 96 input signals from various locations of the KTeV detector. The signals were primarily NIM pulses which originated from PMTs on the photon vetoes, muon counters, trigger hodoscopes and the CsI ECAL. In addition, there were signals from the Drift Chambers (known as DC-OR signals), which provided a veto on events with inadequate drift chamber activity. All of these signals were transferred from the experimental hall via delay cables to the counting room and then entered an array of programmable logic units. The delay cables were semi-rigid coaxial cables through which the signals would travel at roughly $0.9c$ [38]. All signals were synchronized so that they all arrived at the logic units simultaneously. As a result, signals from downstream detector elements went through shorter delay cables than signals from upstream elements.

Aside from the DC-OR and spill timing signals, all other signals were 19 ns in length. All L1 signals were synchronized to within 2 ns of the 53 MHz RF bucket structure [37]. Due to the aforementioned synchronization, L1 is referred to as a *deadtimeless* trigger. When the signals arrived at the logic units after synchronization, a CAMAC interface downloaded a memory lookup table, which was consulted in order to determine if the event passed the Level 1 Trigger.

3.1.1 Level 1 Signals

The Level 1 Trigger has a variety of different signals (sources) that stem from the detector including photon vetoes, trigger hodoscopes, DC-ORs, energy thresholds and muon counters. Two signals which do not stem from the detector are the *GATE* and the *NEUTRINO PING*. These signals shall be described in the following section.

Beam Timing Signals

The two beam timing signals were the *GATE* and the *NEUTRINO PING*. The *GATE* signal was created from the spill structure of the Tevatron beam. To be precise, the *GATE* signal could be transferred to experiment when the beam was on-spill. As mentioned in Section 2.1.1, the beam was on-spill for 20 seconds of every Tevatron cycle during the 1997 run. During the 1999 run, the beam was on-spill for 40 seconds of every Tevatron cycle. The *NEUTRINO PING* signal was activated when beam was being delivered to an experiment in an adjacent beamline. Occasionally leakage in the adjacent beamline would occur, which caused very high activity in the KTeV detector. To prevent this leakage, the *NEUTRINO PING* was used as a veto in such circumstances.

Photon Vetoes

Level 1 signals from the photon vetoes originated in the ring counters (RC6-RC10), the spectrometer anti (SA2-SA4), the calorimeter anti (CIA) and the collar

antis (CA). There was one signal per counter bank for the ring-shaped vetoes (RC6-RC10, SA2-SA4, CIA). The threshold for the RCs was 0.5 GeV, while the SAs and CIA fired for more than 0.4 GeV of in-time energy. The CA was composed of two sources, one from the east and one from the west detector referred to as CA_LEFT and CA_RIGHT respectively. These sources fired if more than 13 GeV was deposited in one of their photomultiplier tubes.

Trigger Hodoscopes

As discussed in section 2.2.4, the trigger hodoscopes were utilized to provide notification of the existence of charged particles in the detector. A total of 14 different signals were provided to the Level 1 Trigger by the V and V' hodoscopes. Analog signals from photomultiplier tubes on the V (upstream) and V' (downstream) hodoscopes were discriminated using 16-channel CAMAC discriminators. A hit in the hodoscope only occurred when one of the modules contained more energy than threshold. An analog sum from each module indicated how many counters had fired in each hodoscope plane. By that token, information on the number of hits in each plane of the system was provided to the Level 1 Trigger. The signal sources were named V0_GE1S, V0_GE2S, V0_GE3S, V1_GE1S, V1_GE2S and V1_GE3S for 1 or more, 2 or more and 3 or more hits in the V and V' planes respectively. The remaining eight signal sources were utilized for identification of two-body kaon decay modes.

E-Total

Signals from the final dynode stage of the 3100 CsI photomultiplier tubes were registered by the *E-Total* system. Dynode signals from every crystal in the CsI were summed and compared to 4 thresholds via a multi-channel NIM discriminator. The thresholds were named ET_THR1, ET_THR2, ET_THR3, ET_THR4 and were valued at 10(11) GeV, 18(16) GeV, 25 GeV and 38 GeV for the 1997(1999) runs respectively. CsI crystals were damaged by radiation over the course of the 1997 and 1999 runs, which caused the thresholds to slowly drift over time. Two methods were used to return the thresholds to their nominal values. One method involved tuning discrimination levels on the NIM module. Another way of resetting the threshold back to nominal was achieved by increasing the high voltage on the CsI photomultiplier tubes, which is known as *gain matching*.

DC-ORs

The DC-OR system allowed for triggering on upstream spectrometer activity in spite of the 200 ns maximum drift time. Each DC-OR *paddle* contained 16 wires divided evenly between two overlapping planes (upstream view and downstream view) of a drift chamber. A hit was registered if the logical OR of all the wires in a paddle returned true. The number of hit paddles in each chamber were counted by eight Level 1 sources: 1DC1X, 2DC1X, 1DC2X, 2DC2X, 1DC1Y, 2DC1Y, 1DC2Y and 2DC2Y. The aforementioned eight terms stand for one or more hits or two or more

hits in Chamber 1 X-view, one or more hits or two or more hits in Chamber 2 X-view and likewise for the Y-views. Through taking the logical OR of all anode wire pairs in each view of the two upstream drift chambers and noting that any track in the drift chambers must pass between two anode wires, one of the two hits is destined to arrive within half the maximum drift time. This allowed hit information to be sent to Level 1 within an acceptable amount of time.

Muon Counting System

The muon counting system is composed of three planes of paddle counters as described in section 2.2.6. Four different signals could be sent to the Level 1 Trigger by the muon counting system based on the number of hits in the paddle counter planes. The signal sources were named 1MU2, 2MU2, 1MU3 and 2MU3. 1MU2 and 2 MU2 corresponded to one or more and two or more hits in the first muon counting plane respectively. 1MU3 identified events with one or more hits in the x and y-views of the second muon counting plane, while 2MU3 indicated events with two or more hits in the x and y-views of the second muon counting plane.

3.2 Level 2 Trigger

If an event was accepted by the Level 1 Trigger, then it was sent off to the Level 2 Trigger to be processed. The Level 1 output rate averaged around 75 kHz. Hardware processors were employed in Level 2 to analyze the structure of an event, which

reduced the output rate to about 10 kHz. The analysis of an event lasted between 0.8 and 2.5 μs . Newly accepted events by Level 1 had to wait in a queue while Level 2 was processing an event. A Level 2 state machine then decided whether to accept or reject an event. If an event was rejected, then the process was aborted, which caused the Level 2 processors to reset. The reset procedure lasted 0.5 μs . Level 2 processing and readout introduced a dead-time of about 35% for the 1997 and 1999 runs. The two Level 2 processors relevant to this analysis are described below.

3.2.1 Hardware Cluster Counter

A custom-made electronic subsystem known as the *Hardware Cluster Counter* (HCC) determined the number of clusters in the CsI on an event-by-event basis. Every decay mode deposits a specific number of clusters in the CsI. In the case of $K_L \rightarrow \pi^0 \pi^0 \mu^+ \mu^-$ there are six electromagnetic final state particles (note that π^0 decays into two photons), which should yield six clusters in the CsI. In normal discourse, one would say that there are four clusters plus two clusters associated with electromagnetic tracks in that decay mode.

There are a total of 3100 HCC input bits corresponding to one bit for every CsI crystal. The Level 1 *E-Total* system supplies the input for the HCC. If the photomultiplier tube dynode signal indicates that the energy deposited in a crystal is greater than 1 GeV, then the corresponding bit is turned *on* by *E-Total*. *Gain matching* was instituted on the 1 GeV threshold every few months to counter gain

loss due to radiation damage in the CsI crystals. An in-time window determined when energy could be deposited in a given crystal. The width of the window varied from crystal to crystal, ranging from 6 to 10 ns, yet remained in phase with the 19 ns Tevatron RF period. The phase of the Tevatron RF and channel characteristics such as the speed of the photomultiplier tube and dynode signal cable length determined the relative location of the channel's in-time window. A number of channels were sensitive to variations in the phase of the Tevatron RF, which could shift by up to ± 3 ns over a data run. Inbetween the 1997 and 1999 data runs, these channels had their dynode signal cables shortened by 1.5 to 4.0 ns, which improved the stability of HCC threshold and width distributions for the 1999 data run.

A clever algorithm implemented by the HCC determined the number of clusters in an event. Consider a cluster in the CsI that is divided into 2×2 crystal groupings, where each grouping is given a weight based on which crystals were *on* (as defined in the previous paragraph). The algorithm works by counting corners. Begin by starting at any point on the border of the cluster and trace out the perimeter of the cluster in the clockwise direction. Increment the corner count by +1 for every 90° right turn and -1 for every 90° left turn. Once one has returned to the starting point, the corner count will be +4. Therefore, the cluster count for the CsI will be the corner count divided by four. The HCC algorithm looked at all possible 2×2 arrays for each CsI crystal and compared them to a lookup table, which is shown in Figure 3.1. The output of the HCC was a four-bit signal. The first three bits in an event allowed for

counting of up to eight clusters, while an overflow bit was used for events with over eight clusters. The time elapsed during the HCC process was approximately $2.5 \mu\text{s}$.

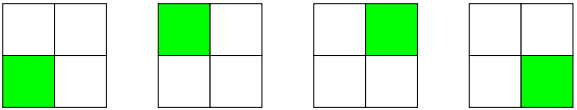
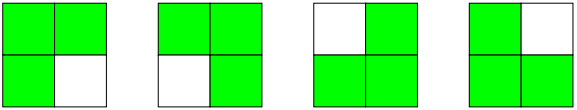
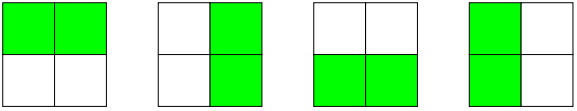
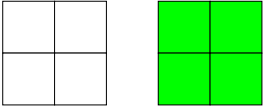
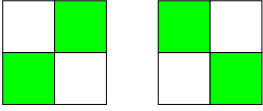
Hit Block Patterns	Pattern Weight
	+1: one right turn
	-1: one left turn
	0: no turns
	0: no turns
	+2: two right turns

Figure 3.1: Possible HCC bit patterns and their weights for 2×2 crystal arrays. Shaded blocks indicate that a bit has been turned *on*.

Certain regions of the grid contained anomalies which necessitated special treatment. If a cluster was enclosed within small and large crystals, then a large crystal was treated as four small crystals. Clusters were found on the outer perimeter of the CsI by bordering the outer edge of the calorimeter with *ghost* crystals. Likewise,

clusters were found along the beam hole boundary by filling the beam holes with *ghost* crystals [39]. A detailed reference on design of the HCC and the HCC algorithm can be found in Ref. [40].

3.2.2 DC Hit Counters

The *Drift Chamber Hit Counter* (DCHC) system enabled the Level 2 Trigger to reject events with insufficient activity in the drift chambers. In order to accomplish this task the DCHC system employed two types of processors called *Bananas* and *Kumquats*. Both modules tallied hits on DC plane pairs to determine whether they were in-time (whether they originated from the same track). The Bananas accomplished this task by using flash TDCs (which matched DC hits to a specific RF bucket) and memory lookup tables. If the Bananas found that the hit pairs had a good sum-of-distance (SOD), then they were in-time. The Kumquats implemented the in-time requirement by seeing if both hits took place within a 205 ns gate. Figure 3.2 gives a pictorial representation of the hit counting procedure employed by the Bananas and Kumquats. An event was processed by the DCHC system 900 ns after arrival from Level 1. Ref. [41] gives a complete description of the DCHC system.

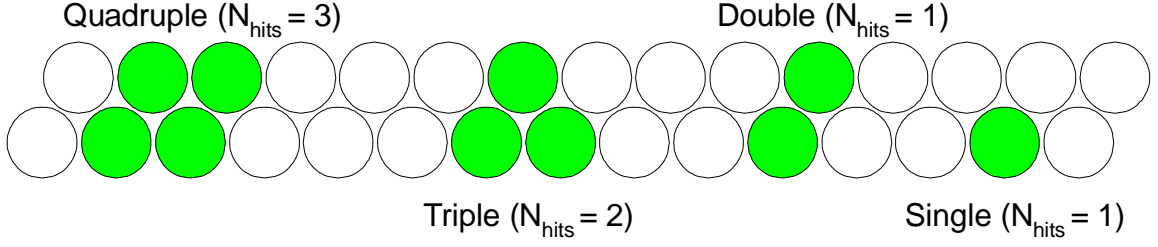


Figure 3.2: Wire hit arrangements in a DC plane pair and the hit counts returned by the Kumquats and Bananas. Shaded circles indicate a DC anode wire with an in-time hit.

3.3 Trigger Definitions

In order to make the selection of events from certain decay modes easier, the KTeV trigger team created 16 different *physics triggers*, which were combinations of Level 1 and Level 2 sources. There were two different *physics triggers* employed in this analysis. The *dimuon* trigger (also known as Trigger 5) was used to search for the signal mode $K_L \rightarrow \pi^0 \pi^0 \mu^+ \mu^-$. The *2E-NCLUS* trigger (also known as Trigger 1) was used to look for the normalization mode $K_L \rightarrow \pi^0 \pi^0 \pi_D^0$. Chapter six will give an in-depth look at the signal and normalization decay modes. The *dimuon* and *2E-NCLUS* triggers are described below.

3.3.1 The Dimuon Trigger

In addition to searching for the signal mode, the dimuon trigger also looked for the muonic dalitz decay $K_L \rightarrow \mu^+ \mu^- \gamma$ and the direct-CP violating mode $K_L \rightarrow \pi^0 \mu^+ \mu^-$.

In the 1997 run, this trigger was defined as:

Level 1 Trigger Symbol	Definition of Trigger Symbol
GATE	This event is on-spill.
2V	VV' requirement: ≥ 2 hits in one plane and ≥ 1 hit in the other.
DC12	≥ 1 DC-OR paddle hit in each view of DC1 and DC2.
2MU3	≥ 2 hits in X and Y views of MU3.
PHVBAR1	veto on all RC, SA and CIA hits.

Table 3.1: L1 trigger symbols and their definitions for the dimuon trigger.

Level 2 Trigger Symbol	Definition of Trigger Symbol
2HCY_LOOSE	≥ 2 hits in every Y View of DC3 and DC4. Also required ≥ 2 hits in DC1 or DC2 and ≥ 1 hit in the other DC.
HCC_GE1	≥ 1 hardware cluster.

Table 3.2: L2 trigger symbols and their definitions for the dimuon trigger.

$$GATE*2V*DC12*2MU3*PHVBAR1*2HCY_LOOSE*HCC_GE1.$$

The definitions of the trigger symbols are given in tables 3.1 and 3.2. In the 1999 run, the definition of the trigger was changed to:

$$GATE*2V*DC12*2MU3_LOOSE*PHVBAR1*2HCY_LOOSE*HCC_GE2.$$

The $2MU3_LOOSE$ requirement was inserted for $2MU3$ in order to allow for a missing hit in MU3. A concise definition would state that one view of MU3 has ≥ 2

hits and the other view has ≥ 1 hit. Naturally, this alteration increased the rate of the dimuon trigger. In order to balance this effect, ≥ 2 hardware clusters were required for the 1999 run.

3.3.2 The 2E-NCLUS Trigger

In addition to looking for the normalization mode, the 2E-NCLUS Trigger was also designed to search for the direct-CP violating mode $K_L \rightarrow \pi^0 e^+ e^-$. Basically, this trigger isolated decay modes that contained a minimum of two electrons, a minimum of 4 hardware clusters and no hadrons in the final state. During a good portion of the 1997 run and all of the 1999 run, this trigger was defined as:

*GATE*2V*ET_THR3*DC12*!HA_DC*PHVBAR1*!CA*2HCY_LOOSE
*HCC_GE4*1HC2X.*

The definitions of the trigger symbols are given in tables 3.3 and 3.4.

One final note on the 1997 definition of this trigger is that no hits were allowed in MU2 before run number 8577. Roughly 5 to 8 % of the signal was lost due to rates as high as 4 MHz in the MU2 counter plane [38].

Level 1 Trigger Symbol	Definition of Trigger Symbol
GATE	This event is on-spill.
2V	VV' requirement: ≥ 2 hits in one plane and ≥ 1 hit in the other.
ET_THR3	≥ 25 GeV total raw energy in CsI calorimeter.
DC12	≥ 1 DC-OR paddle hit in each view of DC1 and DC2.
!HA_DC	No AC-coupled HA 2.5 MIP threshold (winter). No DC-coupled HA threshold (summer & 1999).
PHVBAR1	veto on all RC, SA and CIA hits.
!CA	veto on Collar Anti energy that is > 14 GeV.

Table 3.3: L1 trigger symbols and their definitions for the 2E-NCLUS trigger.

Level 2 Trigger Symbol	Definition of Trigger Symbol
2HCY_LOOSE	≥ 2 hits in every Y View of DC3 and DC4. Also required ≥ 2 hits in DC1 or DC2 and ≥ 1 hit in the other DC.
HCC_GE4	≥ 4 hardware clusters.
1HC2X	≥ 1 Banana hit pair in the DC2 X View.

Table 3.4: L2 trigger symbols and their definitions for the 2E-NCLUS trigger.

3.4 Level 3 Trigger

If an event passed Level 1 and Level 2 it was then digitized and stored for read-out. The output of the Photon Vetoes was sent to a CAMAC ADC for digitization. Bitmasks of Level 1 and Level 2 sources were recorded by latch modules. Spill and event numbers were provided by 16 bit scaler modules. At the end of the digitization process, an event was composed of ADC, TDC, latch, scaler and pipelined CsI information. Digitized events were then stored in one of four VME memory modules. Each module belonged to a DAQ plane. Three of the DAQ planes were assigned to the physics triggers, while the last plane was employed for 14 calibration triggers and monitoring events.

Four Silicon Graphics Challenge L computers read out the modules over the duration of a spill and ran the Level 3 Trigger software. The Level 3 Trigger essentially used various software routines to find tracks, vertices and clusters to perform a basic reconstruction of events. Chapter 4 provides a discussion of the reconstruction process. The software was optimized so that the Level 3 Trigger yielded virtually no deadtime at normal beam intensities. Table 3.5 lists the Level 3 requirements for the Dimuon Trigger and the 2E-NCLUS Trigger. Events which passed all Level 3 requirements were written to Digital Linear Tapes (DLTs).

Level 3 Requirement	Dimuon	2E-NCLUS
# of reconstructed tracks	≥ 2	≥ 2
# of vertex candidates	≥ 1	≥ 1
# of track-cluster matches	2	2
# of clusters in the CsI	≥ 3	≥ 4
Energy of track-clusters	≤ 5 GeV	
Energy of each cluster in CsI		≥ 2.5 GeV
E/p		≥ 0.75

Table 3.5: Level 3 Requirements for the Dimuon and 2E-NCLUS Triggers.

Chapter 4

Event Reconstruction

The first important step in the search for $K_L \rightarrow \pi^0 \pi^0 \mu^+ \mu^-$ is to turn the information stored on the tapes into kinematical quantities that are useful for this analysis. When an event was stored onto tape it contained ADC, TDC and DPMT readouts. This chapter describes how the counts in each event coupled with a program called KTeVANA (v6_04) are used to construct useful physical quantities such as calorimeter cluster energy and position, charged track momenta and z-vertex position. Once the three aforementioned quantities are constructed, the event reconstruction is performed. At that point, a full analysis of the signal and normalization modes can now be undertaken.

4.1 Tracking

The first step in reconstruction is to use spectrometer information to find the position and momentum of tracks. Track segments are created from good DC hits. Furthermore, track segments create track candidates, which can also be paired to clusters (primarily MIPs) in the CsI calorimeter. Finally, once a good track has been acquired, one can then compute the track momentum. This next section will give a basic description of how the tracking process is accomplished.

4.1.1 TDC and SOD

Time to Distance Conversion

An issue still left unaddressed in the calculation of SODs is the conversion of TDC counts to drift distances. Calibrating the timing of individual wires is the first step in formulating a time to distance expression (written as $X(t)$) and is known as $X(t)$ calibration. Factors which contribute to differences in timing include variations in electronics channels, in cable length and in the wide variety of trigger signals delivered to the TDCs from throughout the experiment. The TDC count that coincides with the zero drift distance (T_0) for a given wire resolves the aforementioned differences. Each TDC distribution contains a plateau area, which corresponds to uniform drift velocity. A zero drift distance is measured with $K_L \rightarrow \pi^\pm e^\mp \nu_e$ (K_{e3}) data as the midpoint between the plateau edge and zero event point of the TDC distribution

being analyzed.

Assuming uniform illumination of tracks across a cell, the T_0 offsets described in the previous paragraph are used to create maps of TDC counts to drift distances for each chamber plane. The drift distance as a function of the TDC count t is expressed as:

$$X(t) = L \times \frac{\sum_{t_0}^{t_m} N(t')}{\sum_{t_0}^{t_m}} N(t'), \quad (4.1)$$

where L is the cell spacing, $N(t')$ is the number of hits at a TDC count of t' and t_m and t_0 are the latest and earliest TDC counts respectively.

Sum of Distances

In order to find good DC hits, one must first look at all *hit pairs* and organize them into a classification system based on their *sum of distance* (SOD). A *hit pair* occurs when two neighboring anode wires each register an in-time hit. The SOD is calculated by taking the sum of the electron drift distances from each hit in the hit pair. Ideally, every SOD should be equal to the 6.35mm cell spacing (see Fig. 2.7). However, due to drift distance resolution effects, a good SOD is defined to be anywhere between 5.35mm and 7.35mm.

In addition, there are a few unfavorable scenarios that can lead to bad SOD's, as depicted in Fig. 4.1. Low SODs often appear when two charged tracks share the same cell. In such a situation, both anode wires will record two in-time hits. Since only the first in-time hits are employed in calculating an SOD, then the SOD

is typically too small. Two tracks occur in the same cell when there's a very high momentum decay, a delta-ray or accidental activity. High SODs are often the result of tracks passing anode wires at a close distance. At such close distances, the drift electrons do not have enough time to avalanche before reaching the anode wire, so a delayed time measurement ensues. Other tracking inefficiencies such as inadequate signal gain, noise from electronics and radiation damage to the drift chambers could also lead to high SODs. An isolated hit occurs when only one member of a plane pair is hit. This can stem from a damaged anode wire. A left-right ambiguity occurs when determining the position of an isolated hit with respect to an anode wire, so both possibilities are analyzed. More precisely, a track can be reconstructed from some isolated hits if good SODs are also present, but track reconstruction is not possible from isolated hits alone. Figure 4.2 shows an SOD distribution from a portion of the 1999 $K_L \rightarrow \pi^0 \pi^0 \pi_D^0$ normalization mode data.

4.1.2 Track Finding Procedure

Track finding was performed separately for the Y and X Views. Since the field in the analysis magnet was oriented in the y-direction, tracks in the Y View were expected to lie in a straight line. The central step in finding a track candidate is matching hit pairs in the drift chambers. For y-tracks, hit pairs in DC1Y were matched to hit pairs in DC4Y and these were then connected by a straight line. In order to form a valid y-track candidate, hit pairs in DC2Y and DC3Y had to be

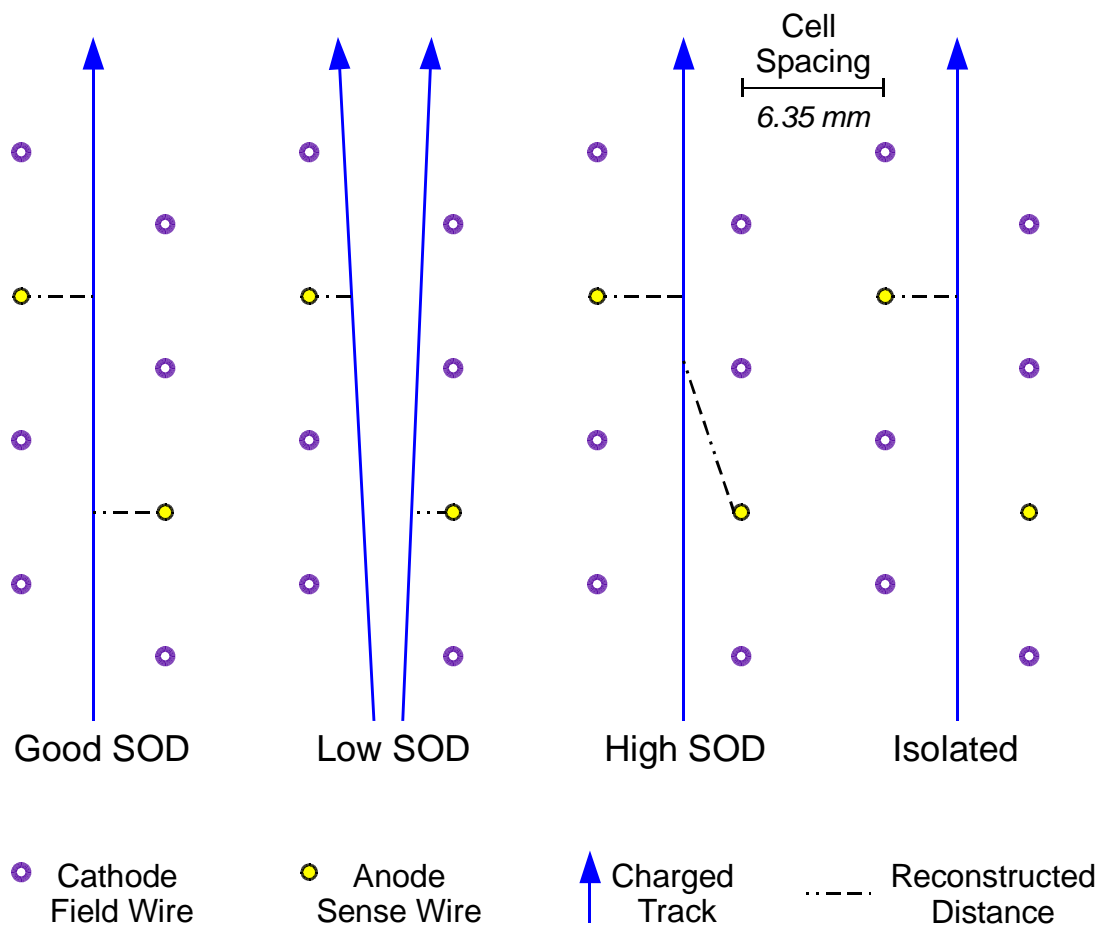


Figure 4.1: SOD Classification System.

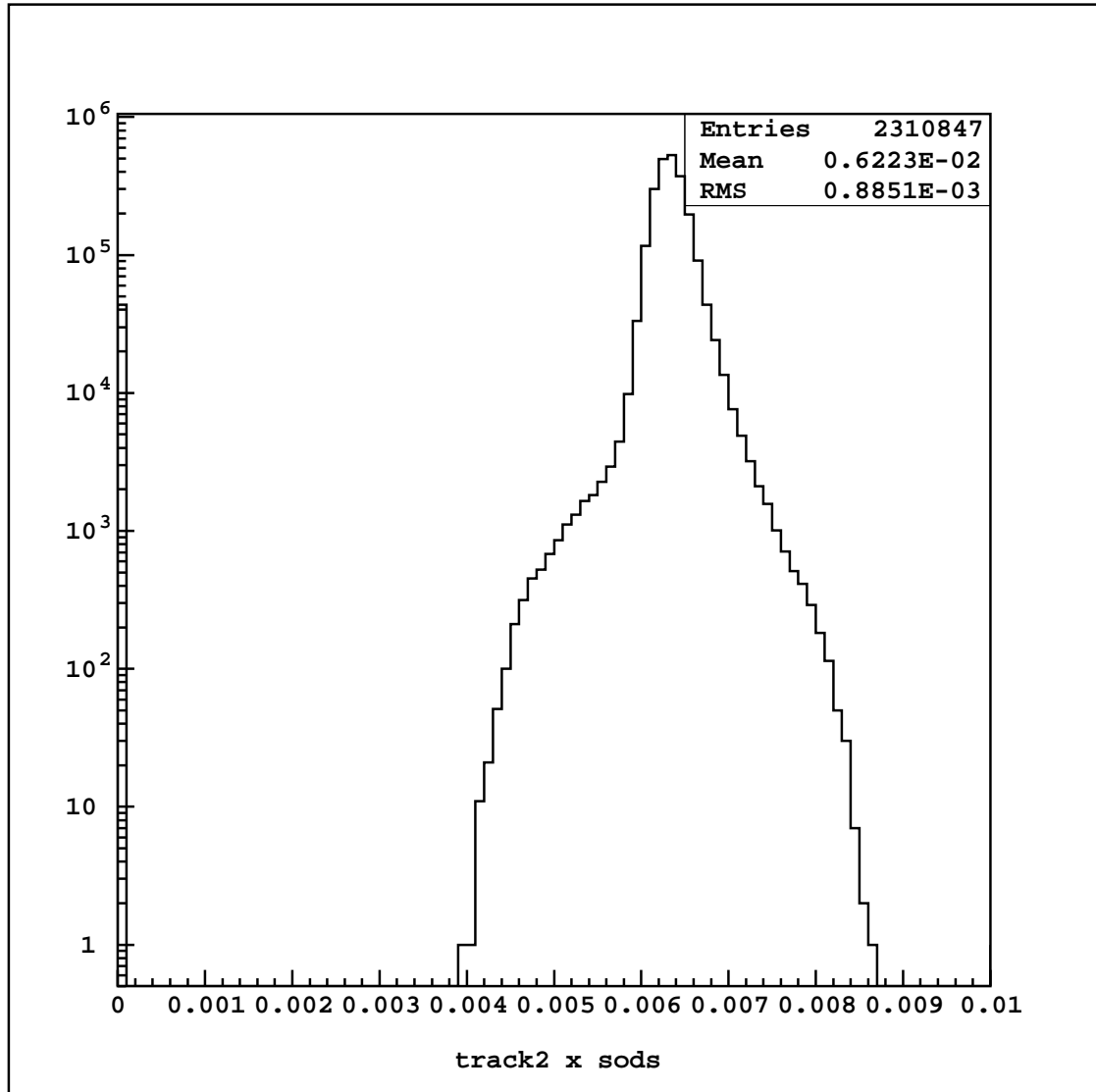


Figure 4.2: SOD X-View distribution for tracks in a number of 1999 $K_L \rightarrow \pi^0 \pi^0 \pi_D^0$ normalization mode events. The distribution is centered on the cell spacing 6.35 mm, but the mean is brought down slightly by isolated hits located at 0.0 mm.

located within 5.0 mm of that line. In order to ascertain how well a track candidate fit the hit pairs, a track χ^2 was calculated. Remember from Section 2.2.2 that the resolution of charged track hit positions in the drift chambers is 100 μm . The SOD resolution is $\sqrt{2}$ times larger. Track candidates were only retained if track χ^2 per degree of freedom was less than 4. Most y-track contained good SOD pairs. However, if a y-track candidate possessed bad SODs, then it was allowed to contain a maximum of two bad SOD pairs or one bad SOD pair and one isolated hit. Only events with two or more valid y-track candidates were retained.

The procedure for finding x-track candidates is a little more complicated since the analysis magnet bends tracks in this plane. A three step procedure was implemented to piece together an x-track. Upstream line segments were formed using hit pairs in DC1X and DC2X. Upstream segments were only allowed a maximum of two bad SOD pairs or one isolated hit. Using hit pairs in DC3X and DC4X, the same procedure is performed for downstream line segments, except only a maximum of one bad SOD pair or one isolated is allowed. If a pair of line segments did not intercept the magnet bend plane (located at $z=170.0m$) to within 6.0mm, then they did not form a valid x-track candidate and were rejected. Valid x-track candidates were only allowed to have a maximum of two bad SODs or one bad SOD and one isolated hit. Only events with two or more valid x-track candidates were retained. Section 4.3.1 will discuss how x and y track candidates are combined to form a 3D track.

4.2 Clustering

The second step in reconstruction is making a proper determination of cluster energies and momenta in the CsI calorimeter. Since we have chosen a neutral z -vertex (see section 4.3) for this analysis, accurate clustering is vital. Finding the hardware and software cluster energies are the first two steps in clustering. Once the cluster energies are found, one can calculate cluster positions. In the final step of clustering, a series of corrections to the cluster energies were made in order to better simulate calorimeter performance.

4.2.1 Hardware Clustering

The procedure for finding hardware clusters relied on HCC bits set in the E-Total system of the Level 1 trigger. Only crystals with HCC bits turned on were considered in this procedure. As discussed in section 3.2.1, an HCC bit may only be turned on when more than 1 GeV is deposited in a crystal. In order to find hardware clusters, one simply looped over all HCC-on crystals to search for local energy maxima. The crystals containing local energy maxima are referred to as hardware cluster *seeds*. Summing up the crystal energies around the local maxima yielded the *raw* hardware cluster energy. In the case of large crystals, the summation was made over a 3×3 array, whereas with small crystals a 7×7 array was implemented. When an array was located in a mixed region of large and small crystals, then the summation is executed over an array of 3×3 large crystals, where 2×2 small crystals played the role of a large

crystal. Since the E-Total system only allowed for calorimeter channel energies within the in-time window, then the effect of out-of-time clusters from accidental activity in determining HCC bit status was suppressed.

4.2.2 Software Clustering

In the previous section, it was noted that hardware clustering could not find clusters below the 1 GeV energy threshold. This poses a problem in the identification of muons, since they are MIPs, which typically deposit only a small fraction of their energy in the CsI calorimeter. The range of MIP energy deposition in the calorimeter was normally between 320 MeV and 400 MeV. As a result, a software clustering procedure was created in order to search for clusters above an in-time energy threshold of 50 MeV. Local maxima which identified hardware cluster seeds, were excluded from the software cluster seed tagging process. Raw software cluster energies were calculated using the same array summation procedure described in the previous section. Only software clusters with raw in-time energies greater than 100 MeV were kept for further analysis.

4.2.3 Cluster Positioning

The transverse positions of clusters were found by determining the x and y center of energy of each cluster. First, the ratio of the energy in the row containing the cluster seed to the energy in adjacent rows was calculated. Comparison of the ratios

was made against values in a look-up table, which yielded the clusters y center of energy. The look-up tables were created experimentally through analysis of cluster photons in the $K_L \rightarrow \pi^0 \pi^0$ decay mode data and Monte Carlo. The look-up tables were cross-checked with K_{e3} calibration events. An identical procedure using columns yielded an x center of energy for the cluster. The position resolution for a cluster in an array of small crystals was 1.0 mm and 1.8 mm in an array of large crystals.

4.2.4 Cluster Energy Corrections

The simple approach that was employed to calculate raw cluster energies failed to address various ‘real-world’ scenarios encountered in the clustering side of event reconstruction. Multiple energy corrections were implemented to alleviate these problems. These corrections are summarized below.

Overlap Correction

In many events, different clusters would share crystals (i.e. overlap). An *overlap correction* was employed to separate clusters that shared crystals. An iterative approach was used to divide the energy of the common crystals based on the energy and position of the clusters. The iteration process yielded new cluster positions and energies. Iterations were performed until energies and positions were constant to within a given range (100 μm in x and y for position and 5 MeV for energy) or until 20 iterations had been attained.

Neighbor Correction

Some clusters deposit energy outside of their 3×3 (large crystal) or 7×7 (small crystal) array region, which could end up in a neighboring (but not overlapping) cluster, which would affect the energy of a neighboring cluster. The *neighbor correction* accounted for these anomalies by estimating the energy leakage from one cluster into a neighboring cluster array using GEANT simulations. GEANT generated mean transverse shower profiles for a 13×13 small block arrays to predict the energy leakage, which was then subtracted from the raw energy of the smaller neighbor. Naturally, neighbor corrections played an important role in this analysis, since a number of events possessed neighboring muon and photon clusters. Note that most muon clusters are low energy since they are MIPs, in which case neighboring photon clusters can have a noticeable effect on muon energies in the calorimeter.

Missing Block Correction

Cluster arrays sometimes traversed a beam hole or the calorimeter edge. A *missing block correction* was applied to account for the average energy that would have appeared in the missing crystals. The lost energy was estimated using the same GEANT simulations employed in the neighbor correction procedure, then added to the raw cluster energy. The missing block correction gave a more plausible energy estimate of clusters that traversed the calorimeter edge.

Sneaky Energy Correction

When a cluster is formed at the edge of a beam hole, energy from that cluster can move through gap in the calorimeter to the other side of the beam hole. Sneaky energy made the energy of a cluster on another side of the beam hole appear larger than the true value. Situations such as these merited a *sneaky energy correction*, which was estimated by investigating clusters from K_{e3} calibration events near the beam hole. A sneaky energy correction table was developed by studying energy deposits in a C-shaped region across from K_{e3} clusters.

Threshold Correction

Recall that if the energy of a DPMT was below a certain threshold, it was not read out. This is referred to as *sparsification*. In some events, the DPMT crystals are on the fringes of a cluster array. If a low energy crystal is not read out in such an array, then the cluster energy is reduced. This effect is balanced out by a *threshold correction*, which adds a certain threshold energy, E_{thr} to each crystal of a cluster array where the effect occurred. The quantity E_{thr} depends on the distance, r , of the sparsified crystal from the cluster center and is given by:

$$E_{thr} = P_1(r) + P_2(r) \cdot \log(E). \quad (4.2)$$

P_1 and P_2 were mapped out during special calibration runs, which contained no sparsification conditions.

Non-Linearity Correction

The *non-linearity correction* counteracted longitudinal non-uniformities in the crystals and energy dependence of the longitudinal distribution of cluster showers. Shower leakage through the back of crystals and uniformity along the length of crystals led to non-linearities in the performance of the CsI calorimeter. Through cross-examining these non-linearities in each crystal with GEANT shower studies, a table of non-linearity correction factors was formed. Since the longitudinal distribution of electromagnetic showers was a function of the energy of the incident particle, the corrections were distributed in energy bins with lower bounds of 2, 4, 8, 16, 32 and 64 GeV.

Intra-Block Correction

The energy of a cluster depended on its point of impact on the face of crystal. In more eloquent fashion, one would say that the cluster energy depends on the transverse position of impact on a crystal face. This effect required an *intra-block correction* to improve the energy resolution. By dividing each crystal into a 25 element array and studying the E/p response of each element of the array to K_{e3} electrons, a map of multiplicative factors to the cluster energy was formed. The variation in response of minimum-ionizing muons over the 25 element array was smaller than that of K_{e3} electrons, but had the same shape [42].

Fudge Factor

Since calibration was performed using highly relativistic K_{e3} electrons, then E/p should naturally be unity in a linear calorimeter. Even after all the aforementioned corrections were applied to the crystal energies there still remained a slight variation in E/p with respect to the electron track momentum p (see Figure 4.3). A *linearity fudge factor* was obtained from E/p vs p distributions for each large and small crystal. These fudge factors were then applied to all crystals in the calorimeter in order to cancel out any variation in E/p with p .

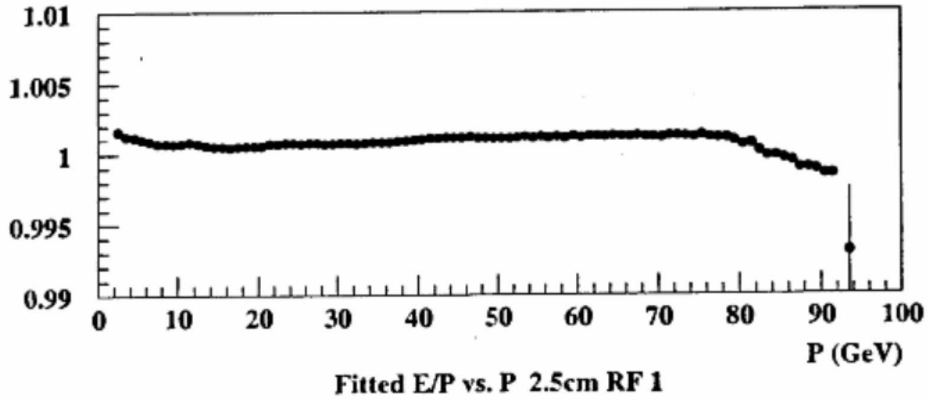


Figure 4.3: Mean E/p vs. p of K_{e3} calibration electrons in small blocks. The plot was made after all cluster energy corrections (except the fudge factor) were applied. The fudge factor cancels out any small deviations in E/p with p [43].

4.3 Vertexing

The $K_L \rightarrow \pi^0 \pi^0 \mu^+ \mu^-$ signal mode decay contains two charged tracks and four clusters (not associated with tracks). The two charged tracks can be reconstructed

into a *charged decay vertex*, while the four clusters can be reconstructed into a *neutral decay vertex*. Either of these decay vertices could be used to describe the K_L decay point, also known as the *z-vertex*. Naturally, the two aforementioned vertex reconstruction methods have a different effect on the reconstruction of critical decay parameters such as π^0 mass, transverse momentum squared (p_T^2) and K_L invariant mass.

Since the muon pairs have such small opening angles, a vertex reconstruction using the charged track information has a large uncertainty in the measurement of the z-vertex. Reconstruction of a neutral vertex using the positions and energies of available clusters (unassociated with tracks) gives a much better z-vertex resolution than the charged case. This, in turn, provides better p_T^2 and mass (K_L and π^0) resolutions. As a result, this analysis employs a neutral z-vertex to describe the K_L decay point. The remainder of this section will describe how tracks are matched to clusters and the neutral vertex reconstruction procedure.

4.3.1 Track-Cluster Matching

In order to construct a neutral vertex, one needs to first eliminate clusters associated with tracks. At the same time one can also match x and y track candidates. First, one projects the position of the x and y track candidates at the spectrometer to the CsI calorimeter. Second, one must compare the cluster positions found using the methods of section 4.2 to the position of track candidates at the CsI. This is done

for all clusters and all track candidates. If an x and y track candidate are matched to the same cluster, then they are matched to one another provided that they are less than 1.5 cm apart. This x and y track candidate pairing combined with the extrapolation from the spectrometer to the CsI yields a 3D track, which shall from now on be referred to as *track*. If the difference between the track position and the cluster position at the CsI calorimeter is less than 7 cm, then the 3D track is matched to the cluster. If the position of a track is extrapolated to one of the calorimeter beam holes, then it does not need to be matched to a cluster. Clusters which did not meet the matching criteria stated above will be considered photon clusters (photons outside the CsI calorimeter) for the rest of this analysis.

4.3.2 Neutral Vertex Reconstruction

Now that the photon clusters have been separated from the clusters associated with tracks, we can proceed to reconstruct the neutral z-vertex. Standard $\pi^0\pi^0$ reconstruction is performed by the KTeVANA driver routine KTPAIRS. A subroutine within KTPAIRS (called KTCHISQ) loops through all π^0 pairs and finds the pair with the minimum pairing chi-squared (χ_z^2), as demonstrated in Figure 4.4. The (neutral) z-vertex for the event is then calculated as a weighted average of z-vertex values for each $\gamma\gamma$ pair in the π^0 pair with the minimum χ_z^2 . The remainder of the chapter shall describe how KTPAIRS and KTCHISQ work together to find the best neutral z-vertex for each event.

In order to reconstruct a neutral z-vertex for two π^0 s, we need four photon clusters in the CsI calorimeter. The signal mode decay $K_L \rightarrow \pi^0 \pi^0 \mu^+ \mu^-$ has four photons, while the normalization mode decay $K_L \rightarrow \pi^0 \pi^0 \pi_D^0$ (where $\pi_D^0 \rightarrow e^+ e^- \gamma$) contains five photons. This yields three different ways that four photon clusters can be paired into two π^0 s and fifteen different ways that five photon clusters can be paired into two π^0 s.

In this procedure, each pair of photons are assumed to have originated in a π^0 decay. This constant on the mass of the photon pairs can be used to calculate the position of the decay (the neutral vertex). The invariance of the mass of the two photons is given by:

$$\begin{aligned}
 m_{\pi^0}^2 &= (E_{\gamma_1} + E_{\gamma_2})^2 - |\vec{p}_{\gamma_1} + \vec{p}_{\gamma_2}|^2 \\
 &= 2E_{\gamma_1} E_{\gamma_2} - \vec{p}_{\gamma_1} \cdot \vec{p}_{\gamma_2} \\
 &= 2E_{\gamma_1} E_{\gamma_2} (1 - \cos \theta_{12}).
 \end{aligned} \tag{4.3}$$

Using the small angle approximation (since the opening angle is small) and expanding to first order:

$$\begin{aligned}
 (1 - \cos \theta_{12}) &\simeq \frac{\theta_{12}^2}{2}, \\
 \theta_{12} &\simeq \frac{r_{12}}{z_{ecal}},
 \end{aligned}$$

where r_{12} is the distance between the two photon clusters on the face of the CsI

calorimeter. This yields:

$$z_{ecal} \simeq \frac{\sqrt{E_{\gamma_1} E_{\gamma_2}}}{m_{\pi^0}} r_{12}. \quad (4.4)$$

The most general expression for χ_z^2 is expressed as:

$$\chi_{z_{1,2}}^2 = \sum_{i=1}^2 \frac{z_{ecal,i}^2}{\sigma_{z_{ecal,i}}^2} - \left(\sum_{i=1}^2 \frac{z_{ecal,i}}{\sigma_{z_{ecal,i}}^2} \right)^2 \left(\sum_{i=1}^2 \frac{1}{\sigma_{z_{ecal,i}}^2} \right)^{-1}, \quad (4.5)$$

where the index i is the photon vertex number and σ_z is the uncertainty on the z-vertex squared. The uncertainty on the z-vertex can be attributed to the limited position and energy resolution of the CsI calorimeter. In essence, the uncertainty on the z-vertex can be calculated as a function of the energy, uncertainty on the energy, position (in x and y) and uncertainty on the position of both photons on the calorimeter face. After some simple steps, $\chi_{z_{1,2}}^2$ can be reduced to:

$$\chi_{z_{1,2}}^2 = \frac{(z_{ecal,1} - z_{ecal,2})^2}{\sigma_{z_{ecal,1}}^2 + \sigma_{z_{ecal,2}}^2}. \quad (4.6)$$

Once again, in the case of the signal mode (four photons) one would compare $\chi_{z_{1,2}}^2$, $\chi_{z_{3,4}}^2$ and $\chi_{z_{5,6}}^2$. The lowest χ_z^2 is considered an indicator of the *correct* pairing and is used to calculate the z-vertex for that event. The z-position of the CsI calorimeter face, z_{CsI} , was acquired through survey measurements. Energy and position resolutions of electrons in K_{e3} events allowed for determination of the errors on the photon cluster energies and positions, which were used to calculate the uncertainties and weighted means. Figure 4.4 illustrates an example of the four photon case. For the

example illustrated in Figure 4.4, the z-vertex (z_{vtx}) of that event would be given as the difference of z_{CsI} and the weighted average of z-vertex values for each $\gamma\gamma$ pair in the best π^0 pairing:

$$z_{vtx} = z_{CsI} - \left(\sum_{i=1}^2 \frac{z_{ecal,i}}{\sigma_{z_{ecal,i}}^2} \right) \left(\sum_{i=1}^2 \frac{1}{\sigma_{z_{ecal,i}}^2} \right)^{-1}. \quad (4.7)$$

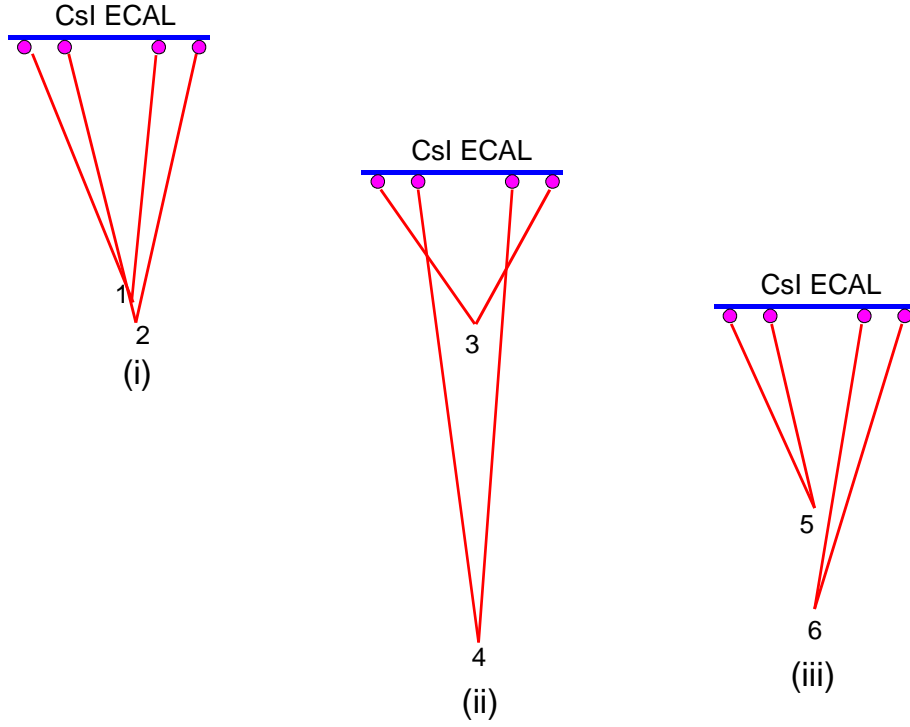


Figure 4.4: Top-view illustration of three possible π^0 pairing combinations from four photons. Each π^0 is assumed to come from a two photon vertex. Numbers one through six are the photon vertex numbers. The best π^0 pairing is taken to be the one with the lowest χ_z^2 . In this case, picture (i) contains the best pairing.

Chapter 5

Monte Carlo Simulation

Two of the most important procedures in this analysis are calculating the acceptance and estimating the number of background events that populate the signal region. In order to accomplish this task, we must first insert a precise description of the detector into the Monte Carlo (MC) simulation framework. The MC simulation is utilized to generate neutral kaons at the target, which were then propagated to the decay region and allowed to decay. The interactions of the neutral kaons and their decay products were then simulated in the MC with all elements of the detector. Essentially, a large database of detector calibration information is used to simulate decays within the MC environment. This information is stored in the same fashion in which data is recorded, which allowed the procedures for analyzing data and MC events to be nearly identical.

An acceptance is obtained by taking the remaining MC events after all cuts and

dividing those by the number of MC generated events. A signal mode acceptance is used in the calculation of a branching ratio for the signal mode. A normalization mode acceptance is employed for estimating the K_L flux in the 1997 and 1999 data sets, which are also used in the calculation of the branching ratio. In addition, the MC provides an estimate on the number of background events within the signal mode region of both the data and the normalization mode data. These estimates are needed in order to get an idea of how many signal and normalization mode events remain after all cuts. Finally, comparisons were made between data and MC to check that the geometry, resolution and efficiency of detector elements were correctly understood. The MC is also used as a tool to estimate the magnitude of the associated systematic effect due to inconsistencies between MC and data. This chapter describes the KTeV Monte Carlo simulation environment.

5.1 Production of Kaon Beams in Monte Carlo

K^0 - \bar{K}^0 production at the BeO target marked the first stage of MC event generation. In the early 1980's, the charged kaon production cross section for 400 GeV/c protons incident on a beryllium target was determined by Malensek [44] as:

$$\frac{d^2N}{dPd\Omega} = \frac{Bx(1-x)^A(1+5e^{-Dx})}{400(1+\frac{P_t^2}{M^2})^4}, \quad (5.1)$$

where P_t is the transverse momentum of the charged kaons with respect to the incoming proton beam and x is a variable defined as the quotient of the momentum of the

Parameter	N_{K^+}	N_{K^-}
A	2.924	6.107
B	14.15	12.33
M^2	1.164	1.098
D	19.89	17.78

Table 5.1: Parameters determined by Malensek after fitting data from production of charged kaons on a 0.5 m Be target [44]. Units are produced particles per *steradian-GeV/c-incident proton*.

charged kaons with the energy of the incident protons. The free parameters A , B , D and M^2 were determined by a minimum χ^2 fit to the charged kaon production data from the 400 GeV/c protons. The results of this fit are given in Table 5.1. However, since our incident beam is produced with 800 GeV/c protons, we need a more general expression, which is also given by Malensek [44]:

$$\frac{d^2N}{dP d\Omega} = KP \frac{(1-x)^A (1+5e^{-Dx})}{(1+\frac{P^2}{M^2})^4}, \quad (5.2)$$

where K is equivalent to $\frac{B}{400}$. The constants in the above equation were adjusted to match the momentum distribution from $K_L \rightarrow \pi^+\pi^-$ data events taken at KTeV.

One can arrive at the neutral kaon production cross section by applying a quark counting argument, whereby the sum of valence and sea quark combinations are employed to arrive at an estimate of the magnitude of the neutral kaon production probability. First, one assumes that the s quark and all anti-quarks only come from the sea, and a u or d can come from the valence or the sea. Since target production occurs via the strong force, then the next step is to use isospin invariance, which leads to the assumption that all $u\bar{u}$ and $d\bar{d}$ content in the sea are equal. Now one can

estimate a relationship between the production cross sections of charged and neutral kaons:

$$K^0 \approx \frac{K^+ + K^-}{2} \quad (5.3)$$

$$\bar{K}^0 \approx K^-. \quad (5.4)$$

The above expressions yield the following formulations for neutral kaons:

$$\frac{d^2 N_{K^0}}{dP d\Omega} = \frac{1}{2} \left(\frac{d^2 N_{K^+}}{dP d\Omega} + \frac{d^2 N_{K^-}}{dP d\Omega} \right), \quad (5.5)$$

$$\frac{d^2 N_{\bar{K}^0}}{dP d\Omega} = \frac{d^2 N_{K^-}}{dP d\Omega}. \quad (5.6)$$

The above expressions predict a mixture of about 55% K^0 and 45% \bar{K}^0 from the target.

MC kaons were generated over a momentum range from 20 GeV/c to 220 GeV/c. While taking into account the oscillation between K_0 and \bar{K}_0 , the neutral kaons are then extrapolated to the vacuum decay region, which is located between 90 m to 160 m from the target. Any kaon possessing a trajectory that intersected the primary collimator or defining collimator was absorbed or scattered. Scattering was also simulated in all other absorbers and collimators located in the NM2 enclosure (see Figure 2.2). If a kaon was not scattered or absorbed, then the K^0 and \bar{K}^0 states were evolved to their decay points in the vacuum region. Since the the vacuum decay region was located so far from the target, the final states were almost purely K_L within this volume.

5.2 Simulation of K_L Decays

After the K_L were allowed to decay, all of the decay products as a system were randomly rotated and boosted into the lab frame. This section describes the generation methods for the major decays employed in this analysis.

5.2.1 The Signal Mode $K_L \rightarrow \pi^0 \pi^0 \mu^+ \mu^-$

As mentioned in chapter 1, the signal mode is feasible within the Standard Model. However, the phase space of $K_L \rightarrow \pi^0 \pi^0 \mu^+ \mu^-$ is limited to a paltry 16 MeV. Due to this constraint, generation of the signal mode using flat four body phase space is a viable option and was used for this analysis. Studies on the decay $K_L \rightarrow \pi^0 \pi^0 X^0 \rightarrow \pi^0 \pi^0 \mu^+ \mu^-$ were performed using flat three body phase space with the additional requirements that the X^0 decay immediately and its' mass be limited to (214.3 ± 0.5) MeV/ c^2 . Chapter 6 will describe the procedure used to extract the acceptance of the aforementioned signal modes.

5.2.2 The Normalization Mode $K_L \rightarrow \pi^0 \pi^0 \pi_D^0$

The normalization mode begins with the decay $K_L \rightarrow \pi^0 \pi^0 \pi^0$, which is based off of a flat three body phase space. The aforementioned generation technique for $K_L \rightarrow \pi^0 \pi^0 \pi^0$ was considered satisfactory, since the effects of the measured form factor are negligible. Once the π^0 's have been generated, two are subject to the decay $\pi^0 \rightarrow \gamma \gamma$ and the remaining π^0 undergoes dalitz decay ($\pi^0 \rightarrow e^+ e^- \gamma$, labeled as π_D^0).

The $\pi^0 \rightarrow \gamma\gamma$ decay is described by a simple two body phase space. Since the lifetime of a π^0 is extremely short ($\tau_{\pi^0} = (8.4 \pm 0.6) \times 10^{-17}$ s [45]), it is assumed to undergo decay at the point of π^0 production. The $\pi^0 \rightarrow e^+e^-\gamma$ dalitz decay is generated in the KTeV MC using the Kroll-Wada matrix element [46], which contains a form factor term:

$$f(x) = 1 + ax, \quad (5.7)$$

$$x = \frac{m_{ee}^2}{m_{\pi^0}^2}, \quad (5.8)$$

where a is a constant that has been experimentally measured to be 0.032 ± 0.004 [47]. The MC generation of $\pi^0 \rightarrow e^+e^-\gamma$ also includes inner bremsstrahlung corrections from $\pi^0 \rightarrow e^+e^-\gamma\gamma$ [48] and virtual-photon corrections to the m_{ee}^2 spectrum. In order to avoid divergences, the inner bremsstrahlung correction was equipped with a cutoff of $m_{\gamma\gamma} > 1$ MeV. Table 5.2 lists branching ratios that are applicable to the normalization mode. A calculation of the $K_L \rightarrow \pi^0\pi^0\pi_D^0$ branching ratio is given below.

$$\begin{aligned} BR(K_L \rightarrow \pi^0\pi^0\pi_D^0) &= 3 \cdot BR(K_L \rightarrow \pi^0\pi^0\pi^0) \cdot BR(\pi^0 \rightarrow e^+e^-\gamma) \cdot BR(\pi^0 \rightarrow \gamma\gamma)^2 \\ &= (6.85 \pm 0.23) \times 10^{-3}. \end{aligned} \quad (5.9)$$

5.2.3 Charged Pions and Backgrounds

Most of the backgrounds to the signal mode $K_L \rightarrow \pi^0\pi^0\mu^+\mu^-$ come from kaon decay channels that possess at least one charged pion in the final state. Such decays

Decay Mode	Branching Ratio
$K_L \rightarrow \pi^0 \pi^0 \pi^0$	0.1952 ± 0.0012
$\pi^0 \rightarrow \gamma \gamma$	0.98798 ± 0.00032
$\pi^0 \rightarrow e^+ e^- \gamma$	0.01198 ± 0.00032

Table 5.2: Branching Ratios for K_L and π^0 decay modes [45].

can manifest as background when the charged pion is misidentified as a muon due to charged pion decay ($\pi^+ \rightarrow \mu^+ \nu_\mu$, $\pi^- \rightarrow \mu^- \bar{\nu}_\mu$) or charged pion punch-through.

The lifetime of π^\pm has been measured to be 2.6×10^{-8} sec. Taking into account the momentum distributions of the charged pions from various background decay modes allows roughly 2% of charged pions to decay into muons upstream of the calorimeter [49]. When studying backgrounds involving charged pion decay, the π^\pm was forced to decay (upstream of the calorimeter) in order to save processing time. Charged pion-punch through is caused when hadronic showers leak through the calorimeter, lead wall and steel filters, then create hits on the MU3 counting plane. Pion punch-through is modeled in the MC by GEANT and includes true punch-throughs as well as charged pion decays downstream of the calorimeter [49]. The probability of a successful punch through depends on the momentum p of the charged pion and is estimated using GEANT to be [37]:

$$P_{punch} = 0.00105 + 0.00017p. \quad (5.10)$$

The MC simulates punch-throughs using the same momentum-dependence as the above relation. Through studying the invariant kaon mass distribution of $K_L \rightarrow$

$\pi^+\pi^-\pi^0$ events generated with the dimuon trigger, the relative ratio of charged pion punch-throughs to pion decays was found to be 0.18 ± 0.04 [37]. Section 5.7 gives a detailed list of all backgrounds studied using charged pion punch-throughs and pion decays.

5.3 Particle Tracing and Interactions

Once a generated kaon had undergone decay, the daughter particles were rotated by a random angle about the axis which defined the parent kaons trajectory. After rotation, the daughter particles were then boosted into the laboratory reference frame and traced through the KTeV detector. The tracing procedure mapped the daughter particles trajectories through all accessible detector elements and included interactions of the daughter particles with each accessible detector element. More specifically, the tracing procedure was performed separately for each intercepted detector element (and the air or He inbetween) along the $+z$ -direction.

Tracing is performed differently for each type of daughter particle. Electrons and photons are traced until they interact with the photon vetoes or the CsI calorimeter. Charged pions were traced until they struck the calorimeter or leaked through to the Hadron Anti from the lead wall. If a pion decays before showering, then the daughter muon is traced through the remainder of the detector. Muons are traced until the final set of scintillator counting planes, *MU3*. If a particle left the detector, then the tracing was stopped. If a particle intercepted a veto counter, then the event

could be rejected. The MC did not perform tracing of neutrinos. Every step of tracing could include several different particle interactions, which are simulated in MC. These interactions are described in the remainder of this section.

5.3.1 Pair Production

A photon can convert into an electron-positron pair through interactions with matter. In the MC, photons with an energy greater than 100 MeV were given an opportunity to convert as they passed through the vacuum window and detector elements upstream of the analysis magnet. Pair production is important in this analysis, since it serves as the only channel for a viable background to the normalization mode, via photon conversion in the decay process $K_L \rightarrow \pi^0 \pi^0 \pi^0$. The probability of pair production in each detector element is given by:

$$P_{\gamma \rightarrow e^+ e^-} = 1 - e^{-\frac{7}{9} \frac{X}{X_0}}, \quad (5.11)$$

where X is the path length of the photon through the element and X_0 is the characteristic radiation length of the element. The z position of pair production was distributed randomly throughout each element of the detector. Table 5.3 gives the radiation lengths of a few pertinent elements of the detector upstream from the CsI calorimeter [50].

The electron-positron energy spectrum was determined by Bethe and Heitler in

Detector Element	Composition	$\left(\frac{X}{X_0}\right) \times 10^{-3}$
Vacuum Window	kevlar/mylar	1.56
Helium Bag 1a (1997)	mylar and air	1.07
Helium Bag 1a (1999)	mylar and helium	0.74
DC1U	primarily mylar	0.50
DC field wire	aluminum	0.885
DC field wire	gold	0.615
DC sense wire	tungsten	5.70
Helium Bag 2	helium	1.62
TRD Chamber	(Sect. 2.2.3)	17.6
TRD beam hole	(Sect. 2.2.3)	5.1

Table 5.3: Radiation length of select detector elements upstream of the CsI. Helium Bag 1a slowly filled with air over the 1997 run, but was replaced with an air tight Helium Bag in the 1999 run. DC1U was composed of Helium Bag 1b, the mylar windows for DC1 and the DC1 chamber gas. Helium Bag 2 was located between DC1 and DC2.

the mid-1930's to be:

$$P(E_{e^+}, E_{e^-}) \approx \left(\frac{E_{e^+}}{E_\gamma}\right)^2 + \left(\frac{E_{e^-}}{E_\gamma}\right)^2 + \left(\frac{2}{3} - \frac{1}{9\varrho}\right) \frac{E_{e^+}E_{e^-}}{E_\gamma^2}, \quad (5.12)$$

where E_{e^\pm} is the electron-positron energy, E_γ is the photon energy and ϱ is a constant approximately equal to 3.74059. The electron and positron were emitted at a small angle with respect to the parent photon direction. In addition, the plane of the electron-positron pair was rotated randomly about an axis describing the direction of the parent photon. The emission angle was a function of E_{e^\pm} , E_γ and X_0 . The actual calculation of the emission angle in the MC was performed using a distribution from the EGS4 code system [51].

5.3.2 Bremsstrahlung

Whenever an electron or positron travels through matter, there is a chance that a photon will be radiated. As a result, the MC allowed for radiation of a photon whenever electrons or positrons passed through any segment of the detector. Under the assumption that the electrons (or positrons) were ultra-relativistic, and that the Born approximation holds, then the probability of photon emission is [41]:

$$P_{k>k_0} = \frac{X}{X_0} \frac{1}{(18\zeta + 1)} \left[2(12\zeta + 1) \left(\frac{k_0}{E_0} - \ln \left(\frac{k_0}{E_0} \right) - 1 \right) + 9\zeta \left(1 - \left(\frac{k_0}{E_0} \right)^2 \right) \right], \quad (5.13)$$

where k is the momentum of the bremsstrahlung photon, k_0 is a cutoff momentum, E is the final energy of the electron, E_0 is the initial energy of the electron and the parameter ζ is equal to $\ln(183/Z^{1/3})$. The cutoff momentum, k_0 , in the KTeV MC is set to $0.001E_0$.

The above probability is only applied downstream of the analysis magnet. This is understood in the case of an electron creating a bremsstrahlung photon downstream of the magnet. In this scenario, the electron and bremsstrahlung photon would not be split apart by the magnet and their clusters in the calorimeter would practically overlap, thus leading them to be indistinguishable. Therefore, a simpler MC bremsstrahlung package governed by the differential cross section given in equation 5.14 (see below) and the probability of photon emission in equation 5.13 is used for bremsstrahlung events downstream of the analysis magnet, which also saves computer

computation time. The full angular MC bremsstrahlung package was only performed on detector components upstream of the analysis magnet and for electrons with an initial energy greater than 1.5 GeV. When bremsstrahlung occurs upstream of the magnet, then the electrons and photons will be able to separate enough to form distinguishable clusters in the CsI calorimeter. The condition on the initial energy is identical to the efficiency threshold for electron cluster identification in the HCC trigger. The complete differential momentum spectrum and full angular distribution of the radiated photon is a complicated expression and can be found in Ref. [41]. The differential cross section for the case of bremsstrahlung downstream of the analysis magnet is given by:

$$\frac{d\sigma}{dk} = 4\alpha_{EM} Z^2 r_e^2 \frac{1}{k} \left[\left(1 + \left(\frac{E}{E_0} \right)^2 - \frac{2}{3} \frac{E}{E_0} \right) \zeta + \frac{1}{9} \frac{E}{E_0} \right], \quad (5.14)$$

where Z is the atomic number and $r_e^2 = e^2/m_e c^2$ is the classical electron radius. The above expression was obtained by integrating over the solid angle. Table 5.4 gives the probability of bremsstrahlung for various upstream detector elements [41,50].

5.3.3 δ -Rays

When any charged track passes through a gas, electrons can be kicked out of the gas molecules, thereby creating a δ -ray. The δ -rays are normally emitted at high angles with respect to the direction of the charged track and carry enough energy to leave a secondary ionization trail. This could naturally result in creating additional hits within the spectrometer, thus causing drift chamber inefficiencies. As a result,

Detector Component	Z_{eff}	Probability
Vacuum Window	5.556	0.01313
Helium Bag 1a (1997)	7.799	0.00825
Helium Bag 1a (1999)	7.799	0.00587
DC1U	5.737	0.00421
DC field wire (Al)	13.501	0.00745
DC field wire (Au)	79.555	0.00518
DC sense wire	74.554	0.04804
Helium Bag 2	2.452	0.01364
TRD Chamber	3.915	0.14816
TRD beam hole	3.915	0.04293

Table 5.4: Probability of bremsstrahlung for upstream detector components.

the MC simulated δ -ray creation within the drift chambers. The KTeV MC assumes that all charged tracks which generate δ -rays are ultra-relativistic with an energy E . Under that assumption, the probability of getting a δ -ray above a kinetic energy T_0 in a path X with a density ρ , an atomic number Z and an atomic weight A is:

$$P_{T>T_0} = (15400 keV cm^2 / gram) \frac{Z}{AE} \rho X. \quad (5.15)$$

The MC simulation takes the gas to be argon. All δ -rays are produced perpendicular to the direction of the incoming track and the momentum taken from the incoming track is assumed to be negligible. Furthermore, δ -rays are allowed to travel a maximum distance equivalent to the width of one cell and a charged track was only allowed to produce one δ -ray per cell traversed. The energy spectrum of δ -rays in the MC was proportional to T^{-2} as suggested in Ref. [52], where T is the kinetic energy of the δ -ray.

5.3.4 Multiple Scattering

Any charged particle traveling through matter will undergo deflections due to interactions with the nuclei via the Coulomb force. The deflection is defined in the MC by an angle θ and is rotated randomly about the axis defining the original direction of the charged particle. Generation of the angle θ is achieved by employing a Gaussian of width θ_0 centered on 0, where θ_0 is given by [52,53]:

$$\theta_0 = \frac{13.6 \text{ MeV}}{\beta c p} z \sqrt{\frac{X}{X_0}} \left[1 + 0.038 \ln \left(\frac{X}{X_0} \right) \right], \quad (5.16)$$

where z , βc and p are the charge number, velocity and momentum of the scattered particle respectively.

Only muons were traced past the CsI calorimeter. Any muon with an energy higher than 1 GeV and lower than 128 GeV was scattered through the calorimeter, lead wall, MF1 and Back Anti. Lateral displacement and scattering angle of muons, d_s and θ_s , are determined by the Gaussian approximation of multiple scattering:

$$\theta_s = R_1 \theta_0 \quad (5.17)$$

$$d_s = \frac{(\sqrt{3} R_1 + R_2) \theta_0 X}{\sqrt{3} (2.387)}, \quad (5.18)$$

where X is the path length (in meters) and R_1 and R_2 are Gaussian random numbers [54,55]. After the lateral displacement and scattering angle are applied to the muon for a given scattering element, the energy loss (to be described in the next section) is then calculated and tracing continues to the next scattering element.

5.3.5 Energy Loss in the Muon System

Correctly modeling energy loss due to the muon filters in the MC was vitally important to this analysis. Since the signal mode $K_L \rightarrow \pi^0 \pi^0 \mu^+ \mu^-$ contains muons, the branching ratio will be sensitive to the momentum threshold of the muon system. Inaccurate modeling of interactions within the muon ID system would cause the signal acceptance and therefore branching ratio to be mismeasured.

Energy loss in a given element of the muon ID system is calculated using the Bethe-Bloch ionization energy loss relation [56]. In order to properly simulate the muon threshold, random fluctuations are applied to the Bethe-Bloch result. The Bethe-Bloch relation is expressed as:

$$-\frac{dE}{dX} = K \frac{Z}{A} \frac{z^2}{2\beta^2} \left[\ln \left(\frac{2m_e c^2 \beta^2 \gamma^2 T_{max}}{I^2} \right) - 2\beta^2 - \delta \right], \quad (5.19)$$

where z is the charge number of the scattered particle, Z and A are the atomic number and weight of the detector element, βc is the velocity of the scattered particle and γ is the relativistic parameter $(1 - \beta^2)^{-1/2}$, T_{max} is the maximum possible kinetic energy transfer to a free electron in a collision (defined below), I is the mean excitation energy of the target and δ is a correction which accounts for density effects and $K \approx 0.31 g^{-1} cm^2$.

The type of distribution employed in the random fluctuations depends on the

value of the parameter κ [37,54], where:

$$\kappa = 153.56 \frac{Z}{A} \frac{\rho X}{T_{max} \beta^2}, \quad (5.20)$$

$$T_{max} = \frac{2m_e p^2}{m_\mu^2 + 2m_e E + m_e^2}. \quad (5.21)$$

Landau fluctuations [57] were employed for $\kappa < 0.01$, Vavilov fluctuations [58] for $0.01 \leq \kappa \leq 10$ and Gaussian fluctuations were applied for $\kappa > 10$.

5.4 Detector Simulation

A comprehensive simulation of each section of the KTeV detector was modeled in the MC. After generation, the MC events would traverse the simulated detector and could undergo the same interactions as those described in the previous section. The following section shall describe how each element of the detector used in this analysis was implemented in the MC coding framework. Only those elements of the detector that were employed in this analysis will be described.

5.4.1 Photon Vetoes

Once an electron or photon is traced to any of the photon vetoes (RC6-10, SA2-4, CIA, CA or BA), it was terminated upon impact. The energy left in a photon veto counter was obtained by cross-referencing calibration constants obtained using data from special runs [32]. In addition, the photon veto response was smeared by a Gaussian distribution whose width was also obtained from data. The other charged

particles were treated as MIPs. The photon veto response for MIPs is also smeared by a Gaussian distribution obtained via calibration constants from different data runs known as muon runs. In the muon runs, a special beam stop was inserted into the detector to stop the hadronic component of the beam. In addition, the analysis magnet was turned off and the settings for the sweeper magnets in NM2 were tweaked in order to create a muon beam. The muon runs served other purposes which shall also be touched upon in the rest of this chapter.

5.4.2 Spectrometer System

The primary aim of the spectrometer simulation was to accurately calculate drift times from the traced out hit positions in drift chambers. Chamber calibrations as well as the method in which SOD distributions (discussed in section 4.1.1) are modeled can affect the calculation of drift times. A simulation of each of the 16 drift chamber planes was incorporated into the MC.

In order to determine drift times, one must begin by calculating the drift distances for each hit within the DCs. The distance between a hit caused by a given charged particle and the nearest anode wire is found in each DC plane. These distances were then smeared using a Gaussian resolution to account for the DC position resolution of $100\ \mu\text{m}$. SODs were then calculated and drift distances were converted into drift times using $X(t)$ calibrations (discussed in section 4.1.1). The muon data runs were also performed in order to create maps of $X(t)$ calibrations. These $X(t)$ maps were

generated in a more accurate offline calibration using $K_L \rightarrow \pi^\pm e^\mp \nu_e$ (K_{e3}) decays. In the last step, the zero drift distance (T_0) for the given anode wire is subtracted from the drift time of the charged particle, which yields the simulated drift time for that hit.

There are a series of SOD effects which necessitate corrections to the drift distances calculated above. Already described in section 4.1.1 were the three different SOD types: high SODs, low SODs and isolated hits. In addition, the ionization density is a function of position with respect to the anode wires, yet DC calibrations assume a constant ionization density. This yields discrete ionization effects for charged particles that pass near anode wires, which in turn magnifies the high-SOD tails. This was corrected by smearing the distances upward in such a way that the mean of the SOD distributions remained at 6.35 mm. Finally, the ionization energy loss is a quantity that depends on the mass of the charged particle. Specifically, K_{e3} data indicated an approximate difference of 15 μm between the SOD distribution means of pions and electrons. This effect was modeled in the MC with a scaling factor obtained from the electron and pion distributions in the K_{e3} data.

Drift Chamber Maps

After the aforementioned corrections, there were still noticeable disagreements between the data and MC for SOD distributions and drift chamber efficiencies. Such an outcome severely affects this analysis, since these disagreements could produce an

inaccurate reconstruction of track segments. Faulty track segments would then lead to mismeasurement of track momenta, which affects the distribution of the dimuon mass spectrum.

In an attempt to counteract these disagreements, precise maps of each drift chamber plane were created using K_{e3} data. The drift chamber maps (DC maps) were functions of chamber position and time in the run. DC maps were composed of high-SOD rates that stemmed from inefficiencies due to early drift electrons and wire damage. Binning of DC maps was performed wire-by-wire and in 1 cm divisions along the wires, for time periods averaging six days. After the DC maps were applied to the corrected MC, the data/MC disagreements were reduced significantly.

Analysis Magnet in the MC

When charged particles passed through the analysis magnet, they were given a transverse momentum kick in the $\pm x$ direction. Once again, in the 1997 data run, the magnitude of this kick was 205 MeV/c and in the 1999 data run the magnitude was 150 MeV/c. The transverse momentum kick was calibrated regularly by measuring the mean value of the invariant mass of reconstructed $K_L \rightarrow \pi^+\pi^-$ calibration events. The transverse momentum kick was then adjusted to match the invariant kaon mass. These kick values were saved into the KTeV database and employed in MC generation and event reconstruction.

5.4.3 VV' Hodoscope System

The MC simulation for the trigger hodoscopes computes which counters were hit by charged particles. In addition, inefficiencies due to cracks between counters are also simulated. Naturally, if a charged particle is traced to a crack, then a hit is not registered in the MC. Efficiencies are measured from the data and then repackaged as probabilities, which determines whether the energy deposited by approaching charged particles can pass threshold for detection.

5.4.4 CsI Calorimeter Simulation

The CsI calorimeter simulation is divided into generation of clusters and the digitization of signals from each CsI crystal. A cluster is generated based on the energy deposited by a particle in the calorimeter and how that energy is partitioned among the CsI crystals. Cluster generation also depends on the type of particle incident on the calorimeter. The digitization process consists of dividing the energy into readout time slices, then transforming the energy depositions into digital signals.

Electromagnetic Showers

Every photon and electron that traversed the CsI calorimeter deposited energy in the crystals via electromagnetic showers. Once a particle crossed the face of the calorimeter, the mean depth of the shower maximum was calculated and is given for

photons and electrons as:

$$\bar{z}_\gamma = 0.12 + 0.18 \ln E_\gamma \quad (5.22)$$

$$z_{e^\pm} = 0.11 + 0.18 \ln E_{e^\pm}, \quad (5.23)$$

where \bar{z} is the mean depth in meters and E is the energy in GeV.

Since the processing time involved in producing showers for every MC event would have taken far too long, a fixed shower library was employed instead. The shower library was generated with GEANT [59] using a 13×13 array of small crystals (where large crystals were considered equivalent to a 2×2 array of small crystals). The shower library is binned with the incoming particle's energy (6 bins with upper bounds of 2, 4, 8, 16, 32 and 64 GeV) and x and y position within the crystal when extrapolated to \bar{z} ($325 \times 500 \times 500 \mu\text{m}$ bins). Every energy-position bin contained 5 different showers, which yielded a total of 9,750 showers within the shower library. In addition, the showers were segmented into 25 bins along z . This scaled the longitudinal energy resolution of the shower to match measured longitudinal responses in the individual CsI crystals.

The energy of the incident particle is smeared to match resolutions found in the data. The type and location of the hit crystal determined the amount of smearing necessary for the situation. Selection of showers from the library was based on this smeared energy. The total energy of the shower selected from the library is then scaled to match the energy of the incident particle. If the energy encompassed within a shower leaked into a beamhole, then *sneaky energy* was added to crystals on the

other side of the beamhole. The library used to simulate this effect was based on the sneaky energy correction, which was discussed in section 4.2.4.

Muon and Pion Interaction with the CsI

Another library was created for hadronic showers within the CsI calorimeter. Only a subset of charged pions hadronically shower within the calorimeter. There are differences between the hadronic and electromagnetic showering routines. A hadronic shower is much larger, and a 41×41 array of small crystals is required to contain a typical hadronic shower. The procedure for handling a hadronic shower was the same as that for an electromagnetic shower. If charged pions did not shower, then they were treated as MIPs, thus leaving an average of 400 MeV in the calorimeter. Muons interacting with the calorimeter deposit the same average energy as non-interacting hadrons in a single crystal and according to the Bethe-Bloch distribution described in Section 5.3.5.

Digitization and Readout

A simulation of the DPMT board for each channel was also included in the MC model of the calorimeter. In order to digitize the signal in a given crystal, one must first impose the time structure of the DPMT readout onto the MC energy deposits. Essentially, the energy in each crystal is divided into a series of time slices according to distributions acquired from pulse shape data. Each energy time slice is then digitized

and converted to a collected charge using the Q/E calibrations described in section 2.2.5. Finally, DPMT calibrations convert the charge to a digital signal.

5.4.5 Muon ID System

The trigger definitions in section 3.3 reveal that the primary trigger difference between the signal and normalization modes is the MU3 requirement in the dimuon trigger. As a result, simulation of the muon ID system in the MC must be made as realistic as possible in order to get an accurate estimate of the absolute MU3 acceptance. The tracing of muons is divided into two steps: upstream and downstream of the CsI calorimeter. Muons are traced in the same fashion as all other charged particles (save the electrons) upstream of the calorimeter.

As they pass through the CsI calorimeter and the muon ID system, muons cease to follow the previous tracing routine and instead enter into a simulation of multiple scattering and energy loss, which has already been described in sections 5.3.4 and 5.3.5. If a muon in this new simulation was traced to an MU2 or MU3 scintillator counter, then a random number was produced and weighed against the counter efficiency distribution to determine if the scintillator counter clocked a hit. Each scintillator counter was calibrated using data from special muon runs. Inefficiencies due to cracks in MU3 were also determined using magnet-on muon run data. The efficiency is calculated through dividing the number of single track events with an MU3 hit by the total number of single track events. Cracks along the sides of all

scintillator counters were simulated. Local muon efficiencies are reproduced in the MC to better than 0.5% (1% at the center splits), while global muon efficiencies were found to agree to better than 0.05% [37].

5.5 Accidental Overlays

Thus far we have described the generation of clean MC events. In reality, all decays within the detector are mixed with a series of accidental events. Accidental activity can manifest from beam interactions, cosmic rays, neutrons (from the target), particles created through interactions in the vacuum window or even an overlapping kaon decay. Naturally, accidental activity can cause a wide variety of problems ranging from misfiring of trigger sources to overestimation of cluster energies. In an effort to simulate accidental activity, data is taken by triggering on the 90° Accidental Counter and added to events in the MC on an event-by-event basis. Basically, every MC event is overlaid with an accidental event. ADC entries from the accidental event directly tacked on to the generated event after pedestal subtraction. TDC values from the accidental event were added to the table of those values in the generated event. Calorimeter CsI crystal energies were added on a slice-by-slice basis. Finally, accidental events were added before threshold or trigger evaluations were performed.

5.6 Trigger Simulation

The MC trigger definitions were an exact replica of those employed during the collection of data. Once an event was successfully generated, the rest of the L1 trigger was evaluated. All L2 and L3 processing routines were also used in the MC coding environment. Event generation would cease if an event failed any aspect of the trigger. Events that passed all levels of the trigger were written to disk in an identical format as the data.

5.7 Monte Carlo Samples

Large Monte Carlo samples were generated for the signal, normalization and background modes. Table 5.5 lists the branching ratio and number of events for each decay mode generated. Generation was performed using the KTeVMC version 6.04 library. Separate samples were generated for the 1997 and 1999 runs. The effective sizes of any background modes containing a charged pion were made larger due to forced pion decay or punch-through. Finally, all backgrounds were generated with accidentals. The presence of accidental photons allowed the backgrounds to be generated with a topology similar to that of the signal mode. This effect shall be discussed in the following chapter.

Decay Mode	Branching Ratio	Generated MC Events	
		1997	1999
Signal:			
$K_L \rightarrow \pi^0 \pi^0 \mu^+ \mu^-$		2.00×10^7	1.99×10^7
$K_L \rightarrow \pi^0 \pi^0 X^0 \rightarrow \pi^0 \pi^0 \mu^+ \mu^-$		2.08×10^7	2.03×10^7
Normalization:			
$K_L \rightarrow \pi^0 \pi^0 \pi_D^0$	$(6.85 \pm 0.23) \times 10^{-3}$	1.84×10^9	1.41×10^9
Backgrounds:			
$K_L \rightarrow \pi^\pm \mu^\mp \nu_\mu$ (P)	(0.2704 ± 0.0007)	2.60×10^9	1.75×10^9
$K_L \rightarrow \pi^\pm \mu^\mp \nu_\mu$ (D)		2.45×10^8	4.22×10^8
$K_L \rightarrow \pi^0 \pi^\pm \mu^\mp \nu_\mu$ (P)	$\sim 5.9 \times 10^{-5} *$	1.20×10^8	9.64×10^7
$K_L \rightarrow \pi^0 \pi^\pm \mu^\mp \nu_\mu$ (D)		9.34×10^7	1.10×10^8
$K_L \rightarrow \pi^+ \pi^- \pi^0$ (PP)	(0.1254 ± 0.0005)	1.85×10^9	1.06×10^9
$K_L \rightarrow \pi^+ \pi^- \pi^0$ (DD)		8.56×10^7	1.07×10^8
$K_L \rightarrow \pi^+ \pi^- \pi^0$ (DP)		4.55×10^8	4.56×10^8
$K_L \rightarrow \pi^+ \pi^- \gamma$ (PP)	$(4.15 \pm 0.15) \times 10^{-5}$	1.50×10^7	2.16×10^7
$K_L \rightarrow \pi^+ \pi^- \gamma$ (DD)		2.03×10^7	1.63×10^7
$K_L \rightarrow \pi^+ \pi^- \gamma$ (DP)		1.42×10^7	1.45×10^7
$K_L \rightarrow \pi^+ \pi^-$ (PP)	$(1.966 \pm 0.010) \times 10^{-3}$	6.84×10^8	6.72×10^8
$K_L \rightarrow \pi^+ \pi^-$ (DD)		8.53×10^6	2.18×10^7
$K_L \rightarrow \pi^+ \pi^-$ (DP)		5.03×10^7	2.66×10^7
$K_L \rightarrow \mu^+ \mu^-$	$(6.84 \pm 0.11) \times 10^{-9}$	1.18×10^6	5.24×10^6
$K_L \rightarrow \mu^+ \mu^- \gamma$	$(3.59 \pm 0.11) \times 10^{-7}$	9.59×10^6	3.01×10^7
$K_L \rightarrow \mu^+ \mu^- \gamma \gamma$	$(1.0^{+0.8}_{-0.6}) \times 10^{-8}$	1.09×10^7	4.90×10^7
$K_L \rightarrow \pi^0 \mu^+ \mu^-$	$< 3.8 \times 10^{-10}$	1.11×10^7	1.31×10^7

Table 5.5: Number of generated MC events for signal modes, normalization mode and all signal mode background samples. (D) refers to charged pion decay and (P) refers to charged pion punch-through. The branching ratio for the normalization mode was calculated in Section 5.2.2, while branching ratios for the background samples were obtained from Ref. [45]. *This branching ratio was estimated in Ref. [29].

Chapter 6

Branching Ratio Analysis

The branching ratio analysis is divided into a set of steps. The primary step is the crunch procedure, whereby loose requirements are applied to the data sets for the signal and normalization mode events that have survived the Level 3 trigger. This is done in order to perform a basic reconstruction of $K_L \rightarrow \pi^0 \pi^0 \mu^+ \mu^-$ and $K_L \rightarrow \pi^0 \pi^0 \pi_D^0$ and reduce these data sets down to a manageable size for the analysis stage. During the analysis stage, new requirements and tighter versions of the crunch requirements were applied in an effort to suppress background events in the signal region. Finally, further studies were performed on the analysis cuts in order to estimate systematic errors on the final result.

6.1 Data Reduction Procedure

A tremendous quantity of data survived the Level 3 trigger. As mentioned in section 3.4, every event that survived the L3 trigger was written to DLTs. The 1997 data set was stored on 950 raw data tapes, while the 1999 data set was contained within 1045 data tapes. A 1997 data tape has a 10 Gb storage capacity, while a 1999 data tape has a storage capacity of 20 Gb. This yields a 10 Terabyte data set for 1997 and a 20 Terabyte data set for 1999. Naturally, running a full analysis on 30 Terabytes worth of data would not be an efficient way of carrying out an analysis, so the data size was reduced by the crunch to allow for quicker and hence easier analysis.

6.1.1 E799 Data Runs

As mentioned in the beginning of chapter 2, E799 was divided into three runs: the 1997 winter run, the 1997 summer run and the 1999 run. However, the term ‘run’ was also used in reference to a period of uninterrupted data collection. Under this definition, a single run could last up to eight hours with nominal beam intensity, which is essentially the time needed to fill an output tape. Due to detector, beam or data acquisition problems, half of all runs were stopped early. Runs 8028 through 8913 encompassed the 1997 winter data run, while the 1997 summer data run was comprised of runs 10460 through 10978. The 1999 data run was composed of runs 14624 through 15548. A few runs contained corrupted data or aborted when analyzed by the crunch code. Such runs were not simulated in the Monte Carlo.

6.1.2 E799 Split Procedure

The first task in the data reduction procedure was to split the raw data according to trigger number and level 3 tags. This splitting routine seems simple in theory, but there a couple of different ways in which it can be implemented. After the 1997 data run, the split was performed tape by tape, which required approximately six months to complete. Since the split was performed after data taking, the 1997 data split is also referred to as the offline split. This procedure produced 20 DLT tapes for the dimuon (signal mode) trigger and 96 DLT tapes for the 2E-NCLUS (normalization mode) trigger, which amounted to roughly 1.16 Terabytes of data.

The six months required to split the 1997 data set offline was considered far too long for practical purposes. In order to speed up the splitting process, an online system was implemented for the 1999 data set. A copy of the data written to raw data tapes was sent to different disk caches based on an events trigger number and L3 tag. Data was written to each disk cache until the cache closed at the level of the storage capacity of a DLT tape (20 Gb for 1999. At that point the online split system would alert shifters to mount a pre-labeled blank tape into a free drive and the run would resume. After the contents of the cache had been transferred to split tape, they were deleted from disk. A total of 59 DLT tapes were written from the dimuon cache and 134 DLT tapes were written from the 2E-NCLUS cache, equalling 3.86 Terabytes of data. MC was generated according to trigger type to simulate the data. Specifically, signal mode MC and signal mode background MC were generated

using a simulation of the dimuon trigger and the normalization mode was generated using a simulation of the 2E-NCLUS trigger.

6.1.3 Crunch Procedure

After the events that passed Level 3 were split, they underwent the final data reduction procedure known as the crunch. The aim of this procedure was to tag and save all events that shared the same topology as the signal or normalization modes. Events only matched the necessary topology when they passed a specific series of loose requirements during the crunch. Any events that do not match the crunch requirements or the analysis requirements (to be discussed in sections 6.3 and 6.4) were cut out of the data set or MC sample being analyzed. Naturally, a few of these requirements are common to the signal and normalization modes, such as the need for two tracks, that these tracks be oppositely charged and that the kaon decays take place in the vacuum region (as specified by the requirement on the z vertex). Both modes also share the same requirement that the reconstructed π^0 mass, $m_{\gamma\gamma}$, be within 15 MeV of the true π^0 mass (see Figures 6.1 and 6.2). The method employed to reconstruct π^0 's from photons was described in section 4.3.2.

The signal and normalization modes are different in a few key areas. First, the signal mode possesses four photons, while the normalization mode has five photons. This is reflected in the requirement on the number of hardware clusters and on the number of clusters not associated with tracks. Second, the signal mode contains two

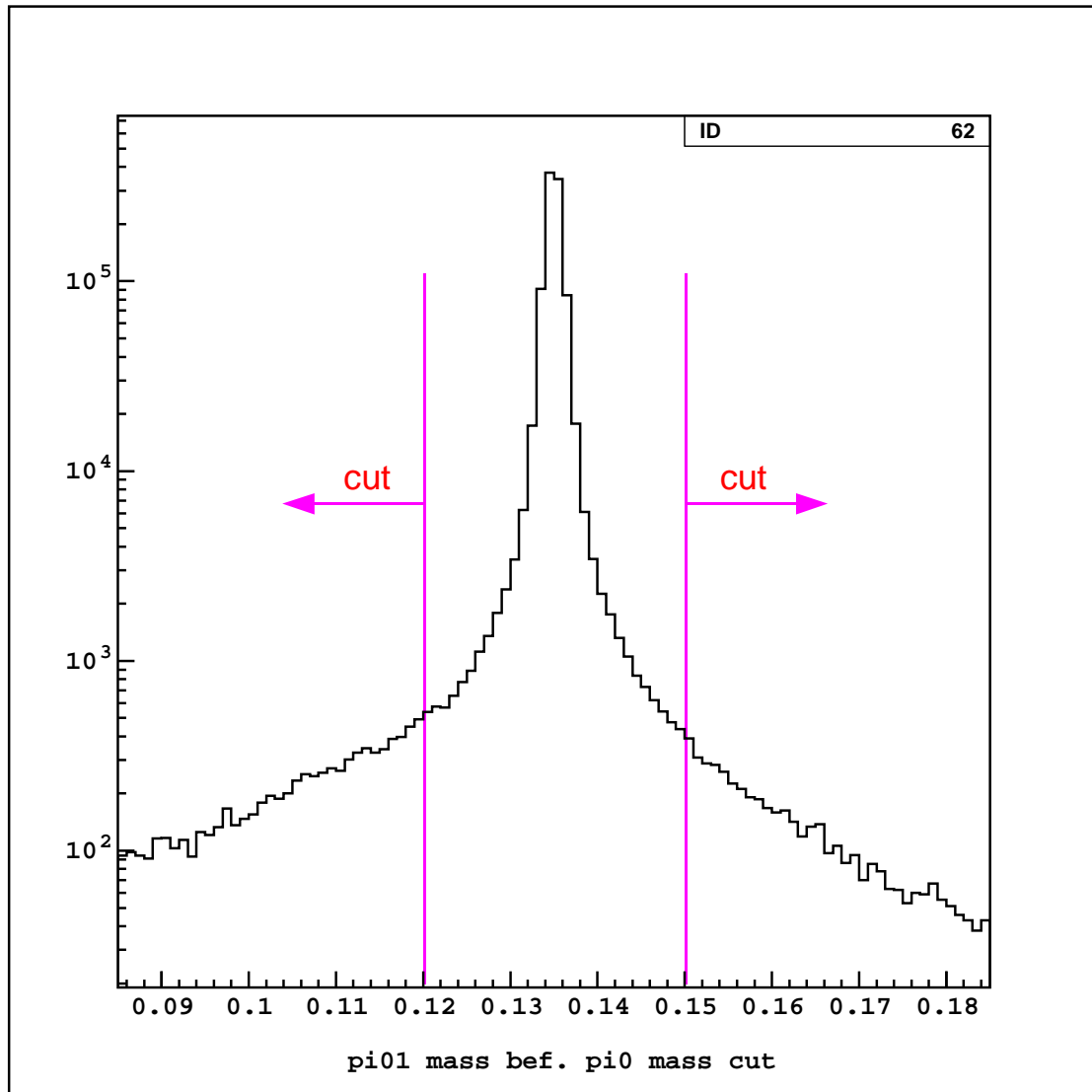


Figure 6.1: Reconstructed π^0 mass (before π^0 mass cut) for the first of two π^0 s (labeling is arbitrary) in the 1997 MC.

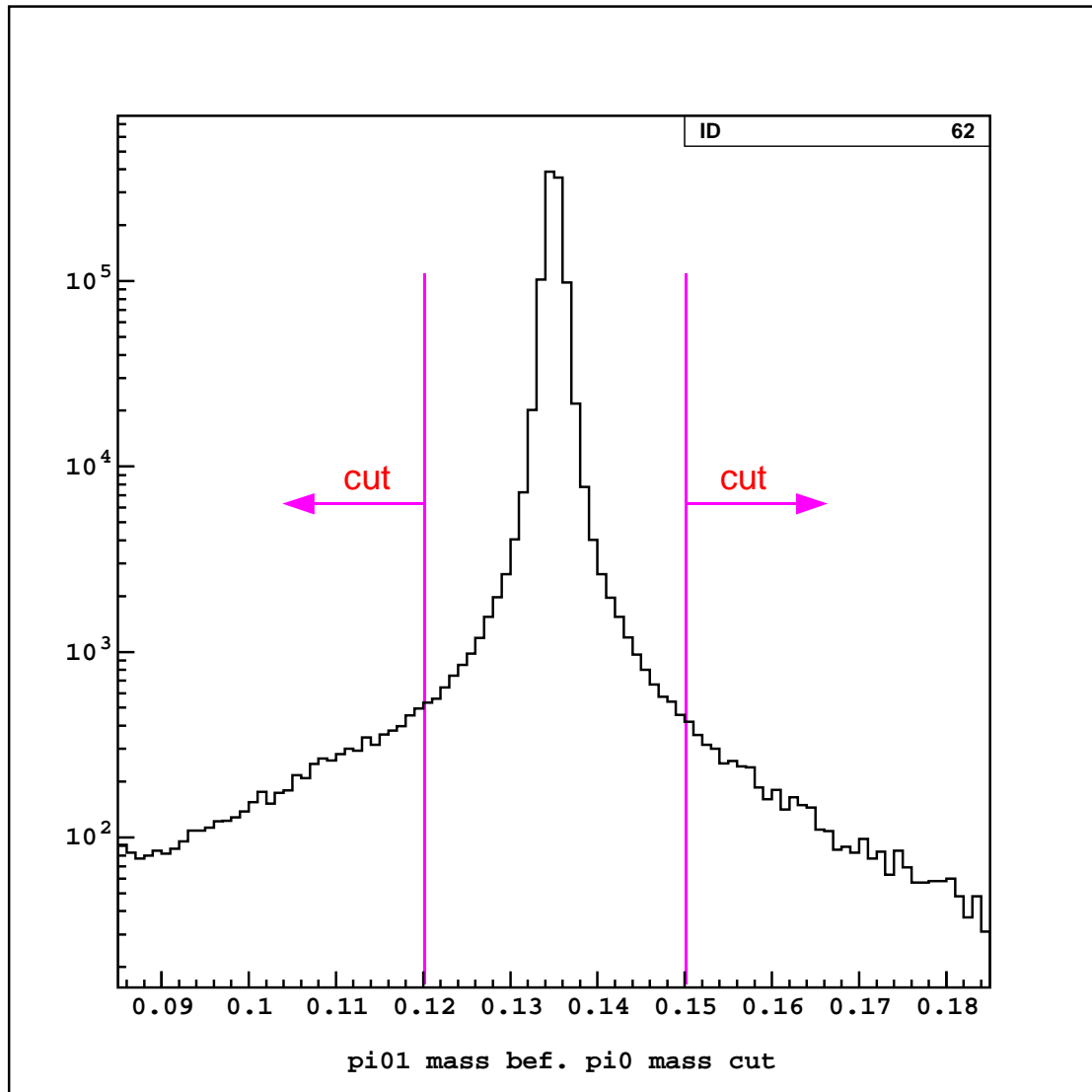


Figure 6.2: Reconstructed π^0 mass (before π^0 mass cut) for the first of two π^0 s (labeling is arbitrary) in the 1999 MC.

muons and the normalization mode has two electrons. By definition, muons are MIPS, so we require the clusters associated with these muons tracks to have a low energy, whereas no requirement on this energy is made with the electrons. Furthermore, the E/p of muons should be small (since they're MIPS), while the E/p of electrons should hover around 1.0 (remember that each CsI calorimeter crystal is 27 radiation lengths, so an electron should theoretically deposit all of its energy within the crystal volume). However, an E/p greater than 1.0 is possible due to resolution effects within the calorimeter and spectrometer, or from accidental activity on top of an electron cluster. Figure 6.3 shows the E/p distribution for one of the two tracks from the signal mode trigger of the 1999 data.

The loose requirement of greater than or equal to one hit in each muon counting plane allows for circumstances in which a muon scatters out of the muon ID system (due to interaction with one of the muon filters) or when a muon interacts with one of the filters to create a knock-on electron (δ -ray) and both particles are registered in the muon counting planes. Although, δ -rays are simulated in the drift chambers, they are not simulated in the muon filters, thus leading to extra hits in the muon counting planes in the data, as demonstrated in Figures 6.4 and 6.5. Finally, in accordance with momentum conservation (of the parent K_L), a requirement on p_T^2 was also implemented. p_T^2 is the square of the component of the reconstructed momentum perpendicular to a line that intersects the target and the K_L decay vertex. Aside from resolution effects, p_T^2 should be zero if all particles from the decay were identified and

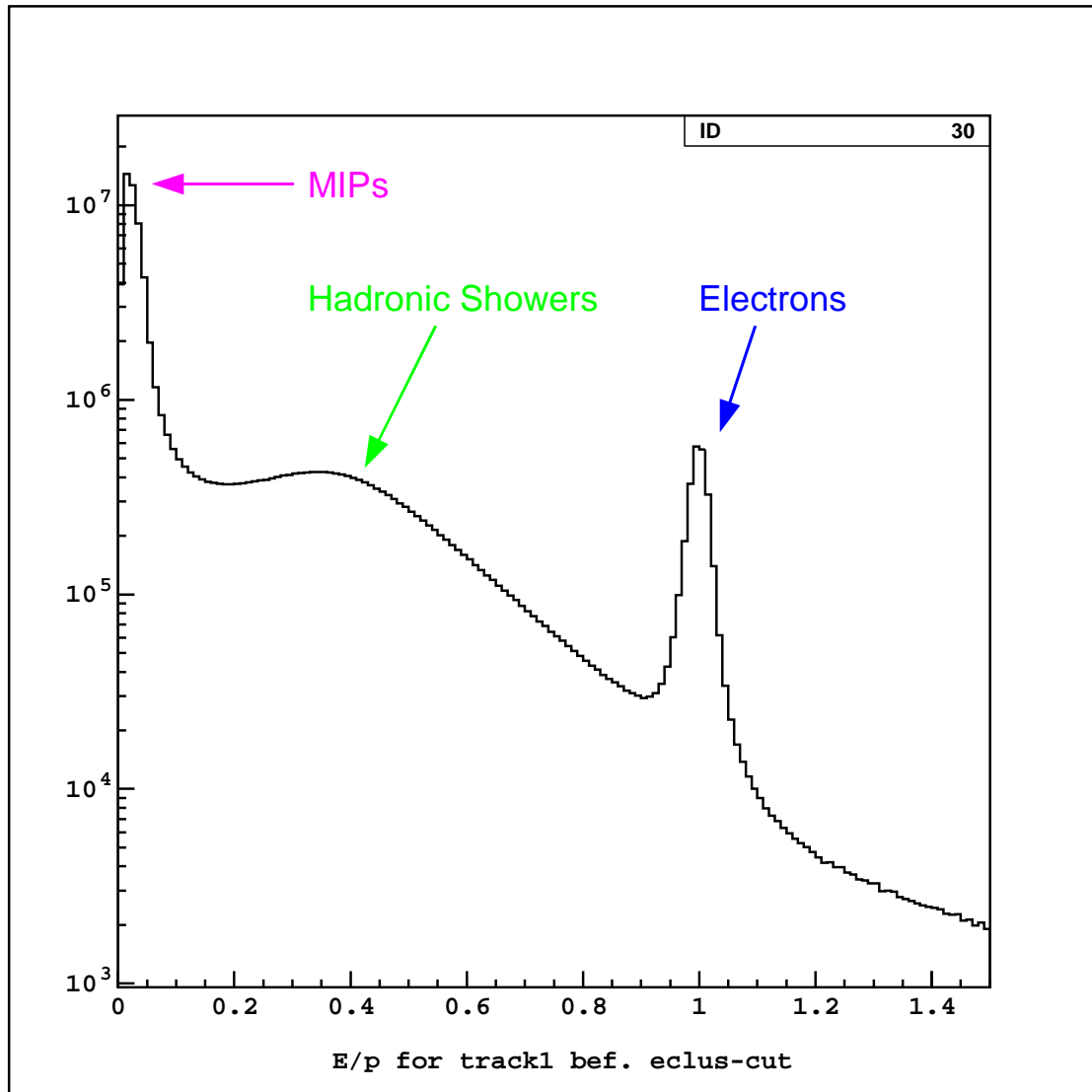


Figure 6.3: Distribution of the variable E/p for one of two tracks in the signal mode trigger of the 1999 data. The peak at zero stems from MIPs, while the peak at one originates mainly from electrons and positrons.

Crunch Requirement	A_{Data} (1997)	A_{MC,γ^*} (1997)	A_{MC,X^0} (1997)
L1, L2 and L3 MC Triggers	—	0.092	0.089
$N_{tracks} = 2$	0.666	0.970	0.969
$C_{track1} = -C_{track2}$	0.999	0.999	0.999
$E_{cl}(\text{track}) \leq 2.0 \text{ GeV}$	0.391	0.913	0.904
$E_{cl}(\text{track})/p_{track} \leq 0.9$	0.999	0.999	0.999
$N_{HCL} \geq 4$	0.056	0.636	0.629
N_{hits} in MU2 and MU3x,y ≥ 1	0.980	0.999	0.999
N_{cl} (not assoc. w/tracks) = 4	0.444	0.964	0.963
$120.0 \text{ MeV} \leq m_{\gamma\gamma} \leq 150.0 \text{ MeV}$	0.437	0.967	0.967
$90.0 \text{ m} \leq Z_{vtx} \leq 160.0 \text{ m}$	0.265	0.985	0.988
Bad Spill Requirement	0.813	0.803	0.802
$p_T^2 \leq 0.06 \text{ GeV}^2$	0.569	0.999	0.999
Total Acceptance	0.03%	3.80%	3.59%

Table 6.1: 1997 signal mode crunch requirement summary. Requirements are listed in the order in which they were implemented.

if the event was reconstructed correctly. Many of the kinematic requirements in the crunch procedure were purposefully made loose, so that backgrounds could be studied in the signal and normalization mode analyses, which will be described in section 6.2. The acceptances after each crunch requirement are given for the signal and normalization modes in Tables 6.1 through 6.4.

6.1.4 Bad Spill Cut

Data from a number of runs was taken in spite of problems occurring in one or more detector elements. Moreover, a detector element could also experience problems while a run was ongoing. A list of problems during data taking was collected on a spill-by-spill basis (hence the name *bad spill*) using calibration data and the KTeV

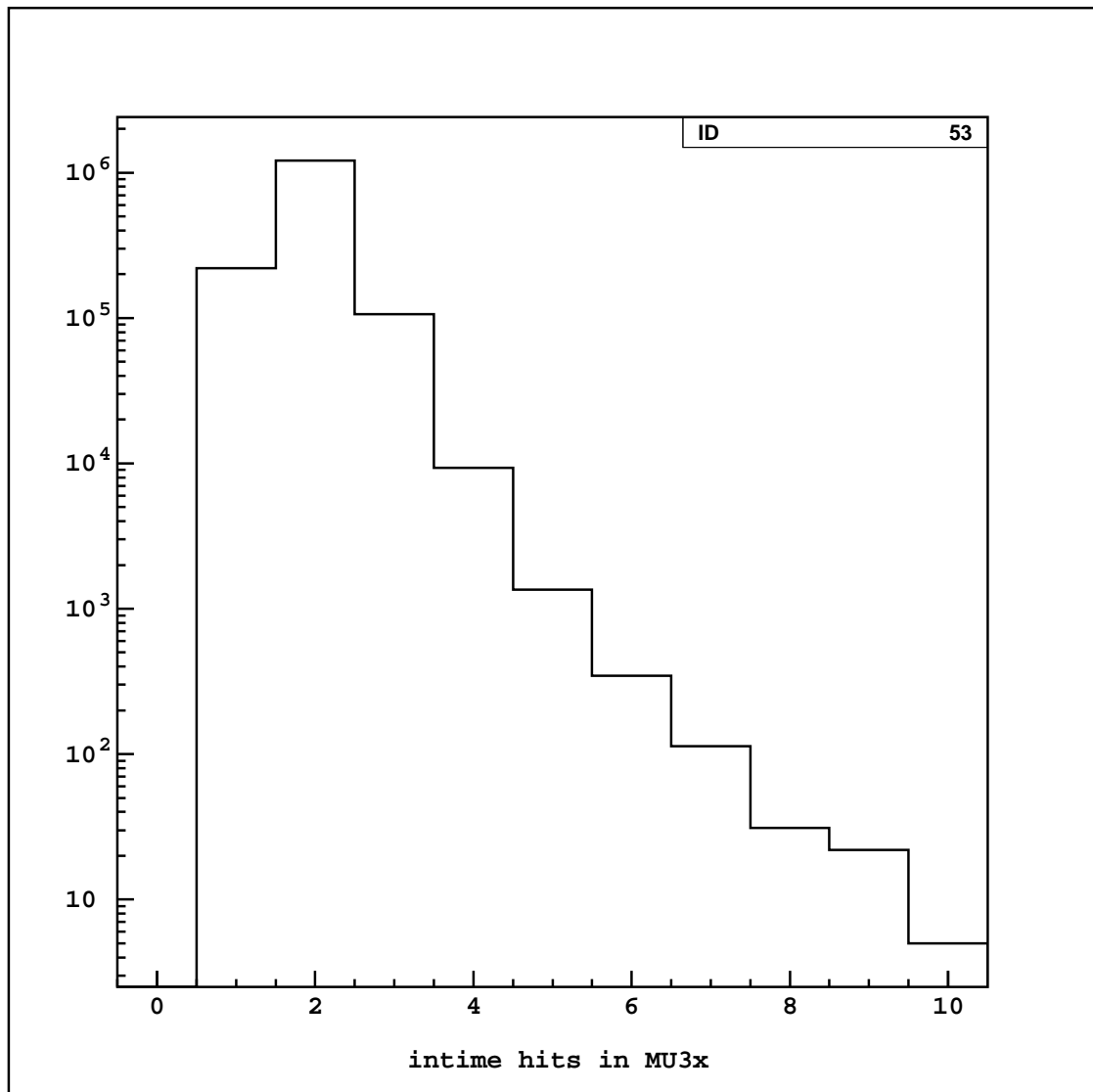


Figure 6.4: Distribution of number of hits in MU3x for the 1999 data immediately after the MU3x hit requirement was implemented.

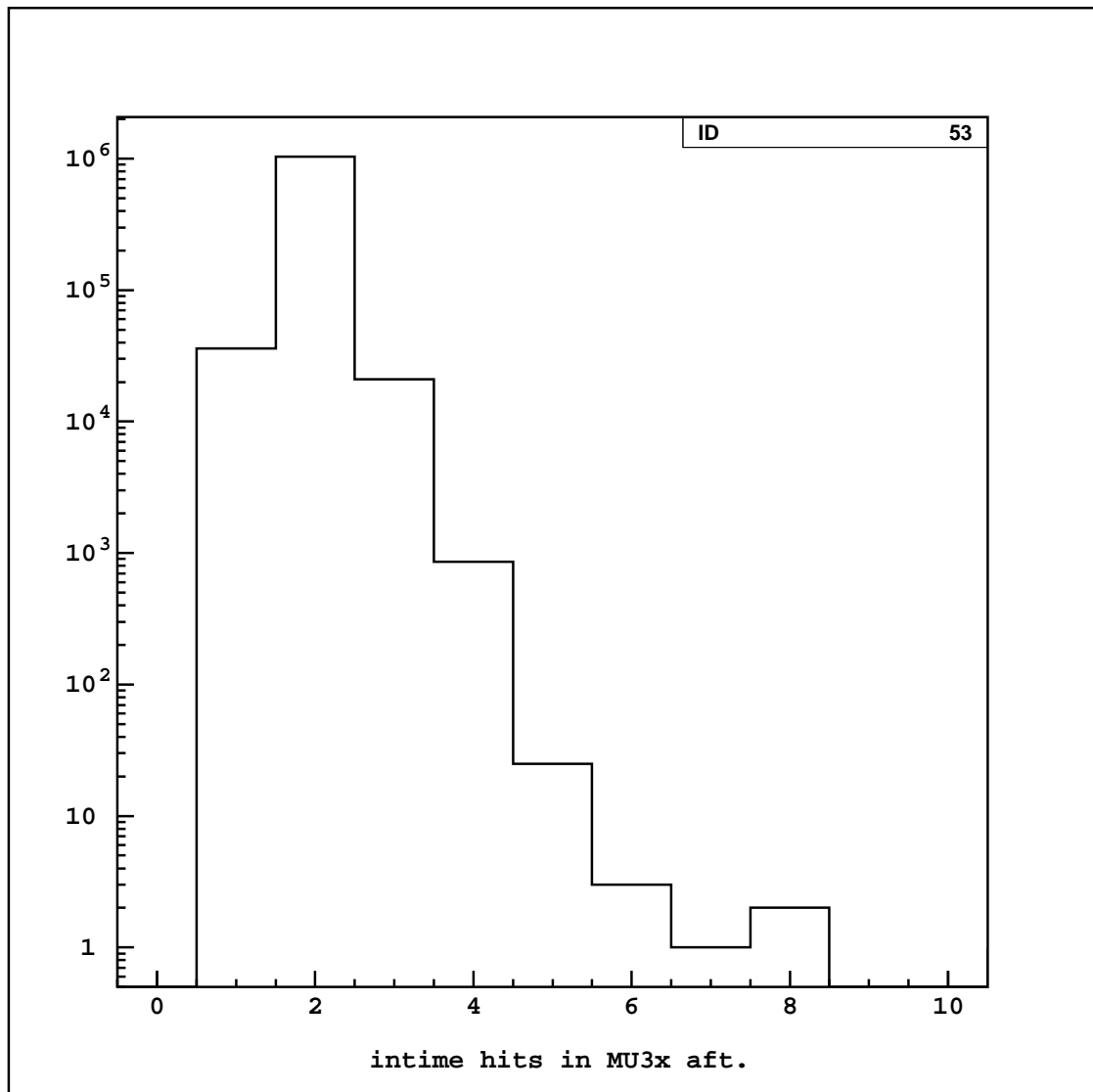


Figure 6.5: Distribution of number of hits in MU3x for the 1999 $K_L \rightarrow \pi^0 \pi^0 \mu^+ \mu^-$ MC immediately after the MU3x hit requirement was implemented.

Crunch Requirement	A_{Data} (1999)	A_{MC,γ^*} (1999)	A_{MC,X^0} (1999)
L1, L2 and L3 MC Triggers	—	0.091	0.090
$N_{tracks} = 2$	0.466	0.971	0.970
$C_{track1} = -C_{track2}$	0.999	0.999	0.999
$E_{cl}(\text{track}) \leq 2.0 \text{ GeV}$	0.436	0.904	0.897
$E_{cl}(\text{track})/p_{track} \leq 0.9$	0.999	0.999	0.999
$N_{HCL} \geq 4$	0.050	0.686	0.681
N_{hits} in MU2 and MU3x,y ≥ 1	0.989	0.999	0.999
N_{cl} (not assoc. w/tracks) = 4	0.471	0.970	0.969
$120.0 \text{ MeV} \leq m_{\gamma\gamma} \leq 150.0 \text{ MeV}$	0.443	0.973	0.974
$90.0 \text{ m} \leq Z_{vtx} \leq 160.0 \text{ m}$	0.310	0.984	0.986
Bad Spill Requirement	0.940	0.966	0.965
$p_T^2 \leq 0.06 \text{ GeV}^2$	0.700	0.999	0.999
Total Acceptance	0.04%	4.92%	4.79%

Table 6.2: 1999 signal mode crunch requirement summary. Requirements are listed in the order in which they were implemented.

Crunch Requirement	A_{Data} (1997)	A_{MC} (1997)
L1, L2 and L3 MC Triggers	—	0.027
$N_{tracks} = 2$	0.889	0.985
$C_{track1} = -C_{track2}$	0.999	0.999
$0.95 \leq E_{cl}(\text{track})/p_{track} \leq 1.05$	0.679	0.886
$N_{HCL} \geq 5$	0.916	0.967
N_{cl} (not assoc. w/tracks) = 5	0.374	0.447
$120.0 \text{ MeV} \leq m_{\gamma\gamma} \leq 150.0 \text{ MeV}$	0.066	0.067
$90.0 \text{ m} \leq Z_{vtx} \leq 160.0 \text{ m}$	0.977	0.985
Bad Spill Requirement	0.792	0.789
$p_T^2 \leq 0.06 \text{ GeV}^2$	0.928	0.934
Total Acceptance	0.98%	0.05%

Table 6.3: 1997 normalization mode crunch requirement summary. Requirements are listed in the order in which they were implemented.

Crunch Requirement	A_{Data} (1999)	A_{MC} (1999)
L1, L2 and L3 MC Triggers	—	0.034
$N_{tracks} = 2$	0.965	0.985
$C_{track1} = -C_{track2}$	0.999	0.999
$0.95 \leq E_{cl}(\text{track})/p_{track} \leq 1.05$	0.848	0.851
$N_{HCL} \geq 5$	1.000	0.972
N_{cl} (not assoc. w/tracks) = 5	0.999	0.463
$120.0 \text{ MeV} \leq m_{\gamma\gamma} \leq 150.0 \text{ MeV}$	0.071	0.072
$90.0 \text{ m} \leq Z_{vtx} \leq 160.0 \text{ m}$	0.970	0.982
Bad Spill Requirement	0.934	0.944
$p_T^2 \leq 0.06 \text{ GeV}^2$	0.928	0.937
Total Acceptance	4.88%	0.08%

Table 6.4: 1999 normalization mode crunch requirement summary. Requirements are listed in the order in which they were implemented. Note that the 1999 2E-NCLUS data set was pre-crunched.

logbooks Cutting out a run on the premise of a bad spill would be careless, since problems associated with bad spills only affect a fraction of events within a given run and perhaps only part of an event not used in this analysis. In order to isolate specific bad spills within a given run, a 32 element binary integer (referred to as a *mask*) was saved after each spill for future analysis. Essentially, each bit in the mask identified a different problem within the detector. The majority of bad spills (such as CsI problems and muon ID system problems) were unacceptable for this analysis. As a result, these bad spills were eliminated. On the other hand, bad spills involving TRDs were acceptable since pion-electron discrimination is not employed in this analysis. These bad spills were retained for the next stage of analysis. Table 6.5 depicts a cut summary of the E799 bad spills.

According to figure 6.6, the largest bad spill losses in the 1997 signal mode analysis

Bit Number	Bad Spill Description	Cut
1, 17, 19, 20	Trigger Problems	Yes
2, 3, 5-8	DPMT Problems	Yes
4	Blown QIE Comparators	Yes
9, 10	CsI Problems	Yes
11	ETOT	Yes
12	FERA ADC	Yes
13	Drift Chambers	Yes
14	Photon Veto	Yes
15	Trigger Hodoscopes	Yes
16	Muon ID System	Yes
18	Hit Counting Problems	Yes
21	DAQ/L3	Yes
22	Not An E799 Run (i.e. Special Run)	Yes
23	Short Run	Yes
24-28	TRD Problems	No
29	Beam Problems	Yes
30, 31	Spares	Yes
32	Miscellaneous	Yes

Table 6.5: E799 bad spill cut summary. The cut applies to the signal and normalization modes.

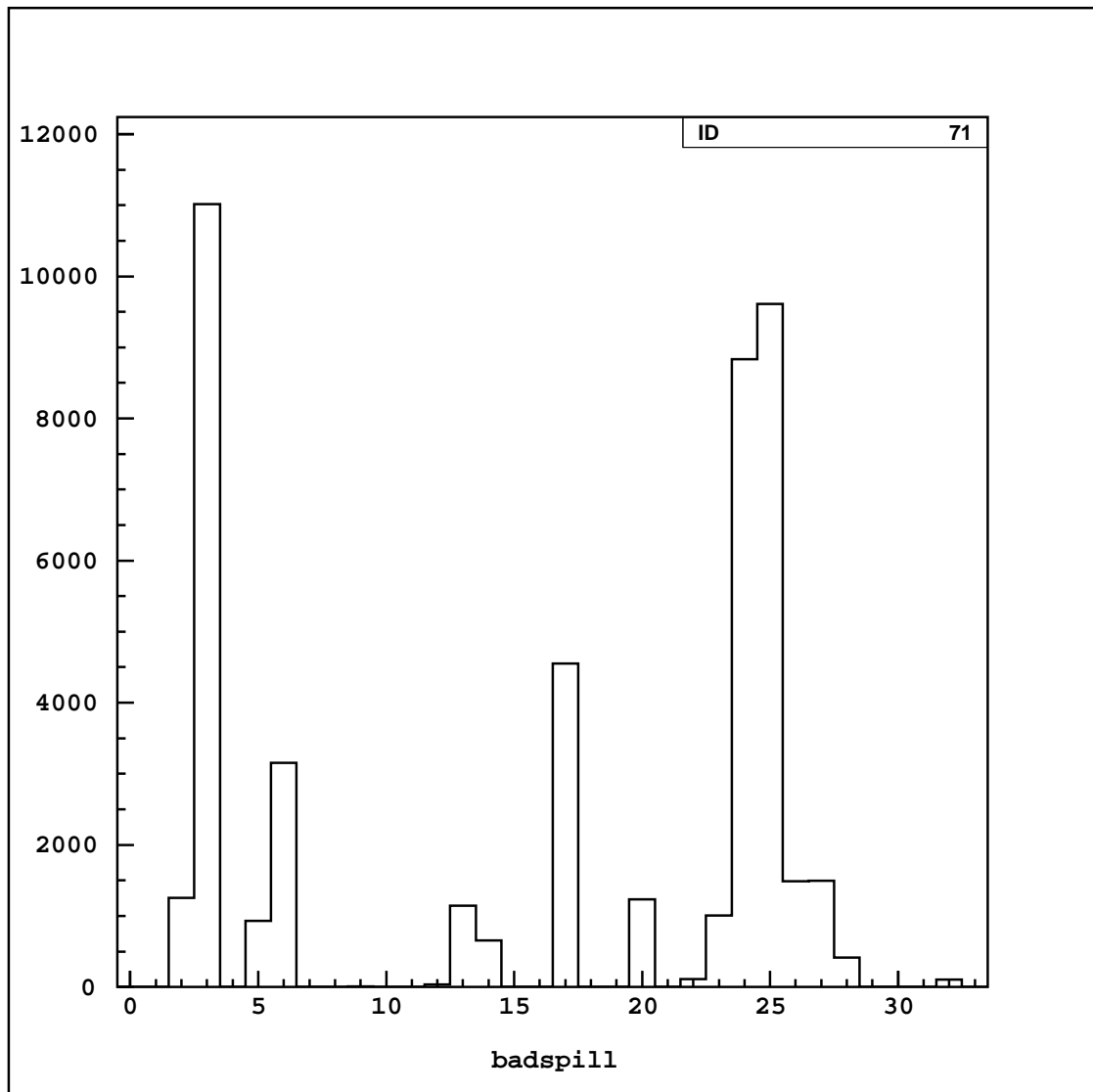


Figure 6.6: Distribution of bad spills for the 1997 data set after the first crunch stage. The meaning of each bit is given in Table 6.1.

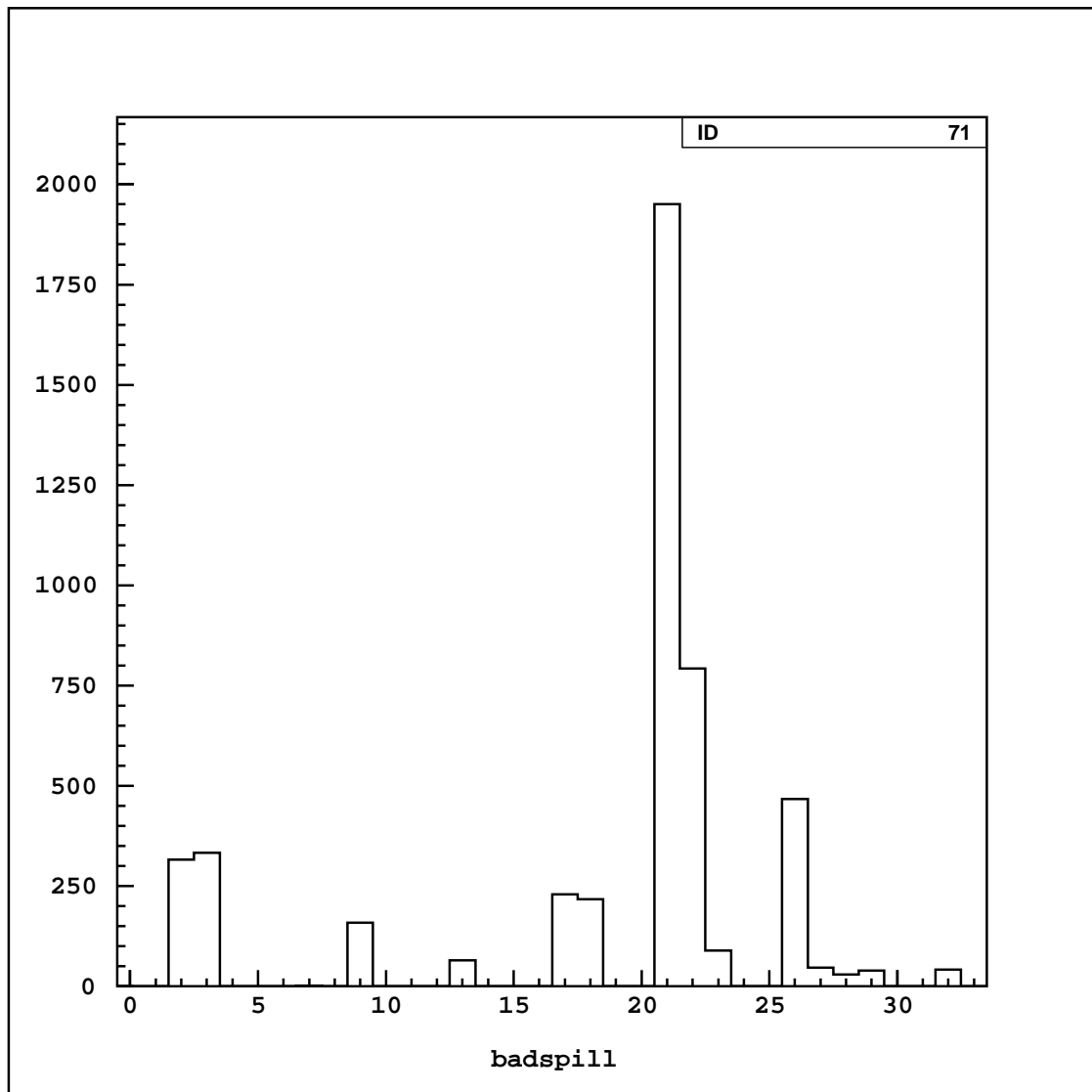


Figure 6.7: Distribution of bad spills for the 1999 data set after the first crunch stage.

came from bad QIEs. Figure 6.7 shows that level 3 trigger problems accounted for the largest bad spill losses in the 1999 signal mode analysis. In the 1999 run, arrays of calorimeter information became corrupted at random intervals for certain physics triggers during L3 processing. This effect caused an abrupt change in the L3 acceptance, which set off an alarm that alerted the shift crew to manually reset the trigger. Since the source of this problem was never found, the data from these bad spills had to be cut as well.

6.2 Protocol of the Analysis

The analyses of $K_L \rightarrow \pi^0 \pi^0 \mu^+ \mu^-$ and $K_L \rightarrow \pi^0 \pi^0 X^0 \rightarrow \pi^0 \pi^0 \mu^+ \mu^-$ were performed with masked signal regions from the beginning of the crunch until the end of the analysis, which occurs when the masked signal region is opened. Definitions of the signal regions and the motivation behind the blind analysis technique will be given in the following sections.

6.2.1 Motivation for Blind Analyses

Blind analysis techniques are essential cogs in the scientific method. The motivation of blind analyses is to eliminate *observer's bias* present in an experiment as effectively as possible. Naturally, blind analysis methods vary from experiment to experiment. New pharmaceuticals are often subject to double-blind testing before they

are released onto the market. This procedure eliminates bias due the pharmaceutical researcher and the experimental subjects. In regards to physics, the motivation for blind analysis is summed up nicely in the book *Surely You're Joking, Mr. Feynman!* [60]:

“It’s a thing that scientists are ashamed of - this history - because it’s apparent that people did things like this: When they got a number that was too high above Millikan’s, they thought something must be wrong - and they would look for and find a reason why something might be wrong. When they got a number closer to Millikan’s value they didn’t look so hard...

The first principle is that you must not fool yourself - and you are the easiest person to fool.”

- *Richard Feynman*

In the search for rare decay channels, the experimenter may be subject to an extremely dangerous pitfall known as *selection bias* [61]. One can easily see how the search for a tiny signal can seduce the experimenter towards a biased result. In such a scenario, the small number of statistics available allow the experimenter to analyze each event on an individual basis. Depending on the judgement of the experimenter, every observed event possesses characteristics that allow it to be included in the signal pool or excluded as unwanted background. This can lead to the creation of an artificial signal peak or an upper limit that’s lower than is merited. In order to eliminate selection bias, this analysis employs the masked signal box technique, where a subset of the data is hidden from the observer. The masked signal box dimensions depend on signal locations in the parameter space containing the signal. The parameter resolutions are determined using the KTeV MC. This shall be described in the next

section.

6.2.2 Defining the Masked Signal Box Regions

Signal events were selected with the combined invariant mass of the six final daughter state particles, $m_{\mu\mu\gamma\gamma\gamma\gamma}$, and p_T^2 . Ideally, $m_{\mu\mu\gamma\gamma\gamma\gamma}$ should be close to the K_L mass and, as mentioned in section 6.1.3, p_T^2 should hover very close to zero. This identification system provides a robust framework out of which the masked signal box can be constructed, namely a two-dimensional region in the variables $m_{\mu\mu\gamma\gamma\gamma\gamma}$ and p_T^2 . In the 1997 and 1999 analyses, the masked signal box region was defined as:

$$495MeV \leq m_{\mu\mu\gamma\gamma\gamma\gamma} \leq 501MeV \quad (6.1)$$

$$p_T^2 \leq 0.00013GeV^2. \quad (6.2)$$

Using the definitions given in equations 6.1 and 6.2, 94% of $K_L \rightarrow \pi^0\pi^0\mu^+\mu^-$ and $K_L \rightarrow \pi^0\pi^0X^0 \rightarrow \pi^0\pi^0\mu^+\mu^-$ MC events that have passed all crunch requirements are located in the masked signal box region. At this point, it was found that all background events which passed the crunch requirements were located in the high mass region, well away from the masked signal box. This will be described further in section 6.3.4. Figures 6.8 and 6.9 display the p_T^2 vs. $m_{\mu\mu\gamma\gamma\gamma\gamma}$ scatter plots with masked signal box open for the 1999 $K_L \rightarrow \pi^0\pi^0\mu^+\mu^-$ and $K_L \rightarrow \pi^0\pi^0X^0 \rightarrow \pi^0\pi^0\mu^+\mu^-$ signal MC respectively. Figure 6.10 shows the p_T^2 vs. $m_{\mu\mu\gamma\gamma\gamma\gamma}$ scatter plot for 1999 data events with the masked signal box closed.

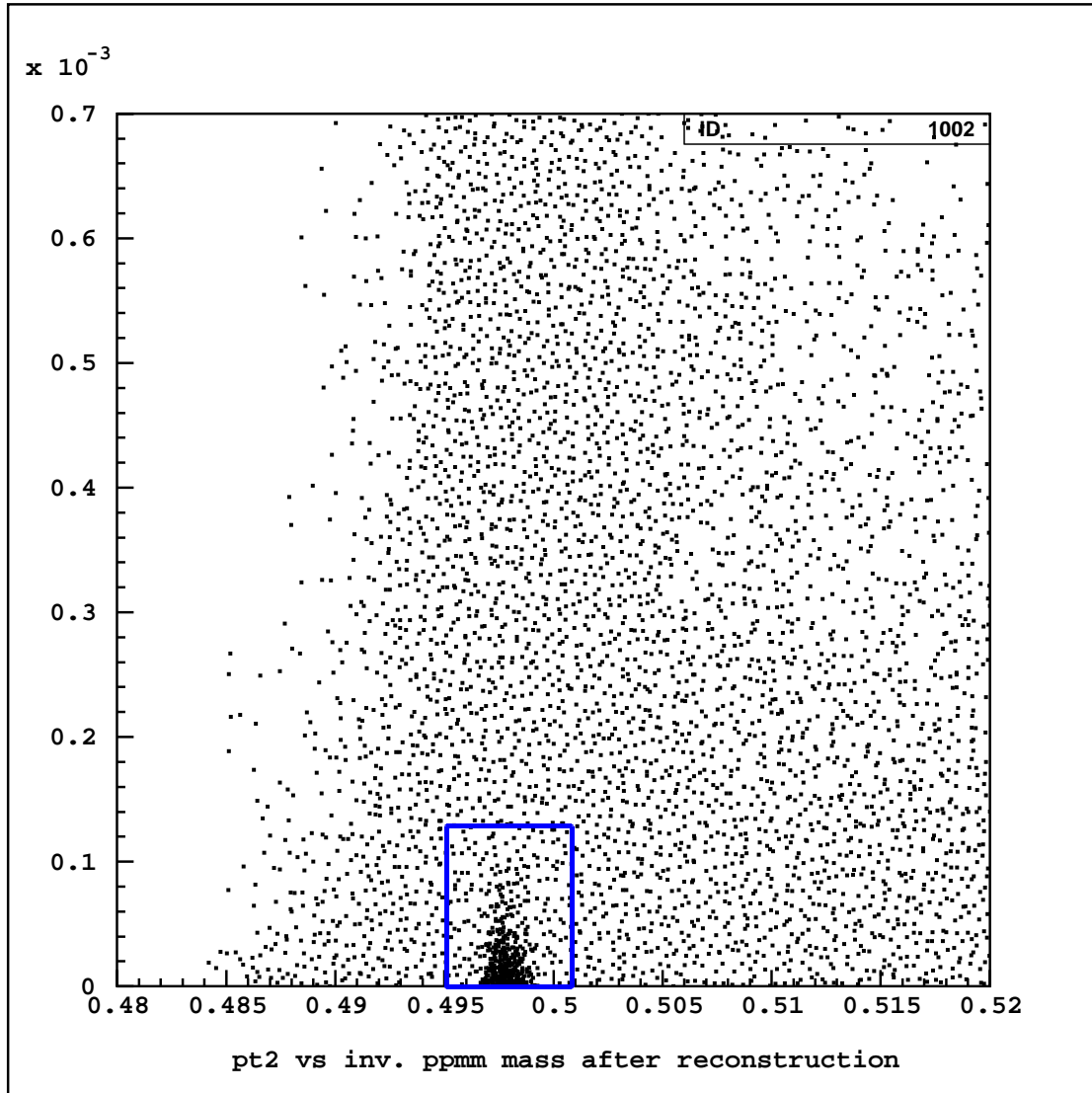


Figure 6.8: p_T^2 vs. $m_{\mu\mu\gamma\gamma\gamma}$ scatter plot for 1999 $K_L \rightarrow \pi^0\pi^0\mu^+\mu^-$ MC events after all crunch requirements have been implemented. The masked signal box is open and is shown for display purposes only.

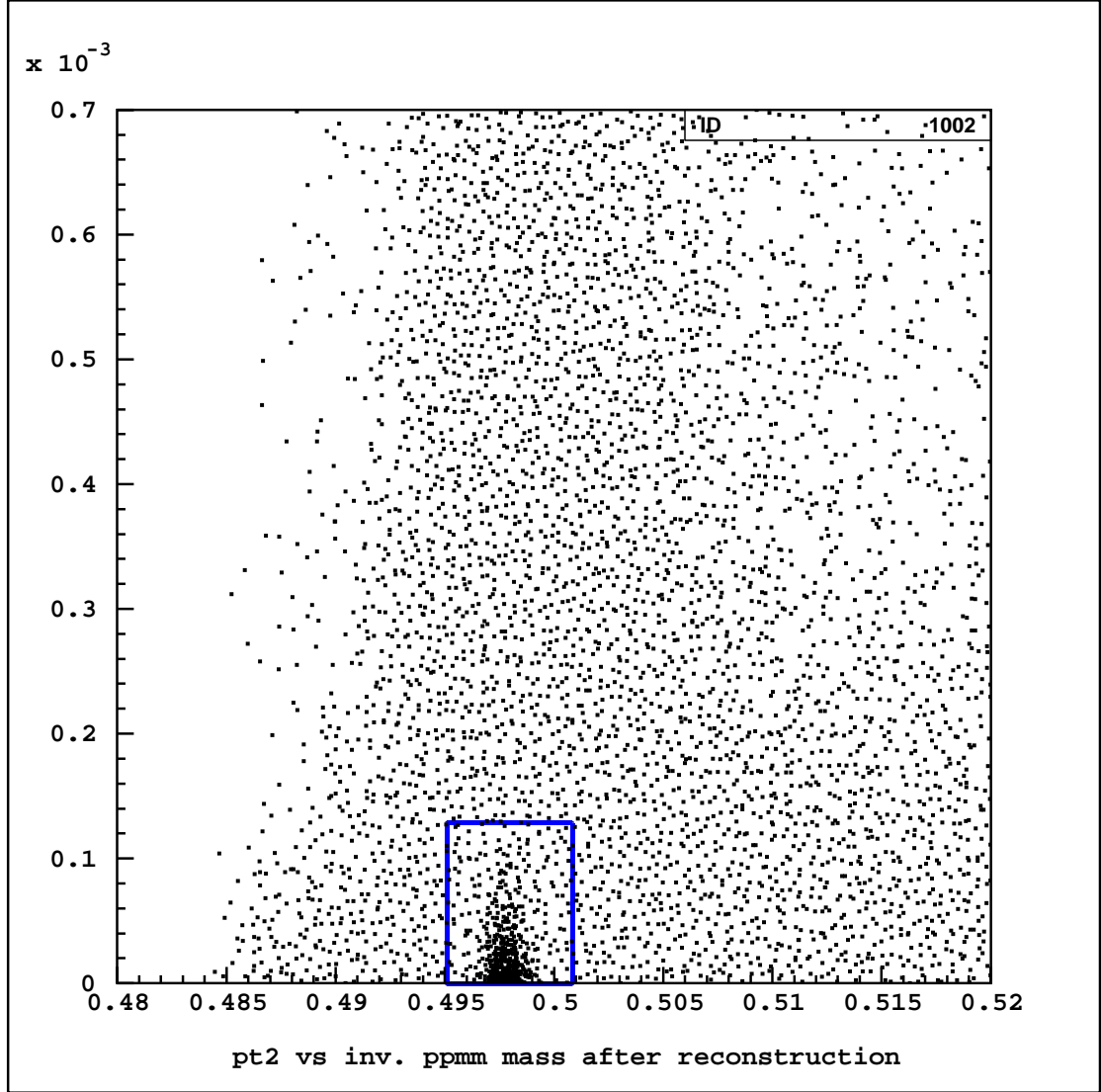


Figure 6.9: p_T^2 vs. $m_{\mu\mu\gamma\gamma\gamma}$ scatter plot for 1999 $K_L \rightarrow \pi^0\pi^0 X^0 \rightarrow \pi^0\pi^0\mu^+\mu^-$ MC events after all crunch requirements have been implemented. The masked signal box is open and is shown for display purposes only.

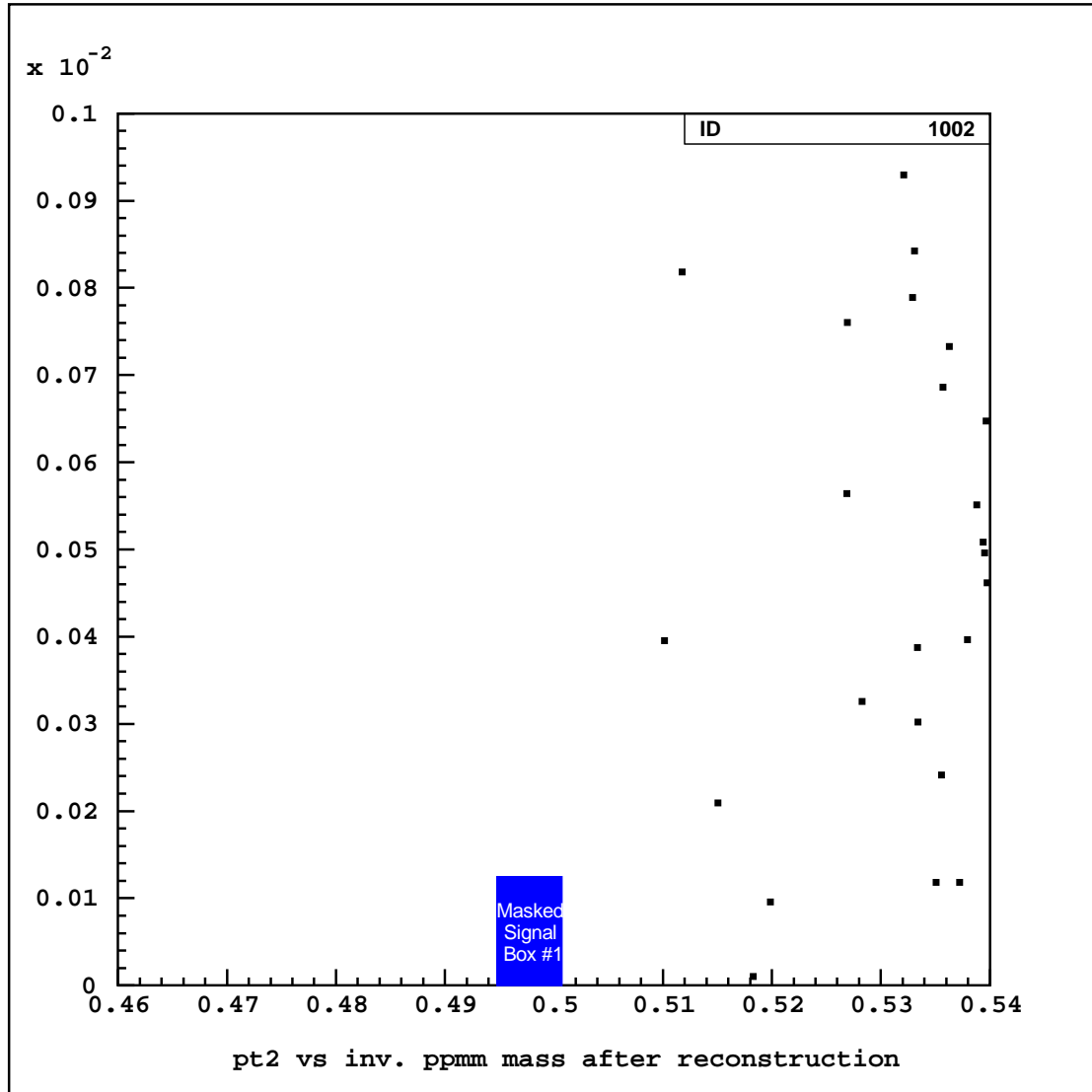


Figure 6.10: p_T^2 vs. $m_{\mu\mu\gamma\gamma\gamma}$ scatter plot for the 1999 data set after all crunch requirements have been implemented. The masked signal box (labeled *Masked Signal Box #1*) is closed.

Only one masked signal box has been defined up to this point. However, this analysis necessitates that two signal boxes be defined, since a search for the rare decay $X^0 \rightarrow \mu^+\mu^-$ is also being performed. The second masked signal box (for $X^0 \rightarrow \mu^+\mu^-$) was composed of $|p_{T,\mu\mu}^2 - p_{T,\pi\pi}^2|$ and the invariant mass of the two muons, $m_{\mu\mu}$. In the 1997 and 1999 analyses, this masked signal box was defined as:

$$|m_{\mu\mu} - 214.3\text{MeV}| \leq 0.5\text{MeV} \quad (6.3)$$

$$|p_{T,\mu\mu}^2 - p_{T,\pi\pi}^2| \leq 0.0007\text{GeV}^2. \quad (6.4)$$

Once again, (214.3 ± 0.5) MeV is the mass of X^0 as determined by HyperCP [21]. Defined by the bounds given in equations 6.3 and 6.4, the second masked signal box contains 85% of 1997 $X^0 \rightarrow \mu^+\mu^-$ MC events that pass all crunch requirements and 86% of 1999 $X^0 \rightarrow \mu^+\mu^-$ MC events. Figure 6.11 displays the $|p_{T,\mu\mu}^2 - p_{T,\pi\pi}^2|$ vs. $m_{\mu\mu}$ scatter plot for the 1999 $X^0 \rightarrow \mu^+\mu^-$ MC. Figure 6.12 shows the $|p_{T,\mu\mu}^2 - p_{T,\pi\pi}^2|$ vs. $m_{\mu\mu}$ scatter plot for the 1999 data set with the both masked signal boxes closed. Finally, an important note to remember is that both masked signal boxes remained closed for the entire duration of the crunch and full analysis (which shall be described in section 6.3) of the 1997 and 1999 data sets.

6.3 Signal Mode Analysis

This section describes the motivation behind each requirement that was implemented in the signal mode analysis. These requirements were applied to both data

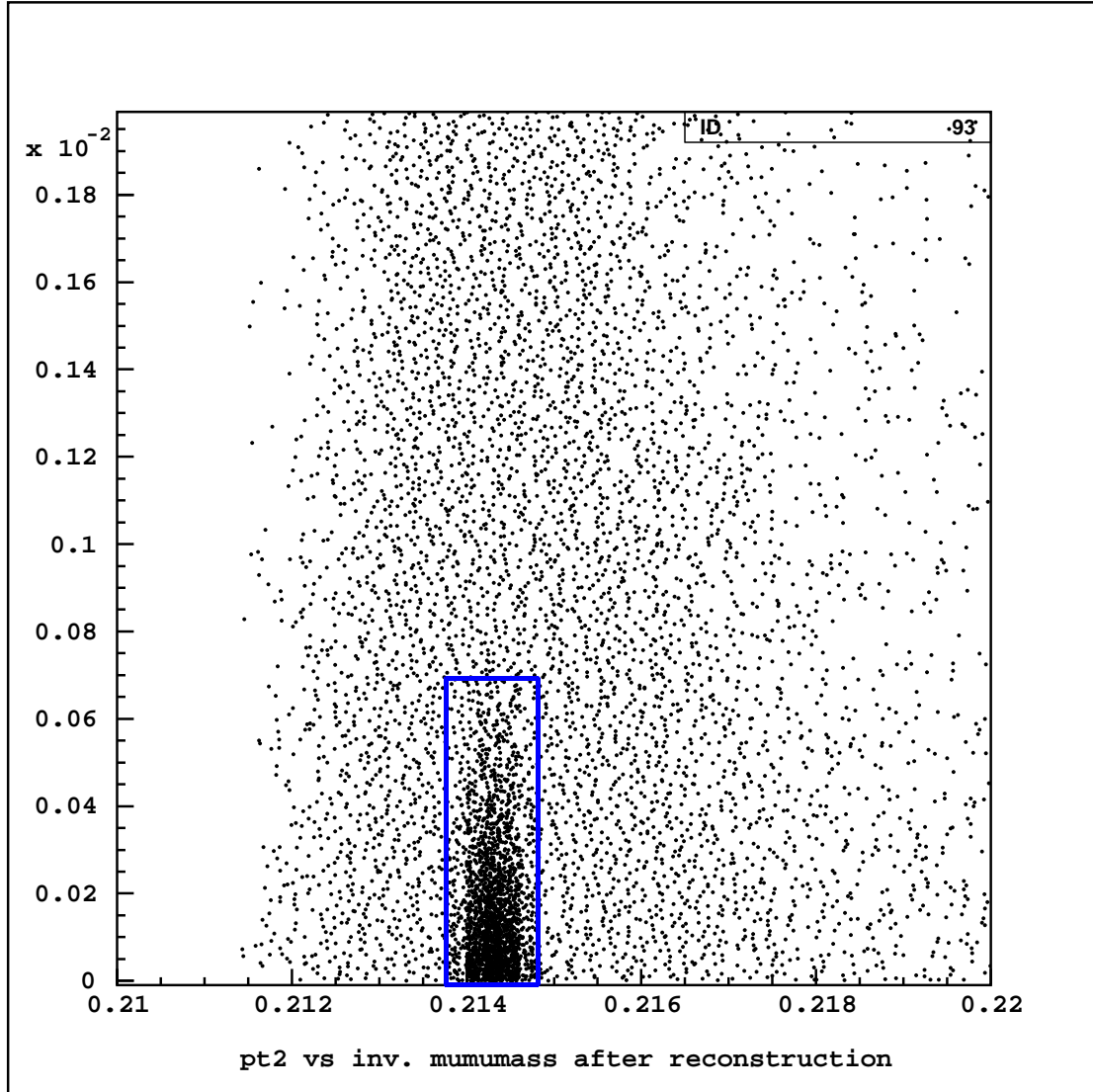


Figure 6.11: $|p_{T,\mu\mu}^2 - p_{T,\pi\pi}^2|$ vs. $m_{\mu\mu}$ scatter plot for 1999 $X^0 \rightarrow \mu^+\mu^-$ MC events after all crunch requirements have been implemented. The masked signal box associated with this decay is open and is shown for display purposes only.

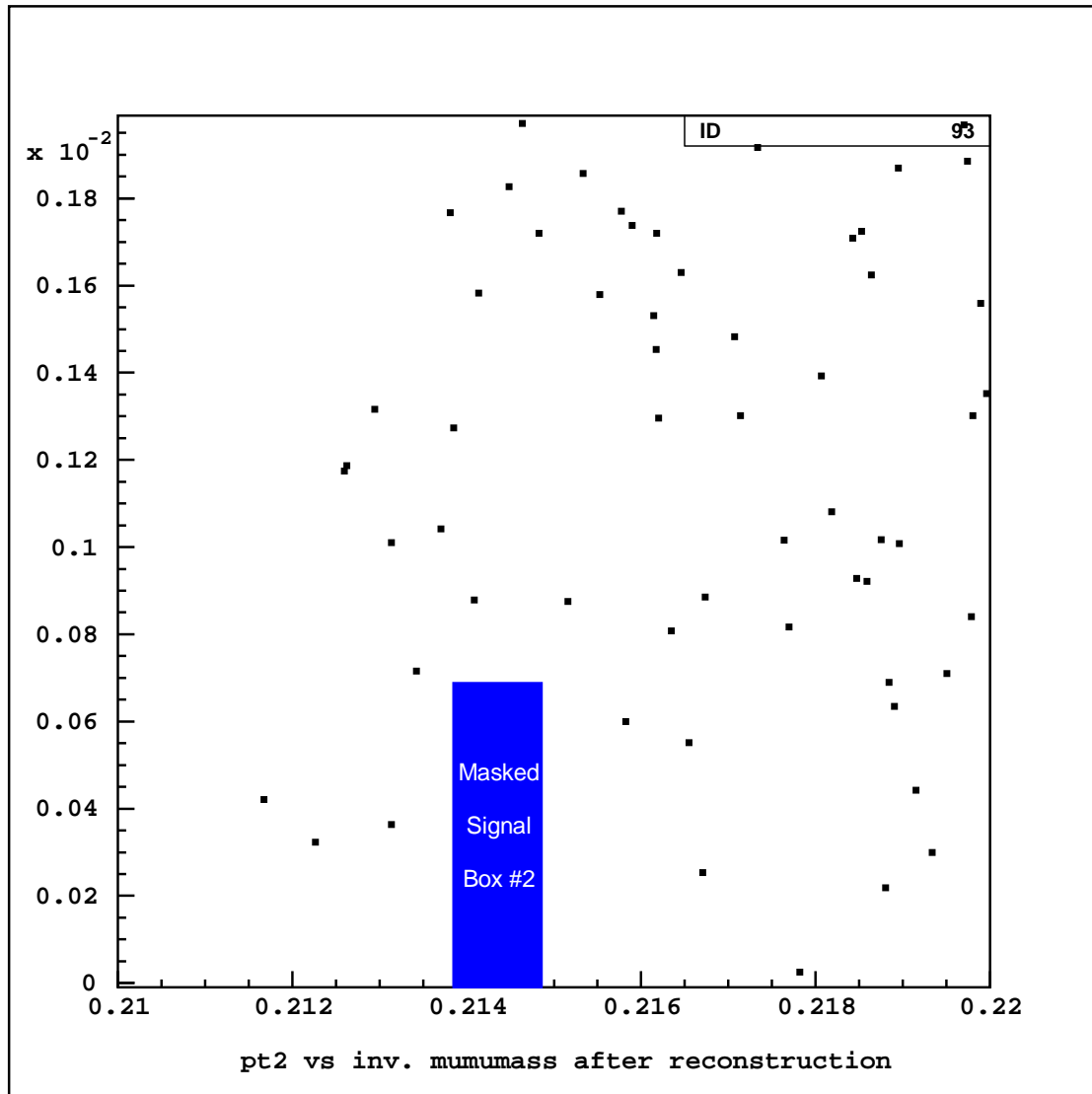


Figure 6.12: $|p_{T,\mu\mu}^2 - p_{T,\pi\pi}^2|$ vs. $m_{\mu\mu}$ scatter plot for the 1999 data set after all crunch requirements have been implemented. The masked signal box (labeled *Masked Signal Box #2*) is closed.

sets, the 1997 and 1999 background MC and to the 1997 and 1999 signal mode ($K_L \rightarrow \pi^0 \pi^0 \mu^+ \mu^-$ and $K_L \rightarrow \pi^0 \pi^0 X^0 \rightarrow \pi^0 \pi^0 \mu^+ \mu^-$) MC. Tables 6.6 and 6.7 list the acceptances obtained after application of each signal mode analysis requirement for the 1997 and 1999 signal mode analyses respectively.

6.3.1 Initial Requirement on $m_{\mu\mu\gamma\gamma\gamma}$ and p_T^2

Loose requirements on $m_{\mu\mu\gamma\gamma\gamma}$ and p_T^2 were implemented in order to study background located in the sideband regions outside the masked signal box. Figures 6.13 and 6.14 show the 1997 and 1999 MC distributions for $m_{\mu\mu\gamma\gamma\gamma}$ respectively. Figures 6.15 and 6.16 display the 1997 and 1999 MC distribution for p_T^2 after the requirement on $m_{\mu\mu\gamma\gamma\gamma}$ has been applied.

6.3.2 Requirements on $E_{cl}(\text{track})$ and p_{track}

The cluster energy associated with a track, $E_{cl}(\text{track})$, is one of a few requirements used to distinguish muons from charged pions. Normally, muons will only leave ionization energy in the electromagnetic calorimeter, which produces an energy distribution with a MIP peak at about 400 MeV (see figures 6.17 and 6.18). However, hadronic showers produced by charged pions interacting with the calorimeter will yield clusters of much higher energy than a MIP. The requirement on $E_{cl}(\text{track})$ ensures that the cluster was left by a MIP and rejects backgrounds due to pion punch-throughs. In order to pass through all the filters in the muon ID system and reach MU3, a muon

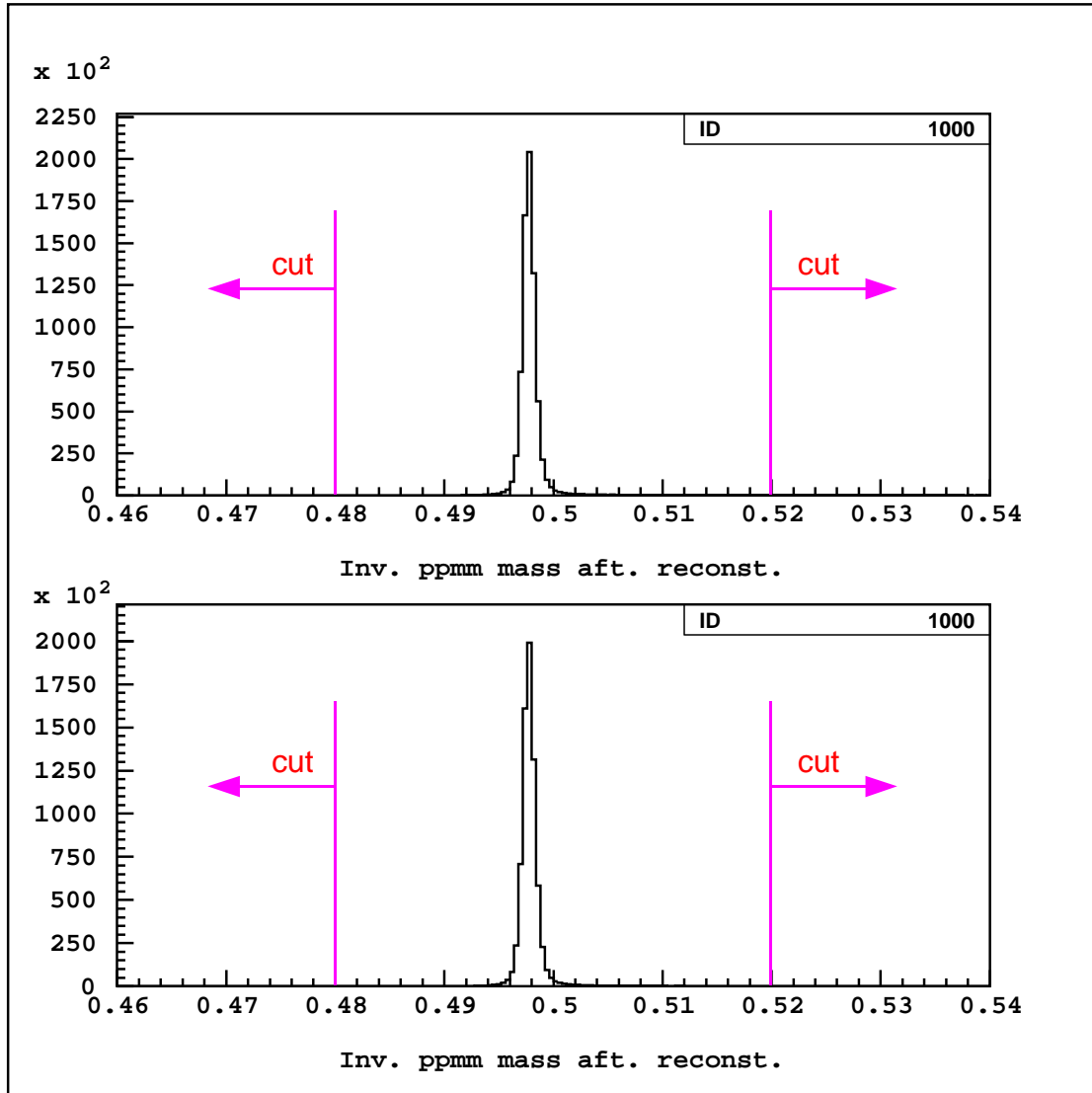


Figure 6.13: Distributions for $m_{\mu\mu\gamma\gamma\gamma}$ in the 1997 $K_L \rightarrow \pi^0\pi^0\mu^+\mu^-$ MC (top) and 1997 $K_L \rightarrow \pi^0\pi^0 X^0 \rightarrow \pi^0\pi^0\mu^+\mu^-$ MC (bottom) after all crunch requirements and just before the first requirement on $m_{\mu\mu\gamma\gamma\gamma}$ was implemented.

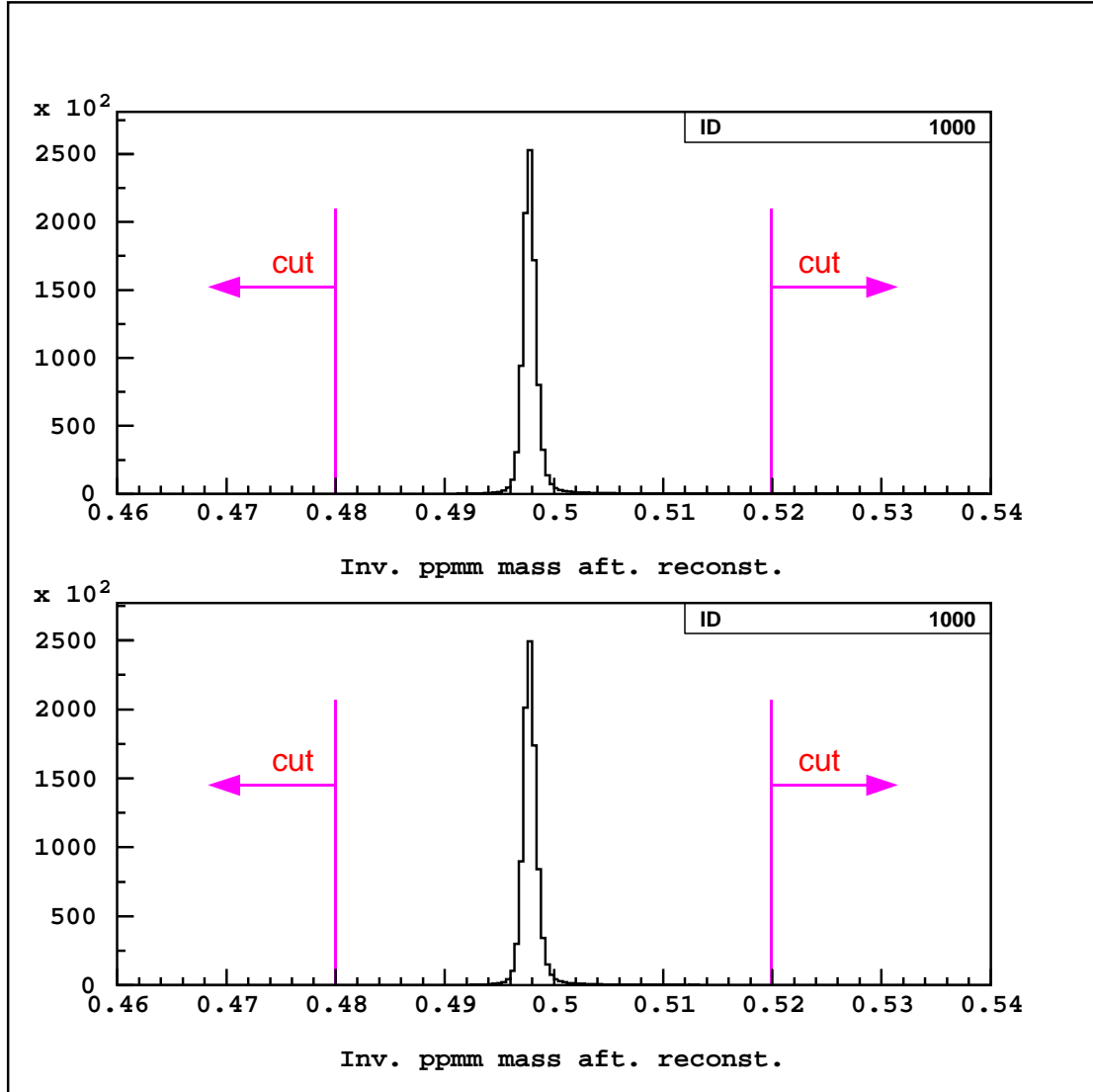


Figure 6.14: Distributions for $m_{\mu\mu\gamma\gamma\gamma}$ in the 1999 $K_L \rightarrow \pi^0 \pi^0 \mu^+ \mu^-$ MC (top) and 1999 $K_L \rightarrow \pi^0 \pi^0 X^0 \rightarrow \pi^0 \pi^0 \mu^+ \mu^-$ MC (bottom) after all crunch requirements and just before the first requirement on $m_{\mu\mu\gamma\gamma\gamma}$ was implemented.

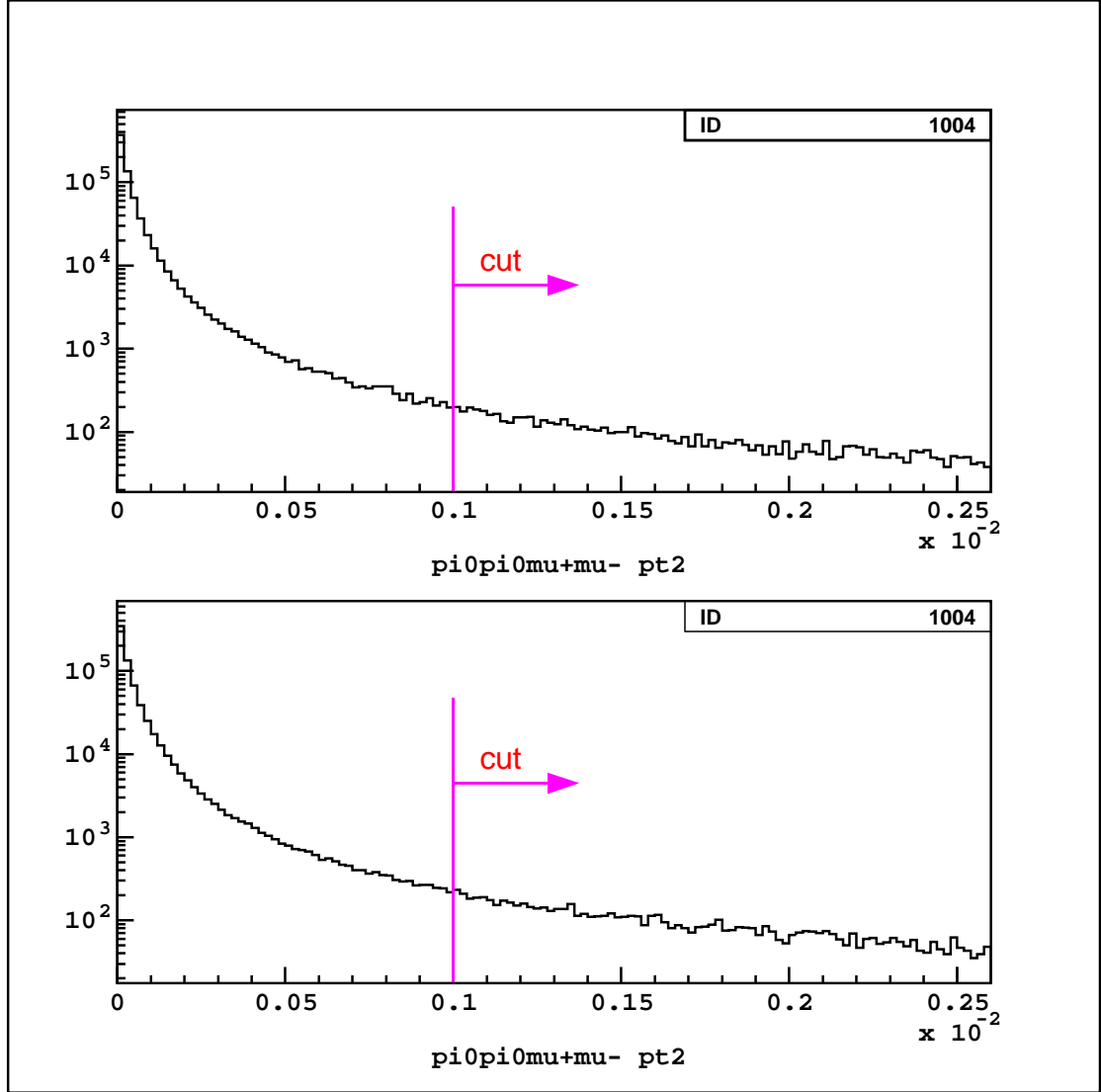


Figure 6.15: Distributions for p_T^2 in the 1997 $K_L \rightarrow \pi^0\pi^0\mu^+\mu^-$ MC (top) and 1997 $K_L \rightarrow \pi^0\pi^0X^0 \rightarrow \pi^0\pi^0\mu^+\mu^-$ MC (bottom) after the requirement on $m_{\mu\mu\gamma\gamma\gamma}$ and just before the requirement on p_T^2 was implemented.

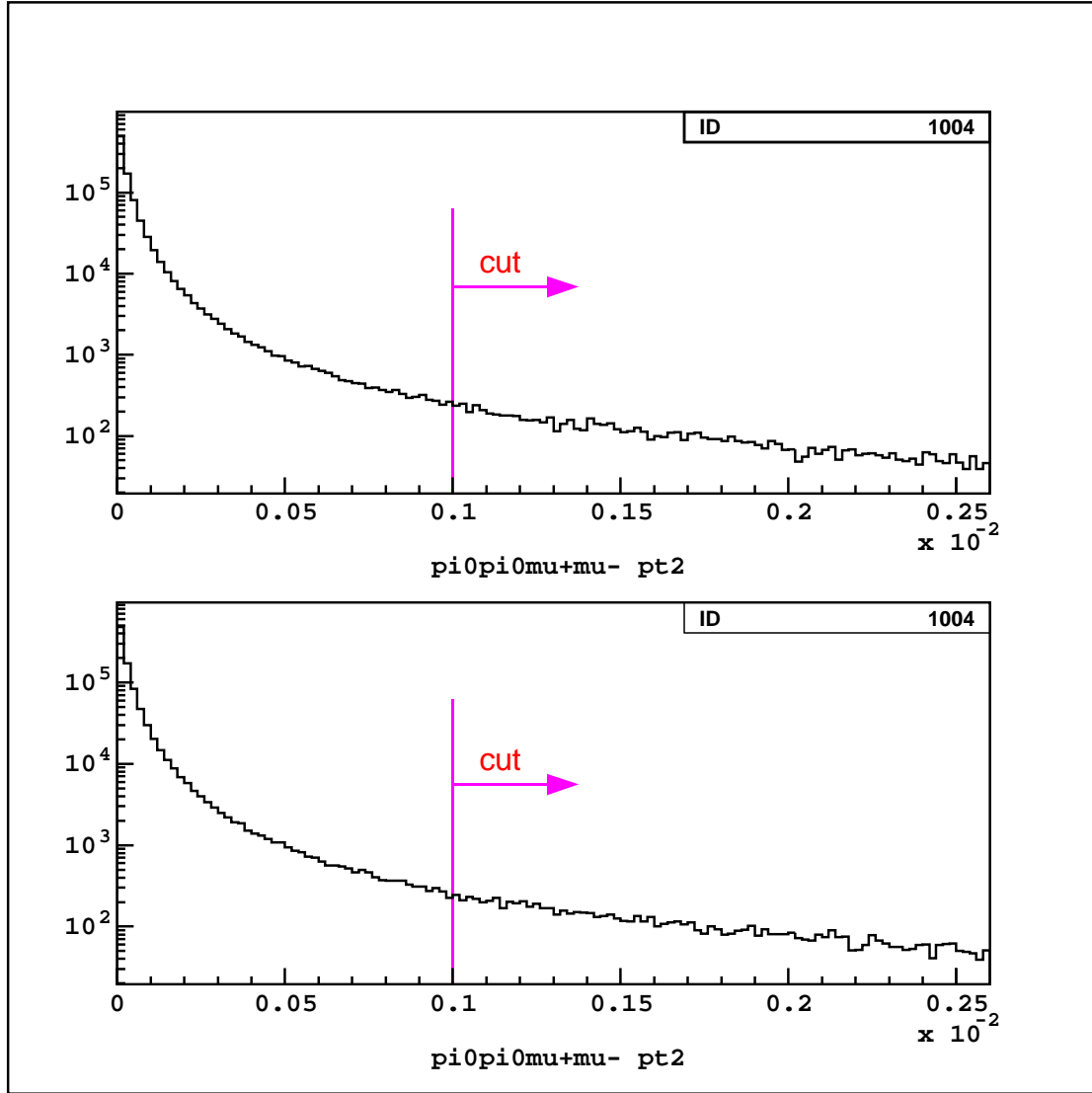


Figure 6.16: Distributions for p_T^2 in the 1999 $K_L \rightarrow \pi^0 \pi^0 \mu^+ \mu^-$ MC (top) and 1999 $K_L \rightarrow \pi^0 \pi^0 X^0 \rightarrow \pi^0 \pi^0 \mu^+ \mu^-$ MC (bottom) after the requirement on $m_{\mu\mu\gamma\gamma\gamma}$ and just before the requirement on p_T^2 was implemented.

needs a minimum momentum of 7 GeV. Therefore, to ensure that tracks register hits in MU3, a requirement that the track momentum, p_{track} , be at least 7 GeV is implemented. Figures 6.19 and 6.20 show p_{track} for the 1997 and 1999 signal mode MC immediately before the requirement on p_{track} was implemented.

6.3.3 Requirements on $m_{\gamma\gamma}$ and $m_{\mu\mu}$

The requirement on the reconstructed π^0 masses, $m_{\gamma\gamma}$, has been tightened from ± 15 MeV from the nominal π^0 mass to ± 14 MeV from the nominal π^0 mass (see figures 6.21 and 6.22). In addition, a requirement that $m_{\mu\mu}$ be less than 232 MeV has been implemented (see figures 6.23 and 6.24). These cuts effectively limit the phase space available to the $\pi^0\pi^0$ and the dimuon and effectively kill the remaining background outside of the masked signal box (according to MC), while retaining nearly all of the signal in MC.

6.3.4 Backgrounds to the Signal Mode

Table 5.4 details all signal mode backgrounds that were studied in this analysis. The K_L sector does not possess any decay channels with four photons and two tracks aside from the unobserved $K_L \rightarrow \pi^0\pi^0 e^+ e^-$. Therefore, the signal mode backgrounds are essentially limited to K_L decay modes with two tracks (charged pions which punch through or muons) and zero, one or two photons plus additional overlapping accidental photons to satisfy the four photon requirement. Naturally, the additional

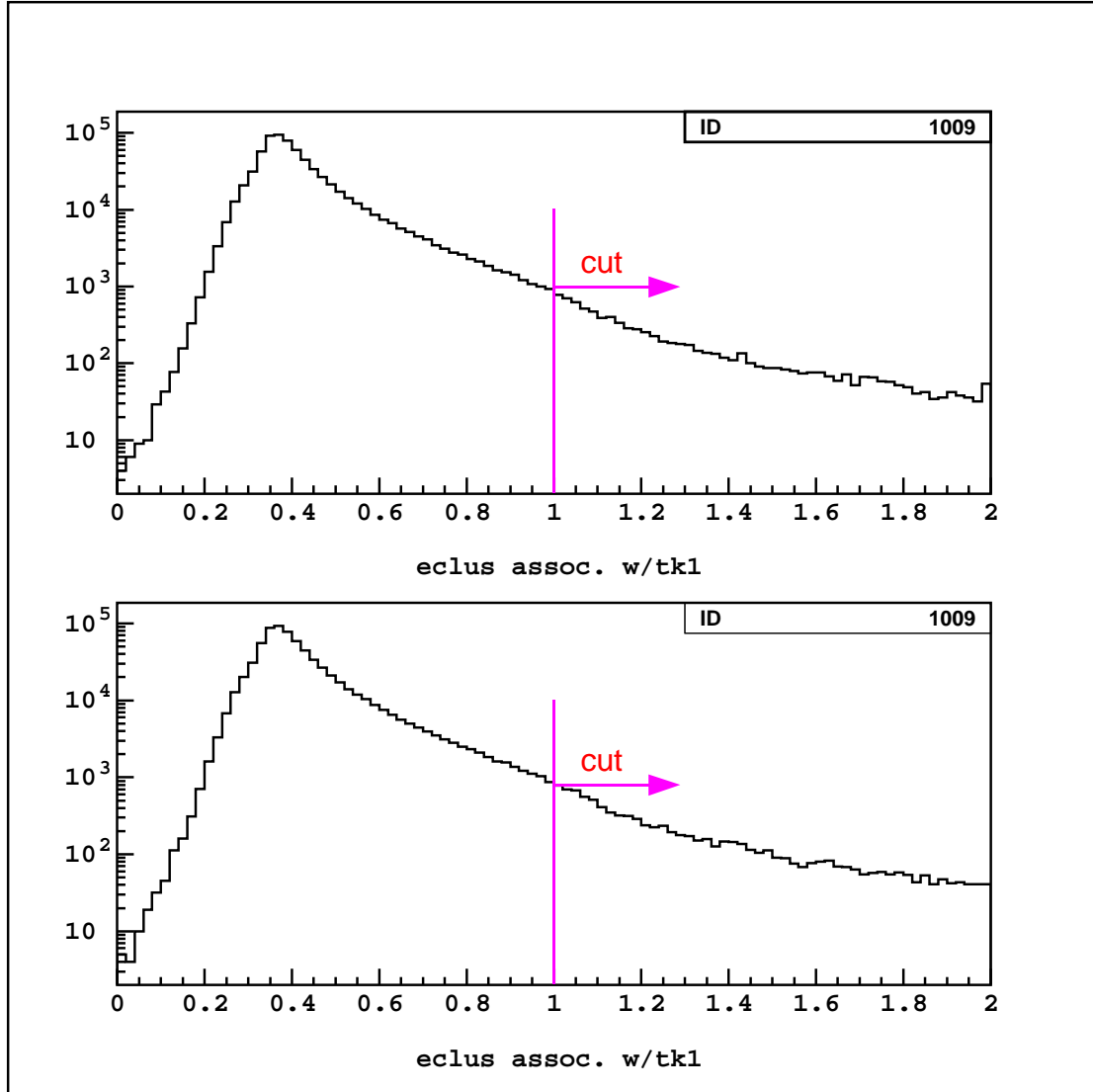


Figure 6.17: Distributions for $E_{cl}(\text{track1})$ in the 1997 $K_L \rightarrow \pi^0 \pi^0 \mu^+ \mu^-$ MC (top) and 1997 $K_L \rightarrow \pi^0 \pi^0 X^0 \rightarrow \pi^0 \pi^0 \mu^+ \mu^-$ MC (bottom) after the requirement on p_T^2 and just before the requirement on $E_{cl}(\text{track})$ was implemented. The requirement on $E_{cl}(\text{track})$ was applied to both clusters associated with tracks.

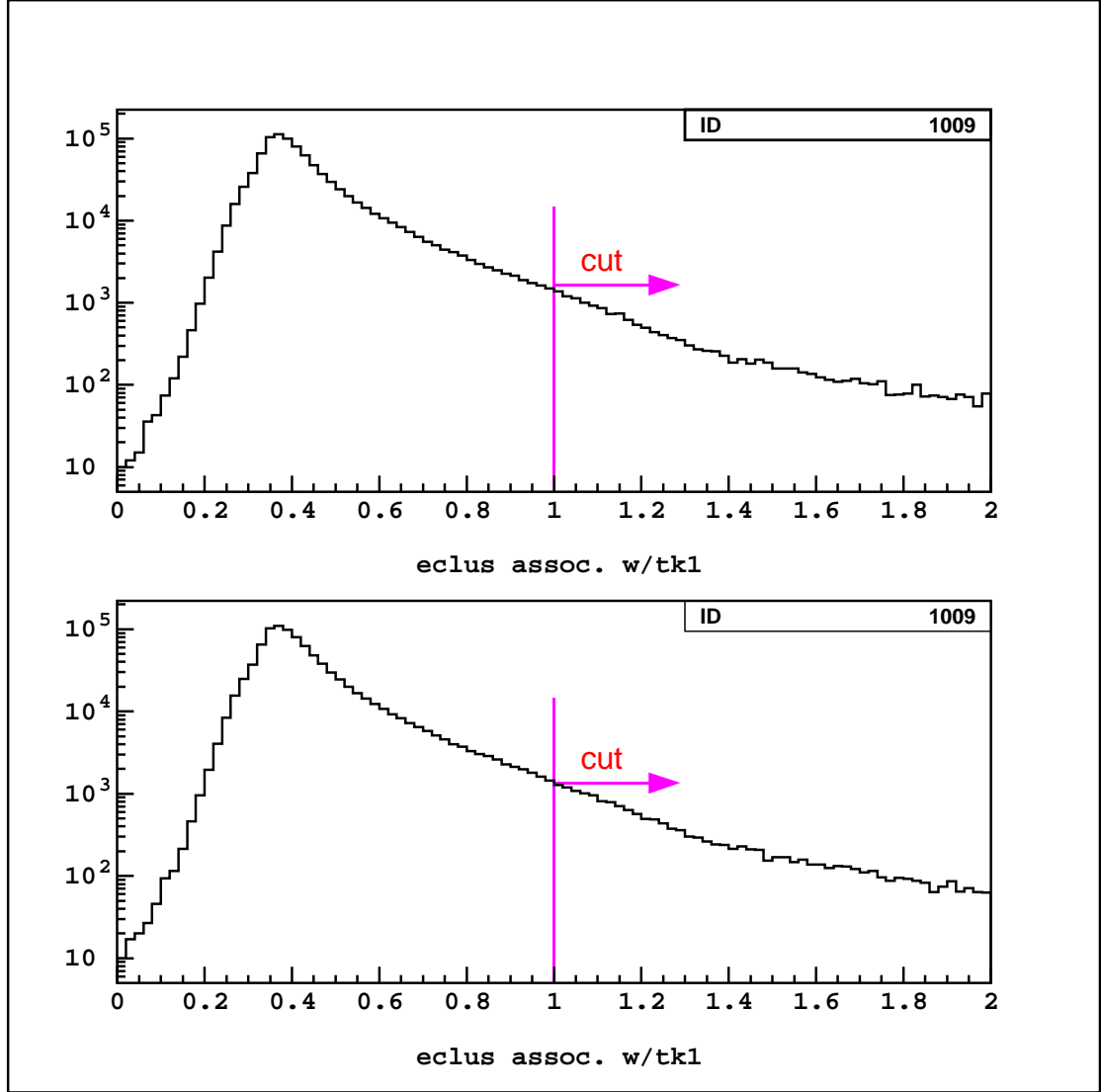


Figure 6.18: Distributions for $E_{cl}(\text{track1})$ in the 1999 $K_L \rightarrow \pi^0 \pi^0 \mu^+ \mu^-$ MC (top) and 1999 $K_L \rightarrow \pi^0 \pi^0 X^0 \rightarrow \pi^0 \pi^0 \mu^+ \mu^-$ MC (bottom) after the requirement on p_T^2 and just before the requirement on $E_{cl}(\text{track})$ was implemented. The requirement on $E_{cl}(\text{track})$ was applied to both clusters associated with tracks.

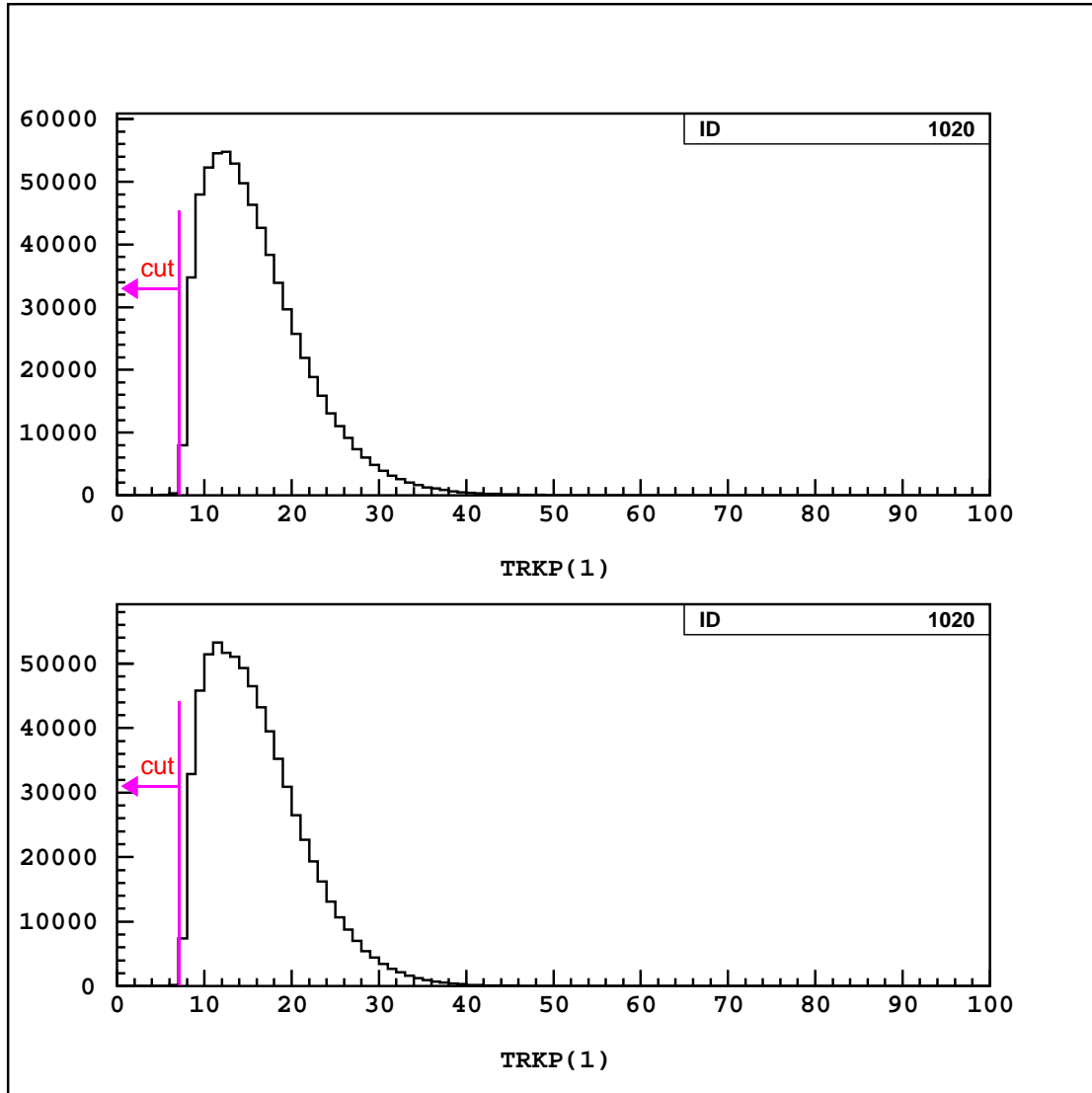


Figure 6.19: Distributions for p_{track1} in the 1997 $K_L \rightarrow \pi^0 \pi^0 \mu^+ \mu^-$ MC (top) and 1997 $K_L \rightarrow \pi^0 \pi^0 X^0 \rightarrow \pi^0 \pi^0 \mu^+ \mu^-$ MC (bottom) after the requirement on $E_{cl}(\text{track})$ and just before the requirement on p_{track} was implemented. The requirement on p_{track} was applied to both tracks.

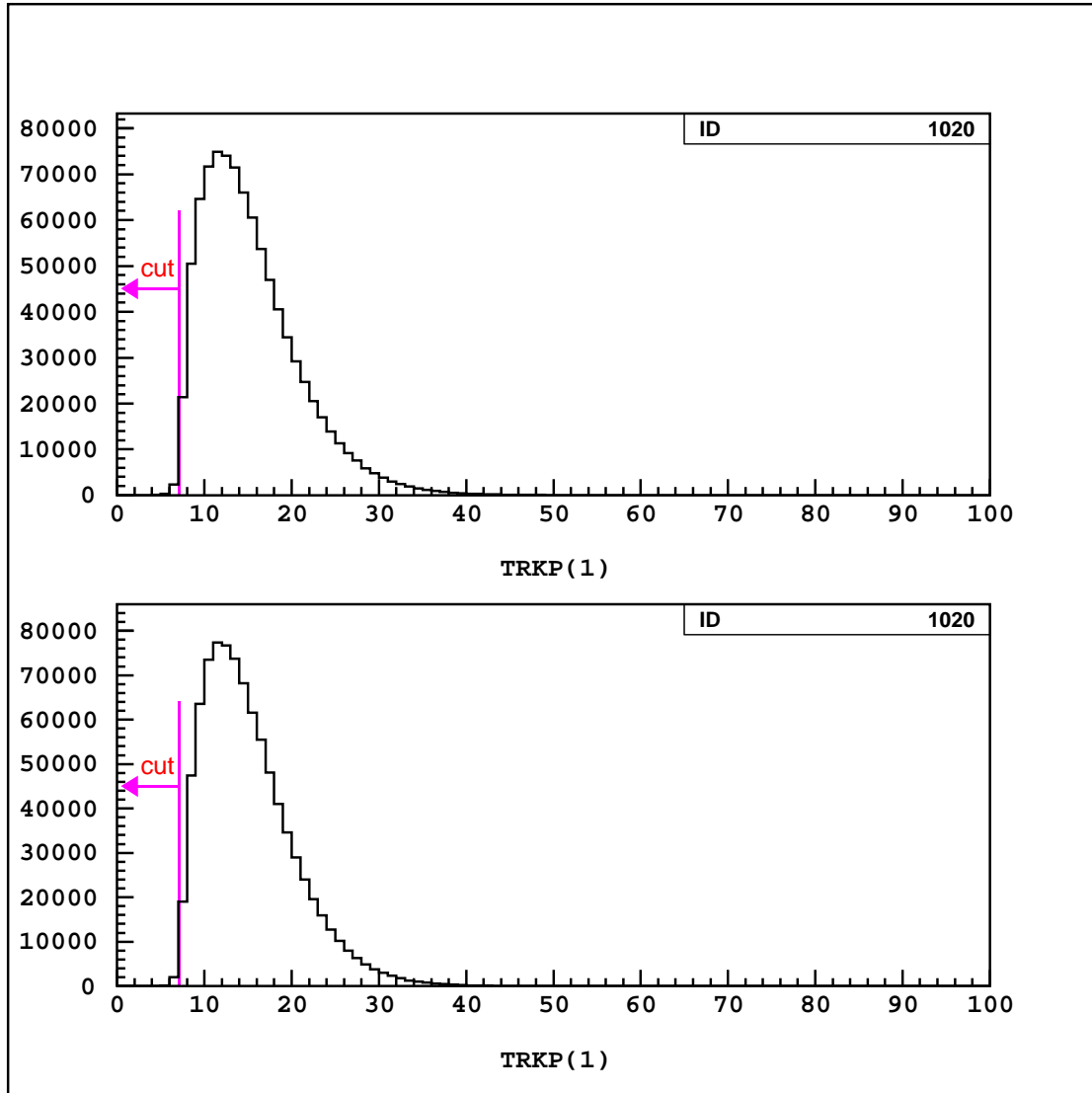


Figure 6.20: Distributions for p_{track1} in the 1999 $K_L \rightarrow \pi^0 \pi^0 \mu^+ \mu^-$ MC (top) and 1999 $K_L \rightarrow \pi^0 \pi^0 X^0 \rightarrow \pi^0 \pi^0 \mu^+ \mu^-$ MC (bottom) after the requirement on $E_{cl}(\text{track})$ and just before the requirement on p_{track} was implemented. The requirement on p_{track} was applied to both tracks.

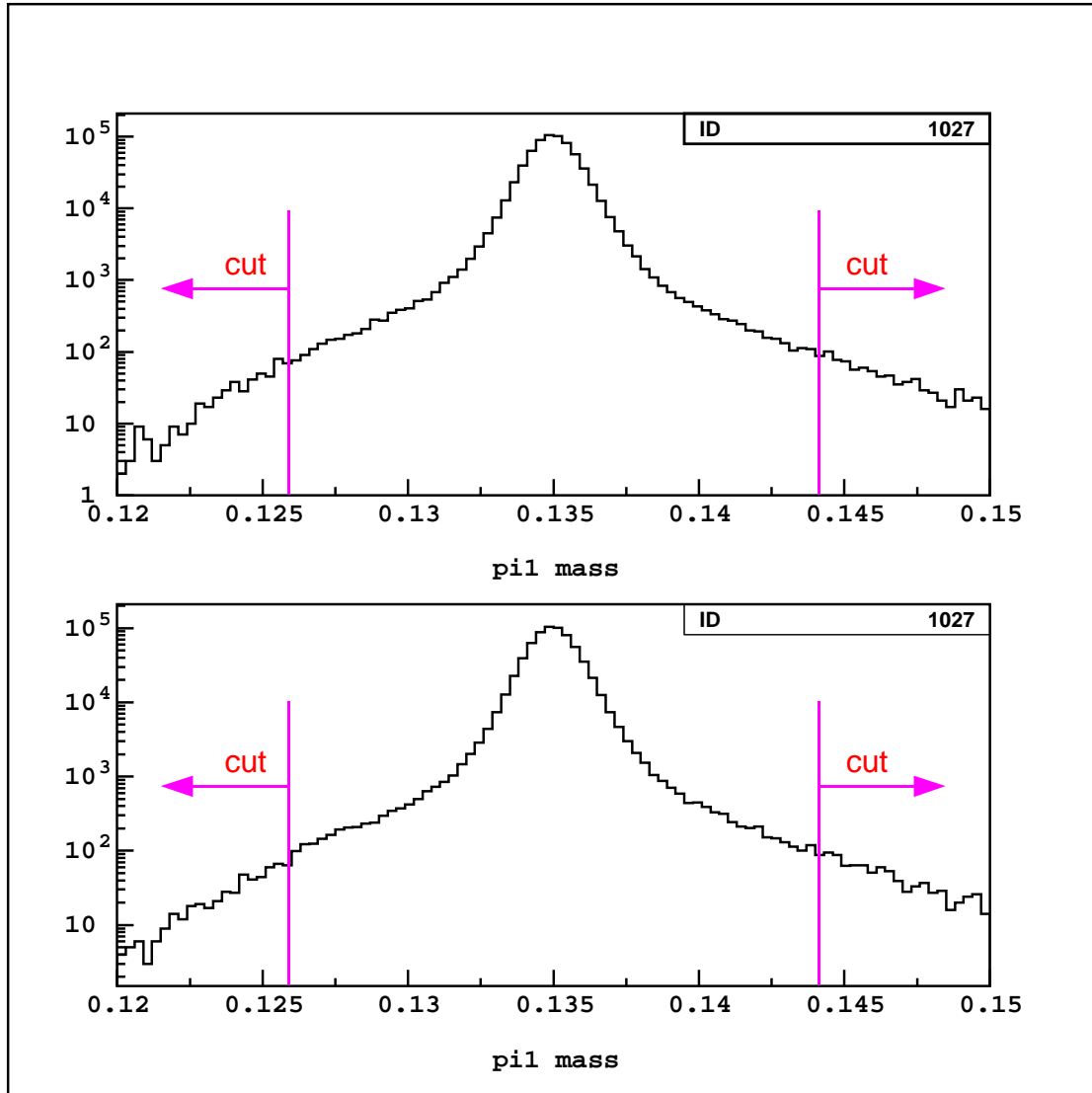


Figure 6.21: Distributions for the first of two reconstructed π^0 masses in the 1997 $K_L \rightarrow \pi^0 \pi^0 \mu^+ \mu^-$ MC (top) and 1997 $K_L \rightarrow \pi^0 \pi^0 X^0 \rightarrow \pi^0 \pi^0 \mu^+ \mu^-$ MC (bottom) after the requirement on p_{track} and just before the requirement on $m_{\gamma\gamma}$ was implemented. The requirement on $m_{\gamma\gamma}$ was applied to both reconstructed π^0 masses.

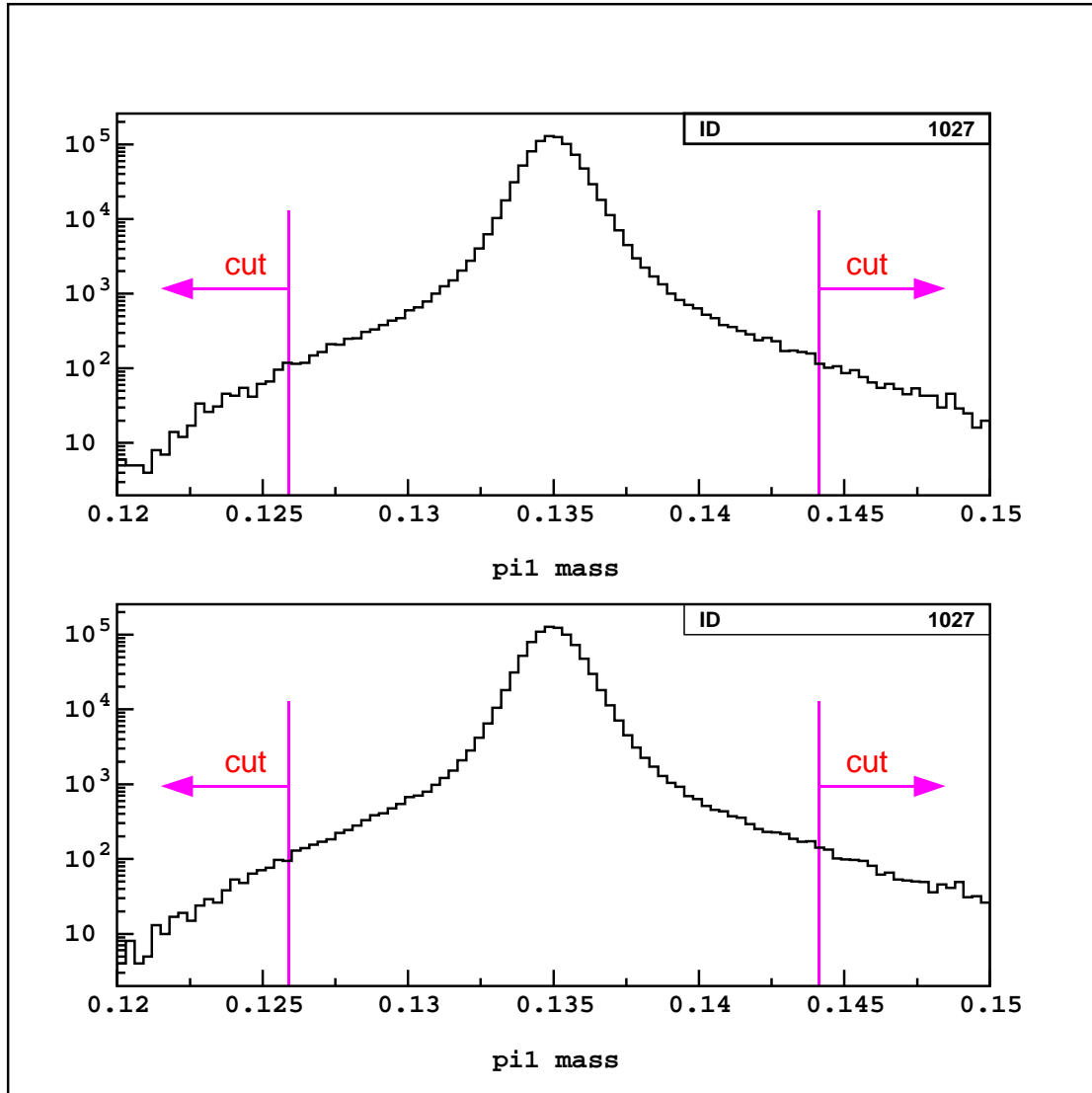


Figure 6.22: Distributions for the first of two reconstructed π^0 masses in the 1999 $K_L \rightarrow \pi^0 \pi^0 \mu^+ \mu^-$ MC (top) and 1999 $K_L \rightarrow \pi^0 \pi^0 X^0 \rightarrow \pi^0 \pi^0 \mu^+ \mu^-$ MC (bottom) after the requirement on p_{track} and just before the requirement on $m_{\gamma\gamma}$ was implemented. The requirement on $m_{\gamma\gamma}$ was applied to both reconstructed π^0 masses.

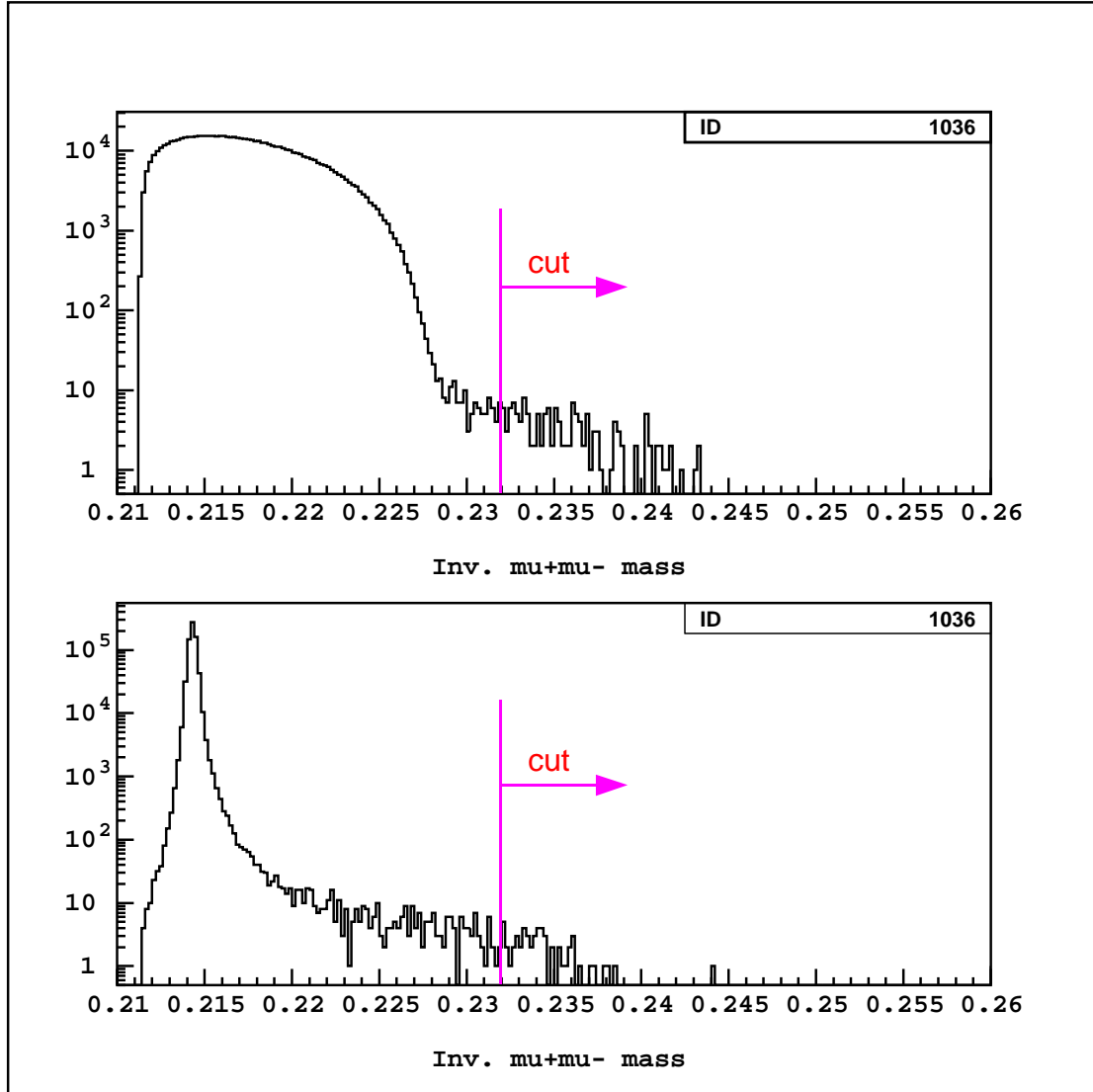


Figure 6.23: Distributions for $m_{\mu\mu}$ in the 1997 $K_L \rightarrow \pi^0\pi^0\mu^+\mu^-$ MC (top) and 1997 $K_L \rightarrow \pi^0\pi^0X^0 \rightarrow \pi^0\pi^0\mu^+\mu^-$ MC (bottom) after the requirement on $m_{\gamma\gamma}$ and just before the requirement on $m_{\mu\mu}$ was implemented.

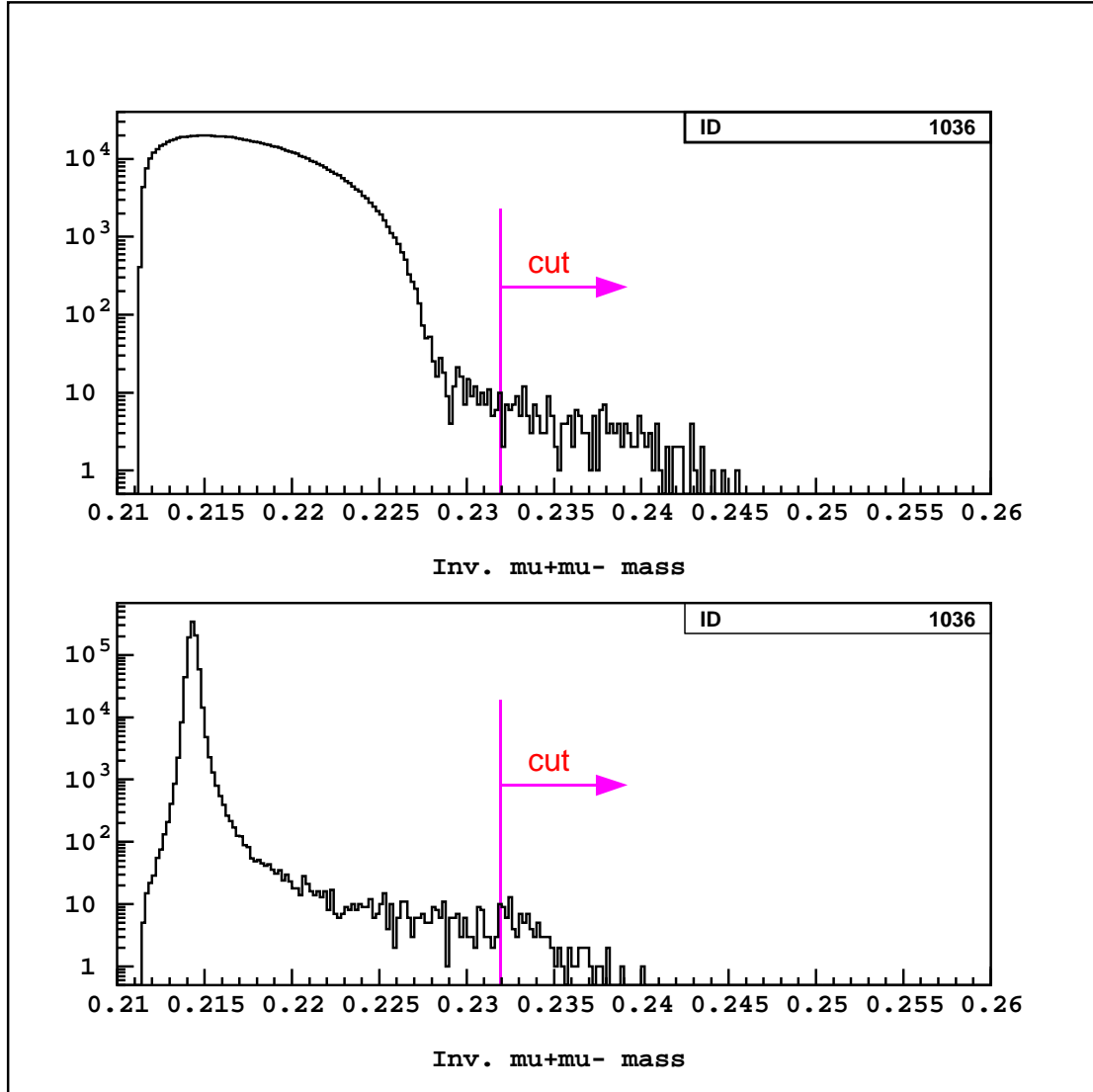


Figure 6.24: Distributions for $m_{\mu\mu}$ in the 1999 $K_L \rightarrow \pi^0\pi^0\mu^+\mu^-$ MC (top) and 1999 $K_L \rightarrow \pi^0\pi^0X^0 \rightarrow \pi^0\pi^0\mu^+\mu^-$ MC (bottom) after the requirement on $m_{\gamma\gamma}$ and just before the requirement on $m_{\mu\mu}$ was implemented.

overlapping accidental photons will increase the value of $m_{\mu\mu\gamma\gamma\gamma}$ beyond the nominal K_L mass and create saturation in the high mass region. This is readily observed in the data (Figure 6.10) and verified in the MC. According to MC studies, the background situated closest to the masked signal region was $K_{\mu 4}$ ($K_L \rightarrow \pi^0 \pi^\pm \mu^\mp \nu_\mu$), which is shown in Figure 6.25. All other backgrounds were located further away from the masked signal region. About 11 billion background MC events were generated and none remained after all previously described signal mode requirements were applied.

6.3.5 Opening the Masked Signal Boxes

After all the previously described analysis requirements had been applied, the masked signal boxes were opened (see Figures 6.26 and 6.27) and no events were found inside of these regions (defined in equations 6.1 through 6.4). Additional requirements (the bounds of masked signal box #1) on $m_{\mu\mu\gamma\gamma\gamma}$ and p_T^2 were made in order to allow for calculation of the acceptance for $K_L \rightarrow \pi^0 \pi^0 \mu^+ \mu^-$. Further requirements (the bounds of masked signal box #2) on $m_{\mu\mu}$ and $|p_{T,\mu\mu}^2 - p_{T,\pi\pi}^2|$ were applied on the $K_L \rightarrow \pi^0 \pi^0 X^0 \rightarrow \pi^0 \pi^0 \mu^+ \mu^-$ MC in order to allow for calculation of the acceptance for $K_L \rightarrow \pi^0 \pi^0 X^0 \rightarrow \pi^0 \pi^0 \mu^+ \mu^-$ (see Tables 6.6 and 6.7). Figure 6.28 shows the p_T^2 vs. $m_{\mu\mu\gamma\gamma\gamma}$ scatter plot for the 1997 $K_L \rightarrow \pi^0 \pi^0 \mu^+ \mu^-$ MC after all analysis requirements. Figure 6.29 displays a scatter plot of the 1997 $K_L \rightarrow \pi^0 \pi^0 X^0 \rightarrow \pi^0 \pi^0 \mu^+ \mu^-$ MC after all analysis requirements have been applied.

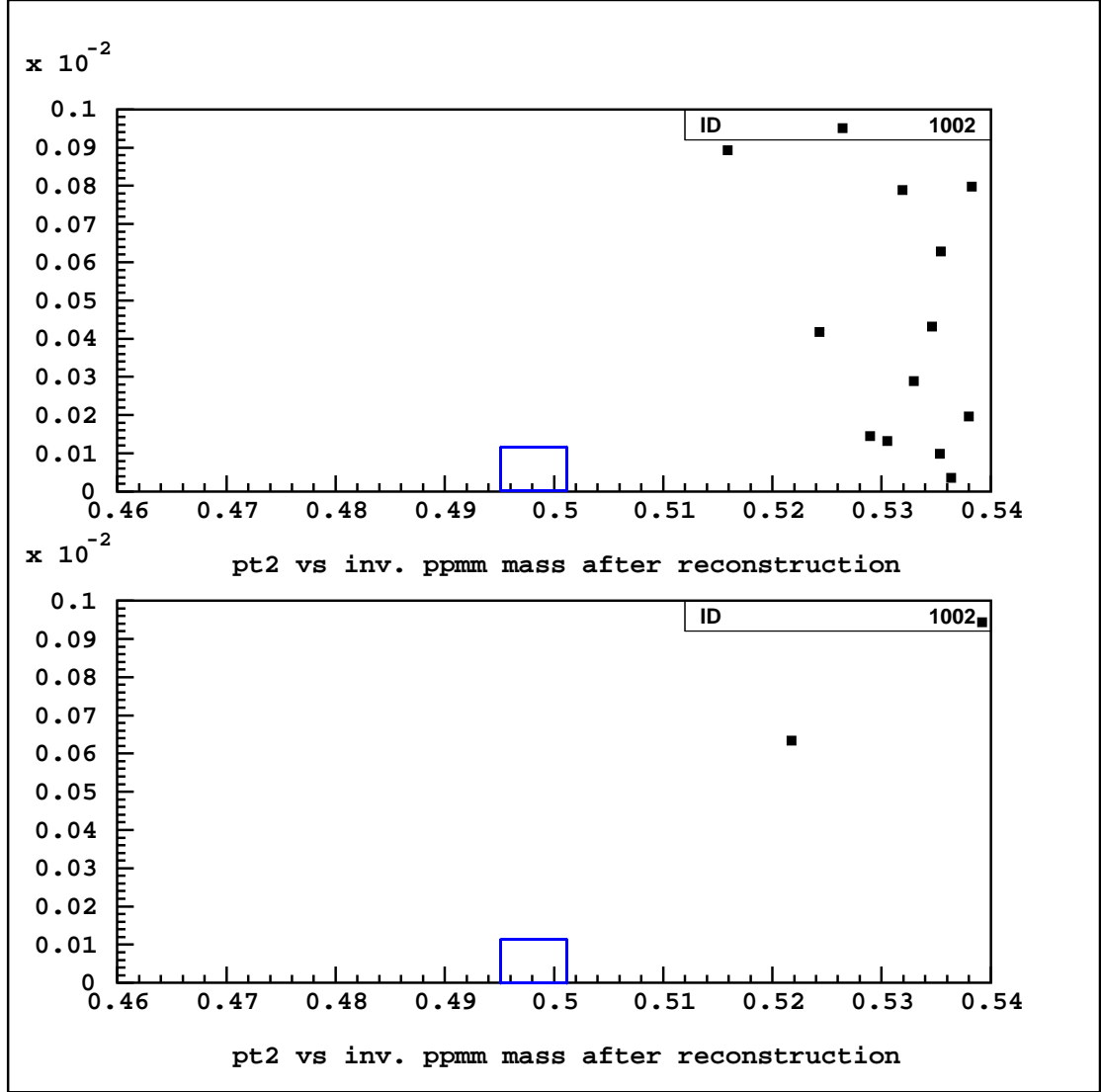


Figure 6.25: p_T^2 vs. $m_{\mu\mu\gamma\gamma\gamma}$ scatter plots for the 1999 $K_{\mu 4}$ background MC sample after all crunch requirements. The top plot is $K_{\mu 4}$ MC when the charged pion decays ($\pi^+ \rightarrow \mu^+ \nu_\mu$, $\pi^- \rightarrow \mu^- \bar{\nu}_\mu$) and the bottom plot is when the charged pion in the $K_{\mu 4}$ MC punches through. The masked signal box is open and is shown for display purposes only.

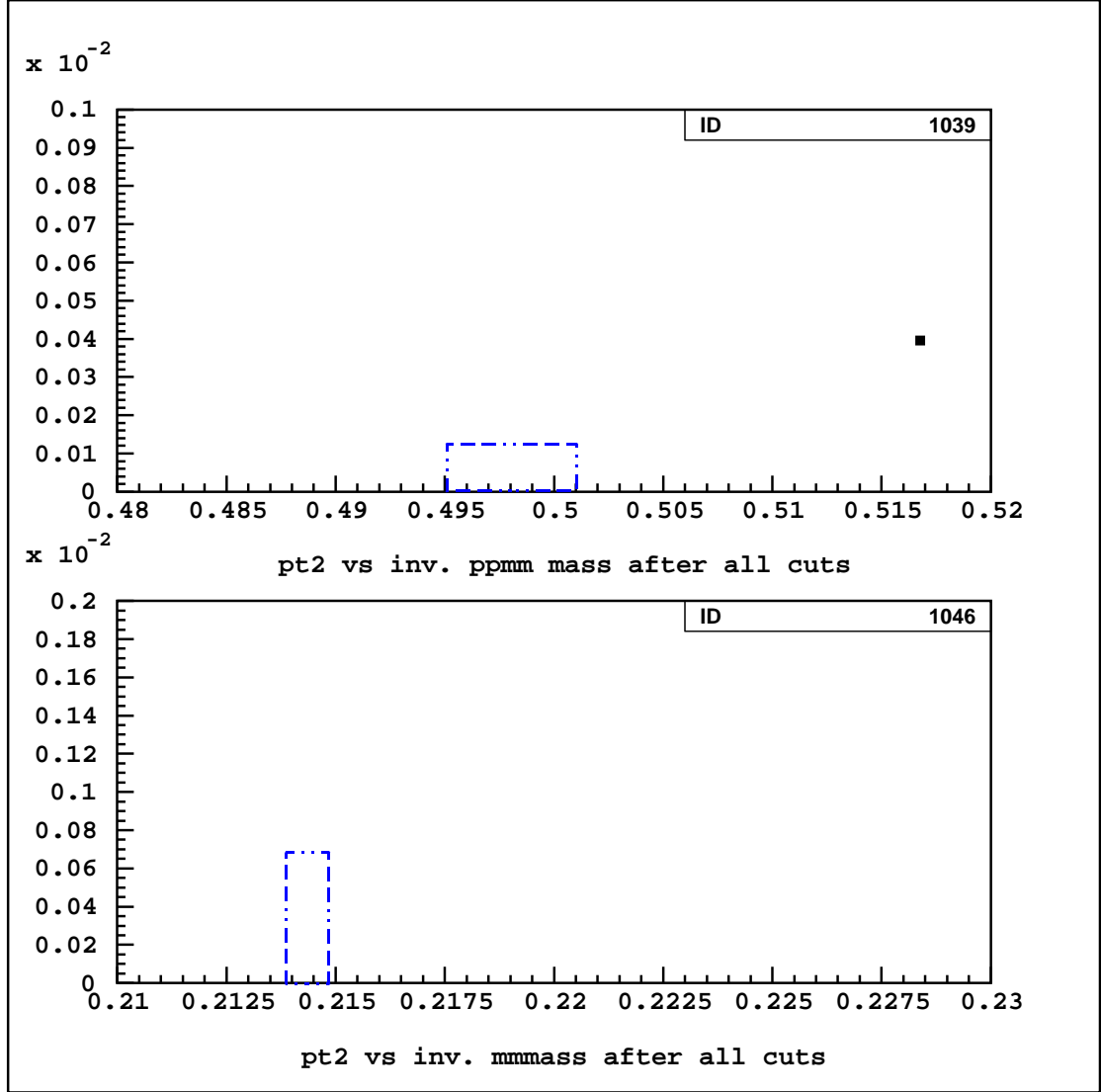


Figure 6.26: p_T^2 vs. $m_{\mu\mu\gamma\gamma\gamma}$ scatter plot for the 1997 data set (top) after masked signal box #1 was opened. $|p_{T,\mu\mu}^2 - p_{T,\pi\pi}^2|$ vs. $m_{\mu\mu}$ scatter plot for the 1997 data set (bottom) after masked signal box #2 was opened. The dotted blue box indicates an opened masked signal box.

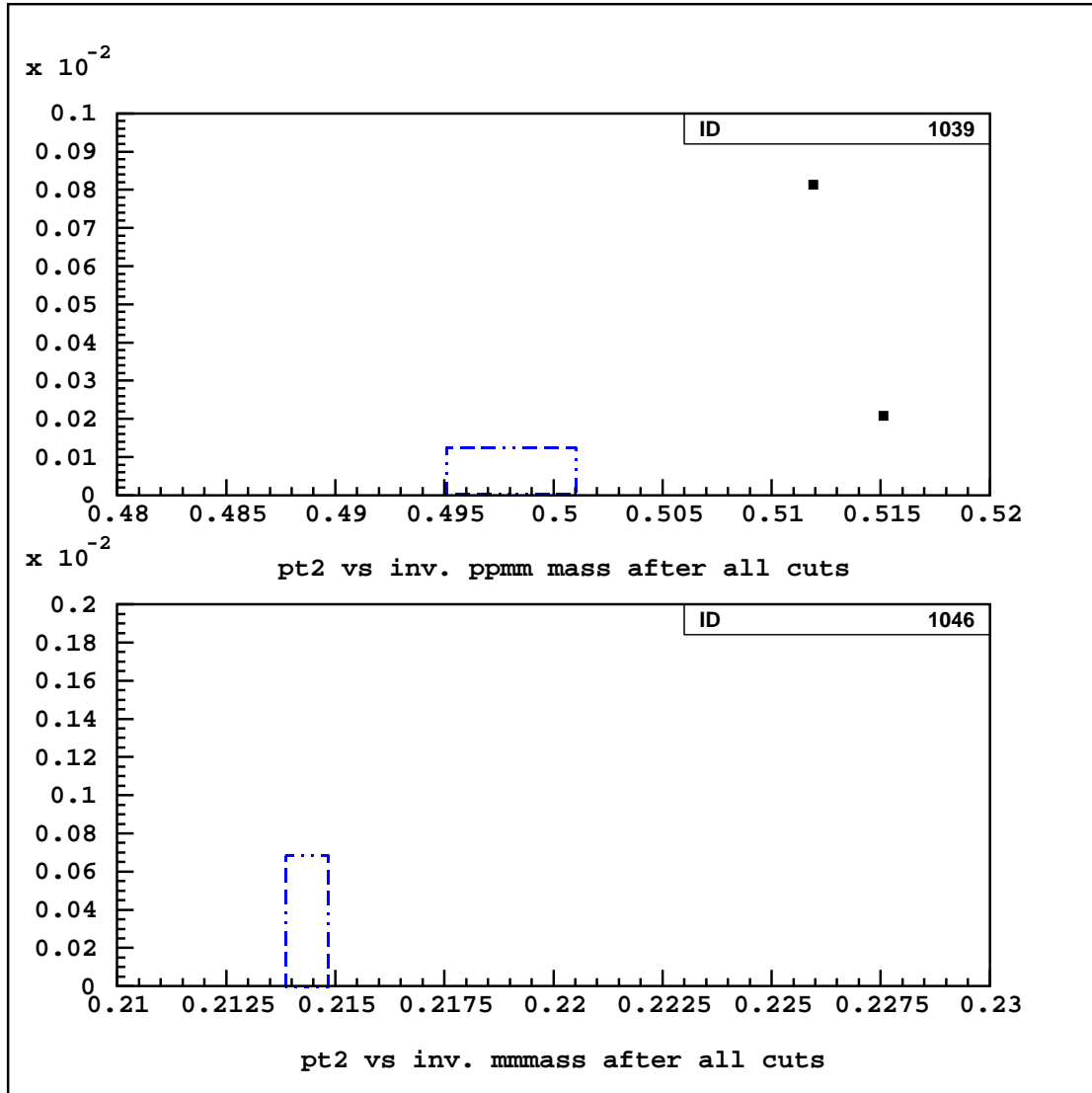


Figure 6.27: p_T^2 vs. $m_{\mu\mu\gamma\gamma\gamma}$ scatter plot for the 1999 data set (top) after masked signal box #1 was opened. $|p_{T,\mu\mu}^2 - p_{T,\pi\pi}^2|$ vs. $m_{\mu\mu}$ scatter plot for the 1999 data set (bottom) after masked signal box #2 was opened. The dotted blue box indicates an opened masked signal box.

Analysis Requirement	A_{MC,γ^*} (1997)	A_{MC,X^0} (1997)
$480.0 \text{ MeV} \leq m_{\mu\mu\gamma\gamma\gamma} \leq 520.0 \text{ MeV}$	0.962	0.966
$p_T^2 \leq 0.001 \text{ GeV}^2$	0.982	0.980
$E_{cl}(\text{track}) \leq 1.0 \text{ GeV}$	0.974	0.974
$p_{track} \geq 7.0 \text{ GeV}$	0.999	0.999
$126.0 \text{ MeV} \leq m_{\gamma\gamma} \leq 144.0 \text{ MeV}$	0.997	0.997
$m_{\mu\mu} \leq 232 \text{ MeV}$	0.999	0.999
$495.0 \text{ MeV} \leq m_{\mu\mu\gamma\gamma\gamma} \leq 501.0 \text{ MeV}$		
$p_T^2 \leq 0.00013 \text{ GeV}^2$	0.901	0.891
$213.8 \text{ MeV} \leq m_{\mu\mu} \leq 214.8 \text{ MeV}$		
$ p_{T,\mu\mu}^2 - p_{T,\pi\pi}^2 \leq 0.0007 \text{ GeV}^2$	—	0.954
Total Acceptance	3.14%	2.80%

Table 6.6: 1997 signal mode analysis requirement summary. A_{MC,γ^*} signifies the acceptance for $K_L \rightarrow \pi^0\pi^0\mu^+\mu^-$ MC, while A_{MC,X^0} represents the acceptance for $K_L \rightarrow \pi^0\pi^0X^0 \rightarrow \pi^0\pi^0\mu^+\mu^-$ MC. Requirements are listed in the order in which they were implemented. Crunch level requirements are included in the calculation of total acceptance.

Analysis Requirement	A_{MC,γ^*} (1999)	A_{MC,X^0} (1999)
$480.0 \text{ MeV} \leq m_{\mu\mu\gamma\gamma\gamma} \leq 520.0 \text{ MeV}$	0.961	0.965
$p_T^2 \leq 0.001 \text{ GeV}^2$	0.984	0.983
$E_{cl}(\text{track}) \leq 1.0 \text{ GeV}$	0.966	0.965
$p_{track} \geq 7.0 \text{ GeV}$	0.994	0.995
$126.0 \text{ MeV} \leq m_{\gamma\gamma} \leq 144.0 \text{ MeV}$	0.997	0.997
$m_{\mu\mu} \leq 232 \text{ MeV}$	0.999	0.999
$495.0 \text{ MeV} \leq m_{\mu\mu\gamma\gamma\gamma} \leq 501.0 \text{ MeV}$		
$p_T^2 \leq 0.00013 \text{ GeV}^2$	0.906	0.902
$213.8 \text{ MeV} \leq m_{\mu\mu} \leq 214.8 \text{ MeV}$		
$ p_{T,\mu\mu}^2 - p_{T,\pi\pi}^2 \leq 0.0007 \text{ GeV}^2$	—	0.954
Total Acceptance	4.03%	3.74%

Table 6.7: 1999 signal mode analysis requirement summary. A_{MC,γ^*} signifies the acceptance for $K_L \rightarrow \pi^0\pi^0\mu^+\mu^-$ MC, while A_{MC,X^0} represents the acceptance for $K_L \rightarrow \pi^0\pi^0X^0 \rightarrow \pi^0\pi^0\mu^+\mu^-$ MC. Requirements are listed in the order in which they were implemented. Crunch level requirements are included in the calculation of total acceptance.

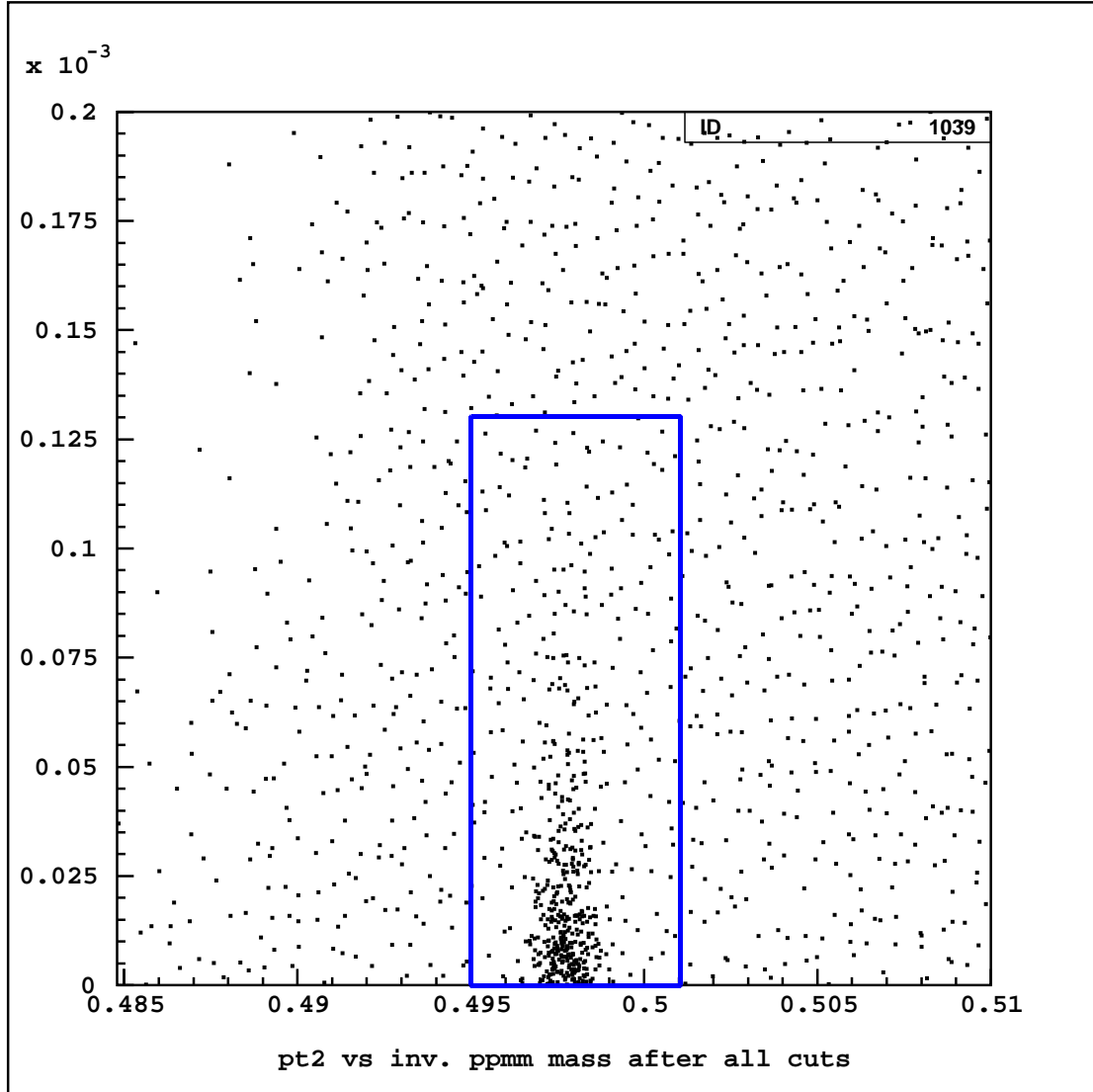


Figure 6.28: p_T^2 vs. $m_{\mu\mu\gamma\gamma\gamma}$ scatter plot for the 1997 $K_L \rightarrow \pi^0\pi^0\mu^+\mu^-$ MC after all analysis requirements were implemented. The blue box indicates the location of masked signal box #1, which is open in the MC.

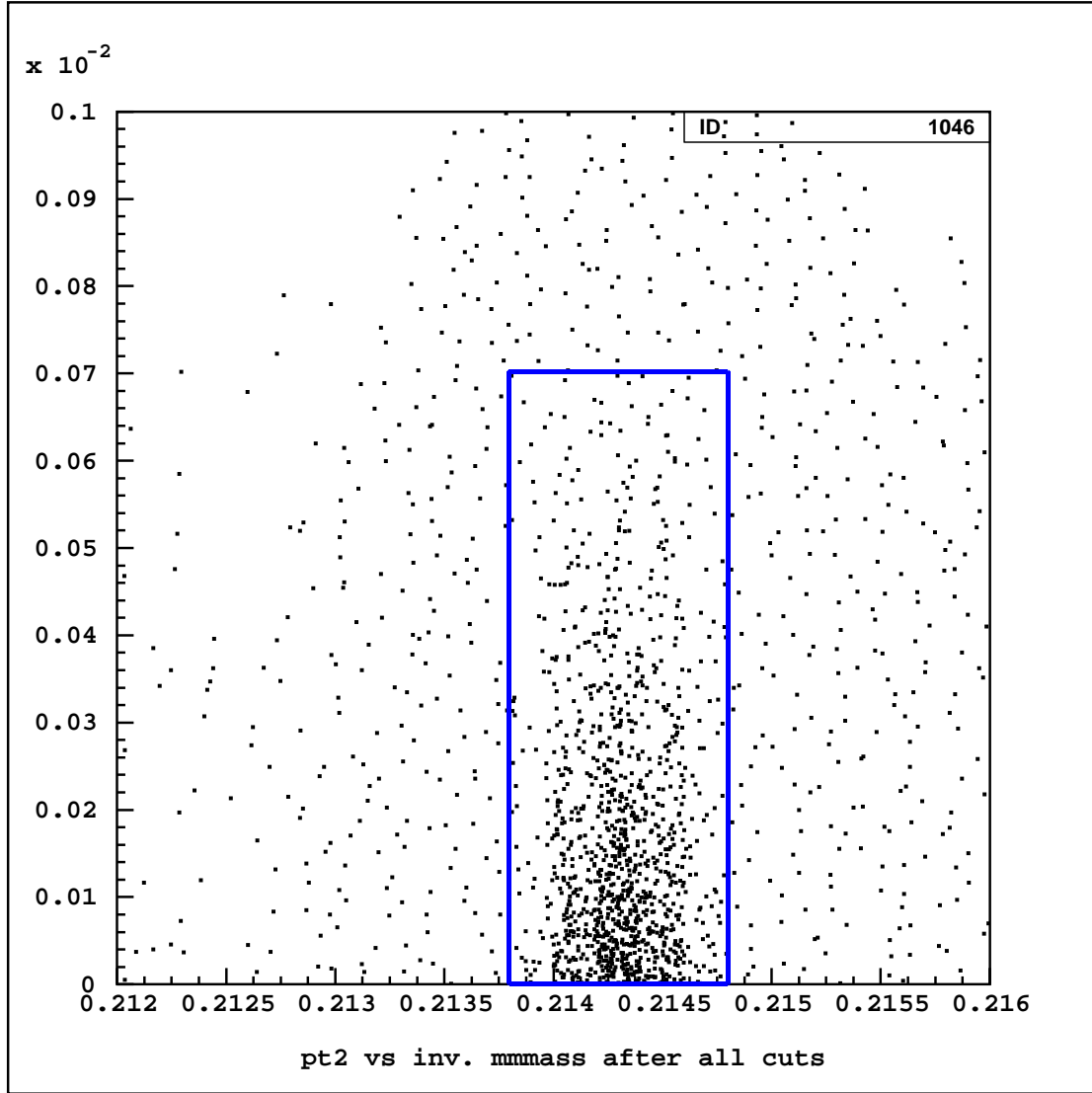


Figure 6.29: $|p_{T,\mu\mu}^2 - p_{T,\pi\pi}^2|$ vs. $m_{\mu\mu}$ scatter plot for the 1997 $K_L \rightarrow \pi^0 \pi^0 X^0 \rightarrow \pi^0 \pi^0 \mu^+ \mu^-$ MC after all analysis requirements were applied. The blue box indicates the location of masked signal box #2, which is open in the MC.

6.4 Normalization Mode Analysis

The normalization mode analysis is performed in order to provide a measurement of the K_L flux, which is defined as the number of K_L 's that decayed in the vacuum region during a data run. In order to normalize the measurement of the branching ratio of the signal mode, a K_L decay channel with a large branching ratio and a topology similar to the signal mode must be chosen. The best bet in the K_L sector to serve these purposes is the $K_L \rightarrow \pi^0 \pi^0 \pi_D^0$ decay mode, which is described in section 5.2.2.

6.4.1 Normalization Mode Analysis Requirements

The only significant background to the normalization mode is when a photon from $K_L \rightarrow \pi^0 \pi^0 \pi^0$ undergoes pair production in the vacuum window or detector material upstream of DC1. The probability of this conversion was found to be about 0.24% in the 1997 run and 0.22% in the 1999 run [39]. Isolating the normalization mode signal and sweeping away the photon conversion background required only very loose cuts on the normalization mode invariant mass ($m_{ee\gamma\gamma\gamma\gamma}$), p_T^2 and $m_{\gamma\gamma}$. As described in section 4.3.2, the four normalization mode photons which give the lowest pairing chi squared will be associated with the π^0 pair. The remaining photon is therefore associated with the π_D^0 state and paired with the dielectron. Figures 6.30 through 6.35 show distributions for $m_{ee\gamma\gamma\gamma\gamma}$, p_T^2 and $m_{\gamma\gamma}$. A requirement on the neutral z vertex (Z_{vtx}) was applied in an effort to extract a cleaner signal. Upon inspection of

Analysis Requirement	A_{Data} (1997)	A_{Data} (1999)
$473.0 \text{ MeV} \leq m_{ee\gamma\gamma\gamma\gamma} \leq 523.0 \text{ MeV}$	0.471	0.494
$p_T^2 \leq 0.001 \text{ GeV}^2$	0.259	0.325
$121.0 \text{ MeV} \leq m_{\gamma\gamma} \leq 149.0 \text{ MeV}$	0.992	0.993
$94.0 \text{ m} \leq Z_{vtx} \leq 158.0 \text{ m}$	0.987	0.986
Accepted Data Events	131526	363531

Table 6.8: Normalization mode analysis requirement summary for the 1997 and 1999 data sets. Requirements are listed in the order in which they were implemented.

Figures 6.36 and 6.37, there is some disagreement between data and MC in the outer regions of the neutral z vertex. At opposite ends of the vacuum region are the final sweeper magnet (extending from $z = 90 \text{ m}$ to $z = 93 \text{ m}$) and the vacuum window (at $z = 159 \text{ m}$). The vacuum window is a source of photon conversions, while the final sweeper magnet will have a noticeable effect on the trajectories of electrons from the pion dalitz decay. As a result, this analysis requires that the neutral z vertex be restricted to a range spanning 94 m to 158 m from the target.

After generating roughly 250 million $K_L \rightarrow \pi^0\pi^0\pi^0$ MC events in which one of the photons is allowed to undergo photon conversion (just under two fluxes), only one $K_L \rightarrow \pi^0\pi^0\pi^0$ MC event was found after all analysis requirements were implemented. This is negligible compared to the number of events in data remaining after all analysis requirements were applied (see Table 6.8). As a result, backgrounds in the normalization mode are unworrisome, since standard subtraction of background procedures will only have a negligible effect on the final K_L flux. Table 6.9 shows the normalization mode analysis requirement summary for the $K_L \rightarrow \pi^0\pi^0\pi_D^0$ MC.

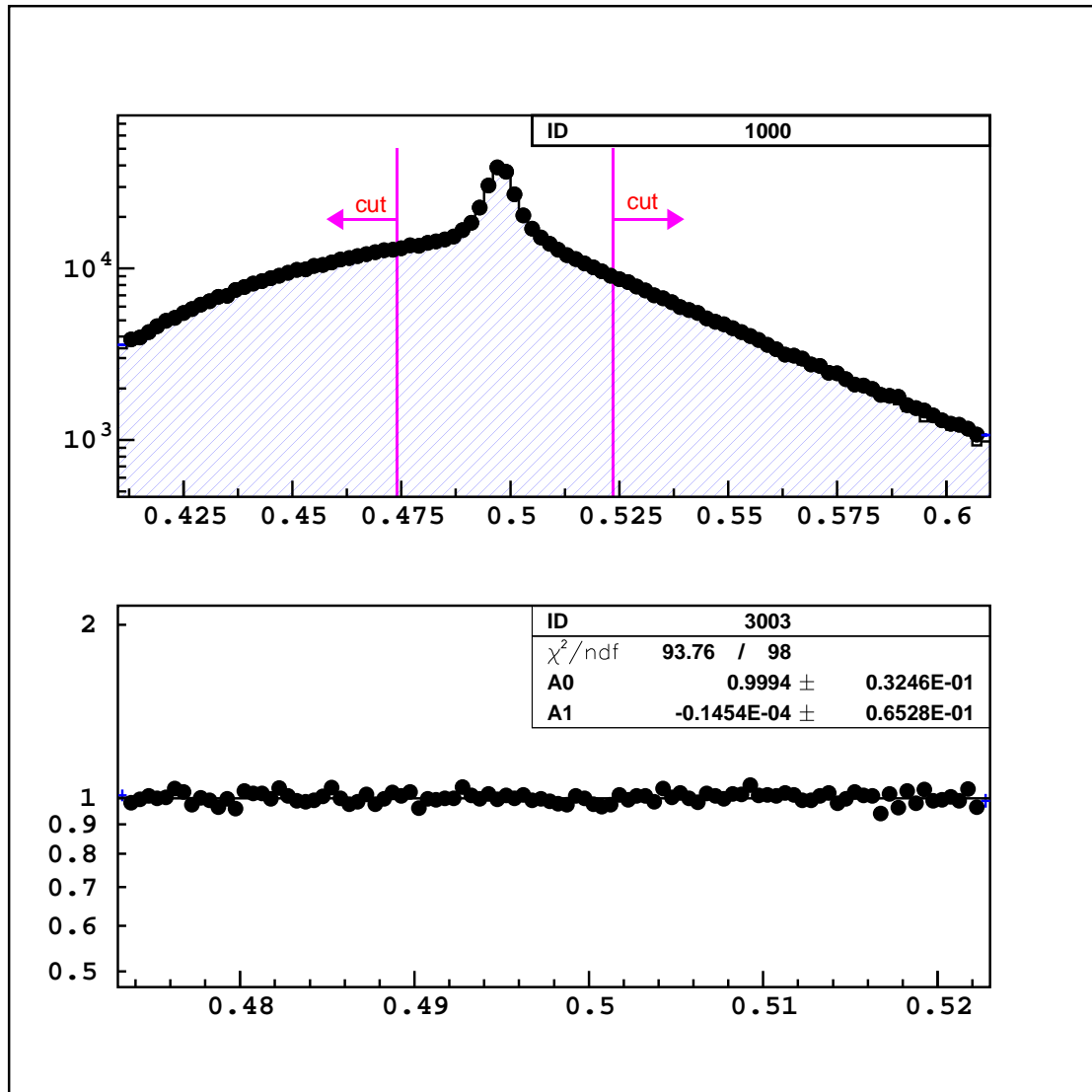


Figure 6.30: 1997 $m_{ee\gamma\gamma\gamma\gamma}$ data/MC overlay just before requirement on this variable (top) and data/MC ratio immediately after the requirement had been implemented (bottom). Dots are data and histogram is MC. Normalization mode requirements are indicated in magenta.

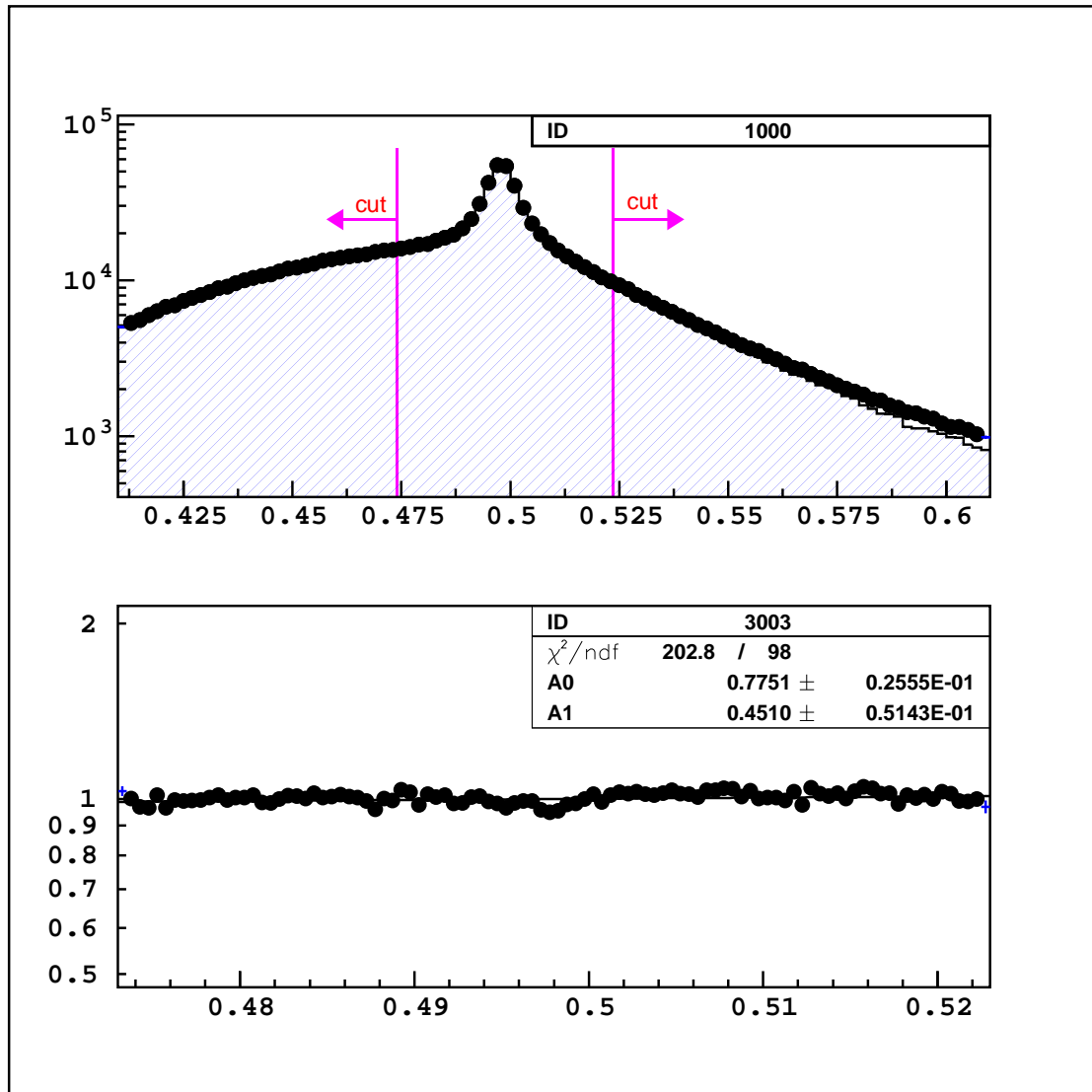


Figure 6.31: 1999 $m_{ee\gamma\gamma\gamma\gamma}$ data/MC overlay just before requirement on this variable (top) and data/MC ratio immediately after the requirement had been implemented (bottom). Dots are data and histogram is MC.

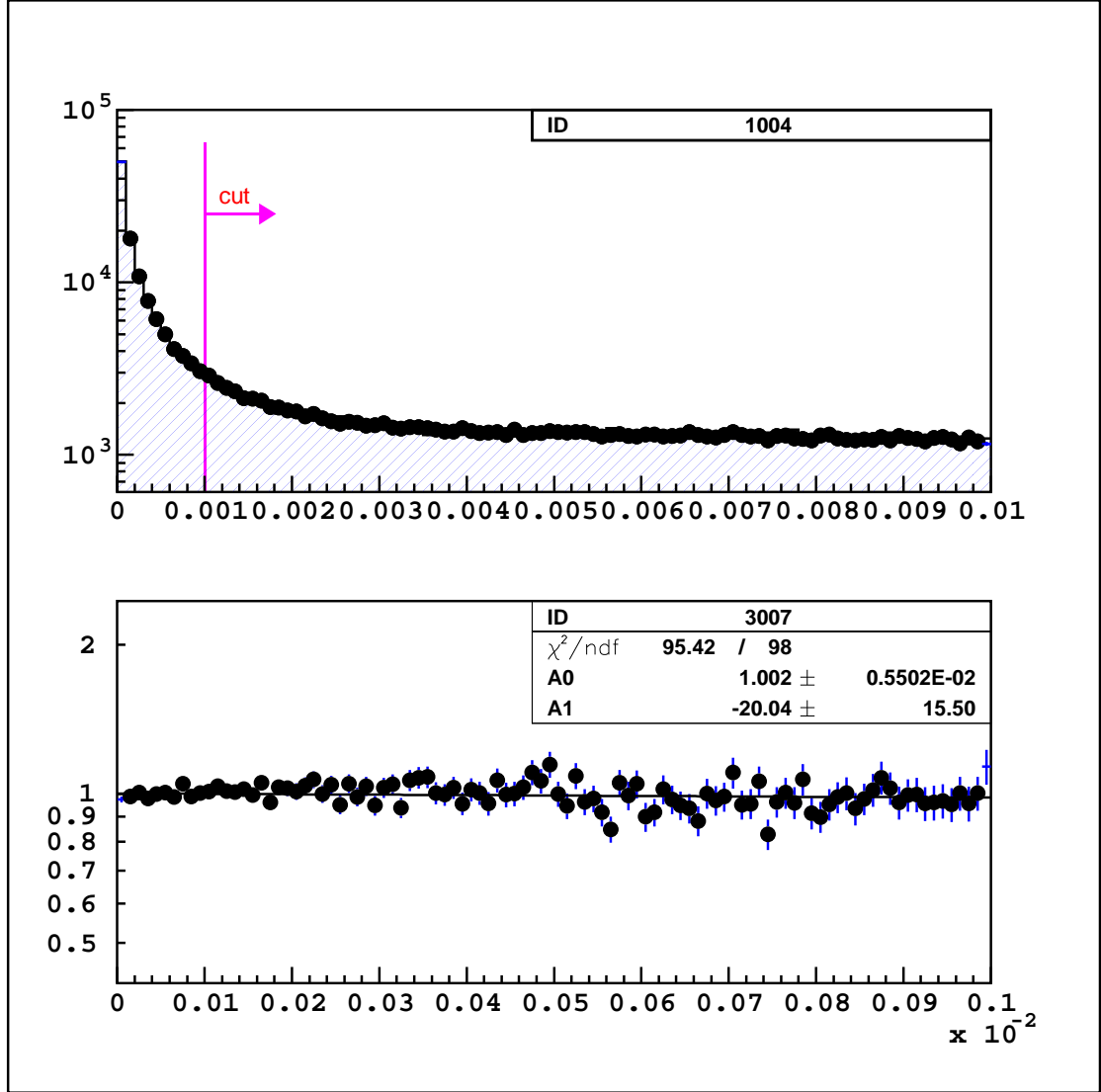


Figure 6.32: 1997 p_T^2 data/MC overlay just before requirement on this variable (top) and data/MC ratio after all analysis requirements were implemented (bottom). Dots are data and histogram is MC.

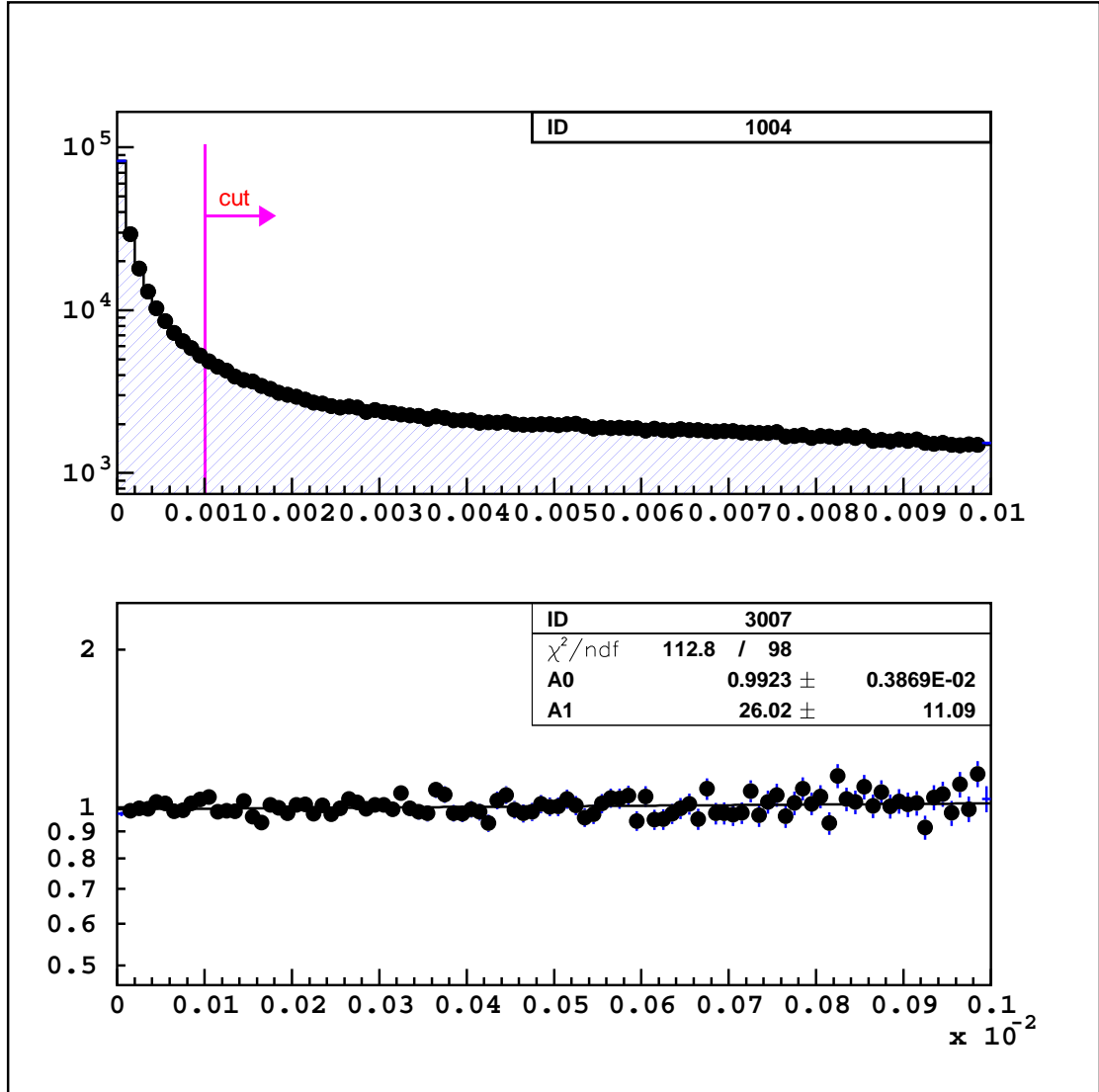


Figure 6.33: 1999 p_T^2 data/MC overlay just before requirement on this variable (top) and data/MC ratio after all analysis requirements were implemented (bottom). Dots are data and histogram is MC.

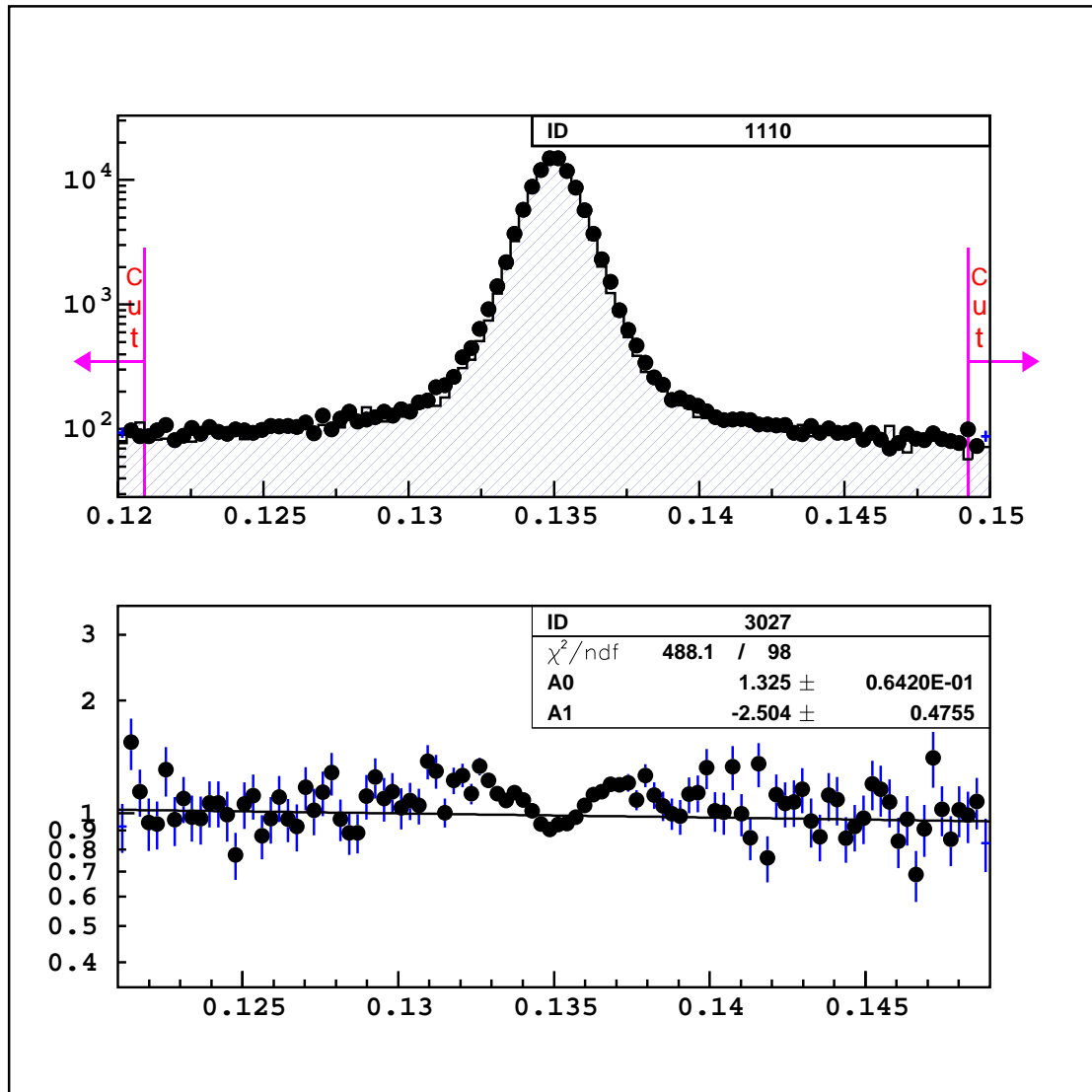


Figure 6.34: 1997 $m_{\gamma\gamma}$ data/MC overlay for one of two reconstructed π^0 's just before requirement on this variable (top) and data/MC ratio after all analysis requirements were implemented (bottom). Dots are data and histogram is MC.

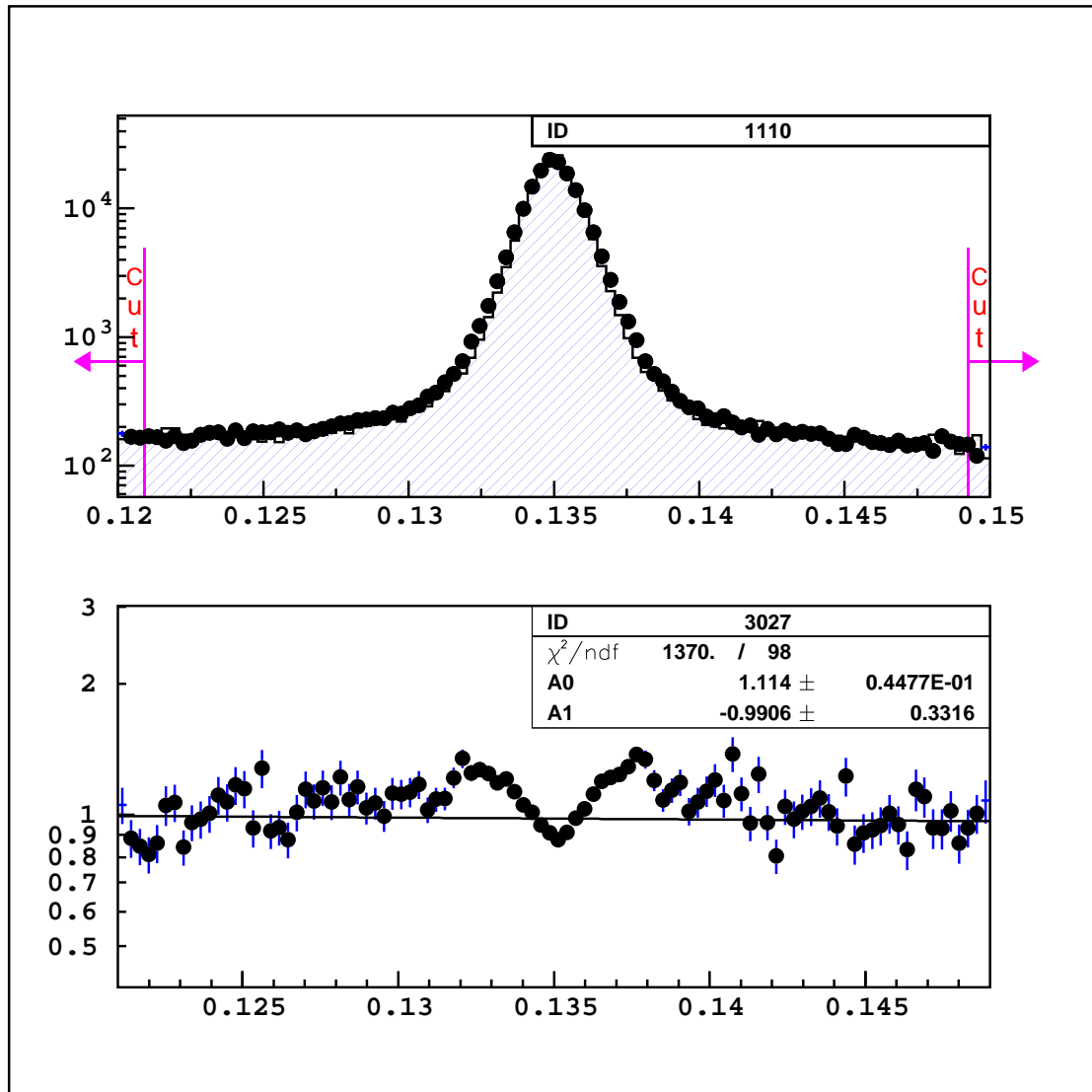


Figure 6.35: 1999 $m_{\gamma\gamma}$ data/MC overlay for one of two reconstructed π^0 's just before requirement on this variable (top) and data/MC ratio after all analysis requirements were implemented (bottom). Dots are data and histogram is MC.

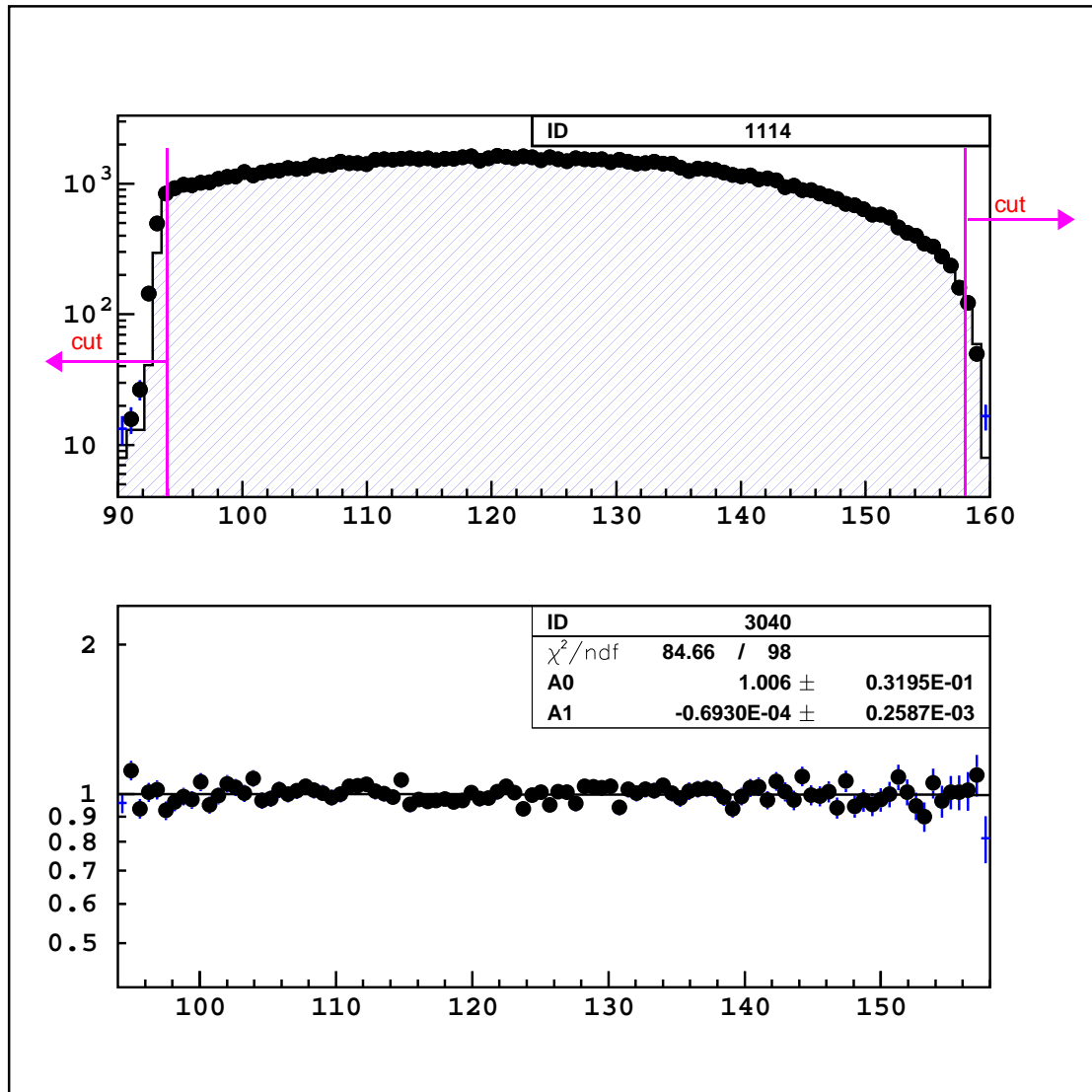


Figure 6.36: 1997 Z_{vtx} data/MC overlay just before requirement on this variable (top) and data/MC ratio after all analysis requirements were implemented (bottom). Dots are data and histogram is MC.

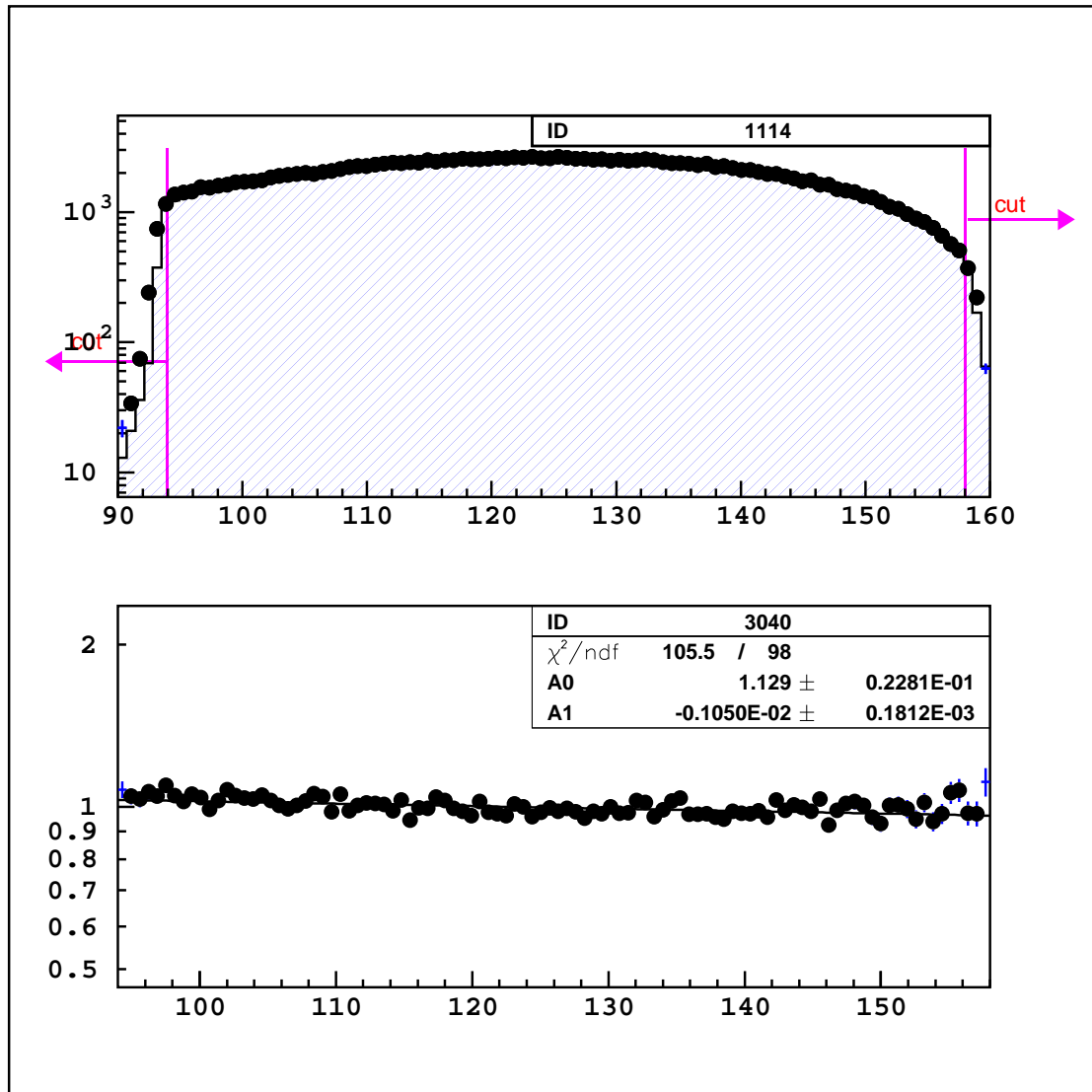


Figure 6.37: 1999 Z_{vtx} data/MC overlay just before requirement on this variable (top) and data/MC ratio after all analysis requirements were implemented (bottom). Dots are data and histogram is MC.

Analysis Requirement	A_{MC} (1997)	A_{MC} (1999)
$473.0 \text{ MeV} \leq m_{ee\gamma\gamma\gamma\gamma} \leq 523.0 \text{ MeV}$	0.477	0.504
$p_T^2 \leq 0.001 \text{ GeV}^2$	0.255	0.323
$121.0 \text{ MeV} \leq m_{\gamma\gamma} \leq 149.0 \text{ MeV}$	0.992	0.993
$94.0 \text{ m} \leq Z_{vtx} \leq 158.0 \text{ m}$	0.990	0.990
Total Acceptance	$(5.94 \times 10^{-3})\%$	$(1.29 \times 10^{-2})\%$

Table 6.9: Normalization mode analysis requirement summary for the 1997 and 1999 $K_L \rightarrow \pi^0\pi^0\pi_D^0$ MC. Requirements are listed in the order in which they were implemented. Total acceptance is calculated by including all crunch and analysis requirements.

6.4.2 K_L Flux Calculation

Tables 6.8 and 6.9 show the total number of accepted normalization mode events left in data and MC after all normalization mode analysis requirements. Combining these numbers with the number of generated normalization mode events in MC and $BR(K_L \rightarrow \pi^0\pi^0\pi_D^0)$ gives one all the information needed to calculate the K_L flux, F_K , via the following formula:

$$N_{Data} = F_K \cdot BR(K_L \rightarrow \pi^0\pi^0\pi_D^0) \cdot A_{MC}. \quad (6.5)$$

N_{Data} is the number of normalization mode events left in data after all normalization mode analysis requirements have been applied. A_{MC} is the acceptance for the normalization mode MC, which is defined as the number of normalization mode MC events left after all normalization mode analysis requirements divided by the number of generated normalization mode MC events (given in Table 5.4). $BR(K_L \rightarrow \pi^0\pi^0\pi_D^0)$ is the branching ratio for $K_L \rightarrow \pi^0\pi^0\pi_D^0$, which is given in equation 5.10. Applying

equation 6.5 yields the following K_L fluxes for the 1997 and 1999 data sets respectively

$$F_{K,1997} = 3.23 \times 10^{11} \quad (6.6)$$

$$F_{K,1999} = 4.10 \times 10^{11}. \quad (6.7)$$

6.5 Uncertainties in the Flux

This section shall describe the uncertainties in the K_L flux. These uncertainties can originate from the branching ratio employed to calculate the flux, the statistical error, uncertainty of analysis requirements, the p_z resolution and the efficiency of the muon ID system. An important note to consider is that there are no systematic errors on the signal modes, since no events were found in the signal regions after the masked signal boxes were opened and since no background events were predicted to be in the signal regions by the MC. Therefore, all systematic errors in this analysis come from the normalization mode.

6.5.1 Branching Ratio of $K_L \rightarrow \pi^0 \pi^0 \pi^0$

$BR(K_L \rightarrow \pi^0 \pi^0 \pi_D^0)$ was employed to calculate the K_L flux. However, $BR(K_L \rightarrow \pi^0 \pi^0 \pi_D^0)$ is a function of $BR(K_L \rightarrow \pi^0 \pi^0 \pi^0)$. The value used for $BR(K_L \rightarrow \pi^0 \pi^0 \pi^0)$ was $(19.52 \pm 0.12)\%$ [45], which yields an error of 0.61%.

6.5.2 Statistical Errors

In the 1997 $K_L \rightarrow \pi^0 \pi^0 \mu^+ \mu^-$ signal mode MC, 627792 events were accepted out of 19988353 generated events, which gave a statistical error on the acceptance of 0.13%. Only 581954 events were accepted out of 20771253 generated events in the 1997 $K_L \rightarrow \pi^0 \pi^0 X^0 \rightarrow \pi^0 \pi^0 \mu^+ \mu^-$ signal mode MC, which yielded a statistical error of 0.13%. For the 1999 signal mode MC, 803989 $K_L \rightarrow \pi^0 \pi^0 \mu^+ \mu^-$ events were accepted (out of 19943625 events generated) and 758136 $K_L \rightarrow \pi^0 \pi^0 X^0 \rightarrow \pi^0 \pi^0 \mu^+ \mu^-$ events were accepted (out of 20290564 events generated), which gave a statistical error of 0.11% in both cases. In regards to the normalization mode, 109532 events were accepted out of 1842926908 generated events using the 1997 MC. This leads to a statistical error of 0.30%. Using the 1999 MC, 183131 normalization mode events were accepted out of 1414181218 generated events, which yields a statistical error on the acceptance of 0.23%. For the 1997 2E-NCLUS data set, 131526 events were accepted which yields a statistical error of 0.28%. In regards to the 1999 2E-NCLUS data set, only 363531 events were accepted which gives a statistical error of 0.16%. These results are summarized in Table 6.10.

6.5.3 Variation of Analysis Requirements

Once again, all systematic errors in this analysis stem from the normalization mode. Any normalization mode crunch or analysis requirement generates systematic errors due to uncertainties in where to set the crunch or analysis requirements.

Decay Mode	N_{events} Accepted	Statistical Error
MC:		
1997 $K_L \rightarrow \pi^0 \pi^0 \mu^+ \mu^-$	627792	0.13%
1997 $K_L \rightarrow \pi^0 \pi^0 X^0 \rightarrow \pi^0 \pi^0 \mu^+ \mu^-$	581954	0.13%
1999 $K_L \rightarrow \pi^0 \pi^0 \mu^+ \mu^-$	803989	0.11%
1999 $K_L \rightarrow \pi^0 \pi^0 X^0 \rightarrow \pi^0 \pi^0 \mu^+ \mu^-$	758136	0.11%
1997 $K_L \rightarrow \pi^0 \pi^0 \pi_D^0$	109532	0.30%
1999 $K_L \rightarrow \pi^0 \pi^0 \pi_D^0$	183131	0.23%
Data:		
1997 2E-NCLUS Data Set	131526	0.28%
1999 2E-NCLUS Data Set	363531	0.16%

Table 6.10: Summary of statistical errors on the signal and normalization mode acceptances.

The requirements on $m_{ee\gamma\gamma\gamma\gamma}$, p_T^2 , $m_{\gamma\gamma}$, Z_{vtx} and $E_{cl}(\text{track})/p_{track}$ were all varied to determine the variation in the flux due to the choice of requirements on these quantities. The formula employed to calculate the systematic error on the flux from these variations is given below. The results are tabulated in Table 6.11.

$$\Delta F_K = \frac{N_{Data} \pm \Delta N_{Data}}{A_{MC} \pm \Delta A_{MC}} - F_K \quad (6.8)$$

N_{Data} is the number of normalization mode events left in data after all normalization mode analysis requirements have been applied. A_{MC} is the acceptance for the normalization mode MC, which is defined as the number of normalization mode MC events left after all normalization mode analysis requirements divided by the number of generated normalization mode MC events (given in Table 5.4). Formula 6.8 was also used to calculate the systematic error on the flux for the 1999 p_z distribution and the muon ID system efficiency, which are described in the next two sections. All

variation of requirements were chosen so that the number of data events varied by less than $\pm 10\%$.

6.5.4 1999 p_z Distribution

A noticeable discrepancy between the data and the MC exists in the 1999 distribution of the total z momentum, p_z , while no discrepancy can be seen in the 1997 p_z distribution (see Figure 6.38). The discrepancy is seen as a significantly non-zero slope in the data/MC ratio (see Figure 6.39). In order to flatten the distribution, a set of weights were applied to the 1999 p_z MC events (see Figure 6.40). After reanalysis using these weights, the variation of the flux due to the flattened distribution was found to be 1.76%. This variation of the flux was used as a systematic uncertainty caused by the slope.

6.5.5 Muon ID System Efficiency

A good amount of effort was placed into fully understanding the muon ID system efficiency. All the details of this systematic study can be found in Ref. [37]. In summary, the aforementioned study finds two systematic errors associated with the efficiency of the muon ID system. One systematic error stems from the energy loss simulation, which affects the muon acceptance. Through varying the thickness of the muon filters by the amount of space between the filters and the next detector element (this would amount to a 6 cm variation in the thickness of MF2, for example), a 0.4%

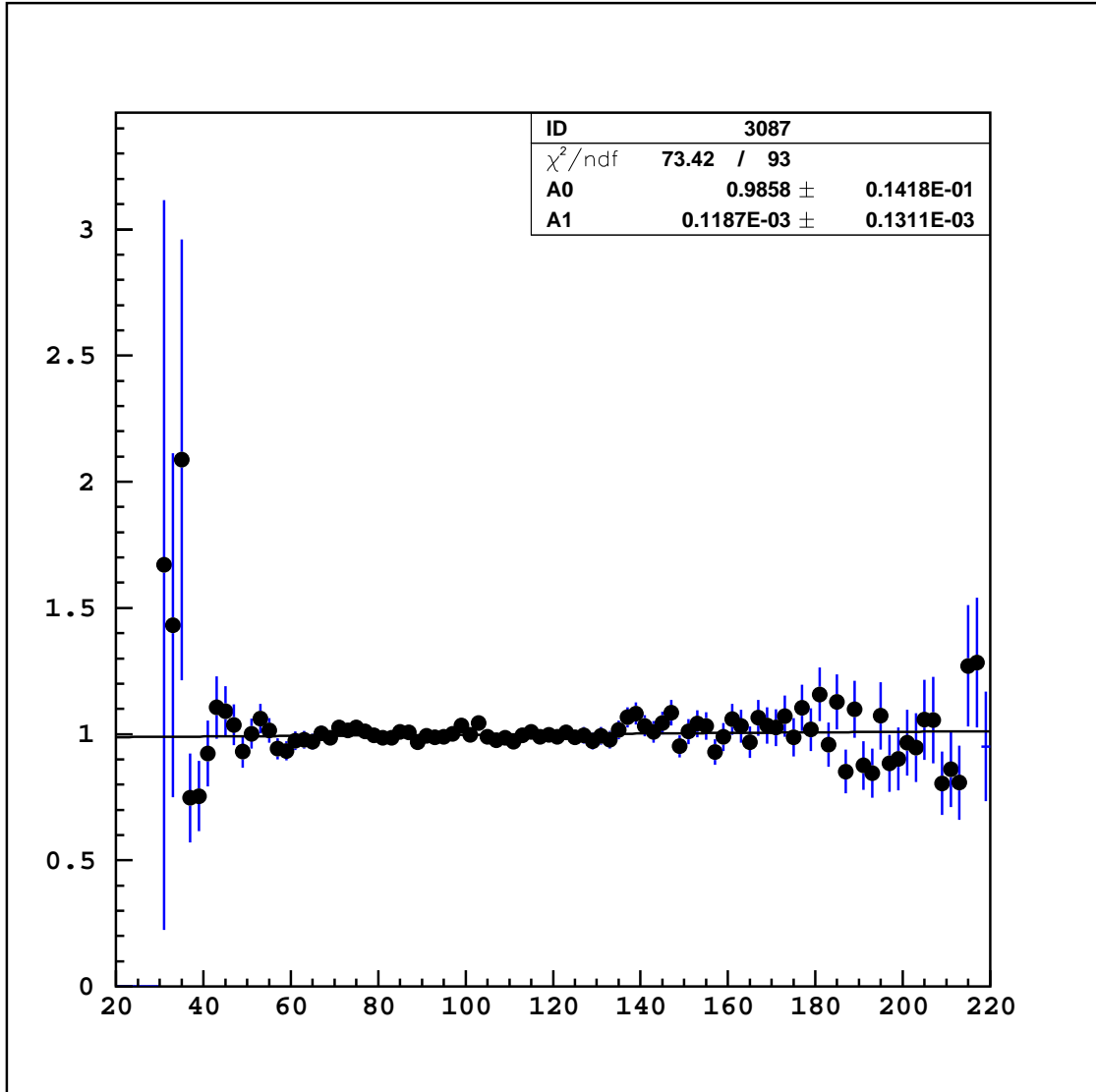


Figure 6.38: Data/MC ratio for the 1997 p_z distribution. Notice that the slope is consistent with zero.

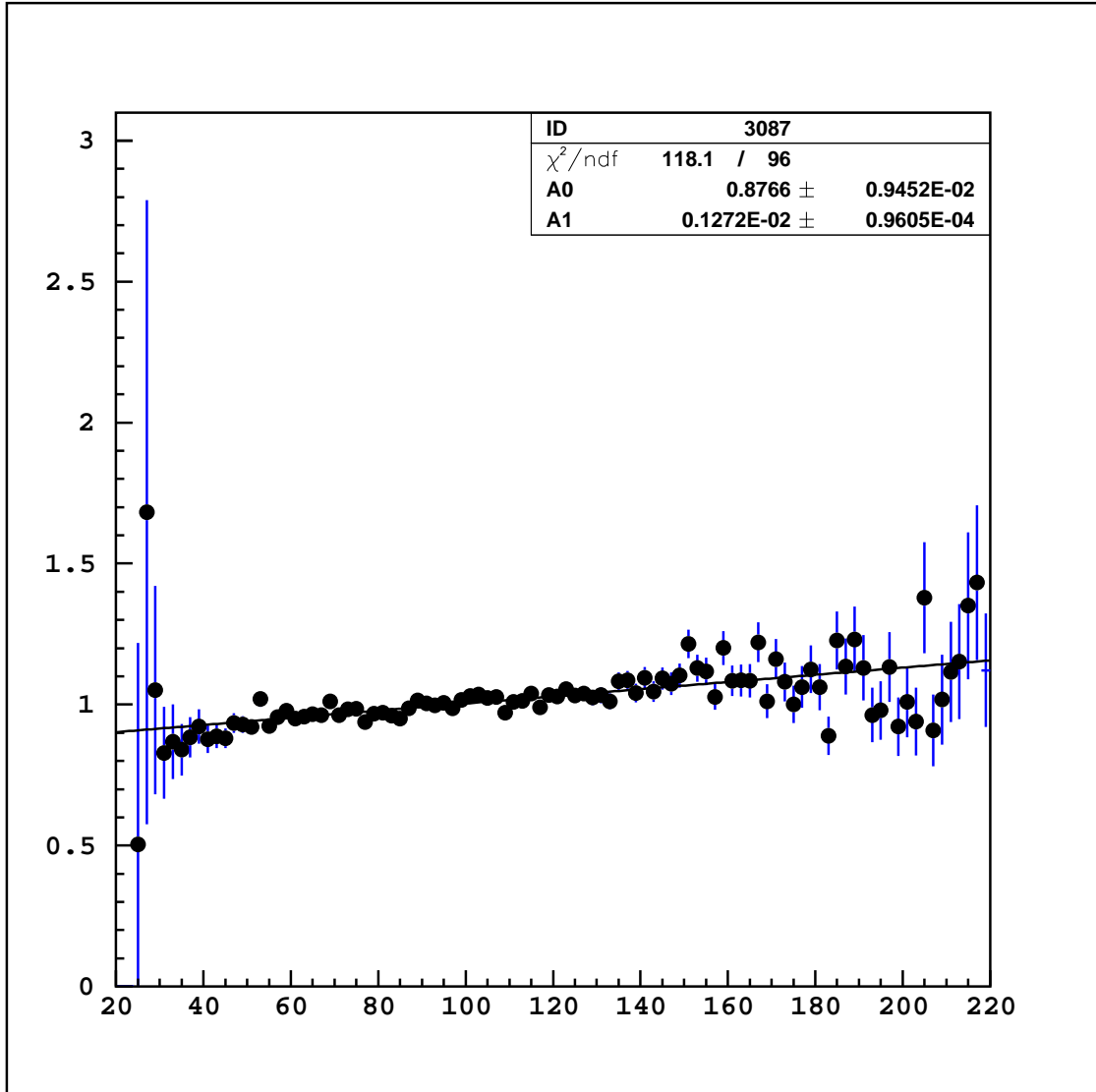


Figure 6.39: Data/MC ratio for the 1999 p_z distribution before weighting. Note that the slope is noticeably non-zero.

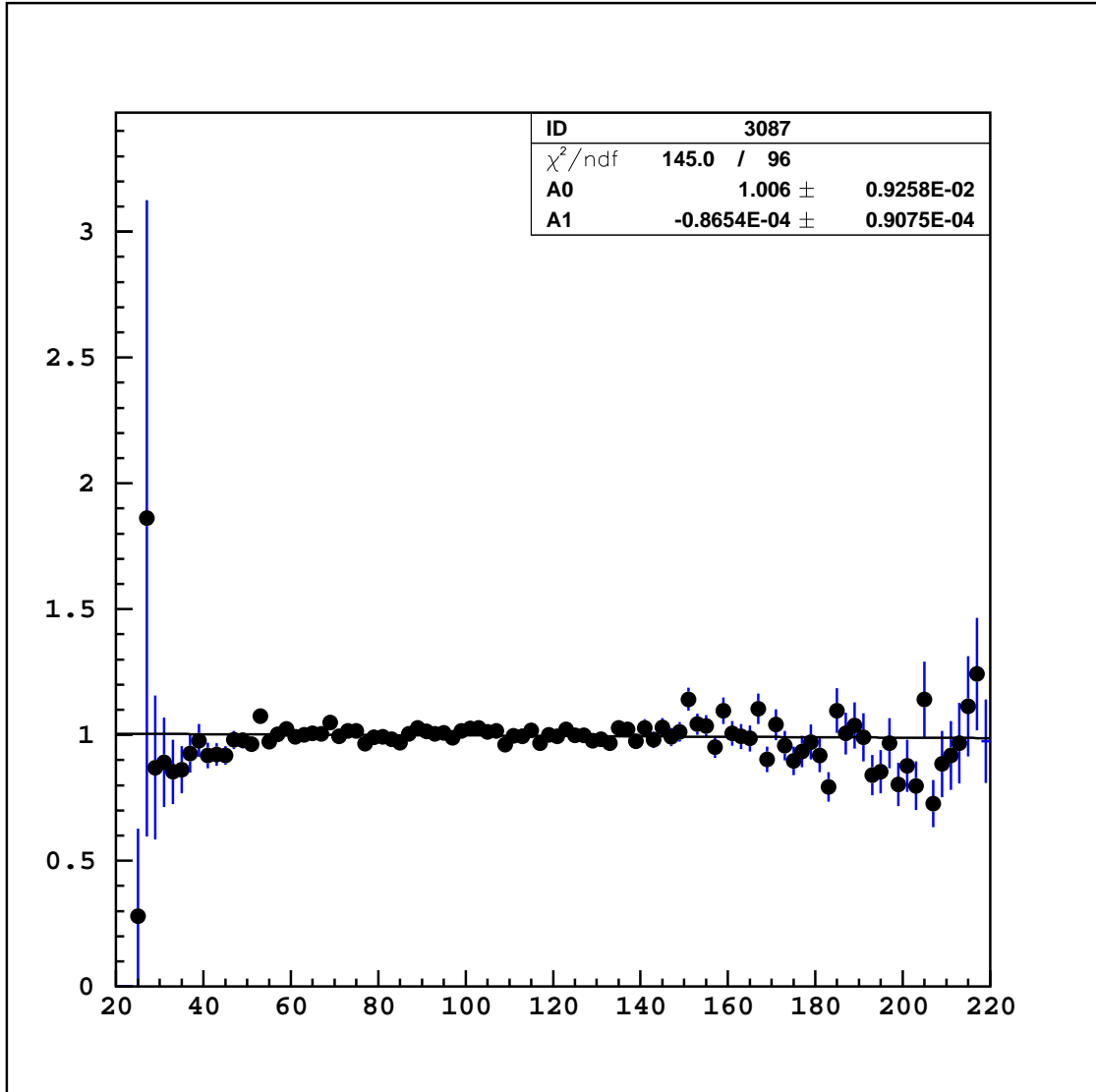


Figure 6.40: Data/MC ratio for the 1999 p_z distribution after weighting. Notice that the slope is now consistent with zero.

Source of Systematic Error on K_L Flux	$\frac{\Delta F_K(1997)}{F_K(1997)}$	$\frac{\Delta F_K(1999)}{F_K(1999)}$
$(473.0 - 1.0) \text{ MeV} \leq m_{ee\gamma\gamma\gamma\gamma} \leq (523.0 + 1.0) \text{ MeV}$	+0.04%	+0.05%
$(473.0 + 1.0) \text{ MeV} \leq m_{ee\gamma\gamma\gamma\gamma} \leq (523.0 - 1.0) \text{ MeV}$	-0.05%	-0.06%
$p_T^2 \leq (1.0 + 0.1) \times 10^{-3} \text{ GeV}^2$	+0.11%	+0.06%
$p_T^2 \leq (1.0 - 0.1) \times 10^{-3} \text{ GeV}^2$	+0.02%	-0.08%
$ m_{\gamma\gamma} - m_{\pi^0} \leq (14.0 + 1.0) \text{ MeV}$	+0.02%	+0.02%
$ m_{\gamma\gamma} - m_{\pi^0} \leq (14.0 - 1.0) \text{ MeV}$	-0.03%	+0.01%
$(94.0 - 1.0) \text{ m} \leq Z_{vtx} \leq (158.0 + 1.0) \text{ m}$	+0.16%	+0.20%
$(94.0 + 1.0) \text{ m} \leq Z_{vtx} \leq (158.0 - 1.0) \text{ m}$	+0.02%	-0.10%
$(0.95 - 0.01) \leq E_{cl}(\text{track})/p_{track} \leq (1.05 + 0.01)$	+1.24%	+2.23%
$(0.95 + 0.01) \leq E_{cl}(\text{track})/p_{track} \leq (1.05 - 0.01)$	-2.41%	-4.05%
p_z Weighting	—	1.87%
Cracks in Muon Counting Planes	0.50%	0.50%
Energy Loss in Muon Filters	0.40%	0.40%
$BR(K_L \rightarrow \pi^0\pi^0\pi^0)$	0.61%	0.61%
Total Systematic Error	+1.54%	+3.05%
	-2.57%	-4.55%

Table 6.11: Summary of systematic errors on the K_L flux.

change in acceptance was found. The other systematic error comes from simulation of cracks between scintillator paddles of MU3. A 0.5% change in acceptance resulted after varying the width of the cracks over a range of 0.2 mm, which was found to be the minimum range for which there was no improvement in muon efficiency modeling.

6.5.6 Summary of Systematic Errors

Table 6.11 provides a summary of all systematic errors. The total systematic error was obtained by summing the systematic errors in quadrature.

6.6 Upper Limit on the Branching Ratio

After all analysis requirements were applied to the 1997 and 1999 data sets, there were *zero* events found in the signal region after the masked signal boxes were opened. Furthermore, there were *zero* background events predicted from the 1997 and 1999 background MC studies. In the case of *zero* signal events and *zero* background events predicted from MC, the upper limit of the branching ratio at 90% confidence level may be calculated with the following formula [62]:

$$BR < 2.30 \left(1 + \frac{2.30\sigma_r^2}{2} \right) \cdot SES_{total}, \quad (6.9)$$

which holds for either a Bayesian or a Classical viewpoint [63]. *SES* stands for single event sensitivity, which is the signal mode branching ratio that will result in exactly one event being discovered in the masked signal box. The expression for SES_{total} is by definition:

$$\begin{aligned} \frac{1}{SES_{total}} &= \frac{1}{SES_{1997}} + \frac{1}{SES_{1999}} \\ &= F_{K,1997} \cdot A_{1997} + F_{K,1999} \cdot A_{1999}, \end{aligned} \quad (6.10)$$

where A_{1997} and A_{1999} are the signal mode acceptances for the 1997 and 1999 MC respectively.

The inverse of the total single event sensitivity is also known as the sensitivity

factor, \hat{S} . Now, $\sigma_r = \sigma_s/\hat{S}$ is the relative error in \hat{S} . σ_s can be defined as:

$$\begin{aligned}\frac{\sigma_s}{\hat{S}} &= \frac{1}{\hat{S}} \sqrt{\left(\frac{\partial \hat{S}}{\partial F_{K,1997}}\right)^2 \sigma_{F_{K,1997}}^2 + \left(\frac{\partial \hat{S}}{\partial F_{K,1999}}\right)^2 \sigma_{F_{K,1999}}^2} \\ &= \frac{1}{1+\beta} \sqrt{\left(\frac{\sigma_{F_{K,1997}}}{F_{K,1997}}\right)^2 + \beta^2 \left(\frac{\sigma_{F_{K,1999}}}{F_{K,1999}}\right)^2},\end{aligned}\quad (6.11)$$

where

$$\beta = \frac{F_{K,1999} \cdot A_{1999}}{F_{K,1997} \cdot A_{1997}}. \quad (6.12)$$

Once again, $F_{K,1997}$ and $F_{K,1999}$ may be found in formulas 6.6 and 6.7. The signal mode acceptances are tabulated in Tables 6.6 and 6.7. The systematic errors on the K_L flux, σ_F/F , are located in Table 6.11. Inserting the values of $F_{K,1997}$, $F_{K,1999}$, A_{1997} , A_{1999} and the systematic errors on the K_L flux into formulas 6.9 through 6.12 yields the following upper limits at 90% confidence level:

$$BR(K_L \rightarrow \pi^0 \pi^0 \mu^+ \mu^-) < 8.63 \times 10^{-11} \quad (6.13)$$

$$BR(K_L \rightarrow \pi^0 \pi^0 X^0 \rightarrow \pi^0 \pi^0 \mu^+ \mu^-) < 9.44 \times 10^{-11}. \quad (6.14)$$

Chapter 7

Conclusion

This analysis has presented the first experimental study of the decay $K_L \rightarrow \pi^0\pi^0\mu^+\mu^-$. The upper limit on the branching ratio for this decay inside the Standard Model at 90% confidence level was found to be $BR(K_L \rightarrow \pi^0\pi^0\mu^+\mu^-) < 8.63 \times 10^{-11}$. The upper limit on the branching ratio for this decay beyond the Standard Model at 90% confidence level was found to be $BR(K_L \rightarrow \pi^0\pi^0X^0 \rightarrow \pi^0\pi^0\mu^+\mu^-) < 9.44 \times 10^{-11}$. The latter result is 85 times lower than the expected branching ratio of $K_L \rightarrow \pi^0\pi^0X_P^0 \rightarrow \pi^0\pi^0\mu^+\mu^-$ in Ref. [27] and 88 times lower than the expected branching ratio of $K_L \rightarrow \pi^0\pi^0X_P^0 \rightarrow \pi^0\pi^0\mu^+\mu^-$ in Ref. [26] (see Table 1.2). However, the upper limit on the branching ratio of $K_L \rightarrow \pi^0\pi^0X^0 \rightarrow \pi^0\pi^0\mu^+\mu^-$ is close to the expected branching ratio for $K_L \rightarrow \pi^0\pi^0X_A^0 \rightarrow \pi^0\pi^0\mu^+\mu^-$ [26] (see Table 1.2). The result presented in this analysis for upper limit on the branching ratio of $K_L \rightarrow \pi^0\pi^0X^0 \rightarrow \pi^0\pi^0\mu^+\mu^-$ rules out the possibility of the two quark flavor changing

$s \rightarrow \bar{d}X_P^0$ process producing the dimuon decay in $K_L \rightarrow \pi^0\pi^0X^0 \rightarrow \pi^0\pi^0\mu^+\mu^-$. In addition, the two quark flavor changing $s \rightarrow \bar{d}X_P^0$ process is ruled out as an explanation of the HyperCP result for an X^0 mediating the dimuon in $\Sigma^+ \rightarrow pX^0 \rightarrow p\mu^+\mu^-$ [21]. However, the two quark flavor changing $s \rightarrow \bar{d}X_A^0$ process is still not ruled out as a possible source of the dimuon in $K_L \rightarrow \pi^0\pi^0X^0 \rightarrow \pi^0\pi^0\mu^+\mu^-$ or as an explanation of the HyperCP result for an X^0 mediating a dimuon in $\Sigma^+ \rightarrow pX^0 \rightarrow p\mu^+\mu^-$ [21].

Bibliography

- [1] T.D. Lee and C.N. Yang, **Phys. Rev.** **104**, 254 (1956)
- [2] C.S. Wu *et al.*, **Phys. Rev.** **105**, 1413 (1957)
- [3] J.H. Christenson *et al.*, **Phys. Rev. Lett.** **13**, 138 (1964)
- [4] M. Kobayashi and T. Maskawa, **Prog. Theor. Phys.** **49**, 652 (1973)
- [5] L.-L. Chau and W.-Y. Keung, **Phys. Rev. Lett.** **53**, 1802 (1984)
- [6] N. Cabibbo, **Phys. Rev. Lett.** **10**, 531 (1963)
- [7] L. Wolfenstein, **Phys. Rev. Lett.** **51**, 1945 (1983)
- [8] A. Buras *et al.*, **Phys. Rev. D** **50**, 3433 (1994)
- [9] T. Alexopoulos *et al.*, **Phys. Rev. Lett.** **93**, 181802 (2004)
- [10] J. Charles *et al.*, **Eur. Phys. J. C** **41**, 1 (2005)[hep-ph/0406184]
- [11] M. Gell-Mann and A. Pais, **Phys. Rev.** **97**, 1387 (1955)

- [12] A. Alavi-Harati *et al.*, **Phys. Rev. D** **67**, 012005 (2003)
- [13] F. Ambrosino *et al.*, **Phys. Lett. B** **632**, 43 (2006)
- [14] D.H. Perkins, **Introduction to High Energy Physics**, *4th edition*, 236 (2000)
- [15] C.O. Dib *et al.*, **Phys. Rev. D** **39**, #9, 2639 (1989)
- [16] G. Isodori *et al.*, [hep-ph/0404127] (2004)
- [17] A.J. Buras *et al.*, **Nucl. Phys. B** **423**, 349 (1994)
- [18] G. Buchalla *et al.*, **Rev. Mod. Phys.** **68**, 1125 (1996)
- [19] G. Buchalla *et al.*, **Nucl. Phys. B** **672**, 387 (2003)
- [20] R. Appel *et al.*, **Phys. Rev. Lett.** **83**, 4482 (1999)
- [21] H.K. Park *et al.*, **Phys. Rev. Lett.** **94**, 021801 (2005)
- [22] L.M. Sehgal, *Private Communication*, Sept. 2006
- [23] P. Heiliger and L.M. Sehgal, **Phys. Lett. B** **307**, 182 (1993)
- [24] L.M. Sehgal and M. Wanninger, **Phys. Rev. D** **46**, 3, 1035 (1992)
- [25] R. Funck and J. Kambor, **Nucl. Phys. B** **396**, 53 (1993)
- [26] X.-G. He *et al.*, **Phys. Lett. B** **631**, 100-108 (2005)
- [27] N.G. Deshpande *et al.*, **Phys. Lett. B** **632**, 212-214 (2006)

- [28] X.-G. He *et al.*, **Phys. Rev. Lett.** **98**, 081802 (2007)
- [29] A. Alavi-Harati *et al.*, **Phys. Rev. Lett.** **84**, #23, 5279-5282 (2000)
- [30] J.R. Batley *et al.*, **Phys. Lett. B** **599**, 197 (2004)
- [31] Fermilab Photo Archive, #00-635D.
- [32] K. Hanagaki, PhD Thesis (Osaka University, Sept. 1998), p.33, 56, 120-124
- [33] N. Solomey, **Nucl. Inst. Meth. Phys. Res. A** **419**, 637 (1998)
- [34] P. Shawhan, PhD Thesis (University of Chicago, Dec. 1999), p.32
- [35] A. Roodman, *The KTeV Pure CsI Calorimeter*, **Proceedings of the VII International Conference on Calorimetry**, Tucson, AZ, World Scientific (1998)
- [36] J. Whitmore, **Nucl. Inst. Meth. Phys. Res. A** **409**, 687 (1998)
- [37] B. Quinn, PhD Thesis (University of Chicago, June 2000), p.31,35, 66, 67, 69-73, 125
- [38] E. Zimmerman, PhD Thesis (University of Chicago, March 1999), p.30,31,51
- [39] J. Hamm, PhD Thesis (University of Arizona, 2002), p.79-82,156
- [40] C. Bown *et al.*, **Nucl. Inst. Meth. Phys. Res. A** **369**, 248 (1996)
- [41] P. Mikelsons, PhD Thesis (University of Colorado, 1999), p.56-79, 118-120
- [42] V. Prasad, PhD Thesis (University of Chicago, June 2002), p.83

- [43] A. Roodman, *CsI Clustering and Corrections*, KTeV Internal Note #577, p.27 (July 1998)
- [44] A.J. Malensek, *Empirical Formula for Thick Target Particle Production*, Fermilab Report FN-341 (1981)
- [45] C. Amsler *et al.* (Particle Data Group), PL **B667**, 1 (2008)
- [46] N. Kroll and W.Wada, **Phys. Rev.** **98**, 1355 (1955)
- [47] H. Behrend *et al.*, **Z. Phys.** **C49**, 401 (1991)
- [48] K.O. Mikaelian and J.S. Smith, **Phys. Rev.** **D5**, 1763, 2891 (1972)
- [49] M. Sadamoto, PhD Thesis (Osaka University, 1999), p. 32
- [50] J.R. LaDue, PhD Thesis (University of Colorado, 2003), p. 96-102
- [51] A.F. Bielajew, *Improved Angular Sampling for Pair Production in the EGS4 Code System*, PIRS-0287 (1991)
- [52] D.E. Groom *et al.*, **Eur. Phys. J.** **C15**, 395 (2000)
- [53] Bethe, H.A., **Phys. Rev.** **89**, 1256 (1953)
- [54] R. Brun *et al.*, *GEANT User's Guide*, CERN, Geneva (1985)
- [55] R. Brun *et al.*, GEANT 3.15 Computer Code, CERN, Geneva (1991)
- [56] W. Lohmann, R. Kopp and R. Voss, Preprint 85-03, CERN (1985)

- [57] L. Landau, **J. Phys.** **8**(*USSR*), 201 (1944)
- [58] P.V. Vavilov, **Sov. Phys. JTEP** **5**, 749 (1957)
- [59] R. Brun *et al.*, GEANT 3.21 Computer Code, CERN, Geneva (1994)
- [60] R. Feynman, *Surely You're Joking, Mr. Feynman!*, New York: W.W. Norton (1985)
- [61] J.R. Klein and A. Roodman, *Blind Analysis in Nuclear and Particle Physics*, **Annu. Rev. Nucl. Part. Sci.** **55**, 141-163 (2005)
- [62] R.D. Cousins and V.L. Highland, *Incorporating Systematic Uncertainties into an Upper Limit*, **NIM A320**, 331-335 (1992)
- [63] W.T. Eadie, D. Drijard, F.E. James, M. Roos and B. Sadoulet, *Statistical Methods in Experimental Physics*, **Americal Elsevier**, New York, 190-202, 213 (1971)